

2012 SUMMER RESEARCH PROGRAM FOR HIGH SCHOOL JUNIORS

AT THE

UNIVERSITY OF ROCHESTER'S

LABORATORY FOR LASER ENERGETICS

STUDENT RESEARCH REPORTS

PROGRAM COORDINATOR

Dr. R. Stephen Craxton

June 2013

Lab Report 375

2012 SUMMER RESEARCH PROGRAM FOR HIGH SCHOOL JUNIORS

AT THE

UNIVERSITY OF ROCHESTER'S

LABORATORY FOR LASER ENERGETICS

STUDENT RESEARCH REPORTS

PROGRAM COORDINATOR

Dr. R. Stephen Craxton

LABORATORY FOR LASER ENERGETICS

University of Rochester

250 East River Road

Rochester, NY 14623-1299

During the summer of 2012, 16 students from Rochester-area high schools participated in the Laboratory for Laser Energetics' Summer High School Research Program. The goal of this program is to excite a group of high school students about careers in the areas of science and technology by exposing them to research in a state-of-the-art environment. Too often, students are exposed to "research" only through classroom laboratories, which have prescribed procedures and predictable results. In LLE's summer program, the students experience many of the trials, tribulations, and

rewards of scientific research. By participating in research in a real environment, the students often become more excited about careers in science and technology. In addition, LLE gains from the contributions of the many highly talented students who are attracted to the program.

The students spent most of their time working on their individual research projects with members of LLE's scientific staff. The projects were related to current research activities at LLE and covered a broad range of areas of interest including experimental concept development and diagnostics modeling, computational modeling of implosion physics, materials science, laser system development and diagnostics, isotope separation, and database development. The students, their high schools, their LLE supervisors, and their project titles are listed in the table. Their written reports are collected in this volume.

The students attended weekly seminars on technical topics associated with LLE's research. Topics this year included laser physics, fusion, holography, nonlinear optics, shape memory polymers, electronic paper, and scientific ethics. The students also received safety training, learned how to give scientific presentations, and were introduced to LLE's resources, especially the computational facilities.

The program culminated on 29 August with the "High School Student Summer Research Symposium," at which the students presented the results of their research to an audience including parents, teachers, and LLE staff. Each student spoke for approximately ten minutes and answered questions. At the symposium the 16th annual William D. Ryan Inspirational Teacher Award was presented to Ms. Sage Miller, a mathematics and computer science teacher at Webster Schroeder and Webster Thomas

High Schools. This award honors a teacher, nominated by alumni of the LLE program, who has inspired outstanding students in the areas of science, mathematics, and technology. Ms. Miller was nominated by Troy Thomas and Avery Gnolek, participants in the 2011 Summer Program.

A total of 297 high school students have participated in the program since it began in 1989. The students this year were selected from over 60 applicants. Each applicant submitted an essay describing their interests in science and technology, a copy of their transcript, and a letter of recommendation from a science or math teacher.

In the past, several participants of this program have gone on to become semifinalists and finalists in the prestigious, nationwide Intel Science Talent Search. This tradition of success continued this year with the selection of Emily Armstrong as one of the 300 semifinalists nationwide in this competition.

LLE plans to continue this program in future years. The program is strictly for students from Rochester-area high schools who have just completed their junior year. Application information is mailed to schools and placed on the LLE website in early February with an application deadline near the middle of March. For more information about the program, please contact Dr. R. Stephen Craxton at LLE.

This program was supported by the U.S. Department of Energy Office of Inertial Confinement Fusion under Cooperative Agreement No. DE-FC52-08NA28302.

High School Students and Projects (Summer 2012)

Name	High School	Supervisor	Project Title
Emily Armstrong	Mercy	M. Barczys and B. E. Kruschwitz	Wavefront Measurements of High-Power UV Lasers with a Hartmann Sensor
Virginia Boy	East Rochester	R. W. Kidder	Integrating Semantic Technology with Legacy Databases
Christa Caggiano	Victor	C. Dorrer and K. L. Marshall	Fabrication and Characterization of Radial and Azimuthal Polarization Converters with Photoaligned Liquid Crystals
Ian Gabalski	Webster Thomas	P. B. Radha	Polar Drive Target Designs for Early NIF Experiments
MaryKate Hanchett	Fairport	W. T. Shmayda	Oxygen Uptake Using a Nickel Catalyst
Aaron Jo	Victor	W. T. Shmayda and N. Redden	Hydrogen Isotope Separation Using Gas Chromatography
Alec Kirkley	Pittsford Sutherland	G. Fiksel	Magnetic Field Penetration into a Conducting Hohlraum
Evan Lustick	Canandaigua Academy	R. S. Craxton and M. D. Wittman	Modeling Density Changes Inside a Cryogenic Target Using a Fabry-Perot Interferometer: A Feasibility Study
Aimee Owens	Home School	T. Z. Kosc and S. D. Jacobs	Performance Degradation of OMEGA Liquid Crystal Polarizers
Jesse Pan	Webster Thomas	S. X. Hu	Opacity Effects in Inertial Confinement Fusion Implosions
Mitchell Perry	Brighton	J. Qiao	Deformable Grating Design Optimization for Large-Aperture Pulse Compressor Systems
Raz Rivlis	Brighton	R. Boni	Optical Modeling and Analysis of a High Throughput and High Temporal Resolution Spectrometer
Lucas Shadler	West Irondequoit	W. D. Bittle	Prediction of Getter Bed Regeneration Intervals Through Absolute Humidity and Flow Rate
Julia Tucker	Brighton	R. Epstein	The Dependence of Plasma Ionization Equilibrium on Electron and Radiation Temperatures
Jack Valinsky	Brighton	W. R. Donaldson and D. H. Froula	Electronic Analysis of Pulse Propagation Through an X-Ray Framing Camera
Charles Wan	Penfield	K. L. Marshall	Dynamic Mechanical Analysis of Cryogenic Target Materials

Wavefront Measurements of High-Power UV Lasers with a Hartmann Sensor

Emily Armstrong

Our Lady of Mercy High School

LLE Advisors: Matthew Barczys, Brian Kruschwitz

Laboratory for Laser Energetics

University of Rochester

Summer High School Research Program

2012

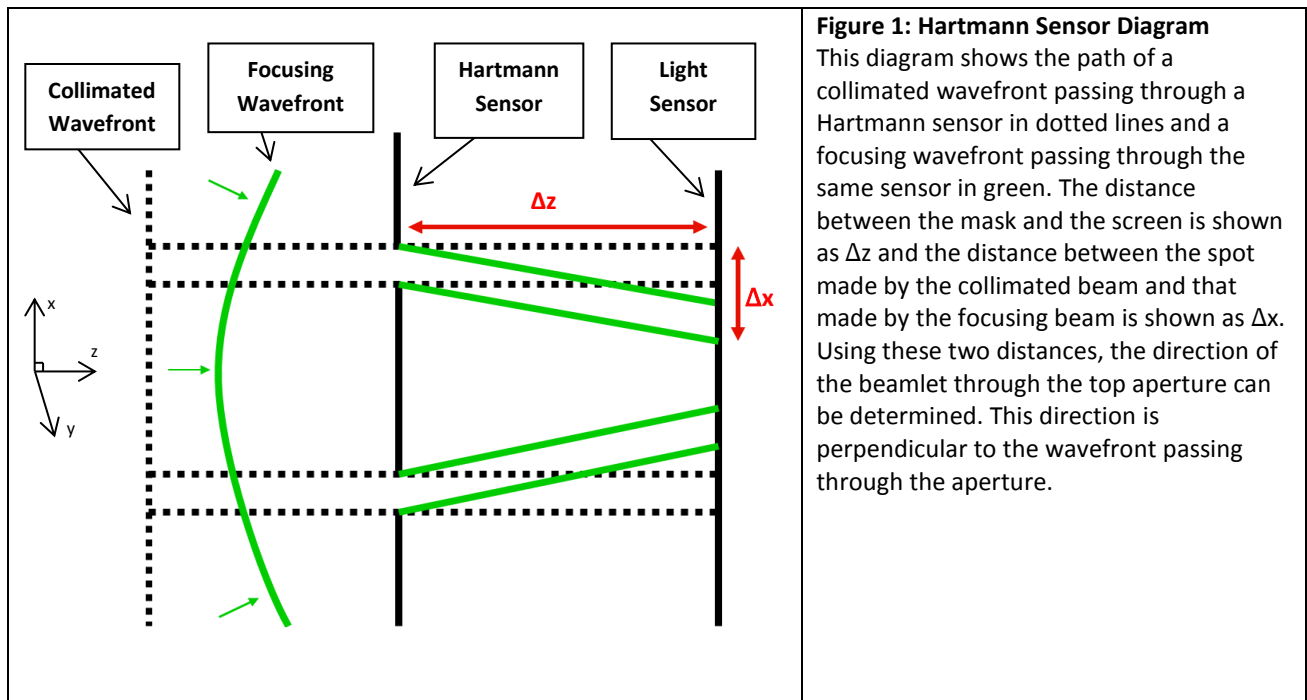
1. Abstract

Experiments were conducted to determine the effectiveness of the Hartmann sensor as a wavefront diagnostic on the UV portions of the OMEGA EP laser system. Programs in MATLAB were used to model Hartmann grid patterns and then reconstruct wavefronts from grid images. Simulations were run to design basic Hartmann grids for a laboratory proof-of-concept setup with a 532 nm visible laser. Sensor masks were then tested in a series of experimental trials to determine the accuracy of a basic Hartmann sensor. Models of the experimental system were created in OSLO, a commercial ray-tracing program, and compared to the gathered data to verify the reconstruction results. A commercial wavefront sensor was also added to the experimental set-up to provide further confirmation of the Hartmann sensor reconstructions. The concept was proven that the Hartmann sensor would be an effective method for optional wavefront analysis on UV beams entering the OMEGA EP target chamber as well as on the fourth harmonic probe beam, operating at 263 nm, used for diagnostics.

2. Introduction

Wavefront sensing is crucial on large laser systems such as OMEGA EP [1]. An accurate wavefront measurement gives information on whether or not the beam is collimated. If the beam is not collimated, it may not focus at the desired location, such as at the center of the OMEGA EP target chamber. Small scale aberrations indicative of damage, misalignment, or manufacturing errors in the optics of the system are also visible on wavefront measurements. In cases when minimal wavefront aberration is desired, it is valuable to have a measurement of the laser wavefront to help diagnose the optical system.

The Hartmann sensor is an example of a relatively simple technique for determining wavefronts known as a screen test [2]. As shown in figure 1, the sensor itself is a grid of apertures through which the beam passes, blocking sections of the original beam. The beam sections passing through the sensor then land on the light sensor of a camera, forming a spot pattern. Using a beam that is close to perfectly collimated, a reference spot pattern is created for a given sensor. By comparing the reference pattern to the pattern made by the test beam, the slope of the wavefront can be determined at each point that passed through an aperture.



To determine the direction of a given beamlet, the camera is used to measure the distance between the reference spot of a given aperture and the spot created by the test beam. The beamlet slope in figure 1 is equal to the distance between the spots (Δx) divided by the distance from the mask to the camera (Δz). By using a Hartmann sensor with many apertures, equations are obtained for the variations in height of the wavefront $h(x,y)$ with respect to x and y :

$$\frac{\partial h}{\partial x} = \frac{\Delta x}{\Delta z} \quad (1)$$

$$\frac{\partial h}{\partial y} = \frac{\Delta y}{\Delta z} \quad (2)$$

where $\partial h/\partial x$ and $\partial h/\partial y$ are components of the slope and Δx and Δy are distances that a spot moves from its reference position. These equations model the local wavefront slopes over the entire section of the beam that passes through the sensor. Integrating these slope equations over the space the sensor occupies gives a reconstruction of the actual wavefront incident on the Hartmann sensor in the form $h(x,y)$.

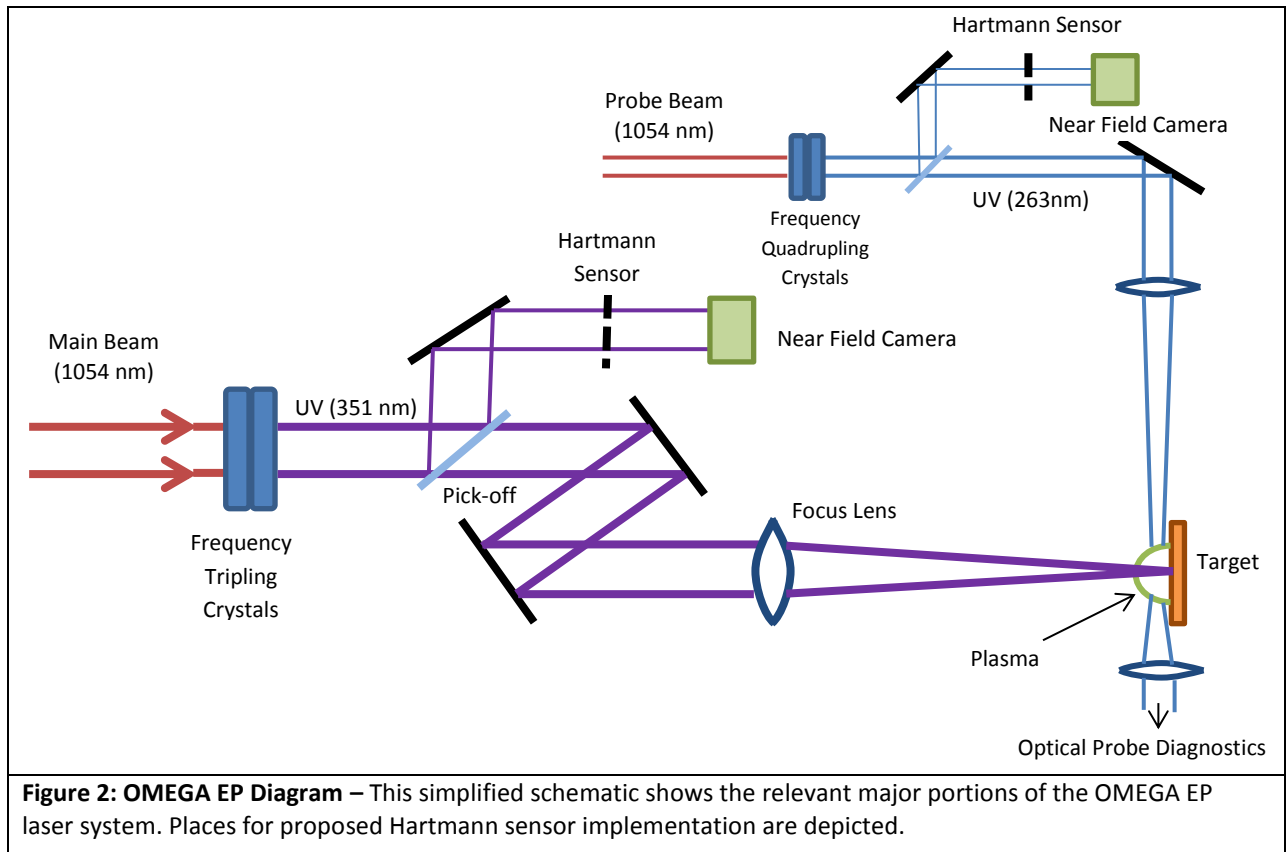


Figure 2: OMEGA EP Diagram – This simplified schematic shows the relevant major portions of the OMEGA EP laser system. Places for proposed Hartmann sensor implementation are depicted.

Portions of the OMEGA EP laser system relevant to the implementation of a Hartmann sensor are shown above in figure 2. The main beams come from a source operating at 1054 nm.

They are amplified at this wavelength, and then pass through the frequency tripling crystals, which shift them to 351 nm. They are then brought to focus on a target, and a plasma is created. A smaller beam, the 1054 nm probe beam, passes through frequency quadrupling crystals and its resultant wavelength is 263 nm. This beam is used to image plasmas created during laser shots with an interferometry technique. Samples of both the probe beam and the main beams can be taken using pick-offs, and their wavefronts can be diagnosed using Hartmann sensors.

The Hartmann sensor was selected as the best method for use with the UV beams on the OMEGA EP laser system for several reasons. First, it is compatible with the system because the sensor masks have no refractive elements, and can therefore be used interchangeably with UV lasers of both wavelengths. In addition, the Hartmann sensor supports use with other wavelengths since the apertures are designed to be large enough to minimize diffractive effects, which would cause interference and blur the spot pattern. Most importantly, the Hartmann sensor mask can be manufactured inexpensively and easily inserted into the existing laser diagnostics on the OMEGA EP system. A Hartmann sensor mask could simply be placed in front of the near field cameras on laser shots for which a wavefront measurement is desired.

The implementation of Hartmann sensors on the OMEGA EP laser would be valuable for several purposes. One use for a Hartmann sensor would be to determine the wavefront of the fourth harmonic probe beam [3] as it enters the OMEGA EP target chamber. Images of the plasma taken using this beam are altered if the wavefront of the probe beam is aberrated. It would be useful to know the wavefront of the beam before it is passed through the plasma to be able to account for this error. A second use for the Hartmann sensor would be to gain an

estimate of the final wavefront on the main UV beamlines (351 nm wavelength). This would give a clearer picture of the aberration introduced to the beams by the optics that transport them from the final measurement point in the infrared sections to the frequency tripling crystals. After the crystals, the beams operate in the UV, and currently there is no way to measure the beamline wavefront. In the future, Hartmann sensors might also be used to determine the exact paths of the focusing beams approaching target chamber center and the area the beams cover on the final optics before entering the target chamber, which can in turn be used to calculate the energy intensity on those optics. Currently, this energy intensity is unknown, and a highest plausible intensity must be assumed in order to avoid damaging the optics. This is a current limiting factor on the energy output of the system, and an accurate wavefront measurement could allow an increase in the total energy output of OMEGA EP.

In this work, a Hartmann sensor was designed to fulfill the need for wavefront sensing in the UV portions of the OMEGA EP laser system. Both the mask itself and the wavefront reconstruction software were tested in an experimental test system. The results from the tested Hartmann sensor were compared to wavefront measurements from a Shack-Hartmann sensor, and found to be accurate. These results affirm the effectiveness of the Hartmann sensor, providing a proof-of-concept for implementing the technique on OMEGA EP.

3. Experimental Set-up

The Hartmann sensor was tested in a small-scale optical system. Figure 3 shows a schematic diagram of the experimental set-up. The laser used for the tests was a 5 milli-watt beam operating at 532 nm, 1 mm in diameter.

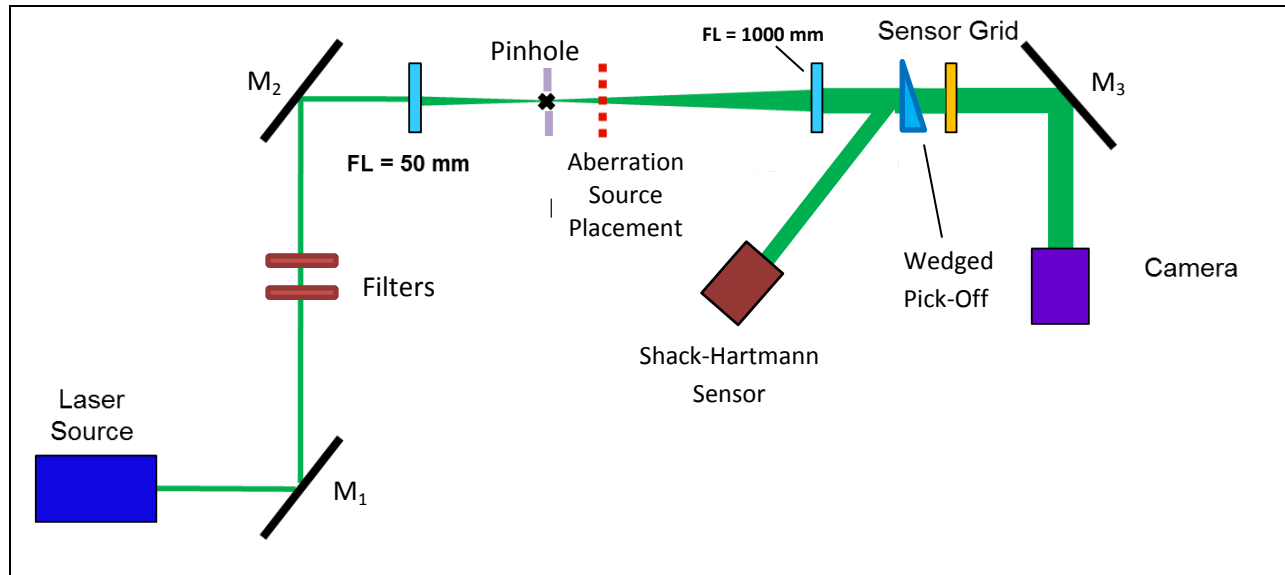


Figure 3: Optical System Diagram – This is a simplified depiction of the optical set-up used to test the Hartmann sensors. Black lines represent mirrors and the black X indicates where the beam comes to focus in the telescope system.

The mirrors M_1 and M_2 are used to precisely position and point the beam. In between these mirrors is a pair of filters to decrease the intensity of the beam and avoid damaging the sensitive light sensor in the camera. A beam expander is used to increase the diameter of the laser in order to fill the approximately 11 mm diameter of the sensor grid. A 50 mm focal length plano-convex lens made of fused silica is used to bring the beam to focus through a pinhole. This has a diameter of 100 μm and blocks light that is not focusing in the desired path in order to smooth the spatial intensity profile of the laser beam. Then, when the beam radius has increased by a factor of 20, a 1000 mm focal length lens collimates the beam. The beam is then passed through the Hartmann sensor. The wedge pick-off shown in figure 3 was added before the sensor grid to allow the use of a Shack-Hartmann wavefront sensor in the system.

Using the spot images from the system itself as a reference, wavefront aberrations were introduced by adding optical elements (aberration sources shown in fig. 3) approximately 5 cm after the focus of the beam expander to disrupt the collimation. Plano-convex lenses were

used, with focal lengths of 200, 300, and 500 mm. By comparing the spot patterns of the system with and without these lenses, the additional wavefront error these lenses introduce can be measured.

3.1 Design Simulations

There are several key parameters for designing a Hartmann sensor. The number of apertures should be maximized within practical limits to ensure a thorough sampling of slope points and create wavefront images with acceptable resolution. However, the apertures themselves must be large enough to minimize diffractive effects. The spacing of the apertures also must be large enough to prevent interference patterns from obscuring the spot image on the image sensor. This spacing is also significant for wavefronts with a high degree of aberration since spots from different apertures can overlap or switch positions relative to the reference image if those apertures are not far enough apart. Machining capabilities for aperture size and spacing must also be taken into account for the final product sensor. To avoid delays getting the simple grids manufactured in metal, the sensors for these tests were created by printing the grid design onto transparency slides using a laser printer. Although not the ideal material to block out the undesired sections of light, the transparency sensors were able to produce completely adequate spot patterns.

The light sensor of the available camera was 15.2 mm square, so the Hartmann sensor grid was also designed with this shape and size. An aperture diameter of 0.0635 cm was selected as the minimum size. Since this diameter is over one thousand times larger than the 532 nm wavelength of light in use on the test setup, the effect of diffraction expected on the resulting image would be minimized. This allows a maximum of 23 apertures on each side of

the square grid. However, this configuration is not likely to result in a clear spot image since the spots will be too close and will blur together. Therefore, simulations were carried out to determine an aperture size and spacing capable of producing an acceptable image.

A MATLAB script was written to model several configurations of Hartmann sensors through which various wavefronts were propagated. The sensors were modeled using logical matrices. Spaces within the apertures of the sensor were given a value of one, while outside areas were set to zero.

Figure 4 shows the logical matrix of the 19 by 19 grid eventually used in the experiment. Wavefronts

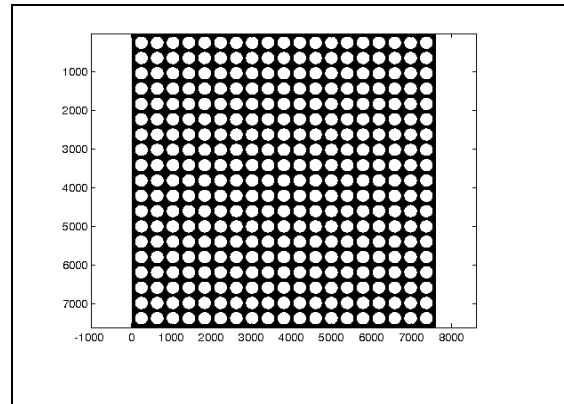


Figure 4: 19 by 19 Hartmann Sensor
This is a representation of the logical matrix used to model the Hartmann sensor used in the experiment. The axis scales represent the number of elements on each axis.

could then be mathematically modeled and multiplied by the logical matrix in order to simulate which sections of a beam would pass through the sensor. Using a MATLAB function, FresnelPropagator [4], the patterns formed by propagating these zonal sections of the beam a specified distance were calculated and displayed. Figure 5(a) is a plot of the simulated spot pattern from the 19 by 19 Hartmann grid, propagated 250 mm from the grid. This simulation shows that the designed sensor can produce clear, acceptable images that a computer should be able to read and reconstruct, without confusing light from adjacent spots. The quality of the images was verified by running the simulated spot patterns through reconstruction code and seeing that the expected wavefront images of various simulated tilts and defocuses were obtained.

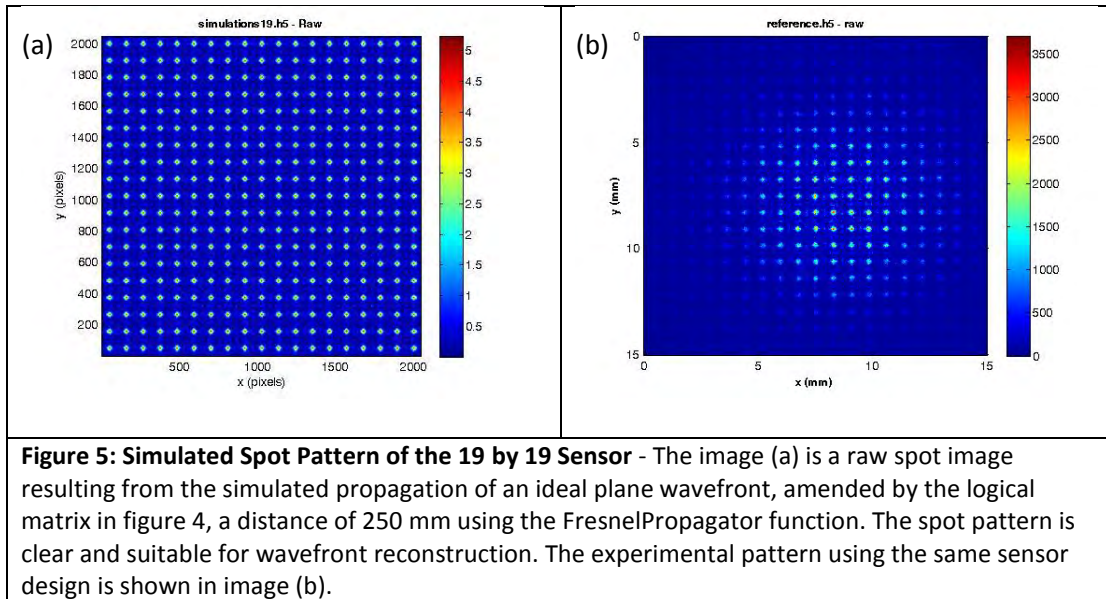


Figure 5(b) shows the spot pattern attained using the designed sensor in the lab set-up. This experimental result agrees quite well with the simulated data. The simulation includes effects from diffraction, causing slight fringes to appear between the spots. The experimental diagram shows these effects as well. The clarity in size and spacing of the spots in the pattern is also consistent. The brightened central area on the experimental pattern is caused by the intensity profile of the experimental laser, which was brightest in the center and faded towards the sides of the beam.

4. Wavefront Measurements

Wavefront measurements were taken for the test laser system with each of the three aberration source lenses. These measurements were taken simultaneously using the Hartmann sensor being tested and the Shack-Hartmann sensor.

4.1 Hartmann Sensor

When examining wavefront images, it is common to remove tilt and power from the image in order to see lower-level and smaller features in the wavefront. Removing tilt fits a plane to the wavefront modeled $h(x,y)$ and subtracts it off, eliminating effects that most often result from misalignment between the beam and the camera. Power is removed because, on an uncollimated beam, the wavefront errors from this aberration often overshadow higher-order aberrations. By fitting a paraboloid shape to the image and subtracting it out, aberrations such as coma and astigmatism become evident. Figure 6 shows all of these images from the three test lenses, as determined by the Hartmann sensor reconstructions.

Peak-to-valley (P-V) and root-mean-square (RMS) values were calculated for each image to provide statistics to compare with results from other wavefront sensors. The P-V measurement is most useful on the raw wavefront reconstructions and those with removed tilt, because it quantifies the amount of power or defocus on the beam. When this effect is removed, the RMS value becomes a more useful statistic since it measures the amount of variation about the mean distance and provides a measurement of the amount of higher-order aberration.

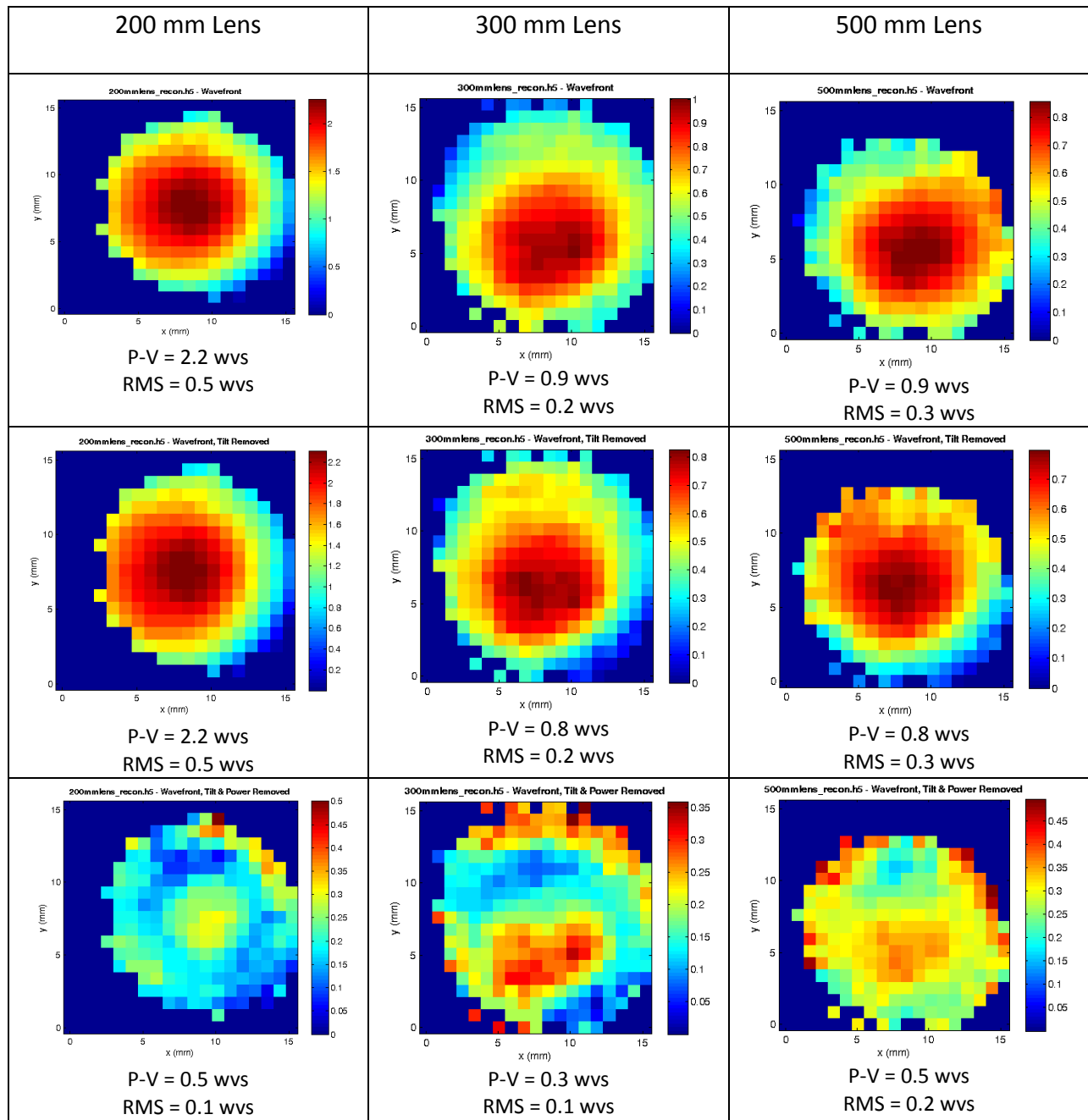
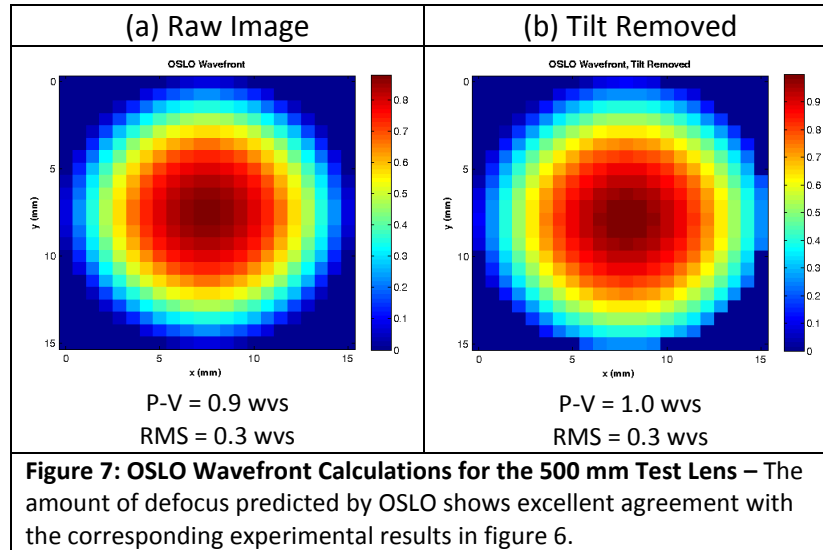


Figure 6: Hartmann Sensor Wavefront Reconstructions – These diagrams show the wavefronts measured using each test lens. The top row shows raw wavefront images, the middle the same images with tilt removed, and the bottom the images with both tilt and power removed. When the defocus seen in the first two rows is removed, each image shows, to varying extents, coma, an aberration that resulted from slight lens misalignment.

In order to provide a reference to assess the accuracy of the reconstructed wavefront images, the system with the 500 mm test lens was modeled using a ray-tracing optical modeling program, OSLO [5]. The shape of each lens surface, the spacing of each surface, and the

material of each lens were entered into OSLO, and an expected wavefront measurement was calculated. The raw and tilt-removed wavefronts measured by the Hartmann sensor for the 500 mm lens in figure 6 show close agreement to the OSLO calculations in figure 7.



By adjusting the model distance parameters within setup and measurement uncertainties, the raw wavefront prediction and tilt-removed wavefront were found to be almost identical. When power was removed from the OSLO wavefront, a perfectly flat wavefront was measured. This occurred because OSLO assumed perfect lens alignment, and no significant higher-order aberration was introduced.

4.2 Shack-Hartmann Sensor

In order to further verify the results from the Hartmann sensor reconstructions, a commercial Shack-Hartmann sensor, a HASO3 128-GE, [6] was added to the optical system. Similar to the Hartmann sensor, this Shack-Hartmann sensor compares spot patterns to make wavefront measurements. However, the use of lenslets instead of empty apertures and a pre-programmed reference image on the Shack-Hartmann sensor distinguish the two techniques.

The Shack-Hartmann wavefronts showed the coma and other higher-order imperfections caused by human error in the alignment of the system, giving greater credibility to the Hartmann results. Figure 8 shows the Shack-Hartmann results comparable to the Hartmann data in figure 6.

Several factors impact the ability to make perfect comparisons between the Hartmann and Shack-Hartmann results. The Shack-Hartmann sensor imaged a reflection of the beam from a pick-off. An unwanted reflection from the second surface of the pick-off optic overlapped with part of the desired reflection, making it possible to measure only a section of the beam on the light sensor. This led to smaller peak-to-valley and root mean square values. By measuring the distance between the center of the beam image and the outer edge and assuming a perfect paraboloid shape (i.e. power dominates the wavefront shape), it is possible to scale the peak-to-valley value to account for the smaller P-V size of the beam and create an estimate of the measurement had the beam size been larger. Using this scaling technique, the wavefront statistics of the Hartmann and Shack-Hartmann sensor results show even closer agreement.

The scaling process is most accurate on the 500 mm lens, since it introduces the least power. The small difference between the tilt-removed Hartmann sensor P-V measurement with the 200 mm lens (2.2 wvs) and the corresponding Shack-Hartmann measurement (1.5 wvs) is likely because of the fact that power is not the only aberration in the wavefront.

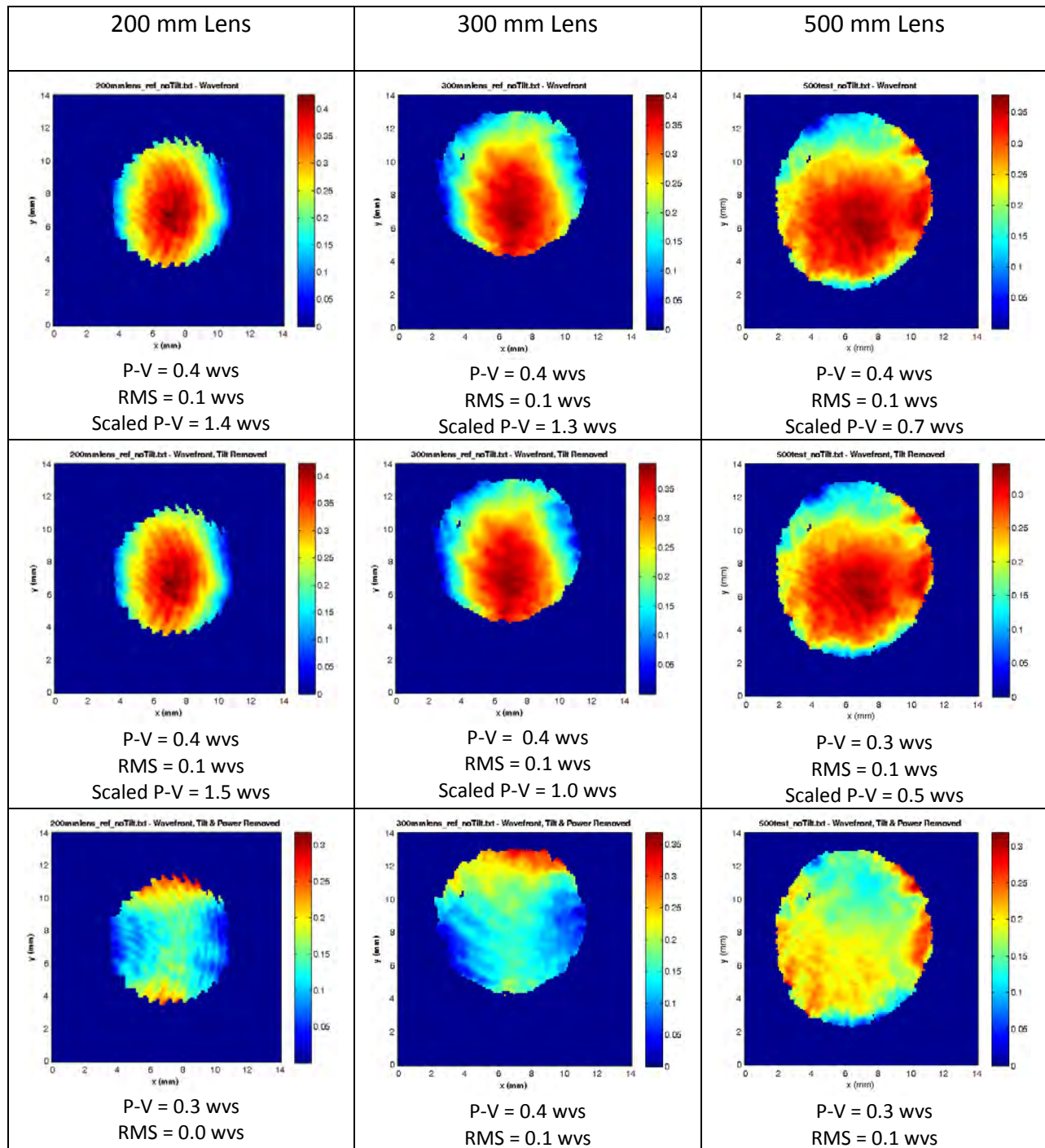


Figure 8: Shack-Hartmann Sensor Wavefront Reconstructions – This figure shows the Shack-Hartmann reconstructions corresponding to the Hartmann wavefronts in figure 6. Raw wavefront measurements and those with tilt removed have scaled peak-to-valley values using the technique discussed in the text. The interference fringing visible on several of the images is due to the overlap of the secondary reflection from the opposite side of the wedged pick-off.

Referencing the Shack-Hartmann images also adds differences between the Shack-Hartmann and Hartmann measurements. Since the reference image for the Hartmann sensor includes minor errors in the collimated system, these aberrations do not appear in the reconstructions. Although a shear plate was used to check the collimation, some error remained present in the optical system. The Shack-Hartmann sensor uses software with a pre-made factory reference pattern, and so does not account for the aberration of the system. In order to remove these effects from the Shack-Hartmann image, a wavefront measurement of the system itself was made and subtracted from the later measurements. Since adding the aberration sources affected the pointing and size of the beam, this manual referencing process was not completely accurate in the removal of system aberrations. These referencing and size errors can account for the discrepancy between the Shack-Hartmann and the Hartmann measurements, which still show excellent agreement.

5. Conclusions

The ability to use Hartmann sensors would be valuable to the OMEGA EP system because it would allow wavefront diagnosis in UV portions of the system, something that is not currently feasible. A simply manufactured Hartmann sensor was tested and proven to have acceptable accuracy in a small system. MATLAB code was used to determine an aperture size and spacing to create legible spot patterns. Comparison between the experimental results from the designed Hartmann sensor and those from a Shack-Hartmann sensor confirmed the Hartmann sensor's accuracy. Hartmann sensing techniques have therefore been proven to be effective and suitable for implementation on the OMEGA EP laser system.

It will benefit OMEGA EP in several ways to incorporate the use of Hartmann sensors. Ultraviolet portions of the system would be diagnosable, as would the UV probe beam used for plasma interferometry. Since the interferometry results are affected by wavefront aberrations, a measurement of the beam prior to passing through the plasma would be a useful diagnostic. On the larger system, UV wavefront measurements would provide information on wavefront aberrations introduced by the final IR optics and the wavefront shape before entering the target chamber. Knowing these measurements will also help determine the area the beam covers on the final UV optics, allowing a calculation of energy intensity there, a current limiting factor for the beam entering the target chamber. Taking measurements with a Hartmann sensor will aid in the adjustment of optics to reduce wavefront aberration, ultimately allowing an increase in the energy output of the system.

6. Acknowledgements

I would like to thank my advisor, Dr. Matthew Barczys, for giving me the opportunity to work on this project and his constant support throughout the summer. Dr. Brian Kruschwitz's assistance was invaluable in creating the simulation code. Parts of the wavefront reconstruction code were written by Dr. Seung-Whan Bahk, and I greatly appreciate this contribution to the project. Finally, I owe gratitude to the Laboratory for Laser Energetics and all who are involved there, and especially to Dr. Craxton for offering me this opportunity.

7. References

- [1]. J. H. Kelly, L. J. Waxer, V. Bagnoud, I. A. Begishev, J. Bromage, B. E. Kruschwitz, T. J. Kessler, S. J. Loucks, D. N. Maywar, R. L. McCrory, D. D. Meyerhofer, S.F. B. Morse, J. B. Oliver, A. L. Rigatti, A. W. Schmid, C. Stoeckl, S. Dalton, L. Folsbee,

M. J. Guardalben, R. Jungquist, J. Puth, M. J. Shoup III, D. Weiner, and J. D. Zuegel. "OMEGA EP: High-Energy Petawatt Capability for the OMEGA Laser Facility," J. Phys. IV France 133, 75 (2006).

[2]. Daniel Malacara, ed., Optical Shop Testing (J. Wiley and Sons, New York, 1978).

[3]. D. H. Froula, R. Boni, M. Bedzyk, R. S. Craxton, F. Ehrne, S. Ivancic, R. Jungquist, M.J. Shoup, W. Theobald, D. Weiner, N.L. Kugland, and M.C. Rushford. Optical diagnostic suite (schlieren, interferometry, and grid image refractometry) on OMEGA EP using a 10-ps, 263-nm probe beam. Rev. Sci. Instrum. 83, 10E523 (2012).

[4]. B. E. Kruschwitz, Unpublished, 2012.

[5]. Optics Software for Layout and Optimization [Software]. (2009). Littleton, MA: Lambda Research Corporation.

[6]. Prosilica GE2040, Allied Vision Technologies.

Integrating Semantic Technology with Legacy Databases

Virginia Boy

East Rochester High School

LLE Advisor: Richard Kidder

March 2013

Abstract:

A study was conducted to find the optimal approach for integrating semantic technology across the extensive data banks utilized by the Laboratory for Laser Energetics (LLE). In addition to the immense amount of information stored by LLE, there are multiple repositories of data, making it difficult to locate and process information critical to the operations of the laser facilities. Semantic technology facilitates information processing by linking data and associated properties into an ontology model. The use of Java frameworks such as Jena and D2RQ was explored in order to allow this scattered data to be imported into a single ontology without duplicating the information.

Introduction:

The Current LLE Database System

Over the years, the Laboratory for Laser Energetics (LLE) has accrued vast quantities of information relating to its operations, spanning from data on the diagnostics and optics used to the scientists and specialists who design and support them. There is also a large quantity of data that is vital to the safe and efficient operation of the Omega Laser Systems. Much of this information is contained in the LLE database system, which currently exists in a scattered and

decentralized form, requiring both knowledge of the nonlinear database setup and SQL queries in order to access. Querying for data in the system can be complicated and confusing; success depends greatly on the querying skills and reasoning of the user. As a result of these difficulties, few people are able to utilize this resource in its entirety. Usage of the database is generally limited to the specific area of LLE in which a scientist works.

An Overview of Semantic Web Technology

Semantic web technology is a primitive artificial intelligence that allows a computer to link meanings to data. This meaning is applied through tags known as metadata, and allows the system to associate relationships within the data and reason on the system [1]. Using this technology, each object is represented by an individual, which is then assigned properties. Various categories of properties exist that allow these individuals to be grouped with both other individuals and corresponding primitive datatypes, creating an interconnected web of information. Object properties link individuals, while datatype properties are used to assign values to individuals. Individuals that are similar or share relationships are grouped into units known as classes. This allows objects of the same type to all be grouped together in one place. Individuals can belong to multiple groups, giving the ontology the capabilities to sort the data in multiple ways. In addition to the categories of relationships that exist, there are also properties and restrictions that can be associated with these relationships, allowing for greater inferencing capabilities of the system. A functional property warrants that each individual can only be related to one other individual through this property. This allows the computer to infer whether multiple individuals refer to the same entity. Properties can also be labeled as transitive, simplifying the linkage of long chains of objects along the same property. Symmetric properties also facilitate groupings of individuals linked to each other by the same property. All of these

properties group together similar information, increasing the efficiency of data processing and eliminating the need for users to parse through large amounts of data in order to find the desired set of information [2].

One of the major benefits of applying semantic technology to the LLE database system is the ability of reasoners to classify and make inferences on the asserted relationships in the system. Reasoners use user-defined properties and a standard set of rules to classify the ontology. Its classification is used to both make inferences on relationships in the ontology and to populate defined classes with corresponding individuals. Reasoners commonly used with Semantic Web technology, such as Pellet and Fact++, use open world reasoning (OWR). OWR dictates that nothing can be assumed that hasn't been explicitly stated. If a reasoner following this assumption is classifying an ontology and detects any sort of ambiguity as to what classifications a class should receive, the reasoner makes no assumptions and the class is not sorted into the questioned groupings. This is an important feature of semantic reasoners, as it eliminates errors based on ambiguity. Although they are highly versatile, reasoners do require that the given ontology has no inconsistencies, and doesn't contain any conflicting data.

Framework Technologies

One of the major obstacles in applying semantic technology to the LLE database system is importing all of the data into a single ontology setup. As was determined by previous studies, it is impractical to attempt to transfer all of this data by hand [3]. This database would be impossible to keep up to date, and data inaccuracies could result. This system would also require duplication of all of the information at LLE. This data replication would be redundant and would require massive amounts of memory storage in order to be maintained.

Previous projects identified Apache Jena as a potential Java framework that would allow a more automated population of the ontology [4]. Jena is an open

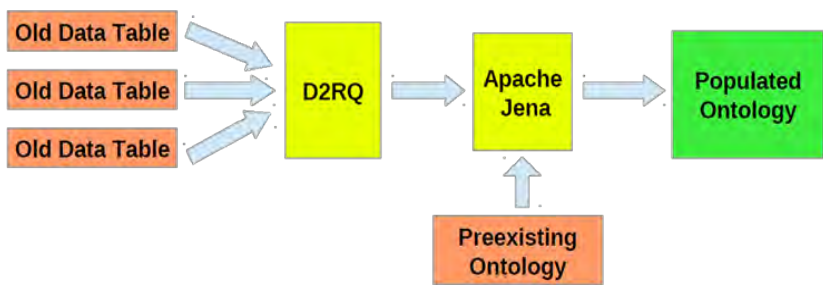


Figure 1: Graphical representation of the framework structure setup used to form the ontology. It is important to note that data is merely referenced through this process, and is not duplicated.

source semantic web framework that contains an application programming interface (API). It has capabilities to extract data from files, databases, URLs, or a combination thereof, and can export to resource data framework (RDF) graphs. In addition to being flexible enough to read data from various types of sources, it is easily queried through SPARQL, a query language for databases, and provides support for OWL, a language commonly used in ontologies. The D2RQ platform was also discovered for use in automating the population of the ontology. D2RQ is used to map non-RDF databases and allows them to be imported and manipulated using Jena. This is invaluable to the function of the LLE ontology as the majority of information currently held in the database system is contained in relational, non-RDF databases. Figure 1 represents a visual model of the framework software setup.

Research and Development

Implementing Jena and D2RQ

The first step in automating ontology population was to implement the Jena framework. This was done by running Jena in a Java programming environment. Jena was used to generate and manipulate an ontology during the runtime of the program, and upon its conclusion the ontology was exported and saved to a file. The saved file could then be opened using Protégé, an

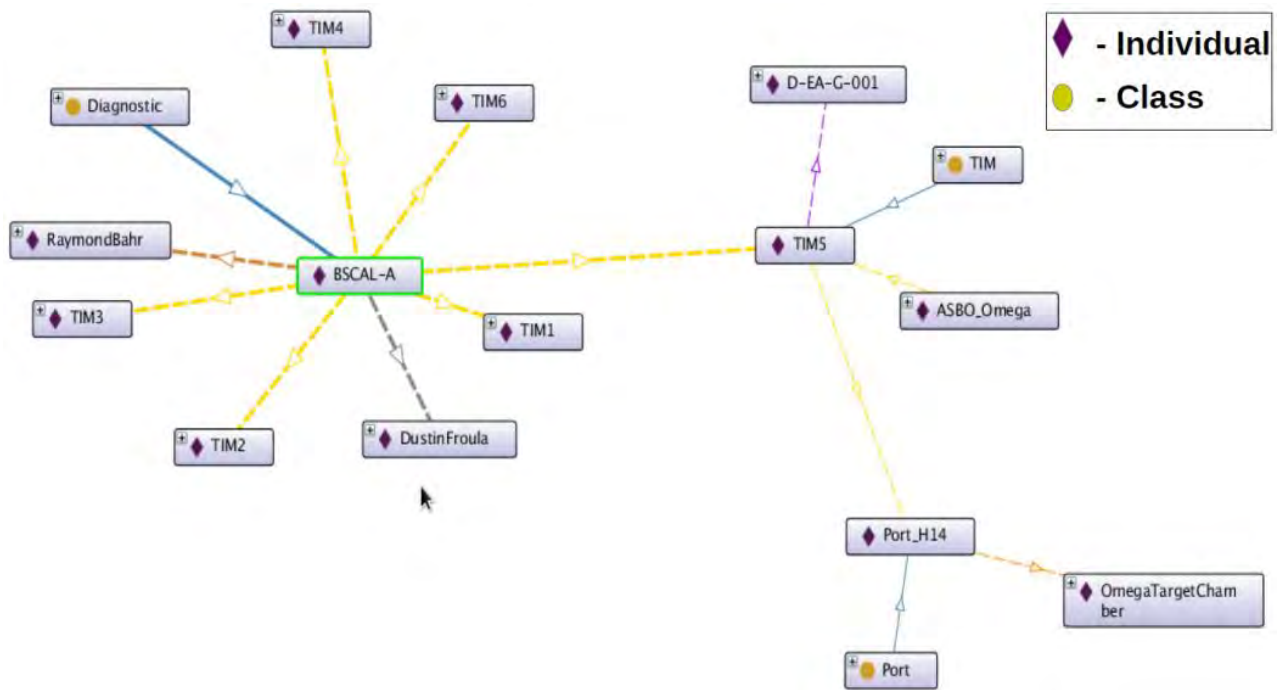


Figure 2: Graphical representation of relationships by Protégé. Each relationship, denoted by a color-coded line, works to join data into an interconnected web of information.

ontology mapping framework as shown in figure 2. Through this method, the produced ontology could be easily analyzed using a visual interface. Using a combination of the Jena frameworks and Protégé, it was demonstrated that Jena could easily import premade ontologies, as well as any other user-provided information. This conglomeration of data could be seamlessly merged to produce a single, coherent ontology. Once Jena had been successfully tested, D2RQ was added in order to expand the capabilities of the reasoning system. This program would allow all of the non-RDF database files in the current LLE systems to be imported into the Jena framework. D2RQ required that each relational database table be mapped, a simple process that required little time to create. The mapping file defined the information contained in the table, declaring the type of objects and relationships contained therein. Since D2RQ acts as a bridge between the program itself and the actual data files, each table needed to be mapped only once. The data contained within the tables was not replicated and stored by the system, so each time

the program ran, it referenced the files anew. This provided some amount of dynamicity to the created ontology, as any changes made to the tables were reflected in the ontology the next time the program ran. Several database tables were mapped, and this data also merged seamlessly to produce a large ontology with many classes of individuals.

Reasoning on and Querying the Ontology

Once an ontology was compiled from various sources, a reasoner was applied in order to draw inferences from the information. The reasoner used, known as Pellet, was applied within the programming environment. Pellet was selected as the reasoner as it was able to draw more conclusions from sets of data when compared to built-in reasoners such as Fact++. Pellet was able to classify and query the ontology almost instantaneously, providing the user with more relevant data, and requiring no extra time or effort from the user. Pellet assigned properties and direct instances to various classes, allowing the computer to draw basic conclusions that would otherwise have had to be made by a person. Most importantly, individuals were classified uniformly, with no real variance based on the source or type of data. This was a crucial aspect of the project, as this program was designed to centralize data.

Once the ontology had been explored using reasoners, the created ontology file was set up on the LLE server system and queried using SPARQL. The ontology was given some sample

BSCAL-A

TIM	Port	Azimuthal Angle	Polar Angle
TIM 4	P6	342	63.44
TIM 6	P7	162	116.57
TIM 2	H3	162	37.38
TIM 5	H14	270	100.81
TIM 1	P3	126	63.44

Figure 3: Results returned from a SPARQL query. This query requested data that was gathered from multiple sources using the reasoning capabilities of the system.

queries, including one for an LLE diagnostic, BSCAL-A. The computer was able to return key pieces of information relating to this diagnostic, as shown in figure 3. It is important to note that all of the returned data was referenced by the system through a single query to a single source.

The results were determined through the logical inference of facts and data asserted in the ontology. On current systems, the same data would have had to be referenced from various data tables scattered throughout the current LLE database system.

Oracle and Future Work

The integration of semantic technology across the LLE database is still in its early stages. This project successfully demonstrated the facility of applying this technology using external frameworks such as Jena and D2RQ in order to unify and reason on various types of data. This is only one of several identified methods to apply semantic technologies. Another potential method that should be explored is through Oracle, a commercial database system in use at LLE.

Oracle has several advantages over the use of external frameworks. In addition to having the same reasoning capabilities, the Oracle system is more dynamic in its setup than external frameworks, providing more-up-to-date information. Oracle has built-in programming to manage the import of various types of data including both RDF and non-RDF data tables. This programming accomplishes the same tasks as the framework setup, without many of the drawbacks, such as incompatibilities and bugs within the third party software used. Oracle also includes capabilities that are able to restrict user access to protected information, adding a level of security that may otherwise be difficult to attain [5].

Further work includes exploring the capabilities of Oracle. Additionally, more work must be done to continue improving upon and populating the LLE ontology with accurate and relevant data and relationships.

Acknowledgments:

I would like to thank Dr. Stephen Craxton and Mr. Richard Kidder for granting me the opportunity to work on this project for the Laboratory for Laser Energetics. I would like to thank Mr. Richard Kidder and Colin Kingsley for all of the assistance and support they gave me on my project. I would also like to thank Robert Cooper and Brandon Avila for their past work relating to my project.

References:

1. "W3C." *Semantic Web - W3C*. W3C, n.d. Web. July-Aug. 2012.
<<http://www.w3.org/standards/semanticweb/>>.
2. Horridge, Matthew. "A Practical Guide to Building OWL Ontologies Using Protégé and CO-ODE Tools Edition 1.3." University of Manchester, 24 Mar. 2011. Web. July-Aug. 2012.
3. B. Avila, "Optimizing LLE Information Operations through Natural Language Processing," 2011 Summer High School Research Program at the University of Rochester's Laboratory for Laser Energetics.
4. R. Cooper, "Designing and Implementing an Ontology for LLE Experimental Diagnostics," 2010 Summer High School Research Program at the University of Rochester's Laboratory for Laser Energetics.
5. Ashdown, Lance, and Tom Kyte. "Oracle Database Concepts." *Oracle Database*. Oracle, Sept. 2011. Web. July 2012.

***Fabrication and Characterization of Radial and Azimuthal Polarization
Converters with Photoaligned Liquid Crystals***

Christa Caggiano

Victor Senior High School

Advisors: Christophe Dorrer, Kenneth L. Marshall

University of Rochester

Laboratory for Laser Energetics

Summer High School Research Program 2012

Abstract

Radially and azimuthally polarized beams have applications in laser technology, such as material processing and microscopy. Radially and azimuthally polarized beams have been produced using liquid crystal polarization converters created through the photoalignment of a coumarin-based photopolymer. In devices assembled with two substrates and nematic liquid crystals in the intersubstrate gap, the nematic liquid crystal molecules align along dimers produced by photoalignment at the surface of each substrate. Radial alignment is achieved by inducing a radial dimerization on one substrate by rotation of the polarization during UV exposure. A defect in the way the liquid crystals align themselves alters the final polarization state by 180° across the disclination line. A π phase step plate compensates for this defect, producing useful radially and azimuthally polarized fields. This investigation focused on integrating this π phase step plate into the polarization converter. Devices with integrated internal and integrated external phase step plates were fabricated and characterized. Characterization data were taken on a transmission set-up at 1053 nm. Far field and near field measurements were taken. The expected properties of radial polarization were seen in the far field of devices with an integrated external phase plate. The expected properties of azimuthal polarization were seen in the far field of devices with an integrated internal phase plate.

I. Introduction

The polarization state of light is determined by the direction of the electric field component of light. Laser light, which is coherent, is usually linearly polarized. In this case, the polarization vector of light oscillates in a fixed direction (Figure 1).

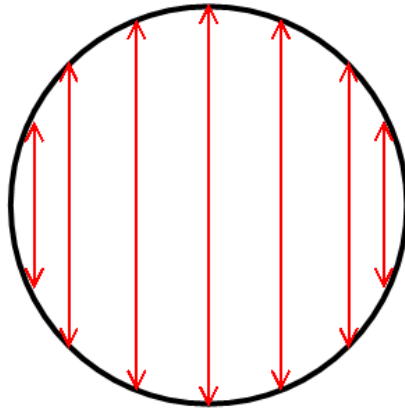


Figure 1: *The direction of the polarization vector in linearly polarized light. The polarization vector remains the same in all parts of the beam.*

Radially polarized beams and azimuthally polarized beams are both cylindrical vector beams — beams where the polarization is locally linear, but where the overall polarization depends on the position in the beam. Radial polarization occurs when the polarization vector points toward the center of the beam. In azimuthal polarization, the polarization vector is tangential to the beam (Figure 2).¹ In both types of polarization, the polarization of the beam is not defined at the center of the beam.

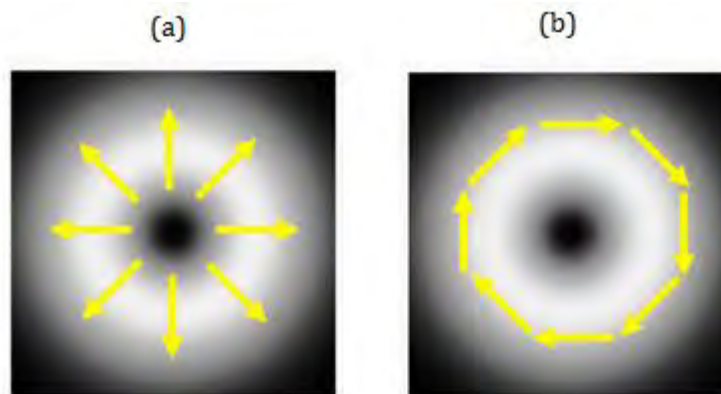


Figure 2: *The direction of the polarization vector in radially polarized (a) and azimuthally polarized (b) beams.¹*

Cylindrical vector beams have been experimentally demonstrated to have advantages in laser

technology. Radially and azimuthally polarized laser beams have been determined to be preferable in materials processing, optical trapping, electron acceleration, optical lithography, and microscopy.²

The generation of cylindrical vector beams, however, is cumbersome. Beams have been generated by inserting specially designed elements into a laser resonator, which is not practical for laser systems with limited space.³ They have also been generated by superimposing two orthogonally polarized Laguerre-Gaussian modes.³ An advantageous alternative to these approaches is the generation of radially and azimuthally polarized beams through patterned liquid crystal cells. This process has previously been demonstrated to be feasible.⁴ This concept is illustrated in Figure 3.

Liquid crystals are in a mesophase — a state of matter between a liquid and a solid. Liquid crystals flow as a liquid would, but retain order reminiscent of a crystalline solid. Liquid crystals can be in several different phases. The phase used in figure 3 is the nematic phase, where the liquid crystals have directional order, but not positional order. A thin layer of this nematic liquid crystal, specifically E7 liquid crystal, was used to fabricate radial and azimuthal polarization converters. This liquid crystal was aligned through the irradiation of a coumarin-based photopolymer coated on fused silica substrates with polarized broadband UV light. This process, known as photoalignment, causes dimers to form parallel to the polarization of the light. One substrate was patterned with linear dimers. The other substrate was patterned with radial dimers. These substrates were then affixed together, and E7 was inserted in the inter-substrate gap. The liquid crystals aligned themselves along the dimers that were patterned on each substrate.

This process of photoalignment is a non-contacting process, which leaves no scratches or embedded particles on the substrates that would disrupt liquid crystal alignment.⁶ It is easily scalable and cost effective, and produces devices with a high laser damage threshold — 60 J/cm² at 1053 nm.⁷

As light propagates through a nematic liquid crystal medium, its polarization rotates with the liquid crystal chain, changing the initial polarization. As shown in Figure 3a a horizontally polarized input field results in a radially polarized output field. In Figure 3b a vertically polarized input field results in an azimuthally polarized output field.

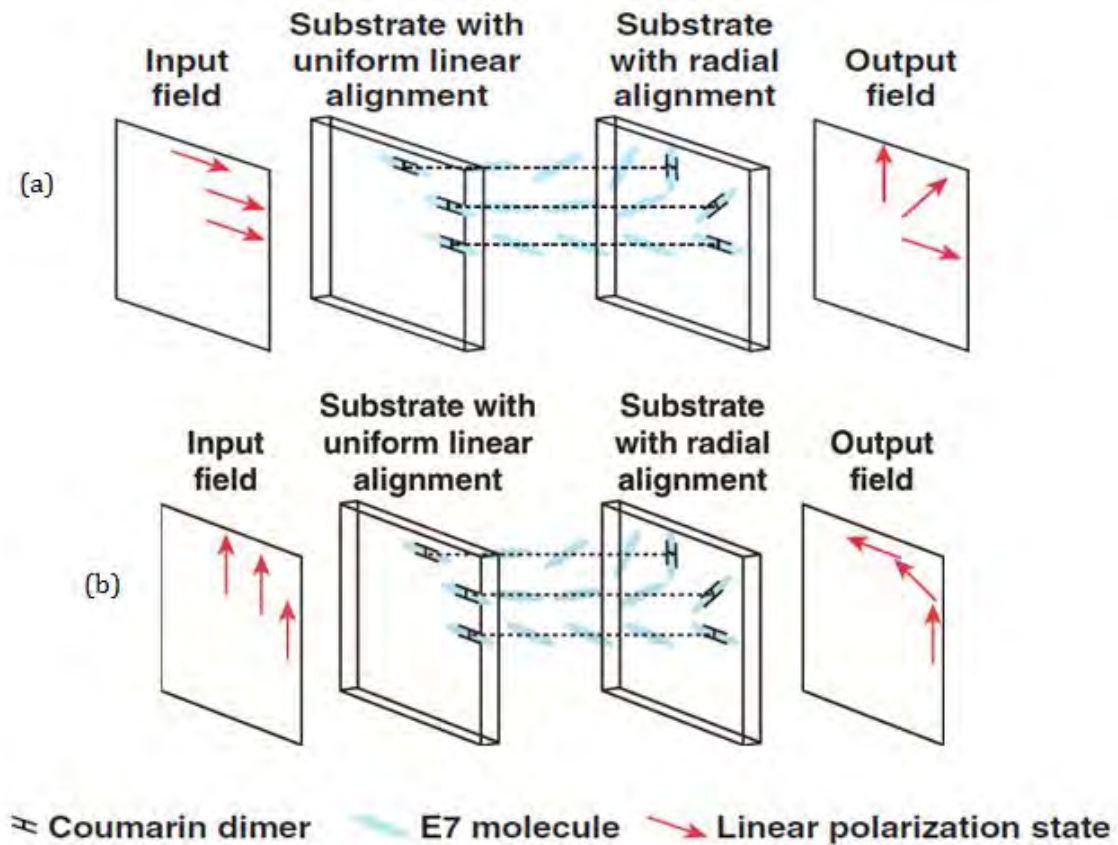


Figure 3: A schematic of an assembled cell. (a) Radial polarization converter. Horizontal linearly polarized light enters the radial polarization converter through a linearly patterned substrate, propagates through a layer of E7 liquid crystal and emerges through a radially patterned substrate to have an output field of radial polarization. (b) The cell becomes an azimuthal polarization converter when the input polarization is vertical.

Figure 4 depicts the result of a defect in the way the liquid crystals align themselves within the cell. On the horizontal line between points A and B in the figure, the polarization state does not change because the liquid crystals are aligned along the light path. The liquid crystal rotates the polarization at other points due to the patterning of the liquid crystals. Directly through the center of the device a disclination line forms – indicated by the dashed line in Figure 4 – where the nematic liquid crystals are twisting in opposite directions. This causes a π phase shift, altering the final polarization state by 180° , as seen in Figure 4b. This causes the output field of radial or azimuthal polarization to not be useful in laser technology applications. This π phase shift can be compensated with a phase step applied to half the cell, so a useful polarization state is achieved, as seen in Figure 4c.

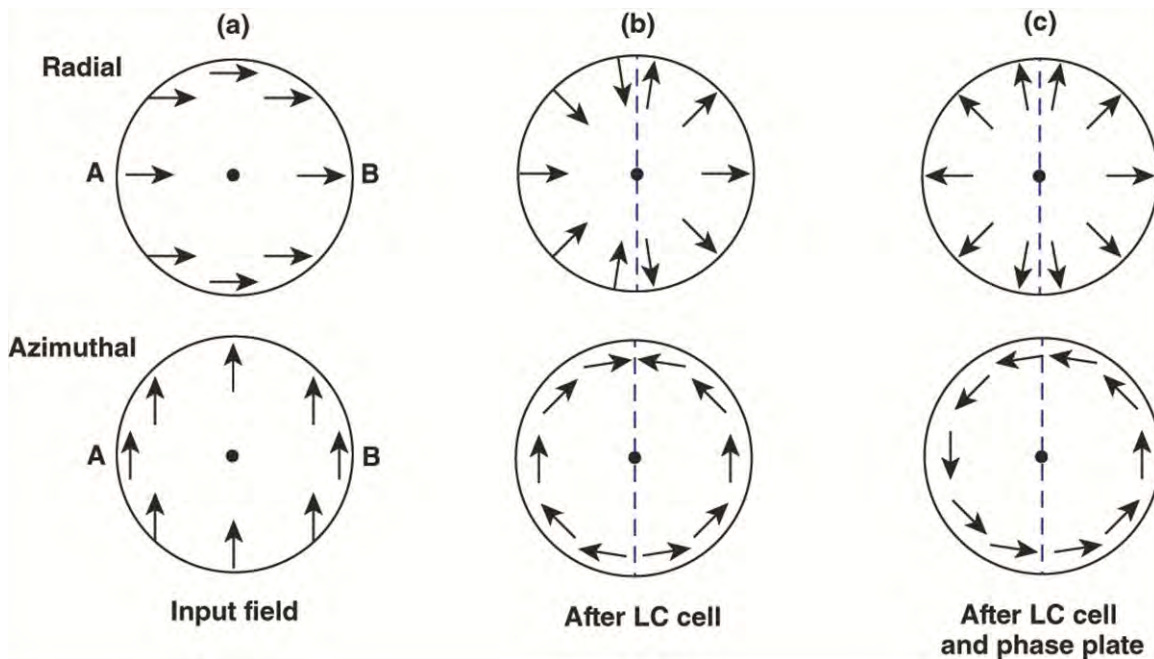


Figure 4: Change in polarization state due to a disclination line formed by liquid crystals in a polarization converter. The input to the devices is linear polarization (a). After propagating through a device without a phase step (b) the polarization state is shifted 180° across the disclination line (shown dashed). With the addition of a π phase plate to the left half of the cell (c) useful radial or azimuthal polarization is achieved.

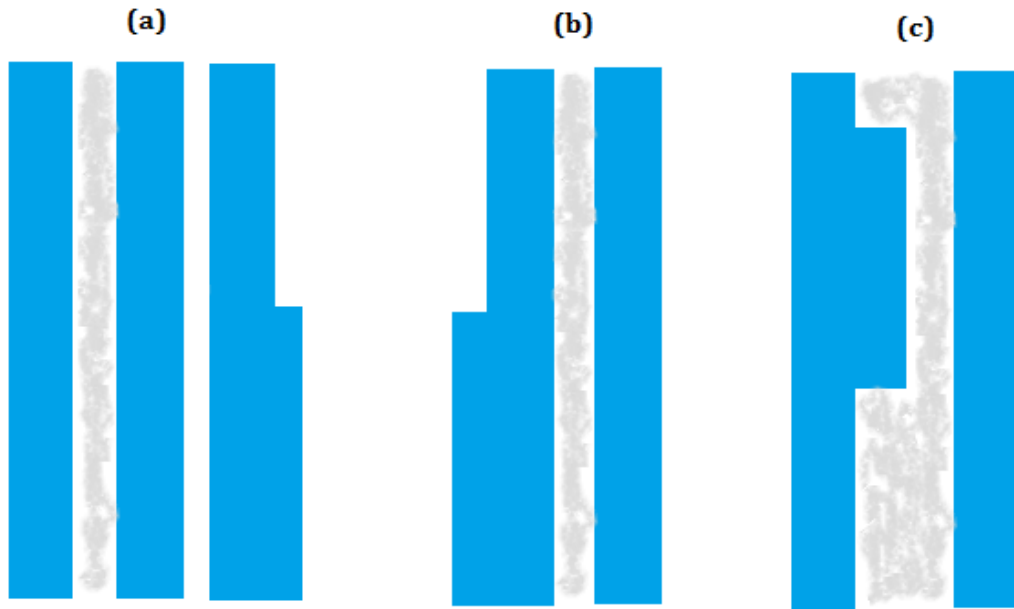


Figure 5: *Three types of phase steps used to correct for disclination lines . Phase steps can be separate external (a), integrated external (b), or integrated internal (c). This research investigated integrated external (b) and integrated internal (c) phase steps .*

A phase step is a substrate with a slight step built into it. Figure 5 shows three types of phase step. Previous fabrication methods⁴ involved creating polarization converters with a separate external phase step, as shown in Figure 5a. This is burdensome because alignment of the device and phase step needs to be performed each time the device is used. Figure 5b shows an external phase step that is integrated into a device – the external phase step is on the non-coated side of the substrate. In Figure 5c the phase step is internal – on the side of the substrate that will be coated with the coumarin-based photopolymer necessary for photoalignment. The index of refraction difference between the air and fused silica, for an external step, or between the liquid crystal and fused silica, for an internal phase step, is used to calculate the phase step height for a particular wavelength of light. Devices with an integrated internal phase step can only be used with one input polarization; therefore they cannot be rotated to produce both radial and azimuthal polarizations

because the refractive index of the liquid crystal depends on the input polarization. Internal phase steps are preferred, because they lead to a cleaner device.

In this study, two devices with an integrated phase step (Figure 5b and c) were fabricated and characterized. The external phase step height was 1.17 μm in the first device and the internal phase step height was 2.03 μm in the other device, calculated to produce azimuthal polarization.

II. Fabrication Procedure

Polarization converters were fabricated with 5-cm diameter fused silica substrates. One substrate was a blank; the other substrate had a phase step, either external or internal. Blank substrates and phase step substrates were cleaned, dried, and spin coated identically.

II.1 Substrate Preparation

Substrates were rinsed with deionized water (DI water) and then polished with 0.05 μm Masterprep® polishing suspension.⁸ Substrates were polished for three to four minutes, with care taken to ensure that all parts of the substrate were scrubbed an equal amount. After polishing, substrates were rinsed again with DI water until they passed a water break test, which tested whether hydrophobic surface contaminants were present. To perform a water break test, substrates were wetted with DI water and held horizontally for seven seconds. If the water did not form a continuous sheet for the duration of seven seconds, hydrophobic contaminants were present, and more cleaning was necessary. After passing this test, substrates were cleaned with nanopure water for one minute. Substrates were then placed in an ultrasonic bath with three milliliters of Extran detergent added, and set to 69° C for 60 minutes. After being cleaned in the ultrasonic bath, the substrates were rinsed for five minutes with DI water to ensure that no residual polish or detergent was left behind. All water was blown from the substrates using a nitrogen air gun. The substrates were then placed under a crystallizing dish on a hotplate set to 130°C for thirty minutes. This was to

assure that no water remained on the substrates. The substrates were then set under a crystallizing dish for thirty minutes in a class-10 clean hood to cool.

After cooling, the substrates were spin-coated in a class-10000 clean room. One substrate was placed on a small circular spin-coating stage. A crystallizing dish was placed so that it encapsulated the stage and substrate. This crystallizing dish had ventilation holes that were taped over prior to use; this allowed for the air to be saturated with photoalignment materials, but also for an easy means of depositing the material. A substrate was first flooded with chloroform, which served as a preconditioning layer for the photoalignment material. A 2-cc glass syringe fitted with a 0.45- μm PTFE 13-mm hydrophobic syringe filter and a syringe needle was used to deposit approximately 3 mL of chloroform onto the substrate. The substrate was then spun at a speed of 4000 rpm for one minute. After this, the substrate was coated with 0.1% wt coumarin polymer 3 in a chloroform solution. A 2-cc glass syringe fitted with a 0.45- μm PTFE 13-mm hydrophobic syringe filter and a syringe needle was used to deposit the photoalignment material onto the substrate. The substrate was then spun at 4000 rpm for two minutes. Subsequent to spin coating, the substrate was placed under a crystallizing dish in a class 10 clean hood to dry for ten minutes. The spin-coating process was then repeated for all remaining substrates.

II.2 Photoalignment

Substrates were removed from the class-10000 clean room to a class-1000 clean hood for irradiation. The irradiation setup (Figure 6) was a photolithographic system emitting non-polarized UV light. This system consists of a broadband xenon light source equipped with a dichroic mirror and lenslet array configured to deliver UV light to a pile-of-plates polarizer at Brewster's angle, which produces linearly polarized UV light. The polarized light passes through a 0.6 mm slit, and then through a cylindrical lens which images the slit onto the substrate placed on the rotation stage,

as seen in Figure 6. The rotation stage is necessary to produce radial patterning. A fixed stage, not shown in Figure 6, is used to produce linear patterning.



Figure 6: Rotation stage set-up used for irradiation of the substrates of polarization converters.

Substrates are placed on a rotation stage which is controlled by LabView software

The phase step substrate was irradiated first (the irradiation process was the same for internal and external phase step substrates). The substrate was tilted so that the phase step line was clearly defined; a line was then drawn along the phase step on the uncoated side of the substrate using a permanent marker. Markings for 0° , 90° , and 270° were made along the edge of the substrate. The substrate was then transferred to the fixed stage used for linear patterning in the irradiation chamber, so that the phase step line was horizontal and the coated side of the substrate was facing upward. The dimers form parallel to the polarization of the UV light. The irradiation chamber was then sealed and the substrate was irradiated for one minute. After the irradiation was completed, the phase step substrate was set aside. The blank substrate was marked similarly to the phase step substrate: 0° , 90° , and 270° were marked along the edge of the substrate. The substrate was then placed on the rotation stage setup, which was controlled by a LabView program that dictated the rotation stage speed and the number of revolutions of the rotation stage. To induce radial

patterning, the substrate was irradiated for one hour at a speed of 10° per second. More time is needed for this irradiation because less of the substrate is exposed.

II.3 Assembly

After irradiation, substrates were assembled in the class-10000 clean room. UV-curing epoxy was mixed with a small quantity of $10\ \mu\text{m}$ glass microsphere spacers. The phase step substrate was placed into a fixed rotation stage, so the 0° , 90° , and 270° markings on the substrate were aligned with 0° , 90° , and 270° on the stage. Three very small dots of the mixture were placed on the coated side of the radially patterned phase step, as shown in Figure 7. The placement of the epoxy was very important for internal phase step devices – if the epoxy was not properly placed on the phase step substrate a wedge would result, and interference fringes would occur. These interference fringes would be an indication that the blank substrate and the phase step substrate were not parallel, which would mean that the π phase shift would not be properly compensated for.

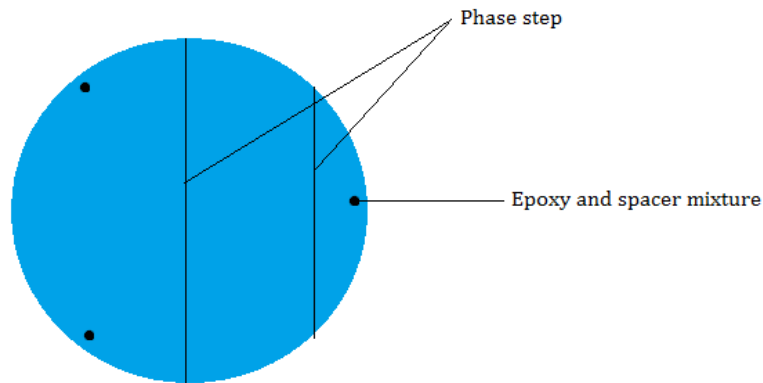


Figure 7: Correct placement of epoxy and spacer mixture for assembly of internal phase step devices

The phase step substrate was then lowered, as flat as possible, onto the radially patterned substrate, with the coated sides facing each other (Figure 8). Considerable care was taken so that the 0° , 90° , and 270° markings were aligned. Misalignment would mean that the phase step and the disclination line would not be aligned, and the desired radial alignment pattern would not be achieved.

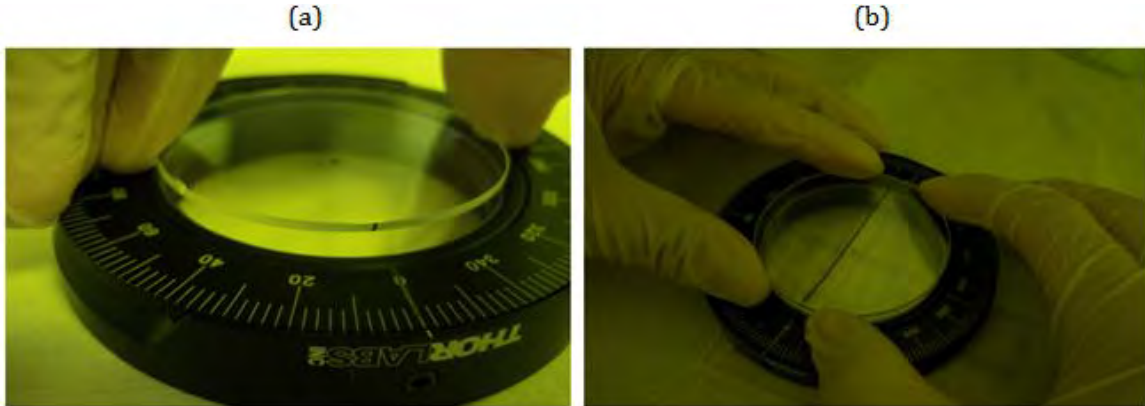


Figure 8: *Assembly of polarization converters. (a) A flat, radially patterned substrate is lowered onto a rotation stage so that the fiduciary markings are aligned at 0° , 90° , and 270° . (b) The phase step substrate is lowered onto the radially patterned substrate so that the fiduciary markings are aligned and the phase step is straight between 0° and 180° .*

Once the device was affixed together, it was placed under a UV lamp for five minutes to cure the epoxy. After curing, the assembled cell was transferred to a hot plate heated to 70°C . A 1-mL plastic syringe fitted with a $0.45\text{-}\mu\text{m}$ PTFE 4-mm hydrophobic syringe filter and syringe needle was used to fill the assembled cell with E7 liquid crystal in the intersubstrate gap. After filling, the substrate was cooled to 25° at a rate of ten degrees per hour.

III. Characterization

Characterization data were taken on a transmission set-up at 1053 nm , where the light source is spontaneous emission obtained from a fiber amplifier and collimated by a lens. Near and far field

data were taken for both devices. The near field of a light source is at the aperture of the beam—right after light passes through the cell. The far field is the light at the focus of a lens.

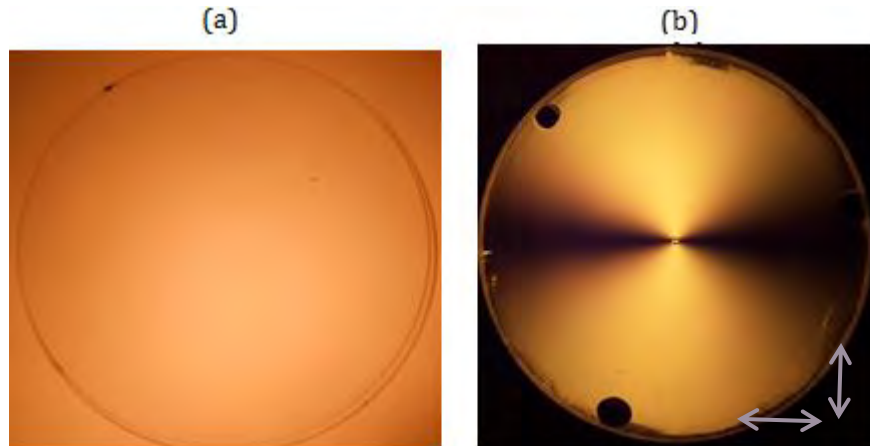


Figure 9: 5 cm polarization converter with an integrated external phase step viewed in broadband light without a polarizer (a) and viewed through crossed polarizers (right).

Characterization data were taken for a polarization converter with an integrated external phase step (Figure 9). In Figure 9a, the cell is seen alone. Figure 9b depicts the device through crossed polarizers and shows good alignment, indicated by a surface free from defects. In the near field without a polarizer, two lines were seen (Figure 10). The straighter of the two is the integrated phase step; the other line is the disclination line. These lines need to be close together in order for the π phase shift to be compensated for. Figure 10 shows good alignment of the disclination line and phase step line.

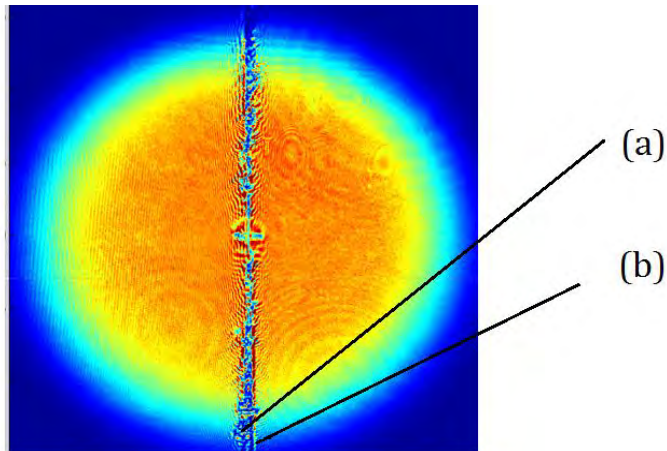


Figure 10: *Near field of a polarization converter with an integrated external phase step characterized at 1053 nm. Two lines can be seen; (a) is the disclination line and (b) is the phase step.*

In the near field, when viewed with a polarizer that selects the part of the beam polarized along the transmission axis of the polarizer, properties of radial polarization are seen, illustrated by the first row of Figure 11. The pattern produced by the radial polarization converter rotates as the polarizer rotates along its transmission axis. These characteristics seen in the near field are confirmed in the far field (bottom row of Figure 11). In the far field, viewed without an output polarizer, a doughnut beam is characteristic of a beam produced by a radial polarization converter .

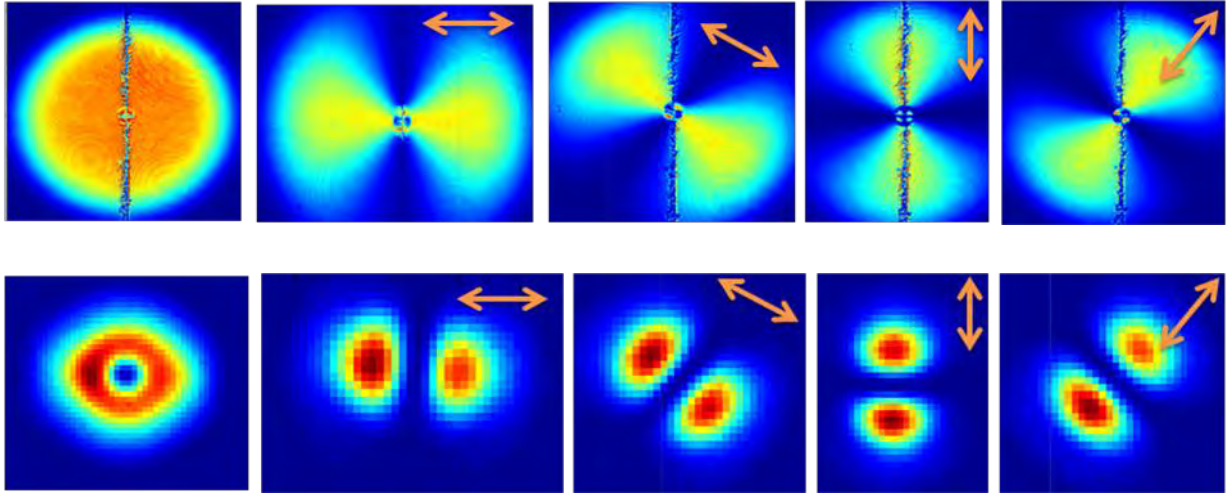


Figure 11: (First Row) Near field of a radial polarization converter with an integrated external phase step. From left, near field without an output polarizer, polarizer at 0° to the horizontal, polarizer at 45° , polarizer at 90° , polarizer at 135° . **(Second row)** Far field of the radial polarization converter. From left, far field without an output polarizer, polarizer at 0° to the horizontal, polarizer at 45° , polarizer at 90° , polarizer at 135° . Input polarization was horizontal.

An azimuthal polarization converter with an integrated internal phase step was characterized. As in Figure 10, the disclination line and phase step are seen in the near field without an output polarizer (Figure 12). The alignment is not as good as in Figure 10, due to an error in the fabrication process. Currently, there is a slight lip on the edge of the stage used to secure the radially patterned substrate when aligning the substrates, as previously seen in Figure 8, that makes it difficult to properly align the phase step substrate. The phase step line is not perfectly in the center of the device. In order for the substrates to be perfectly aligned, the blank substrate needs to be placed slightly left of center, but the lip causes the blank substrate to be higher than the phase step substrate, making the blank substrate prone to slipping. A way to address this would be to eliminate the use of the stage. Instead, substrates could be placed flat on the surface of the clean hood, so utmost care could be taken to align the substrates properly. There is also a large center defect in this

device, which was due to misalignment of the slit used to produce radial patterning during photoalignment.

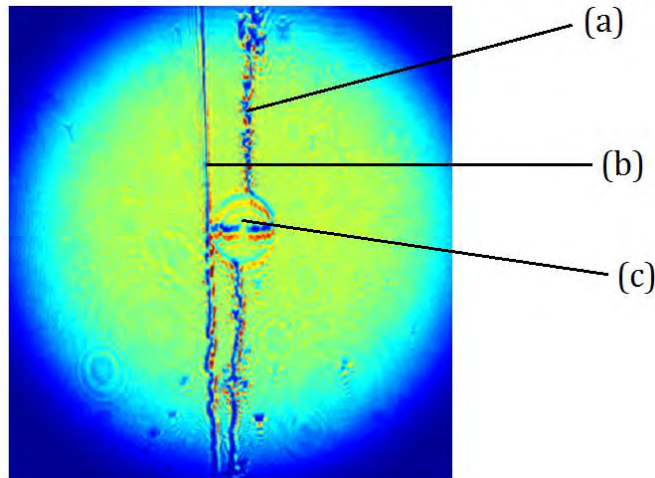


Figure 12: *Near field of an azimuthal polarization converter with an integrated internal phase step. Two lines can be seen; (a) is the disclination line and (b) is the phase step. (c) is a center defect caused by misalignment of the slit used to produce radial patterning during photoalignment.*

Azimuthal polarization characteristics were confirmed in the near and far fields (Figure 13). In Figure 13, the near and far field characterizations are shown. The patterns are very similar to those seen in Figure 11. As in Figure 11, the beam pattern also rotates with the rotation of the transmission axis of the polarizer; this is characteristic of both azimuthal polarization and radial polarization. In the far field, the azimuthally polarized beam is a doughnut beam, which is seen in the bottom left corner of Figure 13. The doughnut beam in Figure 13 is not as good as the doughnut beam in Figure 11, due to the fabrication error depicted in Figure 12.

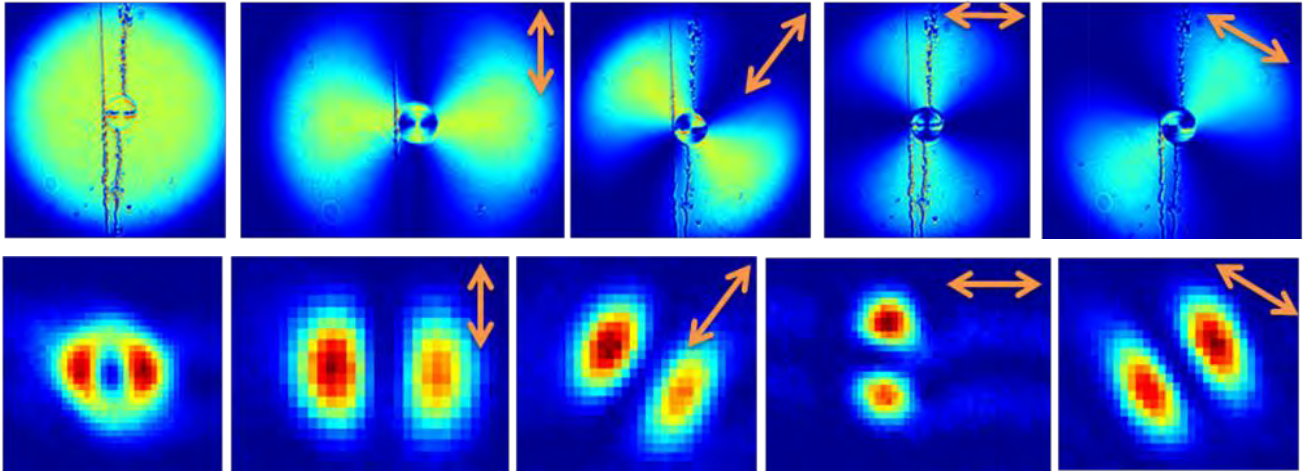


Figure 13: (First Row) Near field of an azimuthal polarization converter with an integrated internal phase step. From left, near field without output polarizer, polarizer at 0° to the vertical, polarizer at 45° , polarizer at 90° , polarizer at 135° . **(Second row)** Far field of the azimuthal polarization converter. From left, far field without output polarizer, polarizer at 0° to the vertical, polarizer at 45° , polarizer at 90° , polarizer at 135° . Input polarization was vertical.

Conclusion

5 cm diameter radial and azimuthal polarization converters with integrated phase steps were successfully fabricated. The integration of phase steps successfully compensated for the π phase shift caused by the disclination line. Radial polarization converters were fabricated using an integrated external phase step. Azimuthal polarization converters were fabricated using an integrated internal phase step. In both devices, the phase step line and disclination lines were aligned. In some cases, such as Figure 10, this alignment was very accurate. In other cases, the alignment was less good due to fabrication errors. However, despite these alignment problems, cylindrical vector beams were produced.

This method of generating cylindrical vector beams is easier to use than previous methods,

needs less space, and does not require alignment of a separate phase step. This is a promising way of producing radially and azimuthally polarized beams for a variety of different applications in laser technology.

Acknowledgments

I would like to thank Dr. R. Stephen Craxton for directing the high school summer research program at the Laboratory for Laser Energetics. I thank my advisors Christophe Dorrer and Kenneth L. Marshall for their guidance and instruction during my research. I also thank the Optical Materials Lab staff and students, especially Marisa Vargas and Michael Statt for their guidance and support.

References

1. L. Xu et al., "All-fiber laser generates cylindrical vector beams," SPIE, last modified March 23, 2011, <http://spie.org/x47733.xml+9>.
2. M. Meier, V. Romano, and T. Feurer, "Material processing with pulsed radially and azimuthally polarized laser radiation," *Applied Physics A* 86: 329 (March 2007)
3. R. Oron et al., "The formation of laser beams with pure azimuthal or radial polarization," *Applied Physics Letters* 77, no. 21:3322 (November 20, 2000)
4. Michael Statt, "Generation of Radially Polarized Beams Using Optically Patterned Liquid Crystals," Laboratory for Laser Energetics Report No. 372, (June 2012)
5. Tanya Z. Kosc, "Motion of Polymer Cholesteric Liquid Crystal Flakes in an Electric Field," PhD dissertation., University of Rochester, Institute of Optics, 3-10 (2003)
6. K. L. Marshall et al., "Liquid crystal beam shaping devices employing patterned photoalignment layers for high-peak-power laser applications," *Liquid Crystals XV* 8114 (September 7, 2011)
7. K. L. Marshall et al., "Laser-damage-resistant photoalignment layers for high-peak-power liquid crystal device applications," *Liquid Crystal XII* 7050 (August 27, 2008)
8. Beuhler, Lake Bluff, IL 60044, USA

Polar Drive Target Designs for Early NIF Experiments

Ian Gabalski

Webster Thomas High School

Webster, New York

Advisor: Radha P. Bahukutumbi

Laboratory for Laser Energetics

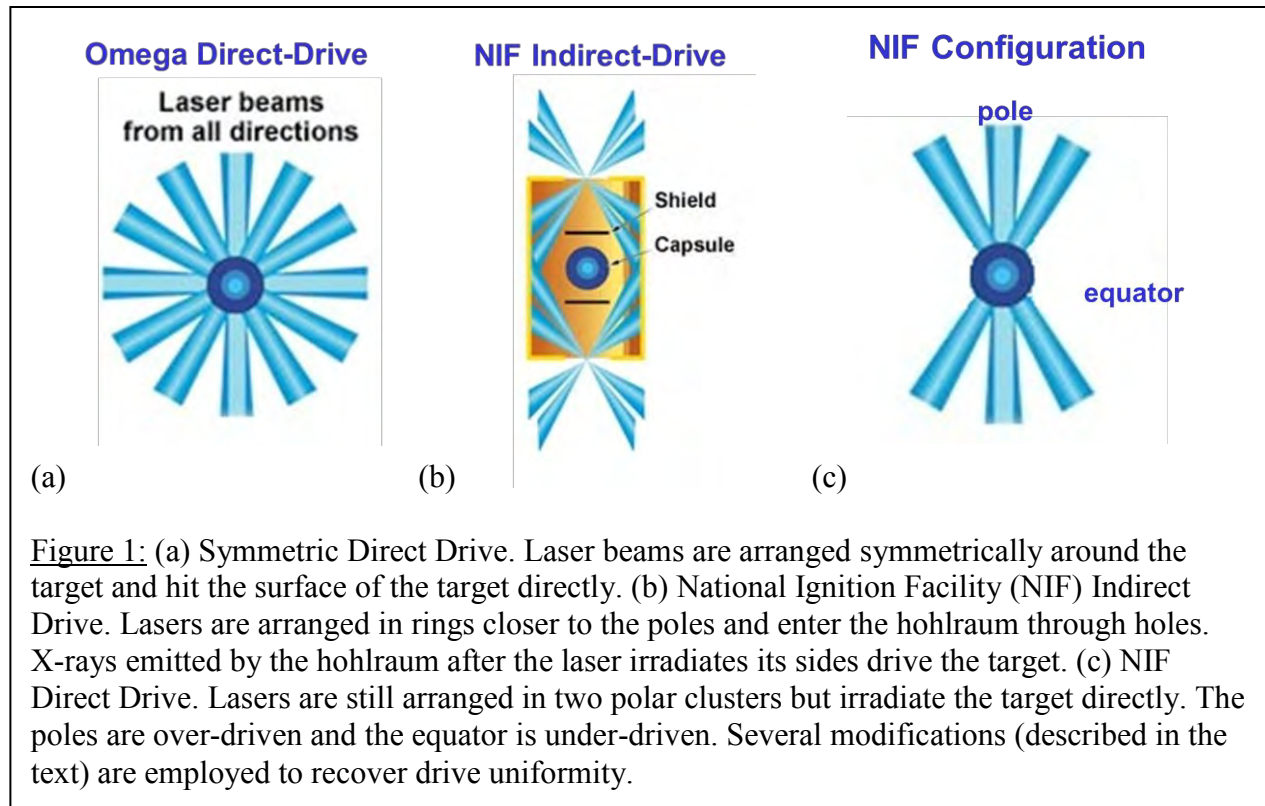
University of Rochester

Rochester, New York

February 2013

1. Abstract

The National Ignition Facility (NIF) is designed to support the indirect-drive irradiation of targets containing fusion fuel. However, direct-drive methods, in which the laser beams directly irradiate the target, are also being explored on the NIF. In order to implode direct-drive targets on the NIF, the indirect-drive configuration must be modified so that the lasers deliver their energy in such a way that the target implodes with a high degree of uniformity. This requires re-pointing the laser beams to adequately illuminate the equator, using laser beam profiles that are not necessarily at best focus, and varying the power in the beams. In order to identify an optimal configuration for these future implosion experiments, different arrangements were explored using the hydrodynamics-modeling code *DRACO*. First, beams were re-pointed towards the equator of the target to maximize initial uniformity. Then, beam powers were adjusted through the remainder of the implosion in order to control the final shape of the target. Control over the final shape was demonstrated in simulations, and a configuration was identified for a uniform direct-drive implosion on the NIF.



2. Introduction

The promise of nuclear fusion is a clean, reliable energy source which does not release large amounts of dangerous or environmentally harmful waste products. However, controlling a fusion reaction in such a way that usable energy is produced in large quantities has proven difficult. The fusion fuel, a mixture of isotopes of elemental hydrogen, must be compressed to thousands of times its solid density while simultaneously being heated. The high temperature is necessary to force the hydrogen nuclei together so that they overcome their electrostatic repulsion and fuse together, forming a helium nucleus and a neutron, and releasing large amounts of energy. The high density is needed to produce enough energy in the form of high-energy neutrons that can be used to produce useful energy.

One proposed method for achieving these conditions is called Inertial Confinement Fusion (ICF). [1] In this method, a small target containing the fuel is irradiated by a high-power laser,

which is designed to deliver its energy simultaneously to a small target of hydrogen fuel enclosed in a shell. The laser heats up the shell, causing the outer portion to ablate outwards while the inner portion is driven inwards. The entire implosion is extremely short in duration, on the order of nanoseconds.

There are two main methods for studying ICF: direct drive and indirect drive. In direct drive, the laser beams are directly incident on the target and deposit their energy. They are usually arranged symmetrically around the target so as to implode it in a uniform manner (Fig. 1a). The OMEGA [2] laser at the University of Rochester is configured symmetrically. In indirect drive, the target is situated in a hohlraum typically made of gold, and the lasers deposit their energy on the inside walls (Fig. 1b). The gold, in turn, emits x-rays, and it is these x-rays which implode the target. The National Ignition Facility (NIF) [3] is primarily configured as in Fig. 1b, except that the shields are not used in current experiments. The main difference between the two laser systems is that while the lasers on OMEGA are arranged in a symmetric fashion around the target, the lasers on the NIF are arranged in a cylindrical configuration, closer to the north and south poles of the target.

While the OMEGA facility is useful in studying the physics of ICF, it does not have enough energy in its laser to achieve ignition; ignition occurs when the helium nuclei begin to deposit their energy back into the fuel, initiating more fusion reactions. Ignition is required to release more energy in the fusion reactions than that which is deposited by the lasers. Simulations indicate that the NIF has adequate energy for ignition, and this is where all of the experiments aimed at achieving ignition are conducted. The NIF is configured to support the indirect drive method. This presents a challenge for direct drive, as the beams are clustered closer to the poles on the NIF (as in Fig. 1c) whereas normally the beams are arranged symmetrically in direct

drive. This would cause the uniformity of a target to degrade rapidly because the poles would implode much faster than the equator. A high degree of uniformity is necessary to conduct a successful ignition experiment because otherwise the fuel will not be compressed to the densities and temperatures necessary for fusion reactions.

The solution to this problem is a method known as polar drive. This entails modifying the configuration of the laser system in such a way that the target implodes uniformly. Generally, this involves a variety of changes. Each beam on the NIF has a phase plate, which defines a spatial shape and diameter at best focus. Existing NIF phase plates are designed for indirect-drive ignition with the constraint that the beams must fit through the laser entrance hole. These beam spot sizes are small and elliptical in shape, and can introduce long wavelength nonuniformities from the asymmetry in the laser drive. Following Ref. 4, beams are defocused to reduce the level of nonuniformity introduced into the beam shapes. In addition, beams are repointed towards the equator to compensate for the lack of irradiation there. Finally, beam powers are adjusted throughout the implosion to provide additional control of the shape of the shell. Since symmetry is a significant challenge for polar drive, preliminary NIF experiments are required to explore the feasibility of a successful polar drive ignition experiment.

In the present work, the 2D hydrodynamics modeling code *DRACO* [5] was used to simulate implosions and identify an optimal configuration which may be used in future experiments. A systematic approach was employed which first modified only beam pointing in order to maximize the initial uniformity of the implosion. After this was accomplished, beam energy changes were used to establish control over the shape of the shell as it is imploded and to identify a configuration which yields a uniform implosion.

3. Beam Pointing Modifications

The NIF has 192 beams, which are grouped into 2x2 arrays, called quads. In this work, each quad is treated as a unit, and all the beams in a quad have the same beam profiles, are defocused to the same extent, and have the same laser-pulse temporal history. Furthermore, the quads are arranged into 4 rings, and all quads in a ring are pointed at the same polar angle while varying in azimuthal angle. There are 24 quads clustered at the north pole of the target and 24 at the south. Figure 2a shows the positions of the northern quads on target with the original NIF configuration. There is reduced irradiation from 50° to 90° , relative to the pole. Fig. 2b gives the normalized initial intensity as a function of polar angle, illustrating that little energy is deposited near the equator. In order to compensate for this issue, a re-pointing scheme was developed and simulated in *DRACO* (Fig. 2c). The initial on-target intensity of the optimized configuration is given in Fig. 2d. The higher intensity at the equator is required to compensate for the reduced energy absorption from the oblique angles of incidence of the repointed beams.

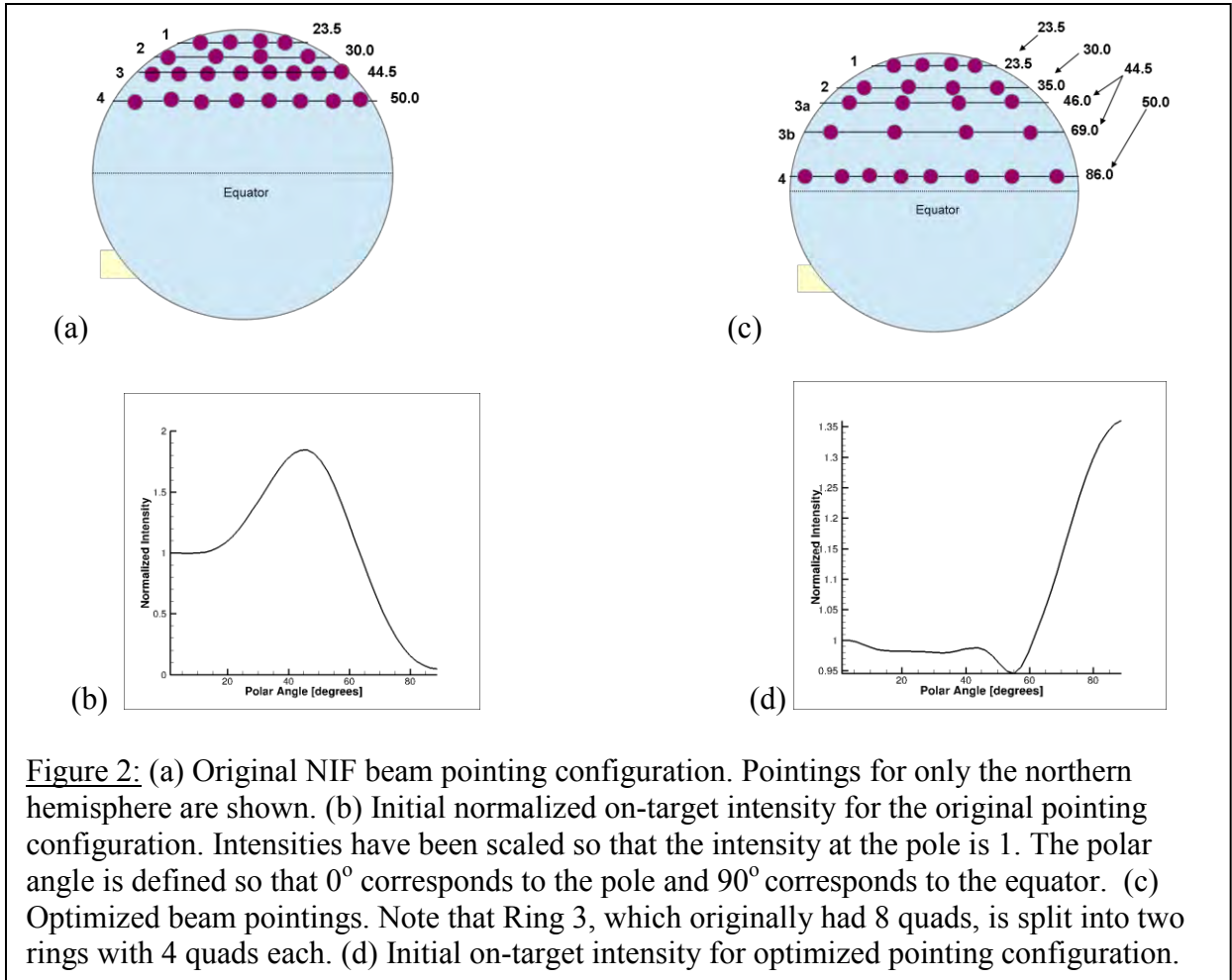


Figure 2: (a) Original NIF beam pointing configuration. Pointings for only the northern hemisphere are shown. (b) Initial normalized on-target intensity for the original pointing configuration. Intensities have been scaled so that the intensity at the pole is 1. The polar angle is defined so that 0° corresponds to the pole and 90° corresponds to the equator. (c) Optimized beam pointings. Note that Ring 3, which originally had 8 quads, is split into two rings with 4 quads each. (d) Initial on-target intensity for optimized pointing configuration.

An 1100- μm -radius room temperature target with an 80- μm -thick plastic CH shell was simulated (Fig. 3a). The target is driven by a laser pulse that has a low-intensity foot (defined as the initial constant power until approximately 2 ns) and a slow rise to a constant-power main pulse. The purpose of the foot is to launch a shock and to begin driving the target inward. However, the target must be compressed adiabatically, meaning that it is not heated in the process, because a preheated target is difficult to compress to densities necessary for fusion. In order to achieve this, the foot has a low power relative to the remainder of the pulse. The duration of the foot is tailored so that it ends at shock breakout, which is approximately 1.5 ns for these designs. After the foot ends, the power increases during the “rise” portion of the laser pulse

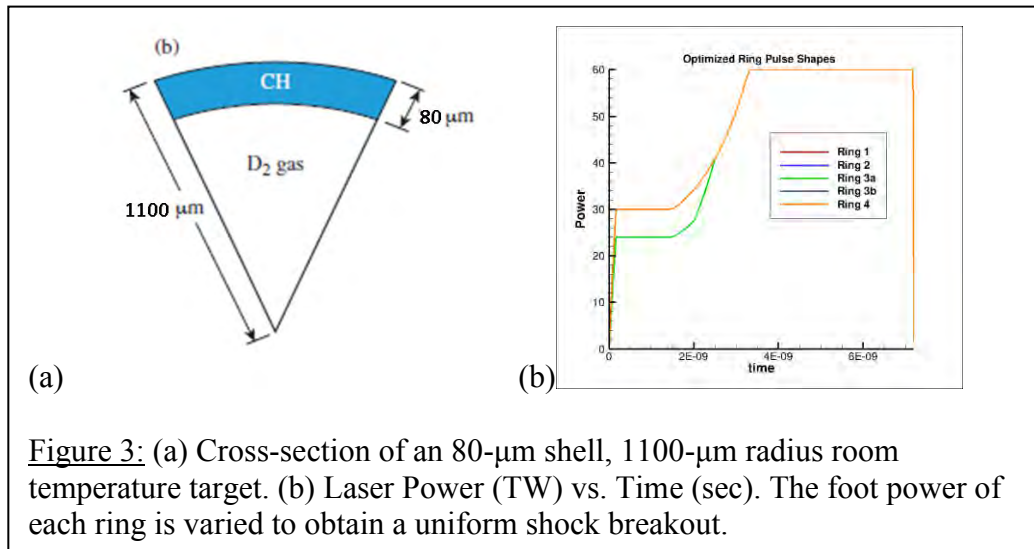


Figure 3: (a) Cross-section of an 80- μm shell, 1100- μm radius room temperature target. (b) Laser Power (TW) vs. Time (sec). The foot power of each ring is varied to obtain a uniform shock breakout.

up to its maximum value. The rise of the pulse is designed to adiabatically compress the target. Finally, the main pulse delivers most of the energy necessary to compress the shell and provides its kinetic energy.

It is necessary to keep the initial conditions of the implosion as uniform as possible because any nonuniformity which is introduced early on in the implosion will grow due to the converging shell. When the laser initially begins to irradiate the target, it launches a shock wave which compresses the target and moves inward faster than the shell. It is the uniformity of this shock which determines the overall initial uniformity of the target. The shock moves through the shell first, compressing it, and then breaks out of the shell and moves into the internal gas. This point in the implosion where the shock changes between media is called “shock breakout,” and this was the point when the uniformity of the shock was determined in the simulation. The pointings of the quads were varied to minimize this nonuniformity.

Three changes to the laser were employed to achieve uniformity. First, the foot of the laser pulse was modified by an overall multiplier (Fig. 3b). These multipliers were iteratively selected; Rings 1, 3b, and 4 use a multiplier of 1.0, whereas Rings 2 and 3a reduce the energy in

the foot by using a multiplier of 0.8. Second, the beams were defocused using the technique described in Ref. [4]. Third, beams were re-pointed away from the center of the target so as to adequately irradiate the equator (Fig. 2c). In conjunction with this, Ring 3 was split into two separate rings so that there was more flexibility with the pointings of its eight quads. Once a semi-uniform configuration was identified, the polar angle of each ring was systematically changed by $\pm 3^\circ$ to identify the most uniform case. The optimized configuration is the same as the one shown in Figure 2c.

In Figure 4, a density contour plot of the northern hemisphere of the target is given at shock breakout, shown in radius vs. polar angle to demonstrate how much the shock deviates from uniform from pole to equator. Fig. 4a shows a nonuniform shock breakout obtained simply by an arbitrary repointing of the beams and Fig. 4b shows a more uniform shock breakout, corresponding to the pointing configuration shown in Figure 2c. The optimized configuration was identified simply by examining these plots of shock breakout for a variety of different pointing changes and deciding on the most uniform case. It can be seen that varying the pointing of the beams has a direct impact on the uniformity of the shock.

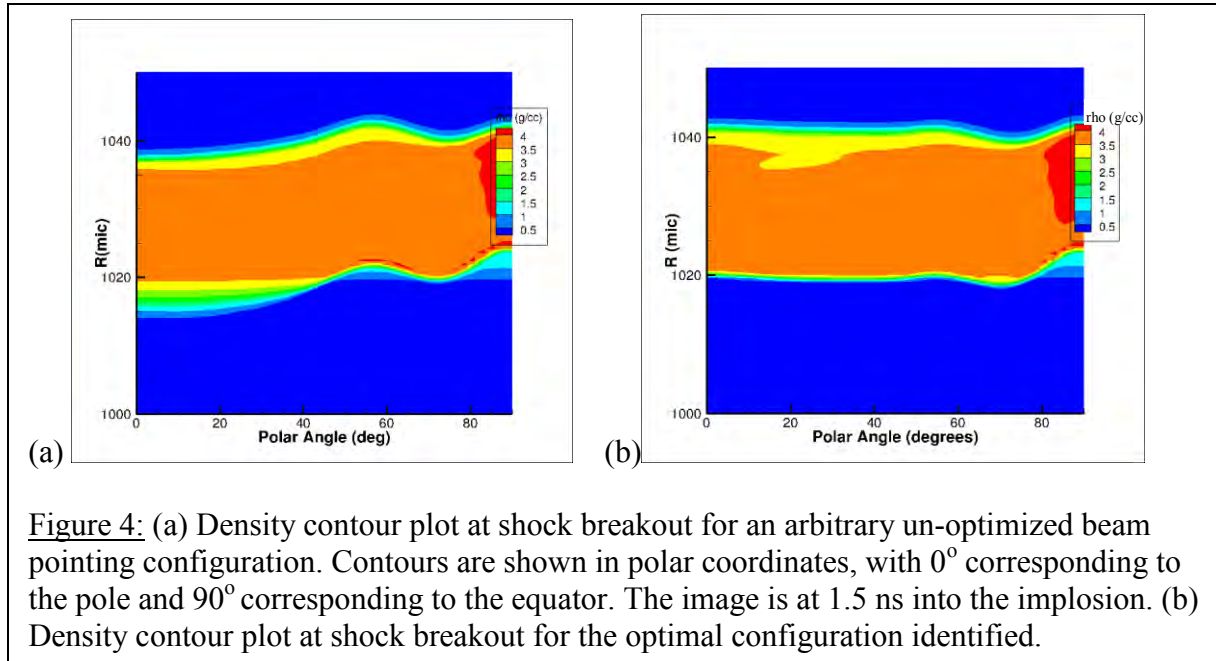


Figure 4: (a) Density contour plot at shock breakout for an arbitrary un-optimized beam pointing configuration. Contours are shown in polar coordinates, with 0° corresponding to the pole and 90° corresponding to the equator. The image is at 1.5 ns into the implosion. (b) Density contour plot at shock breakout for the optimal configuration identified.

In Figure 4b, the more uniform case, there is a small ripple near the equator. This occurs because the significant re-pointing of the laser beams results in reduced absorption at the equator and insufficient drive. This problem is difficult to fix solely with a re-pointing scheme. For example, as Ring 4 is re-pointed more toward the equator, more of its energy misses the target. A solution proposed to this problem is to engineer phase plates which would concentrate more energy locally at the equator [6]. These new phase plates will not be available for several years. However, the level of uniformity shown in Fig. 4b is adequate for the proposed preliminary experiments as the goal is to predictably model the symmetry of direct drive implosions on the NIF. The goal of achieving ignition will be pursued at a later stage. In Table 1, the final optimized beam pointing scheme, defocus length, and relative initial powers of the beams are shown. The distance Δr corresponds to the beam shift perpendicular to the beam axis and is given by $\Delta r = R_t \sin(\theta_r - \theta)$, where R_t is the target radius.

	Original Angle θ [deg]	Repointed Angle θ_r [deg] (Δr [mic])	Defocus Length	Energy Multiplier (Foot)
Ring 1	23.5	23.5 (0 mic)	1.0 cm	1.0
Ring 2	30.0	35.0 (96 mic)	1.0 cm	0.8
Ring 3a	44.5	46.0 (29 mic)	1.5 cm	0.8
Ring 3b	44.5	69.0 (275 mic)	1.0 cm	1.0
Ring 4	50.0	86.0 (647 mic)	1.0 cm	1.0

Table I: Parameters of the laser used to obtain the uniform shock breakout shown in Fig. 4b. The repointed angle gives the intersection of the beam axis with the initial target surface, and Δr gives the corresponding shift of the beam perpendicular to its axis

4. Beam Power Modifications

In order to control the shape of the imploding shell after shock breakout, the beam power must be modified. By changing the power in the polar and equatorial rings, control over the final shape of the shell can be established in simulations. Since the aim of the preliminary experiments on which these simulations were focused is simply to examine the feasibility of a controlled direct drive implosion for the NIF, it is necessary to demonstrate that some control over the final shape of the target can be established. Therefore, laser parameters have been identified in simulations that will produce three different shapes: prolate, where the poles lag behind the equator; spherical, which is round to within experimental error; and oblate, where the equator lags behind the poles. These shapes are shown in Figure 5(a,b,c).

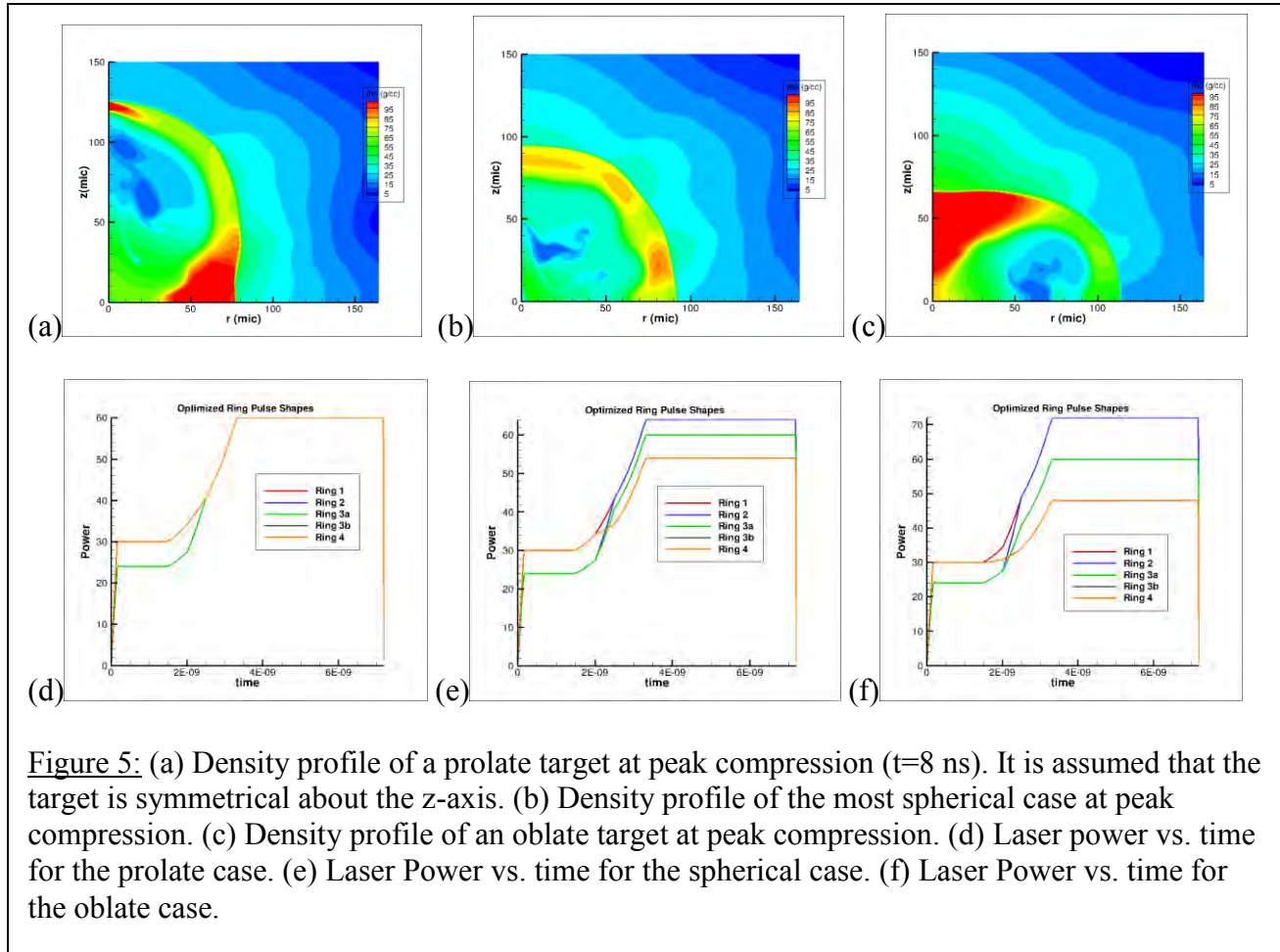


Figure 5: (a) Density profile of a prolate target at peak compression ($t=8$ ns). It is assumed that the target is symmetrical about the z -axis. (b) Density profile of the most spherical case at peak compression. (c) Density profile of an oblate target at peak compression. (d) Laser power vs. time for the prolate case. (e) Laser Power vs. time for the spherical case. (f) Laser Power vs. time for the oblate case.

Since the beam pointing configuration was already optimized to achieve a uniform shock at breakout, it is important to leave the foot unmodified. The laser power for each ring was modified only during the rise and main pulse to change the shape of the target after shock breakout. Figure 5(d, e, f) shows the pulse shapes of each ring for the prolate, spherical, and oblate cases. Notice that each of the three pulse shapes is identical during the foot. In order to achieve the three distinct final target shapes, the powers of the equatorial and polar rings were modified accordingly. For the prolate case, the power of each ring in the main pulse was left unmodified (Fig. 5b). For the oblate case, Rings 1 and 2 have higher power during the main pulse relative to Rings 3b and 4, while the power of Ring 3a was left unmodified. In order to

achieve a spherical shape, some fine-tuning of the ring powers was necessary, and the difference between the equatorial and polar rings is smaller (Fig. 5e).

The dynamics leading to the shape of the compressing core is a complicated combination of shock velocity and shell kinetic energy across different angular regions of the target. For instance, the initial configuration, which was then iteratively adjusted to provide the different shapes, resulted in a prolate shape for the compressed shell. As seen in Figure 4(b), the shock in the vicinity of the equator lags behind the rest of the target, meaning that it is traveling inwards at a lower velocity. Eventually this shock reaches the center of the target and begins to travel outwards again, and when it reaches the imploding shell, it causes the shell to impulsively decelerate. The shell soon stagnates and disassembles. However, the shock at the equator moves at a lower velocity than that at the poles, so it does not travel as far out after it has reached the center of the target before it meets the imploding shell. This means that the shell at the equator will implode farther than the shell at the poles before the target disassembles, creating the prolate shape seen in Figure 5a. This illustrates the importance of shock nonuniformity on the final shape of the compressed shell. The initial shock and shape of the target must be as uniform as possible in order to limit the additional complications introduced by the interaction of the nonuniform shock and the nonuniform converging shell.

5. Ablation Surface Position as an Experimental Measurable

The shape of the converging core can be obtained by using x-rays produced by an external source to image the high-density portion. [7] However, for these initial NIF experiments, x-rays emitted by the converging capsule will be used to study asymmetry. Simulations indicate that the maximum intensity in x-ray images for photon energies corresponding to ~ 2 keV corresponds closely to the ablation surface. [8] The ablation surface is important because it is

where the pressure that drives the shell inward is established by the laser. As mentioned earlier, when the laser beams irradiate the outer plastic shell of the target, they cause the target to heat up, and material from the outer shell begins to ablate. The rest of the target moves in like a rocket driven by the pressure set up by the ablating material. The ablation surface is defined as the location where this action occurs. As this location moves inwards during the implosion, the shell material spontaneously emits x-rays at a specific range of wavelengths, and by measuring the location where these x-rays are emitted, the location of the ablation surface can be determined. Thus, this provides an experimentally measurable quantity which provides useful information about the shape of the target.

While the x-ray self-emission images provide an observable, the quantity of direct-interest is the shape of the high-density shell. In these early experiments the high-density shell will not be directly imaged. It is, therefore, important to identify if the nonuniformity at the ablation surface is adequate to characterize the asymmetry. The difference between the locations of the ablation surface at the pole and the equator as a function of time is plotted in Fig. 6. This provides a measure of the nonuniformity of the ablation surface. The asymmetry of the high-density shell is characterized by the difference in the location of the center-of-mass of the shell between the pole and the equator. Fig. 6 also indicates that if the implosion were uniform and symmetric, this difference would be zero for all time. Both measures of asymmetry closely track each other till the end of the laser pulse (~ 7.2 ns), indicating that the ablation surface nonuniformity should provide equivalent information on shell asymmetry.

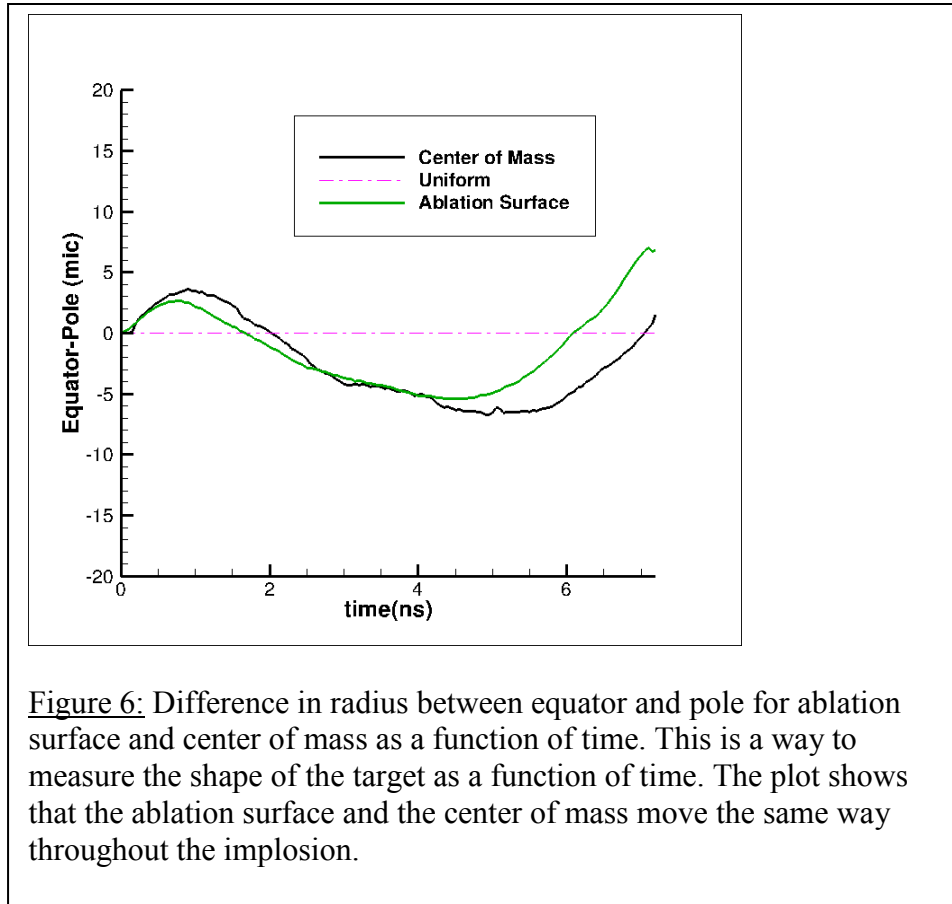


Figure 6: Difference in radius between equator and pole for ablation surface and center of mass as a function of time. This is a way to measure the shape of the target as a function of time. The plot shows that the ablation surface and the center of mass move the same way throughout the implosion.

The ablation surface position was determined for all three shapes achieved in simulations and plotted throughout time. Figure 7 shows the difference in ablation surface position plots for the prolate, spherical, and oblate cases as a function of time. It can be seen that the ablation surface differences follow what would be expected: for the prolate case (Fig. 7a), the pole lags behind the equator, and for the oblate case (Fig. 7c), the equator lags behind the pole, while for the spherical case (Fig. 7b), the difference remains less than 10 μm , corresponding to approximately 2.5% peak-to-valley in amplitude (the shell is approximately at 400 μm at the end of the laser pulse), which is smaller than the estimated error in the measurement. These graphs are only plotted to the end of the laser pulse at 7.2 ns because once the lasers stop irradiating the target, ablation no longer occurs and any measurement of the ablation surface would have no significance.

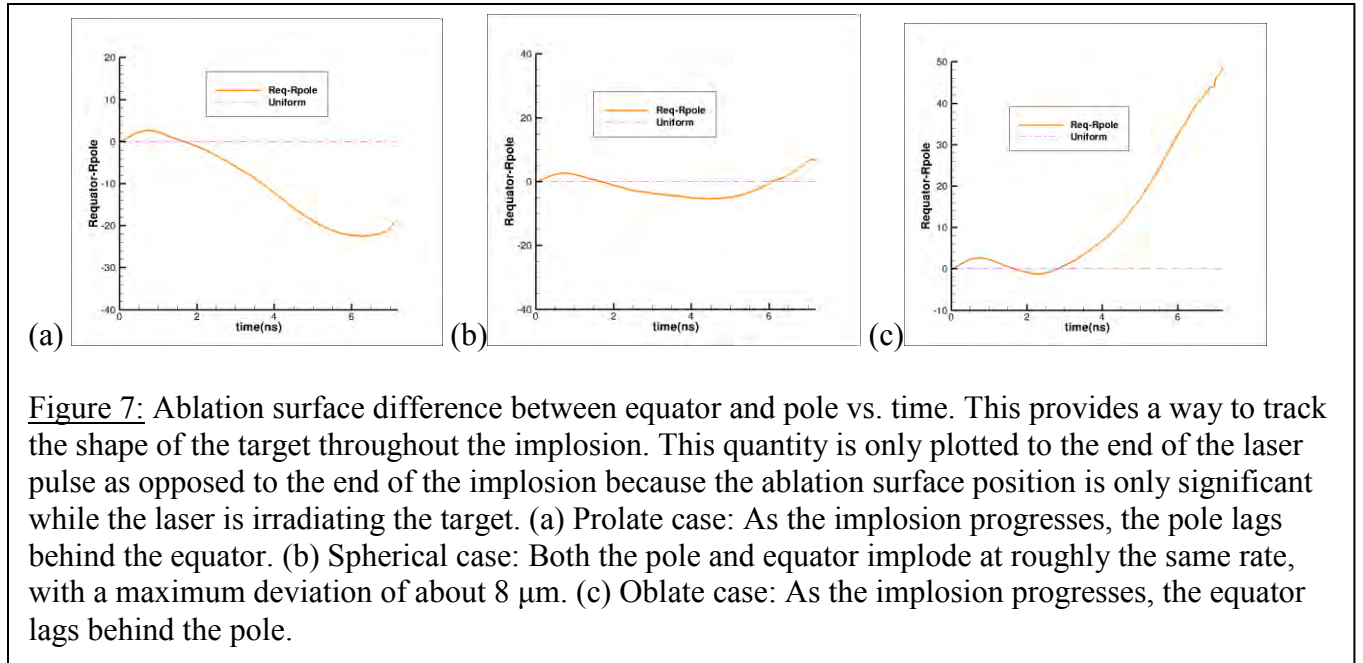
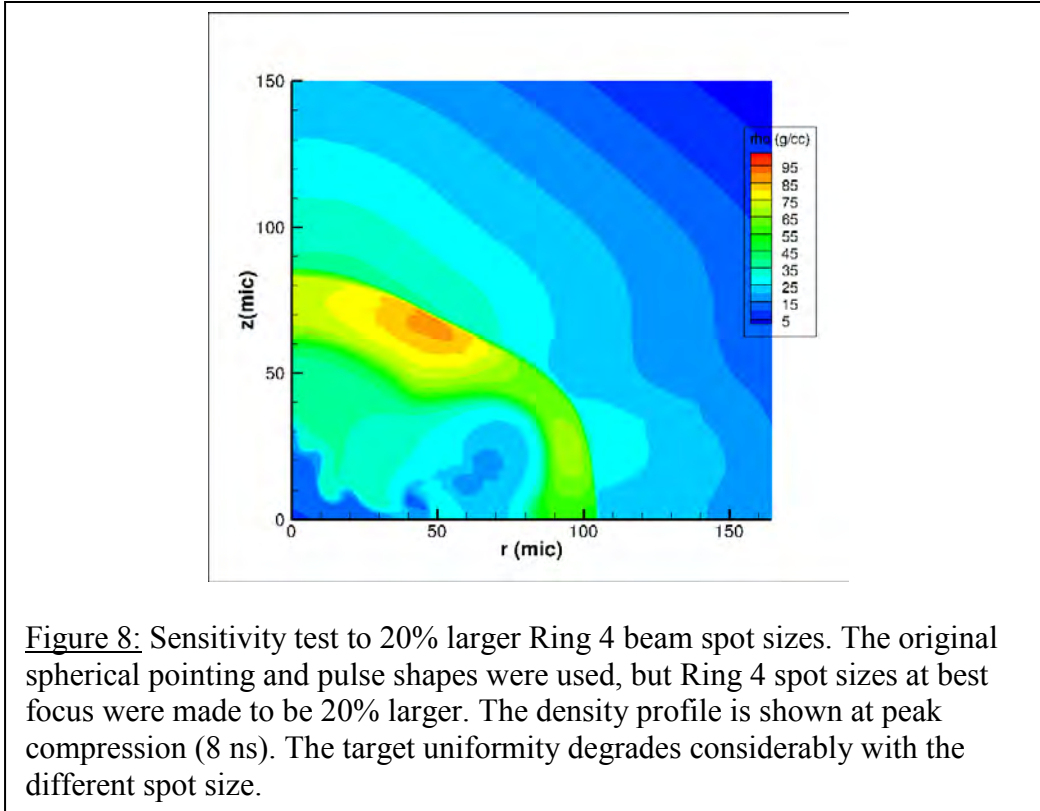


Figure 7: Ablation surface difference between equator and pole vs. time. This provides a way to track the shape of the target throughout the implosion. This quantity is only plotted to the end of the laser pulse as opposed to the end of the implosion because the ablation surface position is only significant while the laser is irradiating the target. (a) Prolate case: As the implosion progresses, the pole lags behind the equator. (b) Spherical case: Both the pole and equator implode at roughly the same rate, with a maximum deviation of about 8 μm . (c) Oblate case: As the implosion progresses, the equator lags behind the pole.

6. Sensitivity Tests

Uncertainties in the beam spot sizes can alter the dynamics of the implosion. Since Ring 4 beam profiles are the smallest of all the beam profiles and the most critical for irradiating the equator adequately, these beam sizes can have a significant impact on the shape. Accurate measurements of the beam profiles have not yet been performed, and Ring 4 spot sizes could be larger in actuality than the ones used in these simulations. In order to examine the level of sensitivity of the target to spot size, simulations were conducted which used a Ring 4 beam profile which was 20% larger at best focus than the original, while keeping the same configuration used to achieve a spherical implosion. Figure 8 illustrates the results of this test, showing the density contour profile for the target at peak compression. It can be seen by comparing this figure with Fig. 5b that the compressed shell is now oblate instead of spherical.



7. 50 μm -Shell Target Tests

Simulations were also performed using a similar target with a radius of 1100 μm , but a CH shell thickness of just 50 μm . The thinner shell causes it to implode much faster than the thicker 80 μm shell, which reduces the duration of the implosion. The higher implosion velocity is relevant for ignition target designs. This increased shell velocity also causes the shape of the target to be more difficult to control. However, despite this difficulty, a level of control over the final shape of the target was established by identifying the same three shapes as the original target: prolate, spherical, and oblate. The density profiles of these three cases at peak compression are shown in Fig. 9(a,b,c), respectively. An analysis of the beam pointings was done for the 50 μm shell target in the same fashion as was done for the 80 μm shell target, and it was found that the same beam pointing modifications produce an optimally uniform shock

breakout. Similar ring power changes were also used in both the 80 μm and 50 μm targets, although there are some subtle differences.

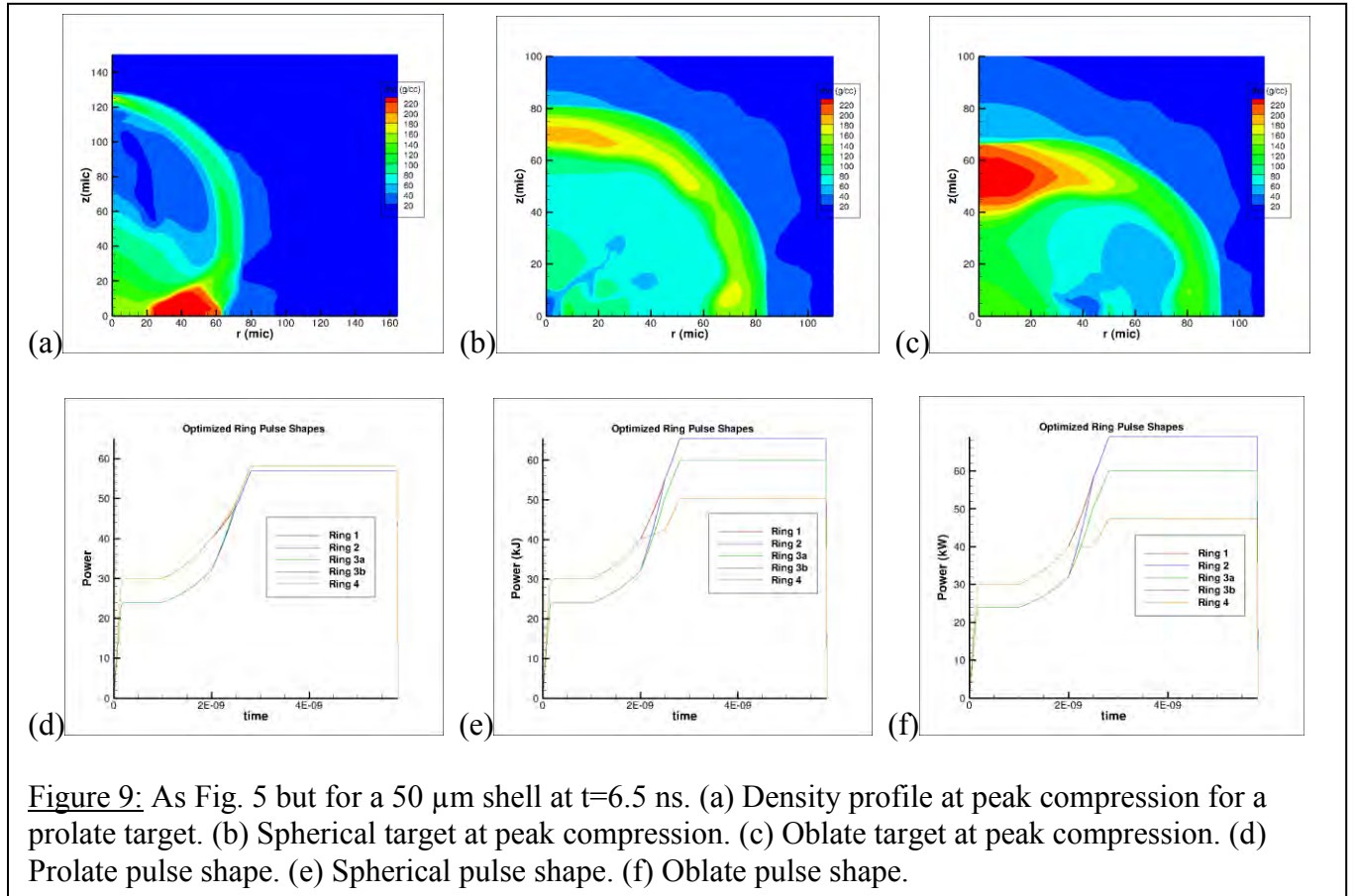


Figure 9: As Fig. 5 but for a 50 μm shell at $t=6.5$ ns. (a) Density profile at peak compression for a prolate target. (b) Spherical target at peak compression. (c) Oblate target at peak compression. (d) Prolate pulse shape. (e) Spherical pulse shape. (f) Oblate pulse shape.

An analysis of the location of the ablation surface was also performed for the 50 μm shell. The shape of the target was quantified in the same fashion as was previously done: the difference between the radii of the ablation surface at the pole and equator is calculated and plotted throughout time. Figure 10(a,b,c) shows these plots for the prolate, spherical, and oblate cases, respectively. It can immediately be seen that the shape of the shell varies much more in the 50 μm tests than in the 80 μm tests. In Fig. 10(b) it appears that the ablation surface is

actually demonstrating prolate characteristics. However, the density profile in Fig. 9(b) indicates that the parameters used produce a spherical shape at peak compression.

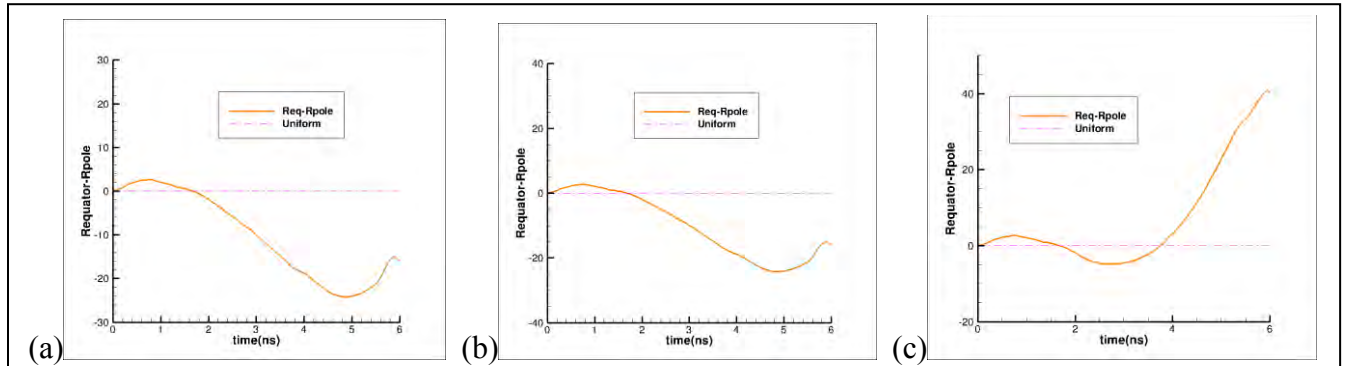


Figure 10: Ablation surface radius difference between equator and pole as a function of time for the 50- μm -shell target. (a) Prolate case. (b) Spherical case. (c) Oblate case.

8. Conclusion

Experiments will be carried out on the National Ignition Facility to explore the direct drive method of inertial confinement fusion. In order to design these experiments and identify a configuration which yields an optimally uniform implosion, simulations were performed using *DRACO*, a 2-D hydrodynamics modeling code. These simulations investigated the pointing of the beams, the defocus length, and beam power modifications in order to obtain different shapes of the compressing shell. It was shown that the nonuniformity of the ablation surface position, an experimentally measurable quantity, is closely related to the overall shape of the target. Finally, the level of sensitivity of the shape of the shell to uncertainties in beam spot sizes was investigated and the resulting shape of the shell was found to be predictable.

9. Acknowledgements

I would like to thank those who helped me in the completion of my project and this paper. First, I would like to thank Dr. Stephen Craxton for giving me the opportunity to participate in this experience. His leadership and guidance during my time at the Laboratory for Laser Energetics were invaluable, and his suggestions helped me immensely to revise and refine this paper. Second, I would like to thank Dr. Tim Collins, who aided me while my advisor was away. Third, I would like to thank my fellow interns, who were eager to help when I had trouble with my work and who made my experience enjoyable and fulfilling. I would also like to thank my parents for encouraging me to pursue this experience and for being supportive both through the application process and during the internship. Finally, I would like to give a special thanks to my advisor, Dr. Radha P. Bahukutumbi, both for her role in designing and focusing my project and for spending countless hours working to help me understand and overcome difficulties I faced with my work. Her research is advanced and time-consuming, yet she chose to spend time mentoring me so that I could make my own contribution, and for that I am extremely grateful.

References:

1. J. Nuckolls, L. Wood, A. Thiessen, and G. Zimmerman, *Nature* **239**, 139 (1972).
2. T. R. Boehly et al., *J. Appl. Phys.* **85**, 3444 (1999).
3. E. Moses, “The NIF: An International High Energy Density Science and Inertial Fusion User Facility”, presented at The Seventh International Conference on Inertial Fusion Sciences and Applications, Bourdeaux-Lac, France 12-16 September 2011.
4. A. M. Cok, R. S. Craxton, and P. W. McKenty, *Phys. Plasmas* **15**, 082705 (2008).
5. P. B. Radha et al., *Phys. Plasmas* **12**, 032702 (2005).
6. J. A. Marozas et al., *Phys. Plasmas* **13**, 056311 (2006).
7. F. J. Marshall et al., *Phys. Rev. Lett.* **102**, 185004 (2009).
8. D. T. Michel et al., *Rev. Sci. Instrum.* **83**, 10E530 (2012).

Oxygen Uptake Using a Nickel Catalyst

MaryKate Hanchett

Fairport High School

LLE Advisor: Walter Shmayda

Laboratory for Laser Energetics

University of Rochester

Summer High School Research Program 2012

December 31, 2012

Abstract

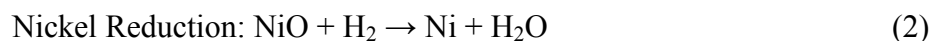
A Zirconium-iron alloy is used to absorb tritium that has escaped from process systems at LLE. Oxygen deactivates the alloy and decreases its ability to remove tritium from effluent streams. A nickel catalyst is used to crack tritiated hydrocarbons and to capture elemental oxygen. The capacity of nickel beds is finite and they require periodic reactivation using hydrogen in a helium carrier stream. Experiments have been conducted to study the efficiency of oxygen uptake and the efficiency of reactivation. Increasing the temperature of the catalyst from room temperature to 400 °C increases the amount of oxygen that can be absorbed by the catalyst. Catalyst reactivation is more efficient as the flow rate of hydrogen increases. Water vapor in the vicinity of the nickel inhibits reactivation; increasing the carrier flow rate decreases the water vapor pressure and improves the reactivation efficiency.

1. Introduction

Tritium process equipment is typically encased in gloveboxes to minimize tritium losses to the environment and to protect operators from tritium exposure. An inert gas is the preferred cover gas in a glovebox because elemental hydrogen (T_2) that has escaped from the process loops can be recaptured. Helium is the inert gas of choice. However, small amounts of air (N_2 , O_2 , H_2O) permeate through the gloves in the box. These impurities contaminate the helium cover gas at the rate of a few parts per million per hour. The impurities are removed from the cover gas by circulating it through a drier to remove water, an oxygen getter to remove oxygen, and finally a zirconium-iron alloy (ZrFe) to capture the tritium. The function of the drier and the oxygen getter is to protect the ZrFe bed.

Air that diffuses into the glovebox and its streams provides an obstacle to absorbing tritium with the ZrFe alloy. Oxygen coats the surface of the ZrFe alloy and retards the ability of the alloy to remove tritium. Oxygen also consumes the ZrFe alloy, reducing its capacity to store hydrogen. The ZrFe alloy can also crack water to absorb the hydrogen and oxygen. This process is irreversible like the absorption of oxygen, and therefore decreases the effectiveness of the alloy to capture tritium and increases the number of times that the alloy must be replaced.

A molecular sieve bed is placed upstream of the ZrFe alloy to remove the H₂O vapor. However, the issue of oxygen consumption remains. This issue can be resolved by the use of nickel or copper catalysts placed in the glovebox's stream. These catalysts can crack tritiated hydrocarbons and capture elemental oxygen. With heat and hydrogen gas, the catalysts can be regenerated. The reaction equations are:



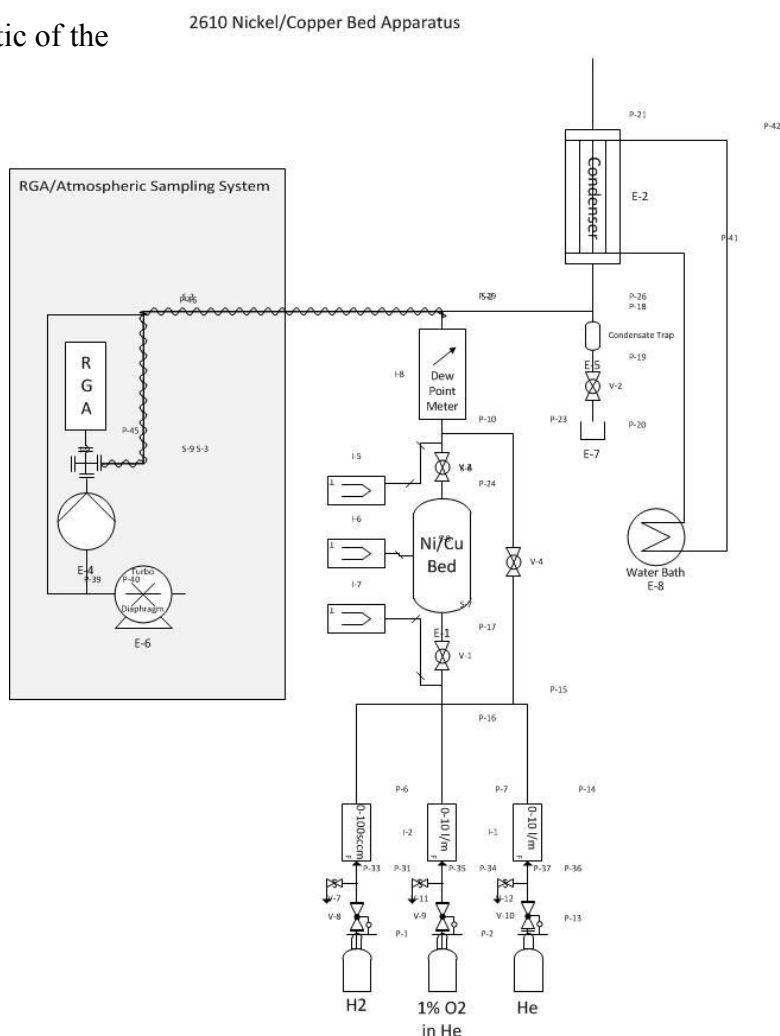
It can be seen that one mole of oxygen will react with 2 moles of activated nickel. In the second equation, one mole of hydrogen gas is required to decompose one mole of NiO. One mole of water is generated in the process.^{1,2}

In this experiment, nickel supported on 1/8" alumina spheres was tested. This type of catalyst is currently in use at LLE. It has a spherical form to maximize surface area within the bulk. The purpose of the experiment was to understand which parameters need to be controlled to maximize the efficiency of this particular nickel bed by adjusting variables such as carrier flow rates and temperature. The objective of this work was to establish a baseline against which new catalysts will be compared.

2. Experimental

An apparatus was constructed to test for the desired temperatures and gas flow rates for maximum efficiency of oxygen uptake and nickel reduction. As shown in Figure 1, paths are available for gases to flow through the nickel bed or around the nickel bed. Heating components, placed around the bed and tubing, prevent water vapor from condensing in the circuit. A condensation unit to collect water vapor produced during the reactivation of the nickel is placed at the top right of the schematic. The Residual Gas Analyzer (RGA), dew point monitor, and thermocouples are used in data acquisition.

Figure 1: A schematic of the apparatus.



2.1 Gases

Three gases were used to test the nickel getter bed. Three mass flow controllers were used to turn on and off the gas flow and to control flow rates. Helium was used to purge the air from the system, as a carrier gas, and to calibrate the data acquisition systems. Helium was flowed at flow rates varying between 100 scc/min and 4 L/min (equivalent to 4,000 scc/min). A mixture of 1% oxygen in helium was used to load the bed with oxygen. Hydrogen was flowed at varying flow rates from 2 to 50 scc/min with varying flow rates of helium to regenerate the bed. The gases can either be flowed through the nickel bed or through a bypass for control and calibration. The sensors for the data acquisition are placed at the junction of the exhaust from both the bed and the bypass.

Breakthrough occurs when the partial pressure of oxygen downstream of the catalyst increases above the background partial pressure during the load phase. The progressive deterioration of the nickel's ability to collect oxygen can be viewed on the RGA computer display as a function of time. When the bed is being loaded, the partial pressure of oxygen read at the exhaust is lower than the feedstock concentration because the oxygen is being removed from the gas stream by the bed. Breakthrough indicates that the bed can no longer absorb all of the oxygen present in the stream; it is approaching its maximum capacity at that temperature.

2.2 Properties of the Nickel Catalyst

The nickel catalyst used for this experiment is manufactured by Johnson Matthey. It is 1/8" nickel supported on alumina spheres, Type 0104. It is 60% nickel by weight and has a surface area of around 125 m²/kg.³

2.3 Data Acquisition Equipment

A Residual Gas Analyzer (RGA) and a National Instruments data acquisition system were used. The RGA has the capability to measure the partial pressure of different species in the carrier and the total pressure of the gas mixture. Thermocouples for the National Instruments system were placed before the nickel bed, on the nickel bed, and at the exhaust of the nickel bed to determine the temperatures of the gases entering the bed, the temperature of the nickel bed, and the temperature of the gases leaving the bed. They are represented in Figure 1 by the horizontal rectangles to the left of the nickel bed. The dewpoint (DP) was also tracked with a National Instruments card. The DP sensor was placed at the exhaust of the nickel bed.

2.4 Heating Components

Both the bed and capillary tubing were heated. The capillary tubing carries the gases from the exhaust of the bed to the RGA. A heating band was placed around the nickel bed and was monitored by the National Instruments system. The temperatures the nickel bed was set to ranged from ambient to 500 °C. Heating tape was placed around the capillary tubing and the entrance to the RGA to keep water in a vapor form. The heating tape was kept at 120 °C.

2.5 Water Collection

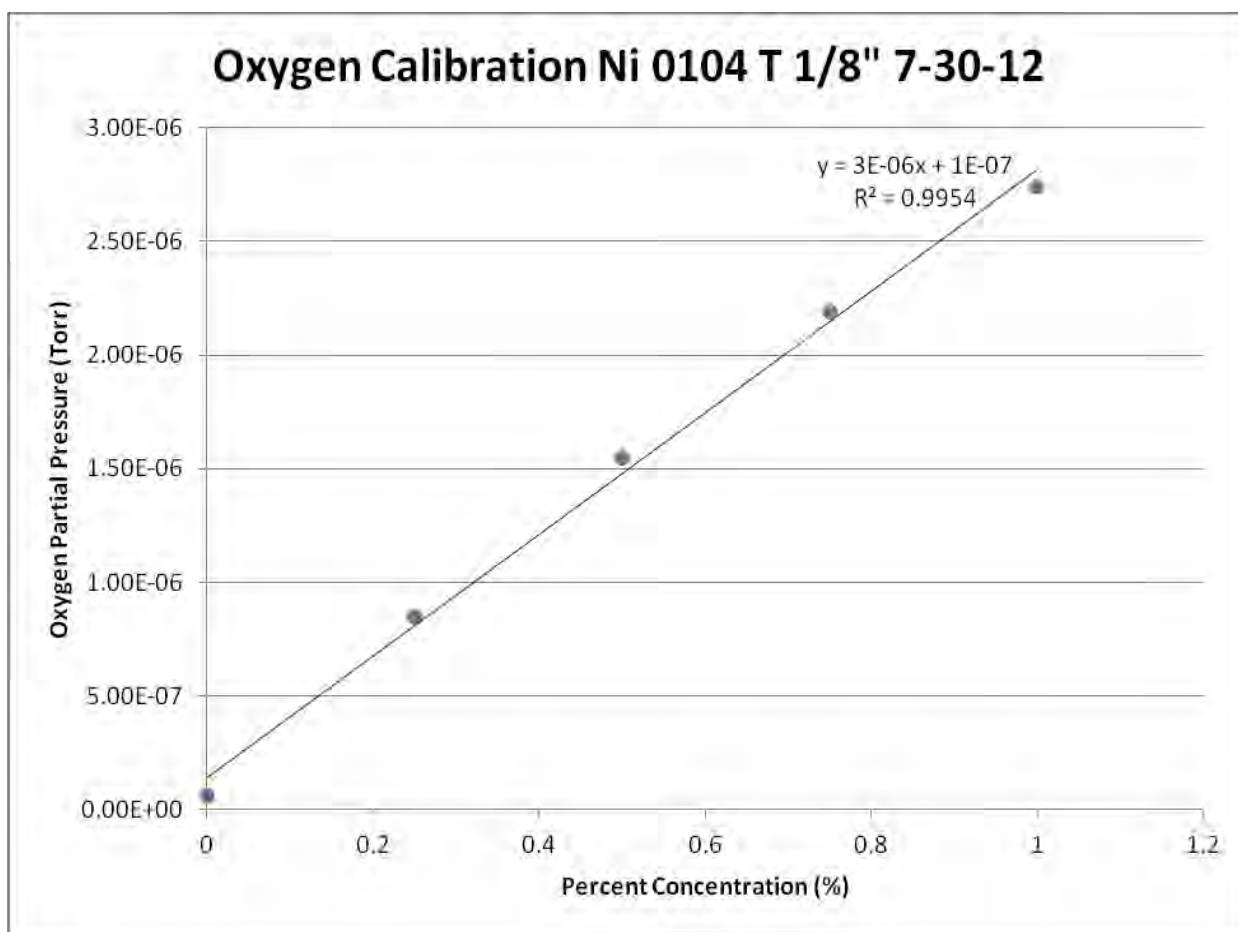
When the bed is regenerated, water is produced. To measure the amount of water produced, and to remove it from the apparatus and experimental system, a condensation unit is placed after the RGA at the exhaust – it is at a lower elevation with sloping tubing so gravity aids the removal of water. A water bath was used to cool the tubing to condense the water vapor into

liquid form. After condensation, the water collected and the amount produced could be measured using a graduated cylinder.

2.6 Calibration

Before starting the experiment, the system was calibrated to determine the partial pressure of oxygen, in Torr, measured by the RGA when different concentrations of oxygen were passed through the system. This was done to provide a reference for when oxygen was loaded onto the bed during the experiment. One can tell from the partial pressure of oxygen measured by the RGA if the bed is nearing its full capacity for oxygen.

Figure 2: Oxygen Partial Pressure vs. Percent Concentration



3. Results and Discussion

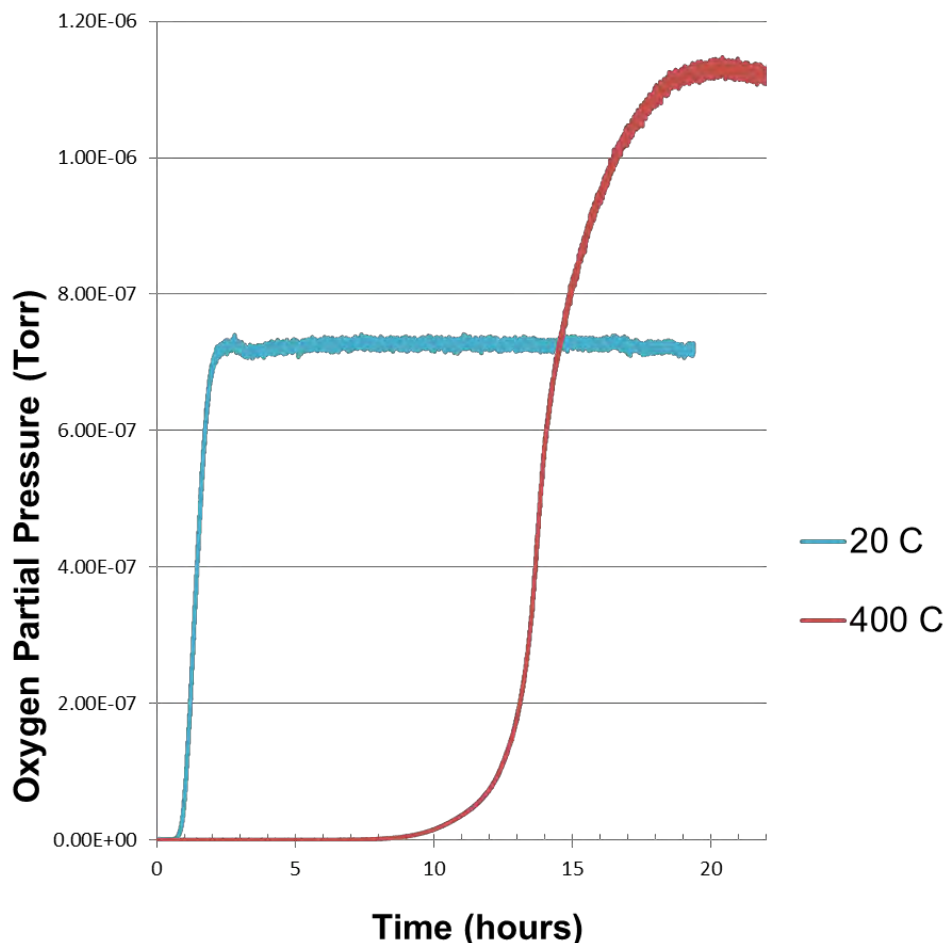
3.1 Oxygen Uptake

The efficiency of oxygen uptake by the Ni bed was investigated in experiments in which the flow rate of a homogeneous mixture of 1% oxygen in helium was held constant at 2 L/min while the temperature of the bed was varied. Results for the oxygen partial pressure as measured by the RGA are shown in Figure 3.1. Defining breakthrough as the time at which the amount of oxygen leaving the bed exhaust is equivalent to 1% of the feedstock concentration, it is found that as the catalyst temperature increases from 20 to 400 °C, the time for oxygen breakthrough to occur increases. The breakthrough time is shown for three bed temperatures in Table 3.1. 400 °C is a practical maximum temperature for loading. At this temperature the nickel exhibits good oxidation properties without generating an excessive heat load around the bed or carrier stream. As demonstrated in Table 3.1 and Figure 3.2, oxygen took around 10 times as long to break through at 400 °C as it did at 20 °C . Clearly, bulk nickel is participating in the oxidation process.

Bed Temperature (°C)	Break Through Time (hours)
20	1
200	2.5
400	10

Table 3.1: Breakthrough time for oxygen flowing over the nickel bed at varying temperatures, obtained from graphs such as that of Figure 3.1.

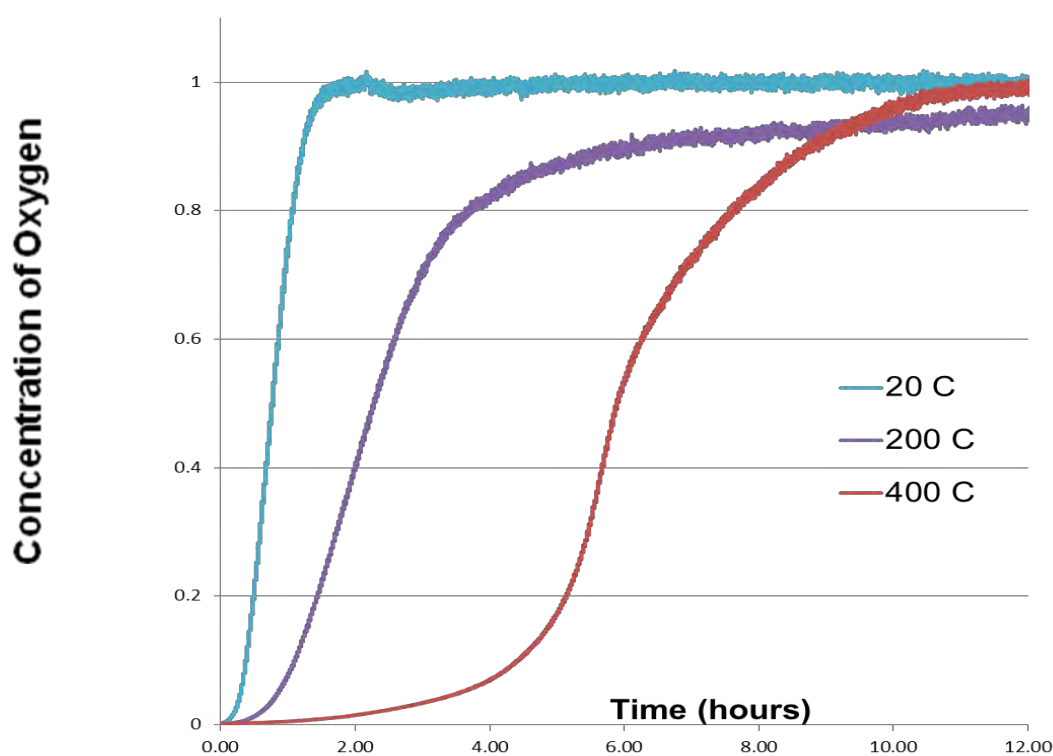
Figure 3.1: Oxygen partial pressure measured by the RGA as a function of time for two different temperatures of the nickel bed at a helium flow rate of 2 L/min.



The Mass Transfer Zone (MTZ) is the transition region in which the oxygen concentration in the carrier changes from the inlet value to the outlet value. In Figure 3.1, the MTZ is on the order of 3 cm, or half the length of the bed, for the flow conditions and operation at 400 °C. The MTZ and capacity for oxygen uptake increase with temperature. Higher operating temperatures are preferred. At lower temperatures the reaction between the oxygen and nickel is limited to a surface reaction; the bulk does not participate. As shown in Table 3.2, the capacity of the nickel to absorb oxygen increases tenfold by increasing the operating temperature from 20 °C to 400 °C.

Table 3.2: Comparison of capacity of nickel bed and fraction of nickel bed at differing temperatures.		
Bed Temp. (°C)	Capacity (mol of O₂ loaded onto nickel bed)	Fraction of Ni Bed
20	.05	.05
200	.13	.12
400	.54	.50

Figure 3.2: Concentration of oxygen measured by the RGA relative to the concentration of oxygen in the incoming helium flow as a function of time for three different temperatures.



The evolution of the oxygen concentration in the carrier leaving the bed is illustrated in Figure 3.2 for three different operating temperatures. The carrier flow rate is fixed at 2 L/min and

contains 1% oxygen. Nickel removes the oxygen from the incoming stream to form nickel oxide. Oxygen-free helium leaves the bed and oxygen is absent from the outlet stream until some fraction of the nickel has been converted to nickel oxide. Once breakthrough occurs, the oxygen concentration in the outlet increases toward 1%, the inlet value. Inspection of Figure 3.2 indicates that the time for breakthrough increases with increasing operating temperature.

Figure 3.3: Partial pressure of oxygen as a function of time, illustrating the mass transfer zone for nickel at 200 °C.

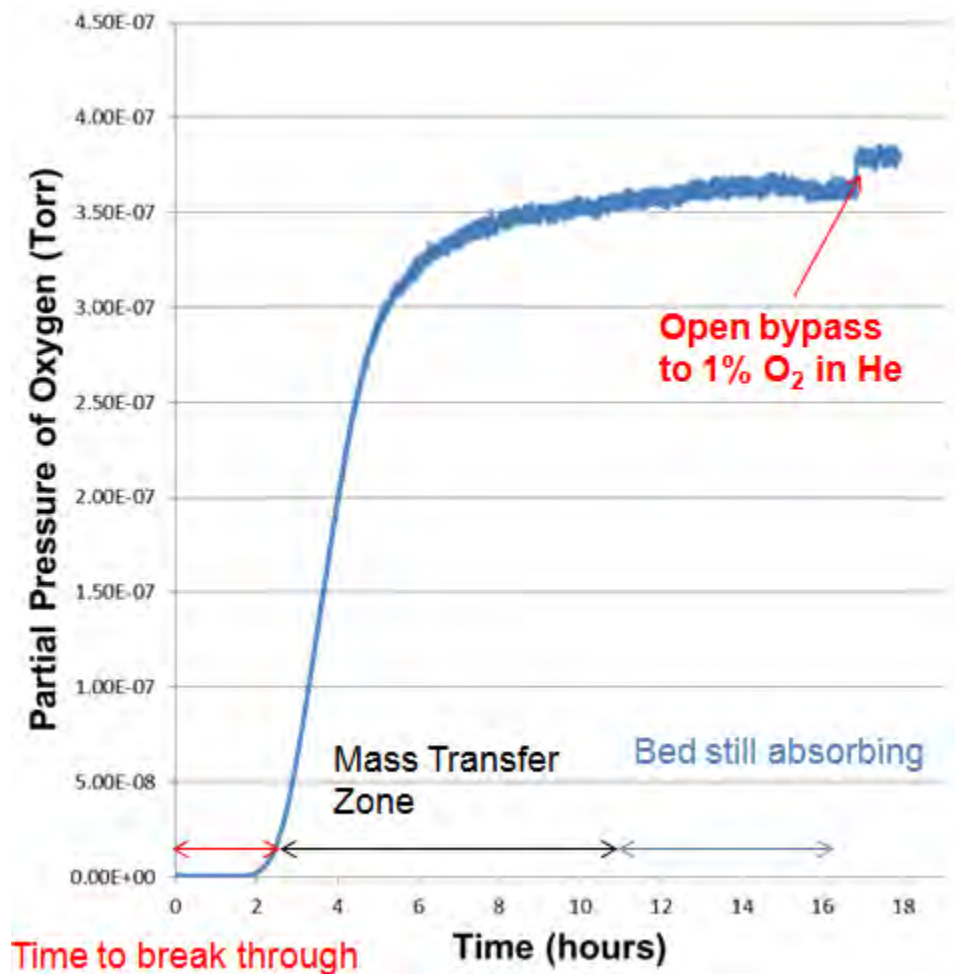


Figure 3.3 indicates that saturation is approached asymptotically. At hour 17, the nickel bed was bypassed to measure the oxygen concentration of the inlet stream. It is evident that the nickel bed continued to remove some oxygen from the stream, albeit not very efficiently. At hour 17, only 12% of the nickel had been converted to oxide. The oxidation process appears to be diffusion limited, either by nickel atom diffusion through the oxide layer or oxygen diffusion into the nickel bulk. Increasing the operating temperature to 400 °C increases the oxygen removal rate. Clearly the diffusion rate at the nickel/nickel-oxide surface has increased. The outlet concentration approaches the inlet concentration in the 400 °C case in Figure 3.2 at hour 12. Fifty percent of the nickel has been oxidized by this time.

3.2 Nickel Reduction (Hydrogen Regeneration)

Nickel oxide can be reduced to nickel at 500 °C in the presence of hydrogen. This means that spent nickel beds can be regenerated with hydrogen to recover their ability to scavenge oxygen from carrier streams. The beds can be re-used.

Figure 3.4: Partial pressure of hydrogen and water, measured by the RGA, as a function of time. Helium carrier flow rate and temperature were held constant at 2 L/min and 500 °C, respectively.

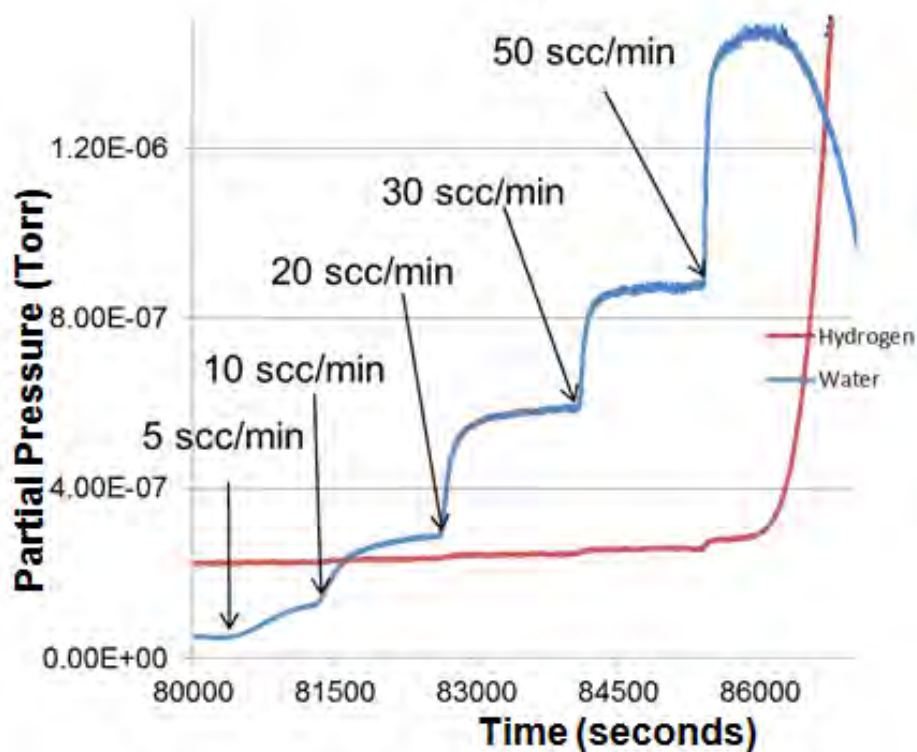


Figure 3.4 illustrates a typical regeneration at 500 °C using a helium purge rate of 2 L/min. As the hydrogen flow rate is increased from 5 scc/min to 50 scc/min the water partial pressure in the carrier at the bed outlet increases proportionately. Towards the end of the run, the water partial pressure is observed to drop and concomitantly the hydrogen partial pressure increases as the quantity of residual nickel oxide in the bed disappears.

Figure 3.5: Partial pressure of water vs. flow rate of hydrogen at three different helium carrier flow rates.

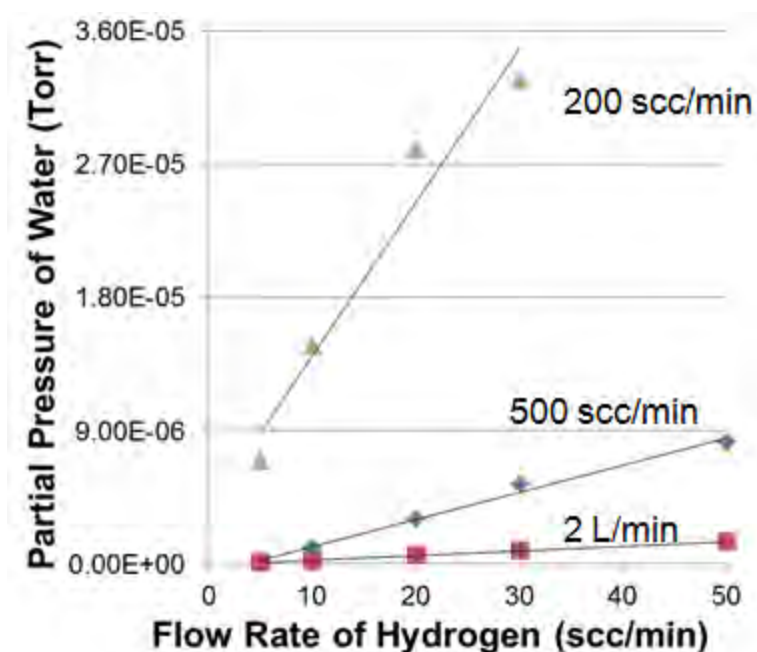


Figure 3.5 summarizes three regenerations at 500 °C for varying helium and hydrogen flow rates. At a helium purge rate of 500 sccm and 2 LPM, the partial pressure of water appears to increase linearly with increasing hydrogen flow rate (or partial pressure). For a helium purge rate of 200 sccm, the water production rate deviates from linearity and appears to approach a saturation value that is independent of the hydrogen partial pressure in the carrier.

Water vapor in the vicinity of the nickel oxide appears to inhibit the reduction process. At low carrier flow rates, water vapor resulting from the nickel reduction remains in the vicinity of the remaining nickel oxide and interferes with hydrogen reaching unreacted nickel oxide. Increasing the helium carrier flow rate encourages the removal of water vapor from the nickel oxide regions and promotes more rapid reduction.³

Figure 3.6: Partial pressure of water and helium vs. time measured by the RGA as the carrier flow was increased at the indicated times.

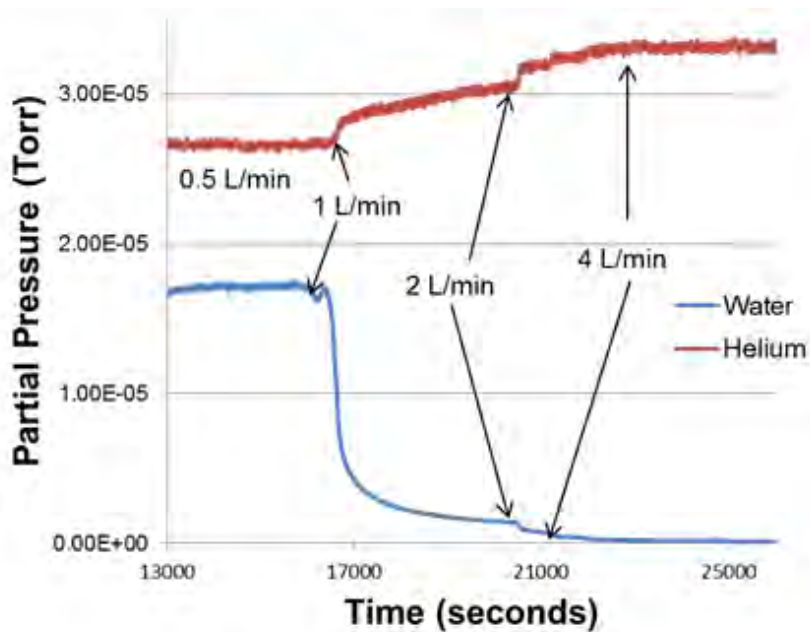


Figure 3.6 illustrates the impact of the helium carrier on the reduction process. In this experiment, the hydrogen flow rate was fixed at 50 sccm and the carrier flow rate varied from 0.5 L/min to 4 L/min. The regeneration temperature was 500 °C. If all water generated in the reduction process is purged from the bed as it is produced, one would expect the water partial pressure in the carrier stream at the bed outlet to be inversely proportional to the carrier flow rate. Doubling the carrier flow rate should reduce the water partial pressure by half. Inspection of Figure 3.6 indicates a dramatic drop in the water partial pressure when the carrier flow rate increases from 0.5 L/min to 1 L/min and significantly smaller changes in the partial pressure when the carrier flow rate is increased further to 2 L/min and then 4 L/min. Evidently the vapor pressure in the carrier at the lowest flow rate is not directly related to the rate of water generation

due to the presence of hydrogen but rather to a balance between the water vapor production rate and the water removal rate from the bed. The increasing helium partial pressure dependence on the increasing helium flow rate is an artifact of the diagnostic used to measure the gas partial pressures. The helium partial pressure should be independent of the flow rate.

Conclusion

Increasing the temperature of the catalyst from room temperature to 400 °C increases the amount of oxygen that can be absorbed by the catalyst. Catalyst reactivation is more efficient as the flow rate of hydrogen increases. Water vapor in the vicinity of the nickel inhibits reactivation; increasing the carrier flow rate decreases the water vapor pressure and improves the reactivation efficiency.

Higher operating temperatures are preferred for both oxygen uptake and nickel reduction. Higher flow rates are preferred in nickel reduction for both hydrogen and the carrier gas.

References

1. W.T. Shmayda, N.P. Kherani, B. Wallace, F. Mazza. "Inert gas secondary enclosure clean-up system." Ontario Hydro, Ontario, Canada. Canadian Fusion Fuels Technology Project, Ontario, Canada. SAES Getters S.p.A., Milano, Italy. 1974-1990.

2. G.P. Wainwright, W.T. Shmayda, R.T. Janezic. "Tritium capture with getter-bed technology at the Lab for Laser Energetics." Laboratory for Laser Energetics, Rochester, New York. 16-21 September 2007.
3. J.T. Richardson, R.M. Scates, M.V. Twigg. "X-ray diffraction study of the hydrogen reduction of NiO/ α -Al₂O₃ steam reforming catalysts." Department of Chemical Engineering, University of Houston, Houston, Texas. (2004)

Acknowledgements

I would like to thank Dr. Craxton for selecting me for this wonderful opportunity. I would like to thank my supervisor Dr. Shmayda for his expertise, advice, and guidance throughout this experience. I also want to thank Neil Redden and Andrew Boyce for their contributions to the experiment and for their support. Finally, I want to thank my fellow interns, especially my lab partner Aaron Jo, for their advice and encouragement.

Hydrogen Isotope Separation Using Gas Chromatography

Aaron Jo

Victor Senior High School

Advisors: Dr. Walter Shmayda, Neil Redden

Dec 2012

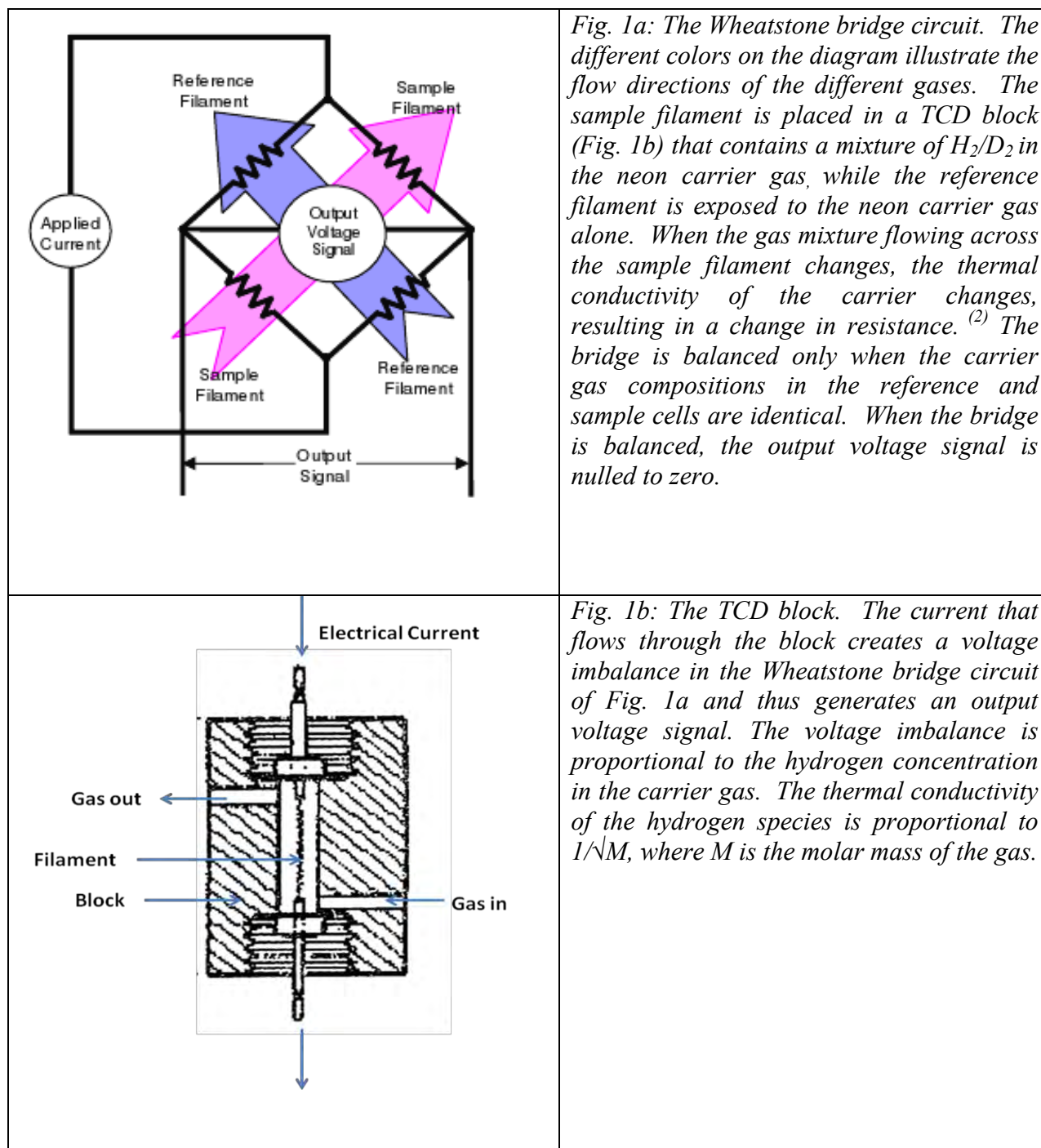
Abstract

A gas chromatograph (GC) system was commissioned to measure hydrogen isotope species. The GC system uses an iron-doped molecular sieve column held at 77 K to separate the hydrogen isotopes and a thermal conductivity detector (TCD) to analyze the separated species. The response of the TCD was shown to depend on the quantity of hydrogen injected, on the carrier flow rate, and on the temperature difference between a heated filament in the TCD and its housing. The instrument is very stable. Measurements are highly reproducible. Baseline separation is easily attained.

Introduction

The Laboratory for Laser Energetics (LLE) requires an in-house capability to monitor the composition of deuterium-tritium (DT) fuel. LLE is also in the process of designing an isotope separation system and requires a method of quantifying the purity of the tritium. To meet both these needs, LLE is developing a gas chromatograph (GC) system.

Gas chromatography is a physical method of separation where components are separated and distributed between a stationary phase and a mobile phase.⁽¹⁾ A Bruker CP-3800 gas chromatograph was configured and calibrated to measure hydrogen isotope concentrations. Gas chromatography with a thermal conductivity detector (TCD) is a good technique to measure the isotopic composition of hydrogen mixtures. The principle of the TCD is shown in figures 1(a) and (b). In figure 1(a), in the ideal case of four identical filaments and equal flow in each cell, the voltage drop across each filament is the same and a zero output voltage signal is recorded. When the sample gas flows, the voltage drops across the reference and sample filaments are



different and an output voltage signal will be observed. In figure 1(b), the applied current is chosen to heat the filament to the desired operating temperature in the presence of gas flow. This current will depend on the thermal conductivity of the gas, as this affects the loss of heat from the filament to the block. The resistance of the filament depends on its temperature. If the current is held fixed and the gas changes to a gas with a different thermal conductivity, the resistance of the filament will change.

Preparation of Sample Cylinders

Six calibration standard sample cylinders were filled using a gas handling system capable of high vacuum in order to calibrate the GC. The cylinders were evacuated and then filled with half of the primary component gas pressure required to achieve 1000 torr total pressure. The cylinders were then filled with all of the secondary component gas required to achieve 1000 torr total pressure. The cylinders were then pressurized with the second half of the remaining primary component gas required to achieve the 1000 torr gas standard. The composition ratios of the cylinders were 1/99%, 20/80%, 40/60%, 60/40%, 80/20%, and 99/1% H₂/D₂. After it was discovered that the 1000 torr cylinders did not have enough gas pressure in them to achieve a high signal-to-noise ratio from the TCD, cylinders of 10/90%, 90/10%, and 46/54% H₂/D₂ were created at 5000 torr.

Configuration and Calibration of the Gas Chromatograph Setup

Figure 2 shows a schematic of the GC setup. The primary flow is that of the neon carrier gas. Either the unknown sample or the gas from one of the standard cylinders can be added to the flow.

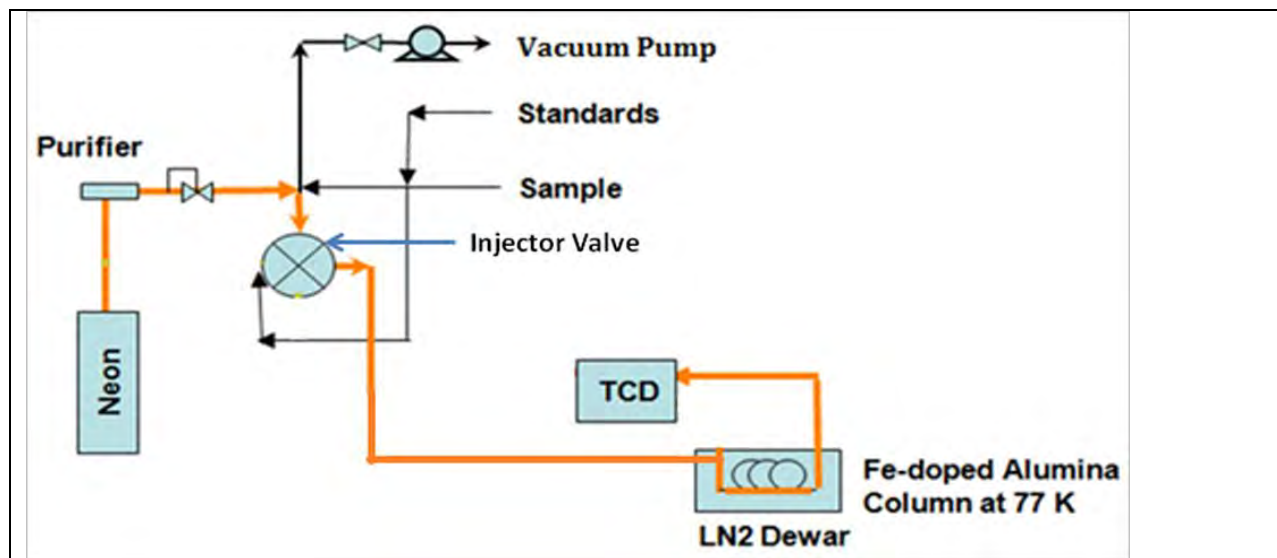


Fig 2: Schematic of the GC setup. The GC comprises the alumina column and the TCD. The injector valve allows different gases to flow into the GC. The orange arrows represent the carrier gas flowing through the GC.

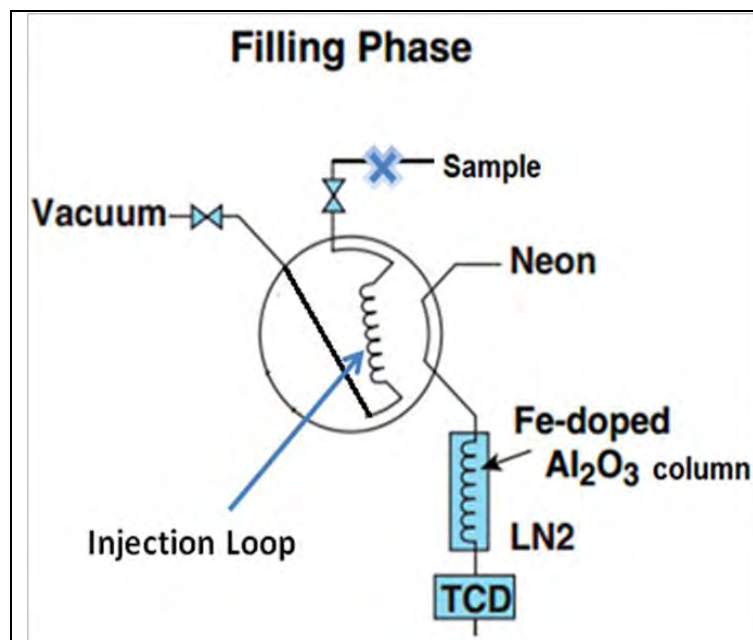


Fig 3: The GC in the filling phase. This stage is where the gas is expanded into the injection loop (the coil). The injector valve is rotated into the filling position. The first step to analyze a sample is to open the sample cylinder valve to pressurize the injection loop then close the valve. Next, all of the valves in the system are opened. As a result, the sample pressure is reduced in a repeatable fashion and is sustained under a static vacuum within the injection loop.

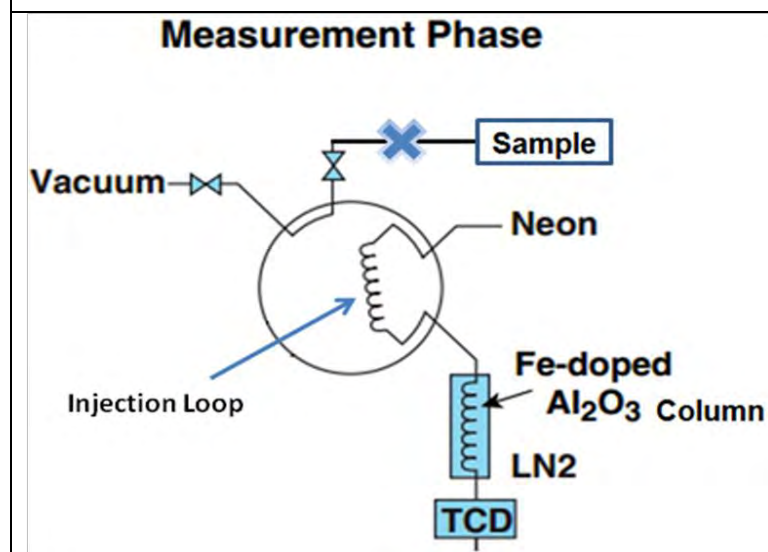


Fig 4: The GC in the measurement phase. In this stage, the components of the sample gas in the injection loop are separated as they flow through the Fe-doped Al_2O_3 column and diagnosed in the TCD.
(3)

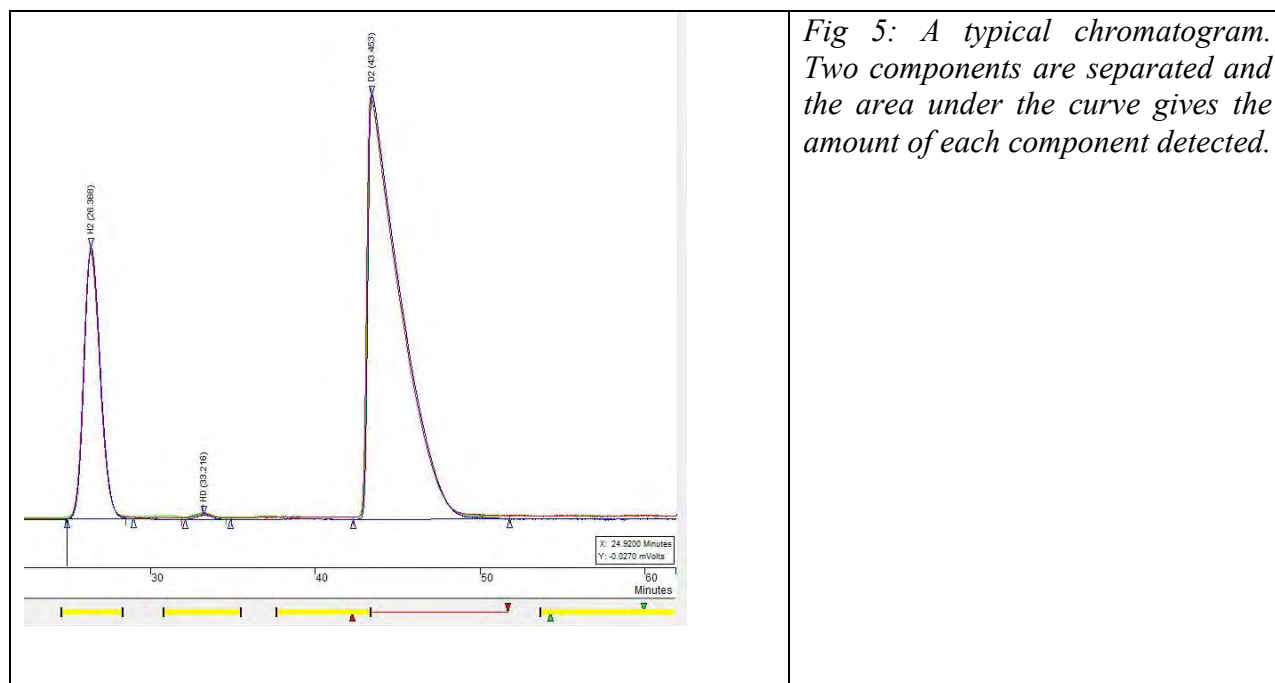
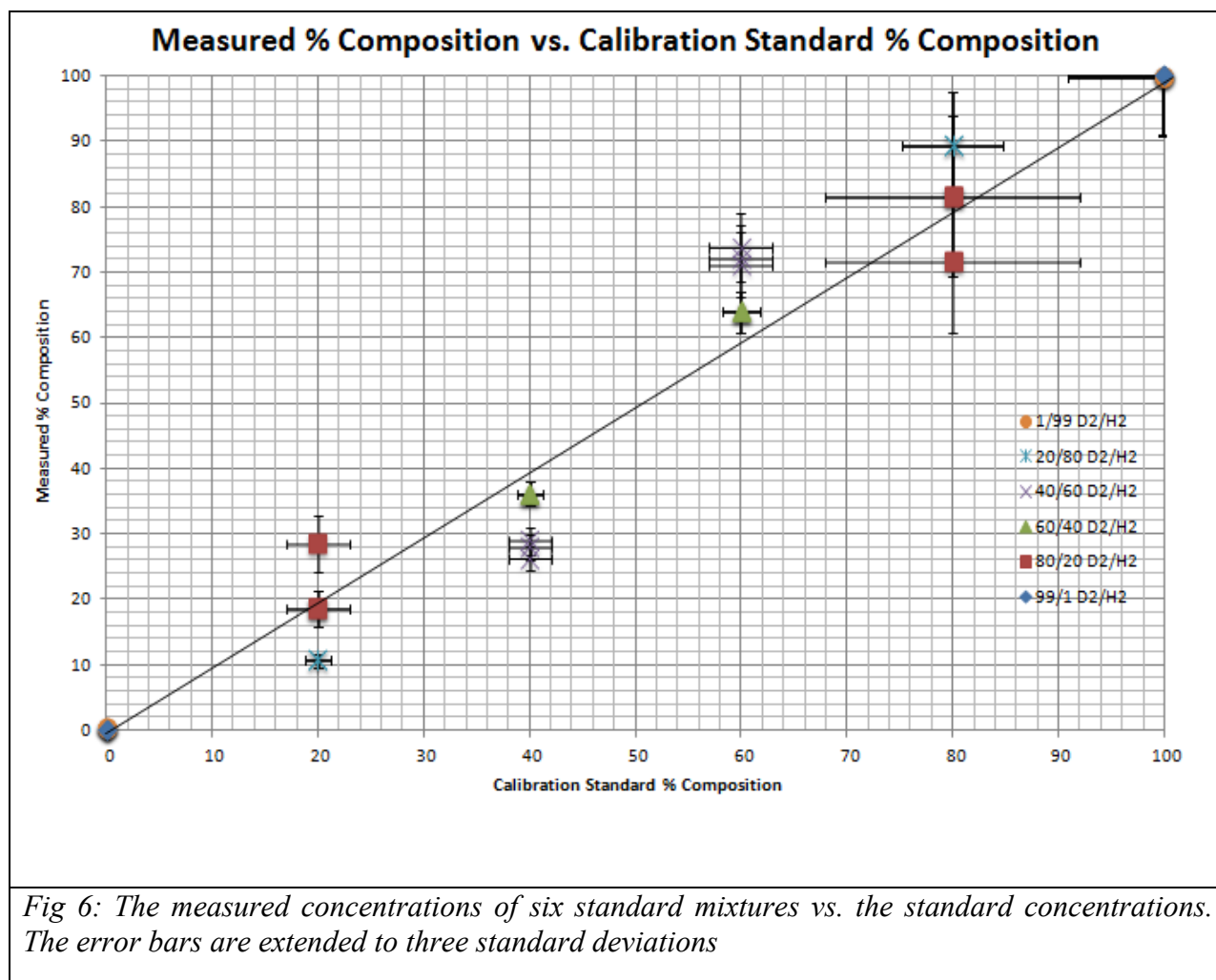


Figure 3 shows the GC in the filling phase. After this, the valves are closed and the injection loop moves into the inject position shown in figure 4. In both stages, the neon carrier gas flows through the alumina column and the TCD. A typical chromatogram is shown in figure 5: this is a graph showing the voltage across the Wheatstone bridge as a function of time. The two pulses correspond to two substances that pass through the chromatography column at different rates. The area of each pulse gives the amount of the substance detected. An earlier calibration relates the measured area in volts*time to the mass of the substance measured conveniently in torr*cc (from the ideal gas law, mass is proportional to pressure times volume).

Measurements Using Six Mixed Standards

The sample cylinders consisting of 1/99%, 20/80%, 40/60%, 60/40%, 80/20%, and 99/1% H₂/D₂ were examined first. The results are shown in figure 6. Each run produces two

points; one for the D₂ concentration and one for the H₂ concentration. Three runs were made for each cylinder, producing 36 points on figure 6. Some of these points are coincident.

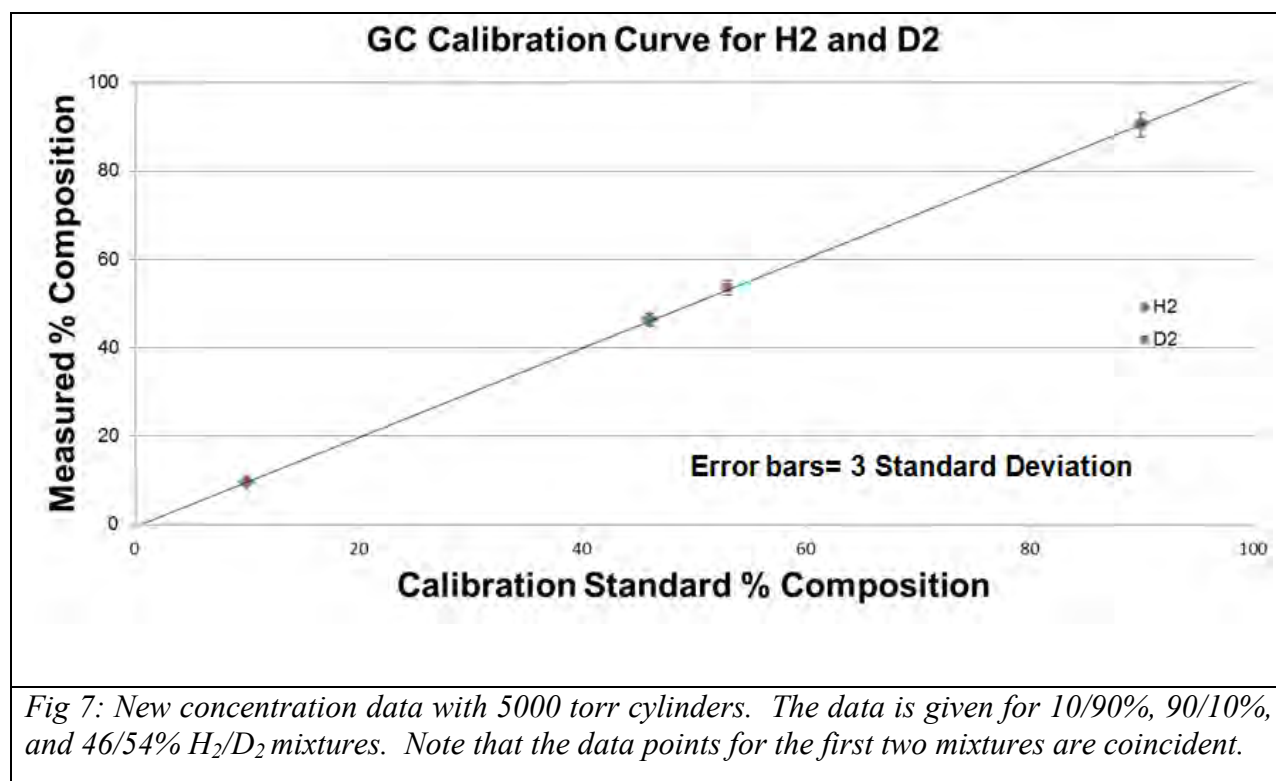


As seen on figure 6, most of the mixed concentrations don't match the measured concentrations. For example, the standard created at 40/60% H₂/D₂ was measured by the GC at 36%/64% H₂/D₂. In addition, even with the error bars at 3 standard deviations, the measured amounts don't match the mixed standard. The y error bar is three times the rms of the three runs.

The x error bar is the accuracy with which the % fill is measured. In order for the GC method to be robust and the instrument properly calibrated, the mixed standard and the measured concentration results must be within 3 standard deviations of each other. Results within 3 standard deviations represent 99.7% of all the results, so GC analysis results within 3 standard deviations would be highly reproducible. The poor correlation between the measured and expected results may be due to inaccuracies in filling the standard cylinders to the correct concentrations. Figure 6 shows a lack of agreement between standard and measured, and a large variability between the three runs with a given standard. The larger error bars are because the pressure injected into the GC was insufficient. As a result, there are weaker signals and hence greater variability.

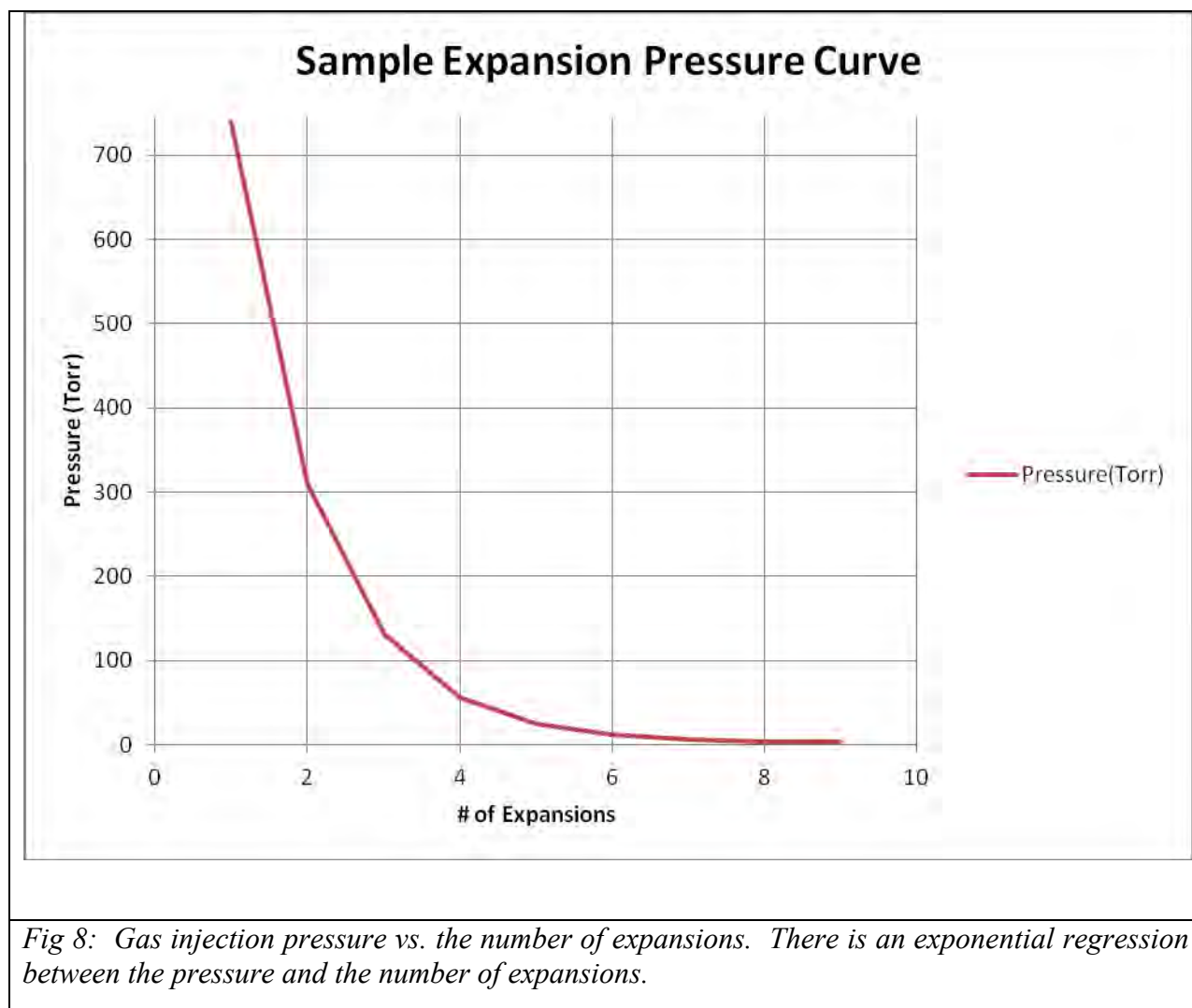
To remedy this problem, three new sample cylinders were prepared with a higher pressure of 5000 torr. The cylinders had H₂/D₂ ratios of 10/90%, 90/10%, and 46/54% H₂/D₂.

Measurements using the new Mixed Standards



The same procedure for loading the GC with the sample gas was implemented except for the pressure adjustments. The results, shown in figure 7, are much more promising. The 10/90% H₂/D₂ was measured to have an average composition of 9.6/90.4% H₂/D₂. The standard deviation within the three runs that were made with this composition was only 0.45%, indicating that the GC is accurate and consistent. The 90/10% and 46/54% H₂/D₂ compositions support the performance of the GC. The 10/90% H₂/D₂ was measured to have an average composition of 90.5/9.5% H₂/D₂, and the standard deviation within the three runs that were made with this composition was 0.06%. The 46/54% H₂/D₂ was measured to have an average composition of 46.4/53.6% H₂/D₂, and the standard deviation within the three runs that were made with this composition was 0.25%.

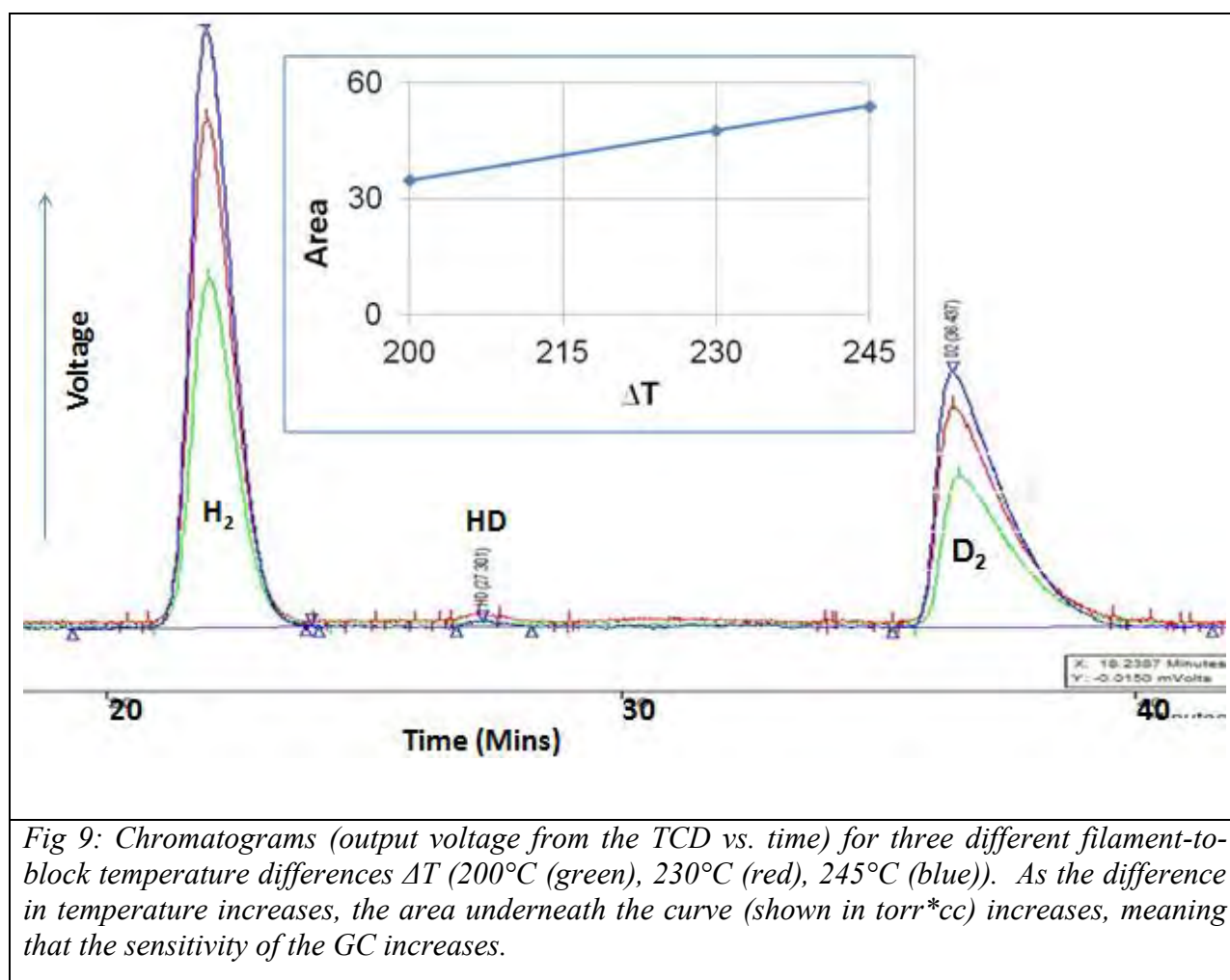
The results of figure 7 show that the measured amount is accurate within 1% of the mixed standard. In addition, the error bars are significantly smaller than on figure 6 and show that the GC is highly reproducible and accurate.



Since the pressure transducer measuring sample pressure attached to the GC can only read up to 1000 torr, the instrument can't read a 5000 torr gas sample. As a result, multiple expansions had to be made in order to bring the pressure down to a readable pressure. An expansion is performed when the sample gas is first injected into the GC, and then placed under

a static vacuum with all the valves opened for a specified amount of time. Figure 8 shows how the pressure decreases exponentially with each expansion. With numerous expansions, the pressure becomes low enough that it can be measured. The original 5000 torr pressure is then inferred by moving the pressure down on each expansion. Expansions were used to investigate the dependence on sample size.

Dependence on Block and Filament Temperature Differences



With Varian detectors, the filament temperature is between 350°C and 490°C. A higher filament temperature setting results in bigger peaks on the chromatogram but the lifetimes of the filament are shorter. To avoid burning out the filament, a moderate filament temperature was used and the block temperature was lowered in order to create the optimum temperature difference. The difference in temperature between filaments and the detector block provides much of the control over the sensitivity of the detector. The block temperature should be high enough to prevent potential condensation of the major sample constituents. The block has a large thermal mass to maintain a consistent temperature, which provides a stable baseline.⁽²⁾

The filament temperature stayed at a consistent 350°C with the 46/54% H₂/D₂ sample, while the block temperature was changed twice. The block typically runs at a temperature of 120°C, but it was altered to be 105°C and 135°C. With a 105°C block temperature, the area count is approximately 53.97 torr*cc, while a 135°C block temperature results in an area count of 34.89 torr*cc. Since a higher block temperature decreases the temperature difference between the block and the filament, there is a decreased sensitivity and therefore a lower area count.

Dependence on Carrier Flow Rate

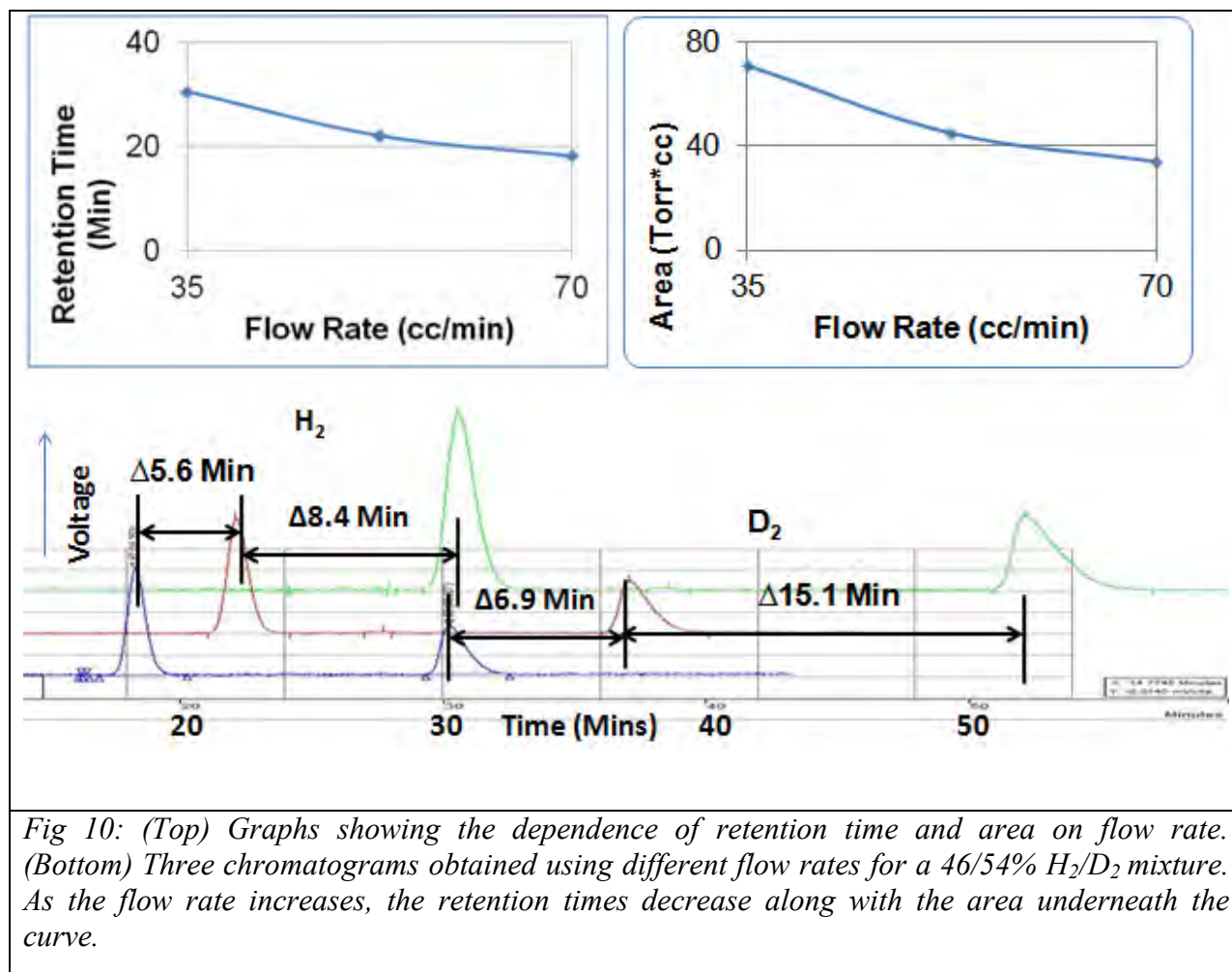


Fig 10: (Top) Graphs showing the dependence of retention time and area on flow rate. (Bottom) Three chromatograms obtained using different flow rates for a 46/54% H₂/D₂ mixture. As the flow rate increases, the retention times decrease along with the area underneath the curve.

The optimum carrier flow rate is a compromise between reasonable analysis time and detector sensitivity. Lower flow rates will maximize detector sensitivity, but will significantly lengthen the overall measurement time. Higher flows, however, achieve fast separations, but will deteriorate performance as the analytes do not reside long enough in the cell to effectively cool the filaments. The TCD is a concentration-dependent detector and its response is critically dependent on the retention time, i.e., how long an analyte spends inside the detector.⁽²⁾

Figure 10 shows chromatograms for the 46/54% H₂/D₂ sample, used with flow rates of 35 (green), 52.5 (red), and 70 (blue) cc/min. With 35 cc/min, the retention times for H₂ and D₂ are 30.6 mins and 52.2 mins, respectively. A 52.5 cc/min flow rate has retention times of 22.1 mins for H₂ and 37.1 mins for D₂. With 70 cc/min, the retention times for H₂ and D₂ are 18.3 mins and 30.2 mins, respectively. The 35 cc/min flow rate has an H₂ area underneath the curve around 76.5 torr*cc. The 52.5 cc/min and 70 cc/min flow rates have H₂ areas of 42.13 and 34.29 torr*cc, respectively. Both the area counts and the retention times decrease with flow. As a result, figure 10 illustrates how smaller retention times decrease the area underneath the curve.

Dependence on Sample Size

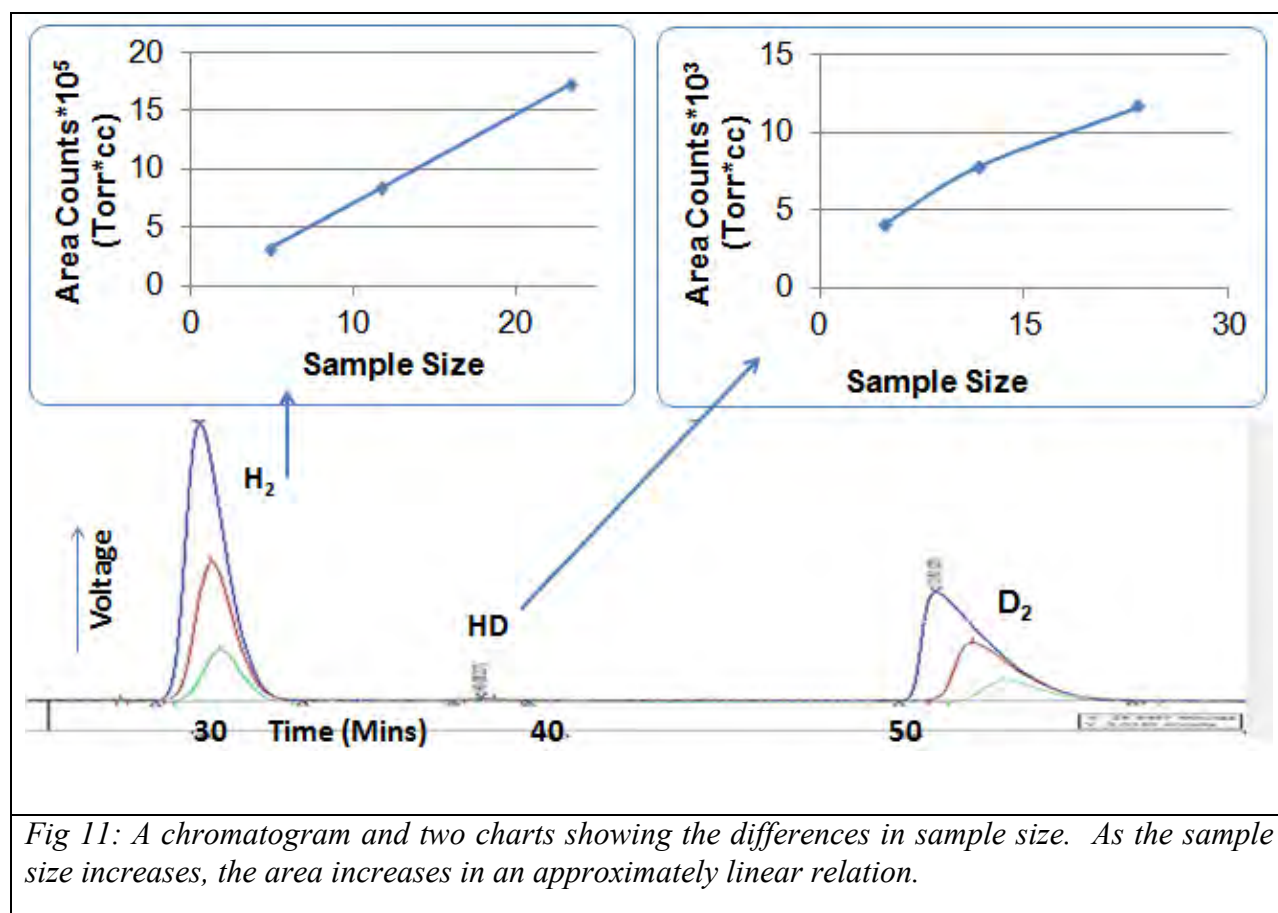


Figure 11 shows three chromatograms with different sample sizes and a different number of expansions. A sample size refers to how much sample is injected into the GC. As more expansions are made, the sample size decreases. The green chromatogram represents 6 expansions, while the red and blue chromatogram represents 5 expansions and 4 expansions, respectively.

With H₂, the area underneath the curve after 4 expansions is 17.28 torr*cc. After 5 and 6 expansions, the areas are 8.31 torr*cc and 3.09 torr*cc, respectively. Based on the data, as the number of expansions increases, the sample size decreases, as does the area underneath the curve.

In order to find the detection limit of the GC for hydrogen isotopes, serial expansions were made and the injection pressure was monitored for each injection. After 9 expansions the area underneath the H₂ curve was 0.085 torr*cc. The injection pressure at the 9th expansion was 3.39 torr. However, the 10th expansion didn't provide enough detector response for the GC to integrate the H₂ peak.

Conclusions

Gas chromatography with a TCD has been demonstrated to be a good technique to measure the isotopic composition of hydrogen mixtures. Using a Bruker CP-3800 GC, it was shown that hydrogen isotope concentrations can be measured to an accuracy of 1%. Best results were obtained for 5000 torr gas samples. The detection limit of this GC configuration for hydrogen isotopes was quantified. Sensitivities of the technique to temperature, carrier rate, and sample size were all measured. Increasing the temperature difference between the TCD block

and filament increases sensitivity. Decreasing the carrier flow rate and increasing the sample size both increase sensitivity.

References ⁽⁴⁾

1. Shmayda, Walter. *Gas Chromatographic Analysis System for the Laboratory for Laser Energetics, University of Rochester*. February 22, 2002
2. Bramston-Cook Randall, Neumann Herb. *Operating Parameters for the Thermal Conductivity Detector in Varian 3800 and 3900 Gas Chromatographs*.
3. W.T. Shmayda, M. J. Bonino. *Gas Composition Changes Due to β -Induced Hydrogen Leaching from Capsule Walls*. October 1-5, 2006
4. Boyce, Andrew, *Water-Stimulated Tritium Release from Metals*, 2011 Summer Research Program at the University of Rochester's Laboratory for Laser Energetics

Acknowledgments

I would like to first thank Dr. Craxton for allowing me to take part of this worthwhile program. I also would like to thank my advisors, Dr. Shmayda and Neil Redden, for the support and advice that they have provided for me. Lastly, I would like to thank all of the high school students in this program, along with Andrew Boyce, for their advice and the help that they have given me throughout this program.

Magnetic Field Penetration Into a Conducting Hohlraum

Alec Kirkley
Pittsford Sutherland High School
Pittsford, NY
Advisor: Dr. Gennady Fiksel

Laboratory for Laser Energetics
University of Rochester
Rochester, NY
September 2012

Abstract

A gold hohlraum will be used for a variety of MIFEDS (Magneto-Inertial Fusion Electrical Discharge System) experiments on the Omega laser system at the Laboratory for Laser Energetics (LLE) of the University of Rochester, NY, and the magnetic field penetration into the hohlraum is of interest. The dynamics of the axial magnetic field penetration into the conductive hohlraum was analyzed theoretically, and a small-scale tabletop experiment was designed to test the predictions. The experiment used a solenoid to generate a magnetic field, which was measured by a multi-turn B-dot probe. For this experiment, the hohlraum was substituted with thin-wall copper tubing with a diameter of 2.54 cm. Three different lengths of tube (2.54 cm, 5.08 cm, and 7.62 cm) were used to measure the attenuation and phase shift of the magnetic field inside the tubing in comparison with the outside. The measured attenuation and phase shift results are consistent with theoretical predictions, and the results are directly applicable to the field attenuation in an actual hohlraum.

1. Introduction

Two light atomic nuclei can combine to create immense quantities of energy in a process called nuclear fusion. The advantage of nuclear fusion over other methods of harnessing energy is that fusion is sustainable and safe for the environment. Nuclear fusion research is being conducted around the world due to its potential for energy production, and the Laboratory for Laser Energetics (LLE) is one major contributor to this research. Inertial confinement fusion is the main topic of interest at LLE, where a cryogenic target is heated and compressed by the Omega laser system.

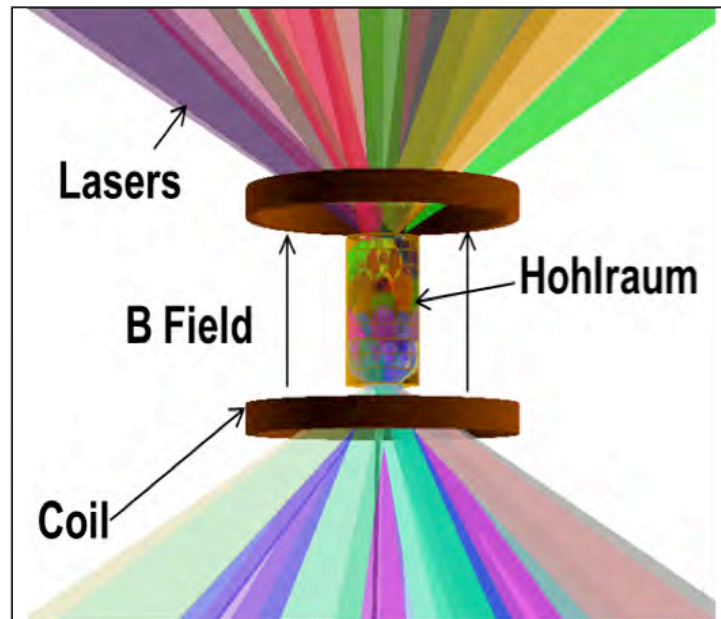


Figure 1. Hohlraum Diagram: A target plasma is confined in a hohlraum by an applied magnetic field during magneto-inertial fusion.

A strong pulse of magnetic field could be used to improve plasma confinement in an inertial confinement fusion (ICF) implosion. The Magneto-Inertial Fusion Electrical Discharge System (MIFEDS)⁽¹⁾ is used to create this magnetic field, which can confine the fusion fuel as it is heated into the plasma state.⁽²⁾ In the process of magneto-inertial fusion, the magnetic field provided by MIFEDS helps reduce the loss of thermal energy, while containing the plasma and allowing it to be heated by inertial compression.

One experiment planned for the Omega laser system using MIFEDS has a goal of studying the effect of a magnetic field on the confinement and transport of fast electrons in a hohlraum plasma. Hohlraum plasma fusion (Fig. 1) is an ICF concept wherein a spherical fusion

target placed inside a thin-wall high-Z metal cylinder is compressed by intense x-ray radiation resulting from the interaction of powerful laser radiation with the inner walls of the hohlraum.

This concept is called “indirect drive” to distinguish it from the “direct drive” concept wherein a fusion target is directly compressed by laser radiation. One of the by-products of the laser-wall interaction in a hohlraum is the production of energetic electrons that can penetrate into the target and adversely affect its compression and heating. A magnetic field can potentially isolate the target from the fast electrons, which is the main motivation behind the planned experiment. It is essential that the magnetic field produced by MIFEDS is strong and can penetrate into the hohlraum.

However, because the hohlraums are made out of conductive metal, they can partially screen

and attenuate the externally applied pulsed magnetic field. The project described in this report was designed to investigate and quantify this effect. The purpose of this project is two-pronged. First, we wanted to understand the mechanism and dynamics of magnetic field penetration so we can predict the field attenuation and the time it takes the magnetic field to penetrate into the

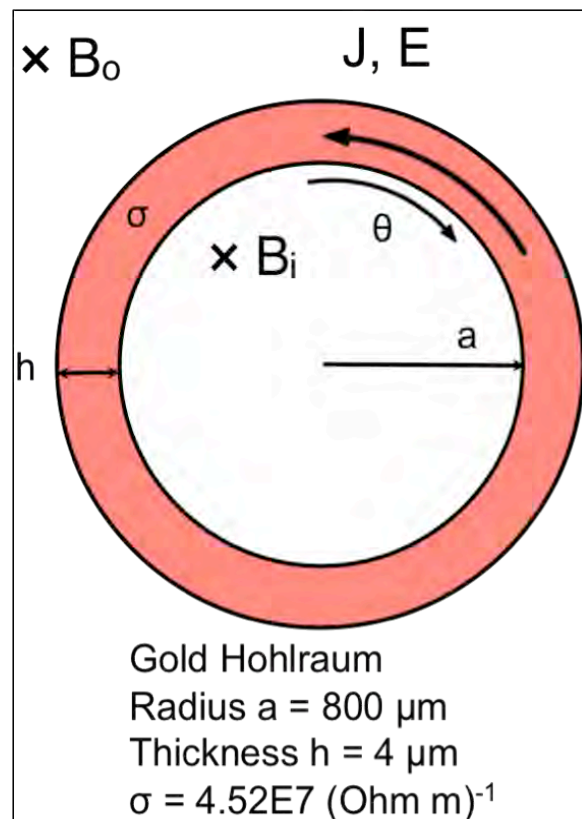


Figure 2. Cross Section of a Hohlraum in an Applied External Field: B_0 is the external magnetic field, J is the induced shell current density, E is the induced electric field, and B_i is the internal attenuated magnetic field. Dimensions for the hohlraum are given. The hohlraum length is 2.4 mm. Note that the current and electric field are in the negative θ direction.

interior of the hohlraum. Second, a table-top-scaled experiment was built to test our predictions. In the future, the magnetic field penetration will be studied using a real hohlraum.

2. Mathematical Modeling

2.1 Background

When an axial external magnetic field B_0 is applied to a conductive cylindrical shell, it induces a poloidal current J that runs around the shell (see Fig. 2, which also shows the hohlraum

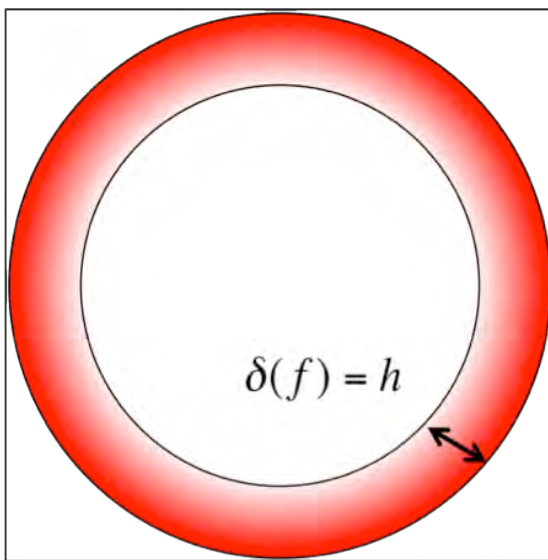


Figure 3. Skin Depth of Hohlraum Shell: The intensity of the red shading indicates J , the current density, which decreases as distance from the surface increases. In this figure the skin depth at frequency f , $\delta(f)$, equals the shell thickness h .

dimensions). The current, in turn, generates a magnetic field opposite to the applied magnetic field, so that the field inside the shell B_i is initially zero. Initially, the current J is concentrated in a thin skin layer on the outside of the cylinder. Later, the skin layer expands to the thickness of the shell and eventually starts decaying so the internal field B_i starts to grow. Overall, the internal field is attenuated and delayed with respect to B_0 . The goal of the model is to describe this process. Two characteristic time scales need to be investigated regarding this attenuation, namely the time for current to equilibrate

across the shell due to the skin effect, and the resistive current decay time in the shell. A mathematical relationship between the inner and outer fields is desired in order to predict the field attenuation.

2.2 Skin Time

The physics associated with magnetic field penetration can be investigated by considering imposed magnetic fields B_0 that oscillate sinusoidally with a frequency f . When current is introduced to a conductive shell, the skin effect causes it to initially concentrate near the surface. As the current density gets distributed through the conductor, it decreases exponentially as a function of depth from the surface. At the skin depth, which depends on f , the current has reached $1/e$ of its initial surface value.⁽³⁾ Figure 3 shows the hohlraum shell, with the decreasing current density across it. The skin depth δ can be shown to be:

$$\delta = \sqrt{\frac{1}{\mu_0 \sigma \pi f}}, \quad (1)$$

where μ_0 is the magnetic constant and σ is the conductivity of the cylinder. When the skin depth is greater than the shell thickness h , it can be assumed that the current has essentially equilibrated across the shell. The frequency f_h at which the skin depth equals the shell thickness h can therefore be used as a figure of merit. For frequencies lower than f_h the current across the shell can be considered uniform. The skin time T_{skin} is defined as $1/f_h$. From Eq. 1,

$$T_{skin} = \mu_0 \pi \sigma h^2 \quad (2)$$

For a gold hohlraum with dimensions as in Fig. 2, $f_h = 349$ MHz, and its inverse, the time for the current to penetrate the shell T_{skin} is 2.9 ns. This is very small compared with the rise time of MIFEDS (600 μ s) so the current can be assumed uniform within the shell.

2.3 Resistive Current Decay Time

Under the assumption of uniform current distribution across the shell, the electric and magnetic fields can be calculated using Faraday's Law (Eq. 3), Ohm's Law (Eq. 4), and Ampere's Law (Eq. 5):

$$2\pi a E_{\theta} = \frac{-d\Phi}{dt} \quad (3)$$

$$E_{\theta} = \frac{J_{\theta}}{\sigma} \quad (4)$$

$$\oint B \cdot dl = \mu_0 I \quad (5)$$

where a is the hohlraum radius, E_{θ} ($= -E$) is the electric field, J_{θ} ($= -J$) is the current density, l is a length element on a rectangular loop in the (r,z) plane of height h connecting the two surfaces, I is the current through this loop, and Φ ($= B_i \pi a^2$) is the magnetic flux across the cylinder's cross section. The magnetic field is in the z direction and into the page in Fig. 2. E_{θ} and J_{θ} are defined in the θ direction, which is in the clockwise direction with respect to the magnetic field.

Algebraic manipulation yields the following expressions for the electric and magnetic fields:

$$\begin{aligned} E_{\theta} &= \frac{-a}{2} \frac{dB_i}{dt} \\ &= \frac{J_{\theta}}{\sigma} \\ &= \frac{B_i - B_0}{\mu_0 \sigma h} \end{aligned} \quad (6)$$

Combining the first and third terms and isolating B_0 gives a differential equation that relates the inner and outer magnetic fields:⁽⁴⁾

$$B_0 = B_i + \tau \frac{dB_i}{dt} \quad (7)$$

where τ is a time constant given by:

$$\tau = \frac{\mu_0 \sigma a h}{2} \quad (8)$$

In the case where B_o is suddenly applied to the outside of the hohlraum with $B_i = 0$ when $t = 0$, Eq. 7 can be integrated to give

$$B_i(t) = B_o(1 - e^{-t/\tau}) \quad (9)$$

so that $B_i(t)$ approaches B_o for times greater than τ . As this happens, J approaches 0 from Eq. 6.

For this reason τ is known as the resistive current decay time.

2.4 Response to a Sinusoidal Magnetic Field

Information on the resistive current decay time can be attained by imposing a sinusoidal external magnetic field. This results in a sinusoidal shell current and internal B field:

$$B_o(t) = B_o e^{i\omega t} \quad (10)$$

$$B_i(t) = A e^{i\omega t} \quad (11)$$

where A is the complex amplitude of B_i and $\omega (=2\pi f)$ is the angular frequency of the B fields.

Solving for A by substituting into Eq. 7:

$$A = \frac{B_o}{1 + i\omega\tau} \quad (12)$$

an expression for a sinusoidal B_i results:

$$B_i(t) = \frac{B_o}{1 + i\omega\tau} e^{i\omega t} \quad (13)$$

Finding the absolute value of the amplitude of B_i yields:

$$|B_i| = \frac{|B_0|}{|1 + i\omega\tau|} = \frac{B_0}{\sqrt{1 + \omega^2\tau^2}} \quad (14)$$

The field attenuation can be defined as:

$$Attenuation = \frac{|B_i|}{|B_0|} = \frac{1}{\sqrt{1 + \omega^2\tau^2}} \quad (15)$$

Taking the inverse tangent of the imaginary component of B_i over the real component of B_i yields an expression for the phase shift (delay) of B_i relative to B_0 :

$$\varphi = \tan^{-1}(-\omega\tau) \quad (16)$$

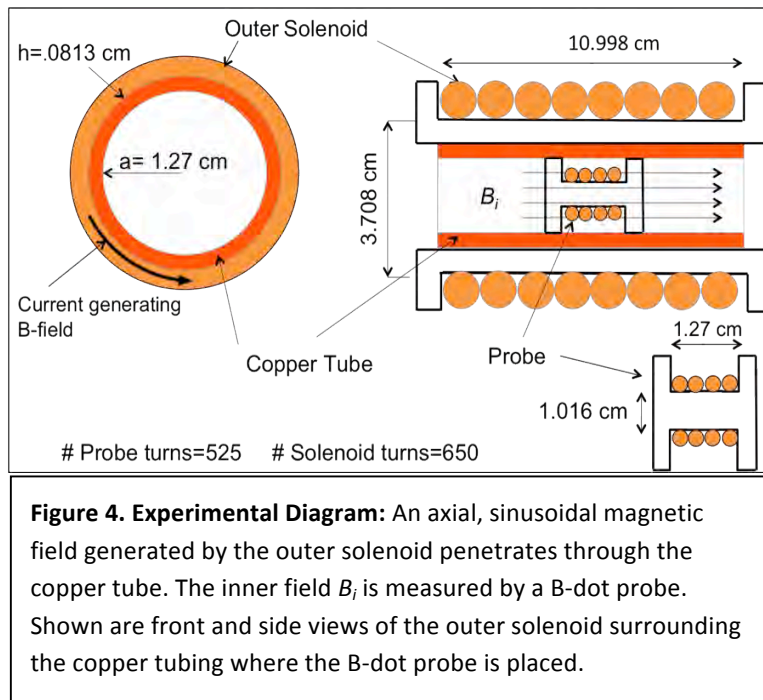
Eqs. 15 and 16 reveal that both the attenuation and phase shift depend on the single dimensionless parameter $\omega\tau$ where τ , given by Eq. 8, contains the important hohlraum characteristics such as dimensions and conductivity. In this sense, the model should accurately describe the dynamics of magnetic field penetration in the real hohlraum as well as in any conductive cylinder. Therefore, in order to test the accuracy of Eqs. 7, 15 and 16, we designed and built a simple tabletop experiment substituting a hohlraum with a copper cylinder. If the predictions (15) and (16) were proven true, then the model could be applied to the real hohlraum.

3. Experimental Design

3.1 Tabletop Experiment

Originally, in order to test the theoretical predictions for field attenuation (Eq. 15) and phase shift (Eq. 16), the hohlraum was to be placed in a sinusoidal axial field, and the experimental results measured with a Faraday probe were to be compared with predictions. The

hohlraum had not yet been manufactured, so in order to test the theory, a tabletop experiment



(Figs. 4 and 5) was designed to test the attenuation and phase shift into copper tubing, which behaves consistently with the same physics. Predictions (Eq. 15, Eq. 16) were derived for an infinite length cylinder, so three copper tubes of different lengths were tested to see if the results became more consistent with predictions as the

tube size increased. In order to provide an axial sinusoidal magnetic field inside the tubing, a

solenoid was constructed out of copper wire, and was

connected to a 1.3 ohm resistor

in series with a sinusoidal

function generator as the

voltage source. The voltage

across the resistor was

measured with an oscilloscope

to determine the electrical

current in the solenoid. The

field inside the tubing was measured with a B-dot probe, which was a smaller solenoid also

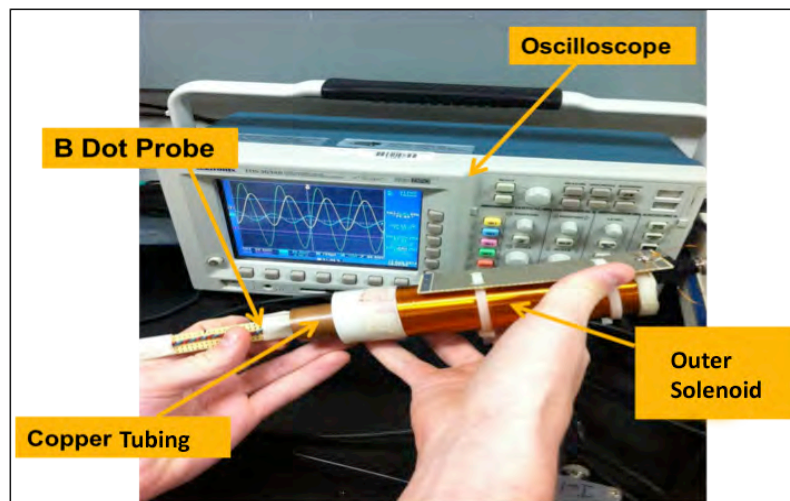


Figure 5. Experimental Set Up: The tabletop experiment was simple and inexpensive, but still involved the same physics as the hohlraum experiment would have.

constructed out of copper wire. The voltage across the B-dot probe was measured to determine

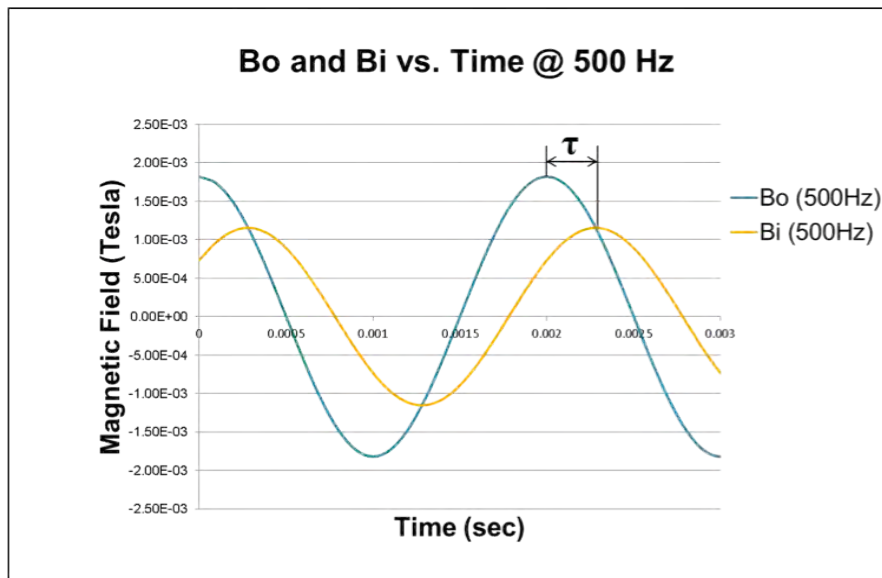


Figure 6. Modeled B_i and B_o : The inner and outer fields were modeled for an infinitely long copper tube of otherwise the same dimensions as the tubes that were tested. Shown is the modeling for an intermediate frequency.

the field inside the tubing.

The measurements were

taken with variable

function generator

frequencies in the range

from 20 Hz to 4000 Hz.

The attenuation and phase

shift were measured as

functions of the generator

frequency for each size of

copper tubing. Figure 6 is

a graph of the expected inner and outer magnetic fields for the copper at a mid-range frequency.

The inner magnetic field lags behind the outer magnetic field by a phase shift τ .

3.2 Data Analysis

The field generated by the outer solenoid is given by:

$$B_0 = \mu_0 \frac{N_s}{l_s} I_s = \mu_0 \frac{N_s}{l_s} \frac{V_R}{R} \quad (17)$$

where I_s is the outer solenoid current, N_s is the number of turns of wire in the solenoid, l_s is the

length of the solenoid, R is the 1.3 ohm resistor, and V_R is the measured resistor voltage. The

field inside the tubing can be evaluated from the B-dot probe measurement:

$$V_p = \pi r_p^2 N_p \frac{dB_i}{dt} \quad (18)$$

where V_p is the measured probe voltage, r_p is the probe radius, and N_p is the number of probe turns. Solving for the time derivative of B_i :

$$\frac{d}{dt}(B_i(t)) = \frac{d}{dt}(B_i e^{i\omega t}) = i\omega B_i(t) \quad (19)$$

Eqs. 18 and 19 can be algebraically manipulated to derive an expression for the experimental field attenuation:

$$\frac{|B_i|}{|B_0|} = \left(\frac{V_p}{V_R} \right) \left(\frac{l_s R}{\pi r_p^2 N_p \mu_0 N_s \omega} \right) \quad (20)$$

4. Results

4.1 Attenuation Results

Figure 7 is a graph of the expected attenuation and the recorded attenuations versus the applied frequency. The experimental attenuation results were consistent with the predictions, as it appears that the graphs for increasing tube

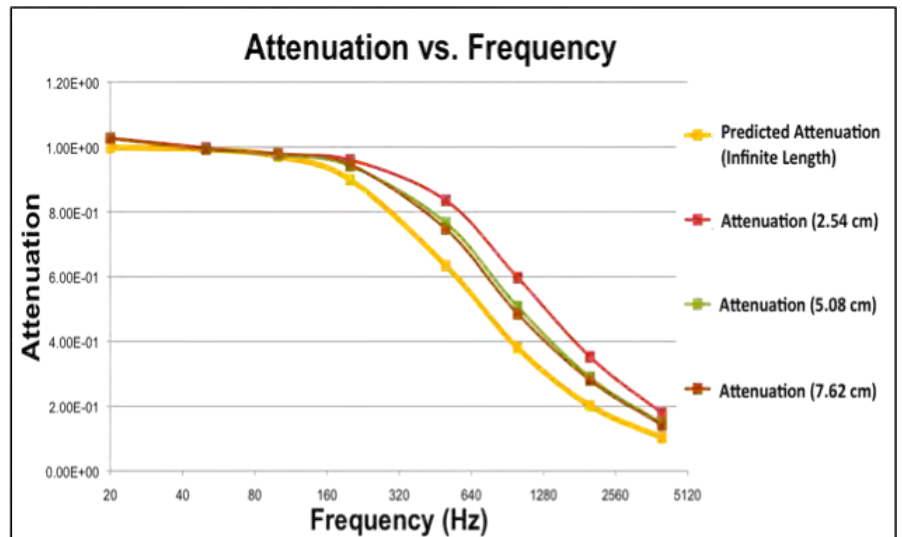


Figure 7. Experimental Attenuation as a Function of Frequency: As the tube size increases, the attenuation results appear to approach the theoretical values for an infinite copper tube length.

lengths approach the theoretical attenuation graph for an infinite tube length.

4.2 Phase Shift Results

Figure 8 shows the expected and recorded phase shifts graphed against the applied frequency. The

experimental phase shift results were consistent with the predictions, as it appears that the graphs for increasing tube lengths approach the theoretical graph for an infinite tube length, as with Fig. 7.

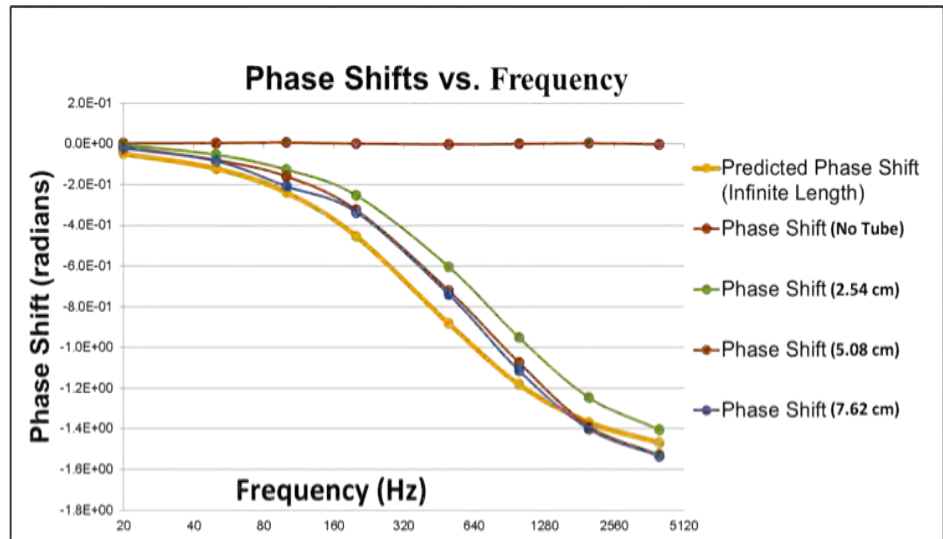


Figure 8. Experimental Phase Shifts as a Function of Frequency: As the tube size increases, the phase shift results appear to approach the theoretical values for an infinitely long copper tube.

4.3 Possible Experimental Error

While all the experimental results were close to the predictions, some small differences are observed. One possible explanation is the effect of a finite wall thickness of the copper tubing. This could cause a smaller magnetic field inside the tube and a greater phase shift at higher frequencies. Also, the conductivity of the copper used may not have actually been exactly the same as the value used for predictions.

5. Conclusions

The magnetic field penetration into a hohlraum was modeled analytically and tested using a tabletop experiment with copper tubing. A differential equation relating an axial external magnetic field and the resulting attenuated internal magnetic field was developed as well as an

expression for a delay time constant between the fields. The resistive decay time for the shell current was found to be the main source of attenuation, and the skin time was found to be insignificant at low frequencies. The tabletop experiment involved the use of three different lengths of copper tubing, since an actual hohlraum was not available, and the phase shift and attenuation results were consistent with mathematical predictions. This physics can now be applied to the real hohlraum.

An attenuation close to 1.0 is predicted for the actual hohlraum, meaning that the magnetic field penetrates into the interior of the hohlraum. Future testing will be done on a hohlraum with a Faraday probe to measure the attenuation and phase shift. Knowing that a magnetic field can successfully penetrate the hohlraum is essential to MIFEDS experiments, so that the fusion plasma can be properly contained to reduce thermal losses.

Acknowledgements

I thank Dr. Gennady Fiksel for his assistance and guidance during this project, Daniel Barnak and Po-Yu Chang for their teaching and help with the assembling of the experiment, and Dr. Craxton for giving me the opportunity to participate in this research.

References

1. Gotchev et al., “Seeding Magnetic Fields for Laser-Driven Flux Compression in High-Energy-Density Plasmas,” *Review of Scientific Instruments*, **80**, 043504 (2009).
2. Gotchev et al., “Laser-Driven Magnetic-Flux Compression in High-Energy-Density Plasmas,” *Physical Review Letters*, **103**, 215004 (2009).
3. W.N Cottingham and D.A. Greenwood, “Electricity and Magnetism,” Cambridge University Press, 1991.
4. Gennady Fiksel, “B-Field Penetration Powerpoint”, 2012.

Modeling Density Changes Inside a Cryogenic Target using a Fabry-Perot Interferometer: A Feasibility Study

Evan Lustick

Canandaigua Academy

Canandaigua, New York

Advisors: Dr. R. S. Craxton, Mark Wittman

Laboratory for Laser Energetics

University of Rochester

Rochester, New York

October 2012

1. Abstract

The use of a Fabry-Perot interferometer has been proposed as a method of measuring changes in deuterium gas density inside a cryogenic target. It is important to determine whether rapidly decreasing the temperature of the helium gas surrounding the target results in the required change in deuterium gas density for use on the National Ignition Facility. A program, *SAKURA*, has been written to investigate the feasibility of this proposal. *SAKURA* calculates the intensity of the interference fringes based on the distance between the two mirrors that make up the interferometer, the temperature of the target, and other parameters. Multiple bounces between the mirrors and refraction through the target layers are taken into account and interference fringes inside the target as well as background fringes are modeled. *SAKURA* has shown that the interference fringes are experimentally detectable and that a high mirror reflectivity is required. Experiments using the interferometer, along with *SAKURA*, will be used to study the thermal lag of heat out of the target following a sudden drop in ambient temperature.

2. Introduction

Nuclear fusion is a potential source of plentiful clean energy. One method used to achieve fusion is to irradiate a plastic spherical target filled with deuterium and tritium, two isotopes of hydrogen, with high-energy laser beams. This method is referred to as inertial confinement fusion (ICF). The plastic shell ablates, and the inner layers are compressed, resulting in very high pressure and

temperature in the deuterium and tritium. These conditions allow the positively charged nuclei of the inner layers to overcome the repulsive electrostatic forces between them, and fuse. Two nuclei fuse to create a helium nucleus, as well as an energetic neutron. If the mass of fuel inside the target is high enough, the helium nuclei can deposit their energy in the remaining fuel, resulting in more fusion reactions. This is referred to as ignition. If ignition occurs, the energy output of the fusion reactions can exceed the energy input of the laser beams. ICF will be a feasible energy source when the energy produced by the reaction is roughly two orders of magnitude greater than the energy output of the laser. Ignition is only currently possible on the National Ignition Facility (NIF) laser. The NIF is the most powerful laser in the world, delivering 1.8 megajoules on a timescale of a few nanoseconds.

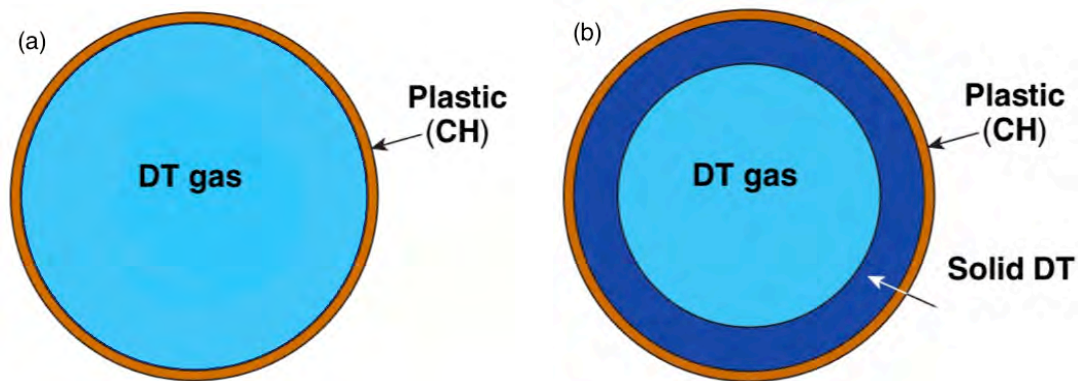


Figure 1: Two main target types used for inertial confinement fusion. (a) A plastic shell encases DT gas. (b) A cryogenic target has a solid DT mantle between its shell and the DT gas core.

There are two main types of targets used for inertial confinement fusion. The first type of target consists of only two layers: a thin plastic shell filled with

deuterium-tritium (DT) [Figure 1(a)]. Cryogenic targets, the second type, consist of a plastic shell with a low density gaseous DT center, but with a relatively thick layer of DT ice between them [Figure 1(b)]. The DT gas density depends on the vapor pressure of the DT ice, which depends strongly on the temperature of the DT ice. A cryogenic target contains a much larger mass of DT, and allows for higher energy output from the same laser energy input. The cryogenic DT ice layer is formed at 19.79 K.¹

In order to achieve fusion on the NIF, the DT gas in the cryogenic target must have a specific density. To achieve the desired density, the temperature of the helium gas is lowered from 19.79 K to 18.0 K. This leads to a rapid deposition of the gas onto the ice layer, lowering the gas density to the required value. If the target has too large of a thermal lag, and does not cool quickly enough, then the DT ice layer can begin to peel away from the plastic, resulting in an unusable target. The use of a Fabry-Perot interferometer was proposed to confirm that the drop in ambient temperature results in the expected change in gas density. The goal of this work was to produce a computer model of this experiment to test its feasibility. The resulting model, *SAKURA*, has shown that it is feasible to use the proposed method to measure gas-density changes in a cryogenic target for use on the NIF.

3. Experimental Setup

A Fabry-Perot interferometer² is a relatively simple device. It consists of two parallel, separated, highly reflective mirrors. The Fabry-Perot device has several applications in interferometry, spectroscopy, and other areas of physics.³

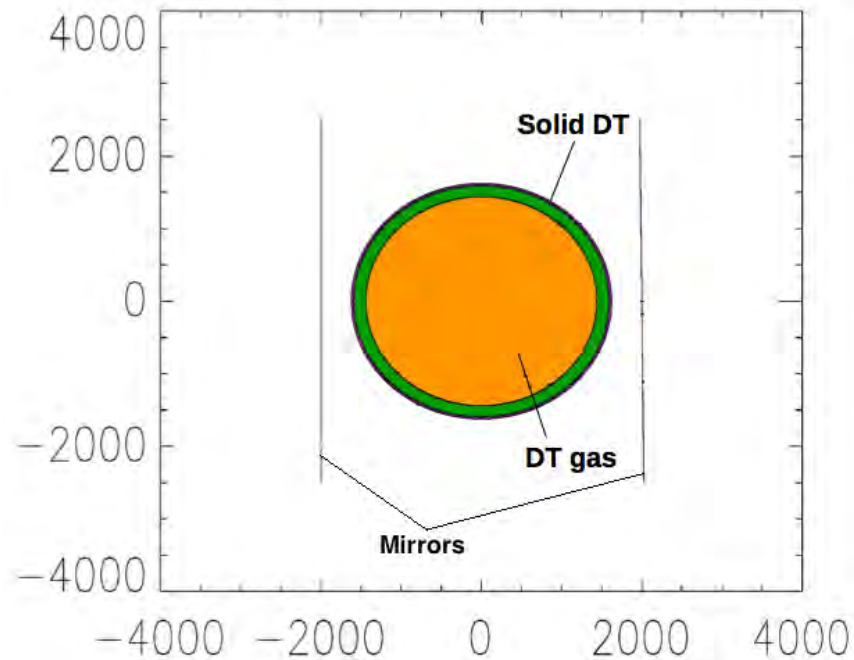


Figure 2: The experimental setup. A cryogenic target is placed in the center of a Fabry-Perot interferometer formed by the two mirrors. Distance in μm is shown on the x and y axes.

In the proposed experiment, which will use D_2 as a surrogate for DT, a cryogenic target is placed between the mirrors of the interferometer, as shown in Figure 2. The interferometer is filled with helium gas. Plane parallel wavefronts from a laser illuminate the interferometer, creating an interference pattern. This pattern is imaged onto a camera by a collection lens, which is oriented opposite the laser. By analyzing the changes in this pattern as the ambient temperature is decreased, one can discern if the desired change in gas density has occurred.

4. Interference Model *SAKURA*

This project entailed writing a program, *SAKURA*, to model the experimental system. *SAKURA* traces a ray of light as it passes through the first mirror, the target, and the second mirror, and records its intensity as it is collected by the lens. It also traces the ray through a given number of bounces between the mirrors, with a new intensity value calculated for every pair of bounces. It traces a few hundred in-phase rays that are just a few microns apart in the vertical direction of Figure 2. This models the behavior of a laser beam with a diameter slightly less than that of the target, which is 3300 μm for a typical NIF target. *SAKURA* collects information that the collection lens would receive to generate an interference pattern. Adjustable parameters in *SAKURA* include the spacing between the two mirrors, the temperature of the target, the wavelength of the laser light, the reflectivity of the mirrors, the tilts of the mirrors, the F-number of the collection lens, and the refractive indices of the plastic, D_2 ice, and D_2 gas. Some adapted segments of previously written code⁴ were used. All code was written in the programming language PV-Wave.⁵

4.1 Refraction and Reflection in the Model

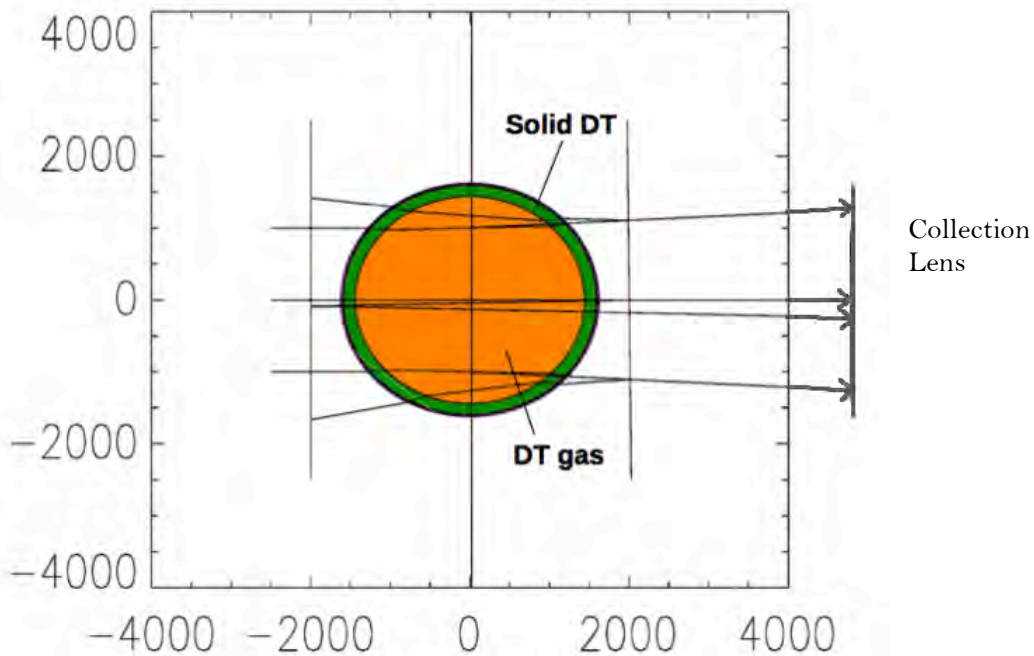


Figure 3: An exemplary run of the code. Three different rays are plotted to show how rays are refracted and reflected within the interferometer. Only one bounce between the mirrors is shown and the rays' paths are extended to the collection lens for ease of viewing. Distance in μm is again shown on the x and y axes.

SAKURA traces rays through the interferometer one at a time. Three rays, shown in figure 3, show how the edges and center of the beam behave within the apparatus. The refraction of the top and bottom rays is clearly visible as they pass through the target, while the center ray hits perpendicular to the surface of the target and does not refract. The reflection of all three rays off the rightward mirror can also be seen, as the right mirror is slightly tilted. The bottom and top rays, however, do not reflect off the leftward mirror in the model, as *SAKURA* recognizes that the reflected ray will not intersect with the target.

SAKURA also recognizes when a ray refracts through the target such that it will miss the lens. Each time a ray reaches the rightward mirror, it is partially reflected, but a beam containing most of its energy continues to the collection lens, where the ray's energy is recorded.

4.2 Primary Intensity Plots

After a ray reaches the collection lens, *SAKURA* traces the ray back to the object plane along the angle at which the ray hits the lens. The object plane is used as a reference plane from which all rays appear to originate and is shown as the central vertical line in figure 3. *SAKURA* calculates the intensity of each ray at its back-traced location on the object plane, then interpolates those intensity values to find several hundred intensity values at regular intervals from the bottom of the image to the top.

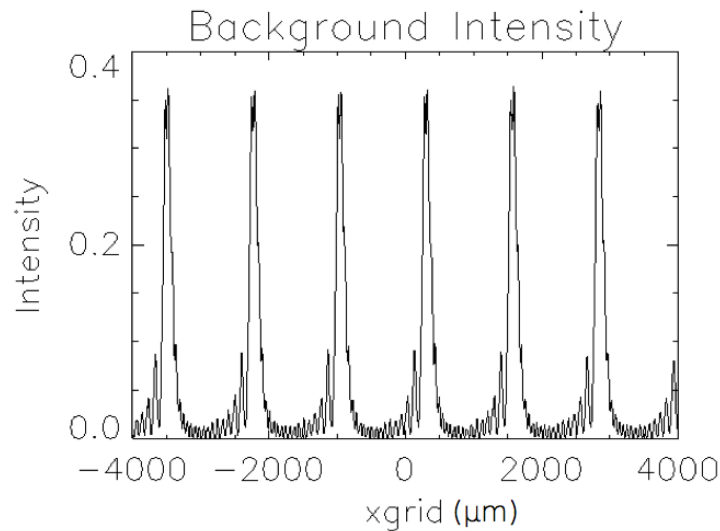


Figure 4: An intensity plot showing background interference fringes, generated with no target present in the Fabry-Perot interferometer. The x-axis shows the interpolated intensity value's location along the vertical direction of figure 3. The y-axis shows intensity as a fraction of the intensity of a beam before it enters the interferometer.

SAKURA plots these intensity values against their calculated position on the object plane. Figure 4 shows the intensity plot generated when the interferometer does not contain a target. The mirrors are 90% reflective, the right mirror is tilted at an angle of 0.57° , and the wavelength of the laser beams is 633 nm. The peaks represent maximum constructive interference between the rays, and the troughs represent maximum destructive interference. The roughness in the pattern between peaks is a result of the slight tilt of the mirrors, which creates areas of relative constructive and destructive interference between the absolute peaks. The plot shown agrees very well with a literature plot of a Fabry-Perot interferometer with slightly skew mirrors.⁶

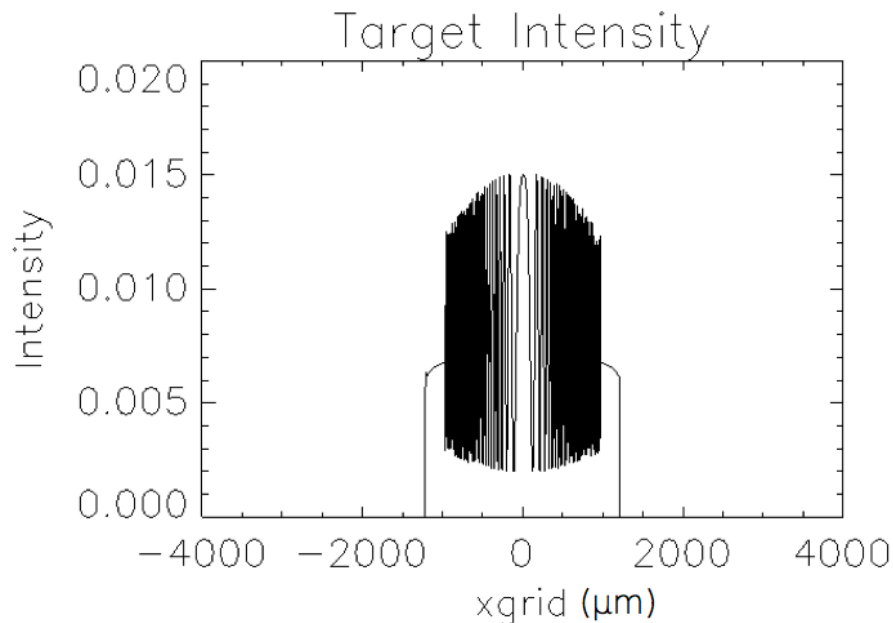


Figure 5: An intensity plot generated only by rays passing through the target. The background intensity plotted in figure 4 is not shown.

A plot showing only the intensity of the back-traced rays that have passed through the target is shown in figure 5. The thickness of the CH shell is $33\ \mu\text{m}$. The thickness of the D_2 ice is $155\ \mu\text{m}$. The D_2 gas layer has a radius of $1440\ \mu\text{m}$. The refractive indices of CH, D_2 ice, and D_2 gas are 1.59, 1.13, and $1 + 3.565 \times 10^{-4}$ (at 18.73 K), respectively.¹ The center region of this plot, where relatively little refraction occurs, is the easiest region to interpret for the purposes of the simulation. This is because of the ease of tracking phase changes within the region. For this plot, the distance between the mirrors has been adjusted so that a ray traveling through the center of the target will have an optical path length equal to a whole number of wavelengths, which will result in maximum constructive interference, and thus a peak at the location to which that ray is back-traced. This location is slightly off-center due to the tilt of the second mirror.

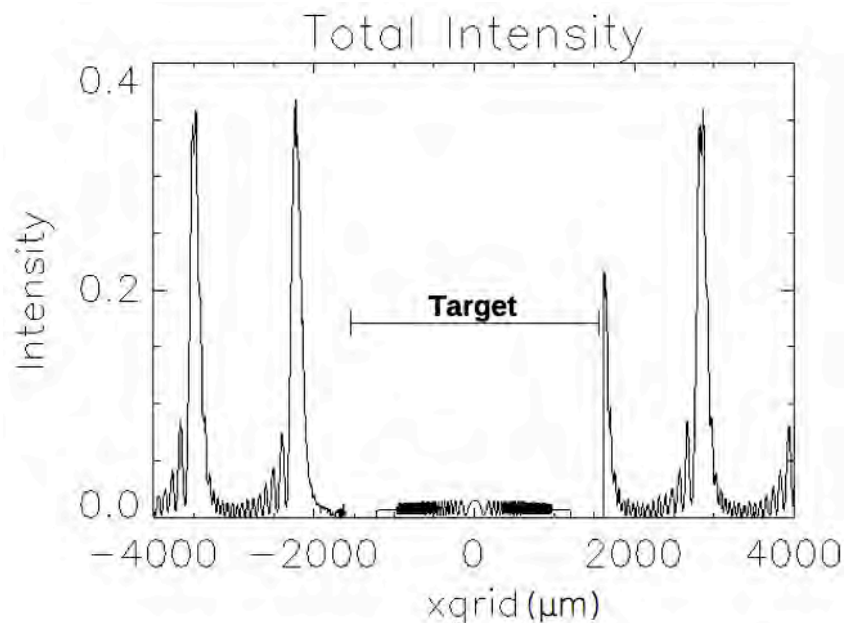
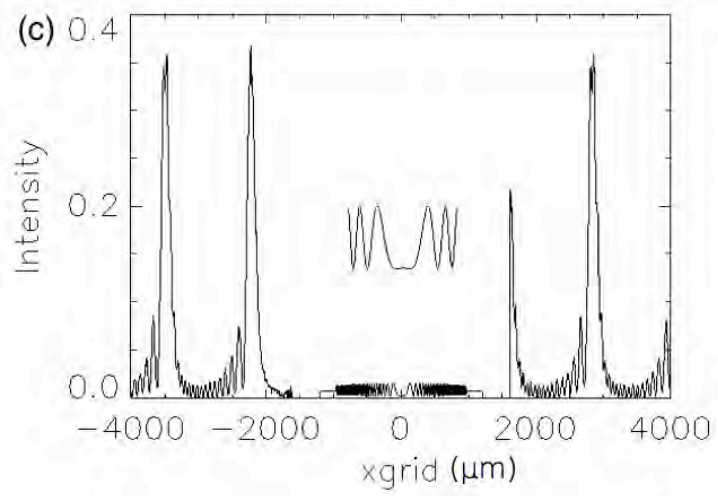
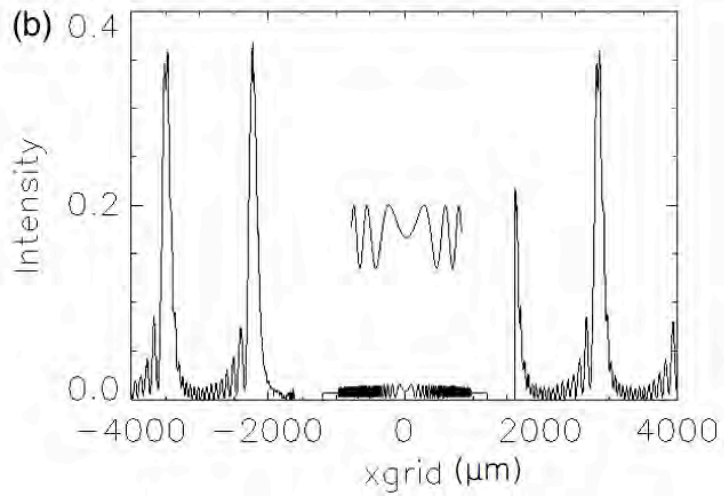
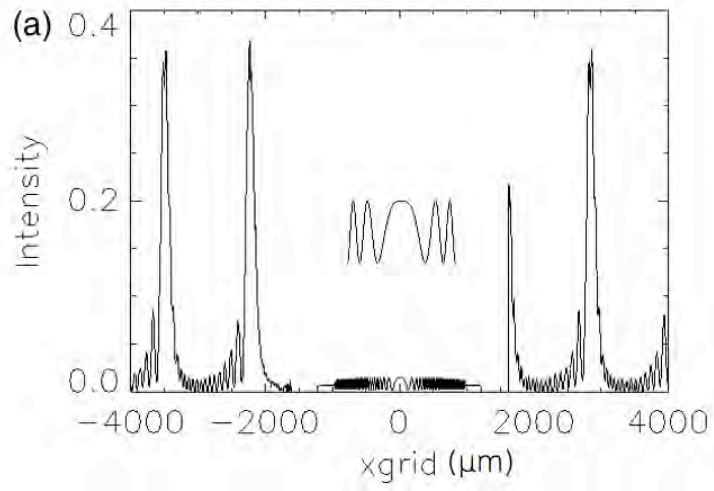


Figure 6: An intensity plot showing the interference pattern generated in the experimental setup, including background fringes and fringes through the target.

An intensity plot for the full experimental setup is shown in figure 6. The background intensity can be seen to smooth out as it approaches the target from the left. This occurs because the target blocks some rays that would normally contribute to the interference pattern in the smoothed area. The areas with zero intensity are where incoming rays never hit the collection lens, as they are refracted at too high an angle. Otherwise, this plot is merely the previous two combined. This plot serves as a base to compare to other plots as the target is cooled.

4.3 Density Change Intensity Plots

As the target is cooled from 18.73 K (the triple point of D₂) to 17.23 K, D₂ gas will deposit on the D₂ ice layer of the target. This will slightly thicken the ice layer, while reducing the density, and thus the refractive index, of the gas in the interior. The gas density drops rapidly as the target is cooled below the triple point. Based on formulae given in Souers,¹ the density drops from 4.529×10^{-4} g/cm³ at 18.73 K to 2.115×10^{-4} g/cm³ at 17.23 K, and $n - 1$ (where n is the refractive index) drops from 3.565×10^{-4} to 1.665×10^{-4} . These changes combine to slightly lengthen the optical path taken by a ray traveling through the center of the target. This results in the optical path length being equal to a non-whole number of wavelengths. As a result, the interference in the center of the target intensity plot is no longer totally constructive. Figure 7 shows the changes in the interference plot as the target is cooled.



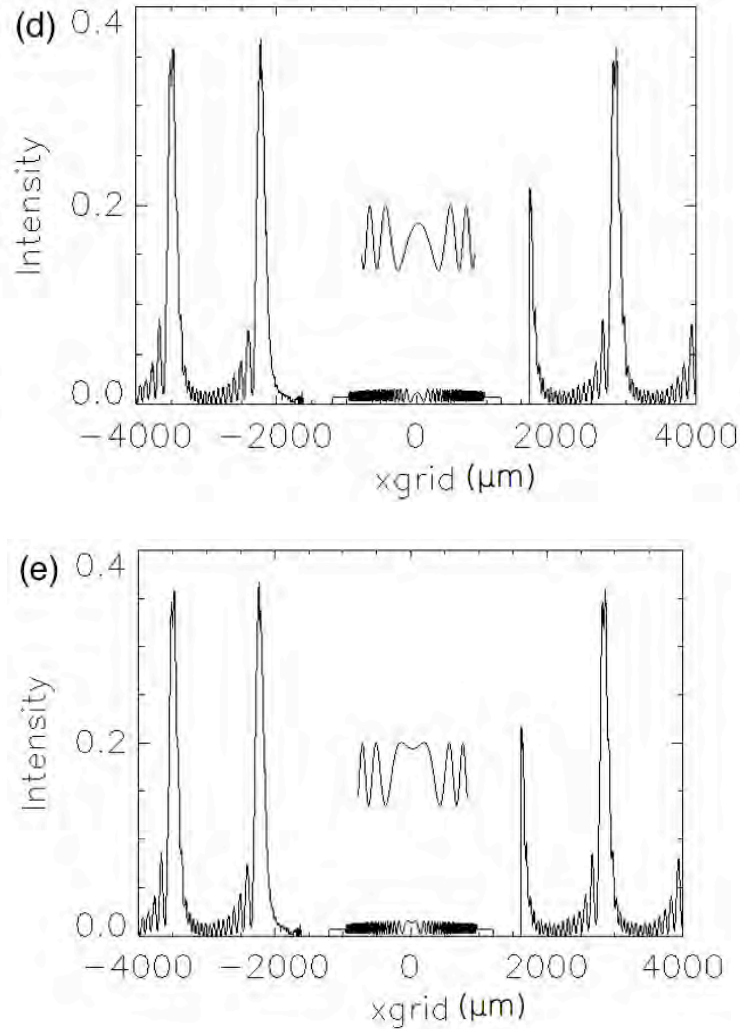


Figure 7: Intensity plots of the target at various temperatures. The center region is enlarged for clarity. (a) 18.73 K, (b) 18.43 K, (c) 18.09 K, (d) 17.70 K, (e) 17.23 K

The total shift as the temperature decreased from 18.73 K to 17.23 K was calculated to be 1.14λ . It is also worth noting that the background interference does not change at all as temperature decreases, as any change in the index of refraction of the helium surrounding the target would be extremely small.

In the future, this result will be compared with the experimental results using an actual Fabry-Perot interferometer. If the experimental results match this theoretical result closely, then it would suggest that the target is cooling properly,

and has the gas density needed for ignition experiments on the NIF.

5. Conclusion

An experiment has been proposed that will use a Fabry-Perot interferometer to measure gas density changes inside a cryogenic target for use on the NIF. A program was written to model this experiment, taking many parameters into account. Using this program, plots were generated that predict the intensity for rays passing through the target, as well as through the helium gas surrounding it. These plots were generated at different temperatures to predict how deposition of gas and the resulting gas density drop would affect the optical path of rays traveling through the center of the target. This result will be compared with the experimental result in the future, and agreement between the two would indicate the readiness of current target designs for use on the NIF.

6. Acknowledgements

I would like to thank the following: Mr. Paul Sedita for encouraging my pursuit of physics and encouraging me to apply to the high school program at the LLE, Mr. Mark Wittman for his insight and advice, my parents for their love and support while I worked at the LLE, and the Laboratory for Laser Energetics and the University of Rochester for making this program possible. I would like to especially thank Dr. R. S. Craxton for his help and guidance, and for providing me with a wonderful learning opportunity.

References

- ¹ P.C. Souers, "Hydrogen Properties for Fusion Energy," University of California Press. Print. (1986)
- ² M. Born and E. Wolf, "Principles of Optics: Electromagnetic Theory of Propagation, Interference, and Diffraction of Light," Pergamon Press. Print. (1975)
- ³ J. Y. Lee et al., "Spatiospectral transmission of a plane-mirror Fabry-Perot interferometer with nonuniform finite-size diffraction beam illuminations," J. Opt. Soc. Am. A. **19**, 973-983 (2002)
- ⁴ S. Jin, "A Ray-Tracing Model for Cryogenic Target Uniformity," Laboratory for Laser Energetics High School Summer Research Program (2002), LLE Report 329
- ⁵ Rogue Wave Software, Boulder, CO 80301
- ⁶ Y. Yoshida et al., "Fabry-Perot Resonator with Slightly Tilted Mirrors," Japan. J. Appl. Phys. **8**, 285-286 (1969).

Performance Degradation of OMEGA Liquid Crystal Polarizers

Aimee Owens

Home School

Fairport, NY 14450

Advisors: Dr. Tanya Kosc, Dr. Stephen Jacobs

Laboratory for Laser Energetics

University of Rochester

Summer High School Research Program 2012

1. Abstract

Liquid crystal polarizers (LCPs) are used in OMEGA to control circularly polarized light due to their unique optical property of selective reflection, whereby light of a specific wavelength and handedness is reflected. This mechanism also acts as a safety feature to prevent potentially damaging back-reflections in OMEGA. It was recently discovered that the selective reflection wavelengths of approximately 42% of the LCPs have shifted by more than 15 nm toward both bluer (shorter) and redder (longer) wavelengths, rendering 21% largely or completely ineffective. Research focused on determining if a mechanical effect could cause these wavelength shifts. Experiments were carried out which demonstrated that a compression or expansion of the gap between the substrates could result in either a blue shift or a red shift, respectively, of the selective reflection wavelength. These results support the hypothesis that a change in the gap thickness of an LCP device could result in a distortion of the pitch of the liquid crystal, which in turn shifts the selective reflection wavelength and degrades the LCP performance.

2. Introduction

2.1. Chiral Nematic Liquid Crystals

The molecules in a crystal possess orientational and positional order, while no molecular order is found in a liquid. There is a state of matter which exhibits the characteristics of both liquids and crystals known as a liquid crystal (LC). The most basic LC is a nematic, which exhibits only orientational order. A *chiral* nematic LC (Fig. 1) is created by adding a twisting agent to a nematic mixture. In the chiral nematic phase, the alignment of the molecules in each layer is rotated with respect to the previous layer.

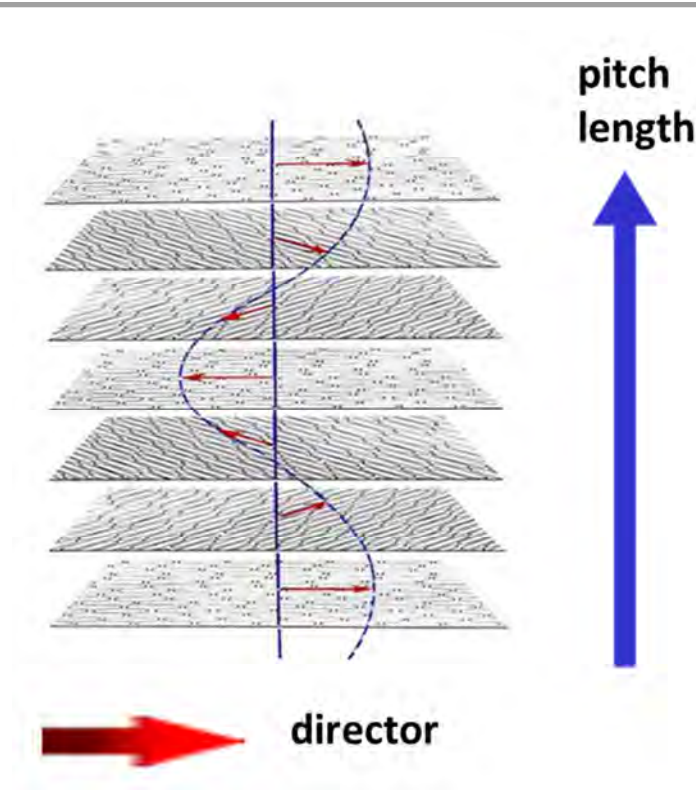


Figure 1: A depiction of a chiral nematic LC. The director denotes the average orientation of the molecules in each layer. The pitch length is the distance required for the director to make a 360° rotation.

This molecular structure leads to the selective reflection of circularly polarized light of a specific wavelength and handedness. Circularly polarized light with the same handedness as the chiral nematic helix will pass through the LC, while light with the opposite handedness will be reflected. A simplified version of Ferguson's equation¹ (Eq. 1) gives the central wavelength (λ_c) for a normal angle of incidence and reflection (See Appendix A):

$$\lambda_c = n \cdot p \quad (\text{Eq. 1})$$

where p is the pitch length and n is the mean refractive index of the LC.

2.2. Liquid Crystal Polarizers (LCPs)

Almost 200 LCPs are used in OMEGA to control the polarization of the laser light (Fig. 2). As a laser beam propagates through various optical components, its polarization state can be altered. On OMEGA, most LCPs are right-handed circular polarizers (CPRs), which restore the proper polarization by reflecting the left-hand circularly polarized components of the light. Propagating properly polarized light improves energy balance between beamlines, but more importantly it acts as a safety feature by preventing light from propagating backwards through the system. The CPRs in the OMEGA system are placed at a 10° angle of incidence so that the reflected light is removed from the system. The CPRs are designed to reflect light at 1053 nm at this placement angle; when they are measured at normal incidence the λ_c red-shifts by about 7 nm to 1060 nm.

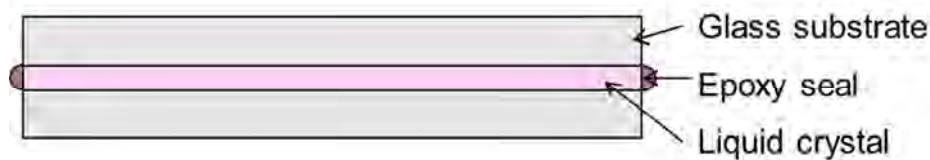


Figure 2. LCPs consist of two glass substrates, a thin layer of chiral nematic LC fluid, and an epoxy seal. The LCPs are filled at an elevated temperature, cooled to room temperature, sheared, and sealed.

The LC mixture used in the CPRs consists of 19.44 %wt CB15 and 80.56 %wt ZLI 1167. The outside surfaces of the substrates, which are made of BK-7 and fused silica, have AR coating. The inside surface of each substrate has three thin film spacers outside the clear aperture resulting in an 18 micron gap.²

2.3. Discovery of the degradation and initial data

In October 2011, it was noted that the contrast ratios of several sets of crossed LCPs (a CPR and a left-handed circular polarizer, or CPL) in the OMEGA laser system were less than 100:1, much lower than the specified 1000:1. Three of the four CPRs scanned in the Lambda-900 Spectrophotometer (see Section 3) showed a λ_c which had shifted away from the desired λ_c and towards the longer (red) wavelengths. Due to this discovery, a portable spectrometer was designed and used to perform *in-situ* characterization of 172 CPRs in the OMEGA laser bay. Surprisingly, these measurements found that while many CPRs had a red-shifted λ_c , the selective reflection of some CPRs had shifted towards shorter (blue) wavelengths (Fig. 3). This comprehensive survey found that 42% of the tested CPRs were ineffective polarizers at 1053 nm.³

Performance degradation due to the spectral shift of λ_c has not been correlated to the age, location, size, or LC batch of the CPRs. Note that none of the four CPLs that were measured have exhibited a spectral shift.

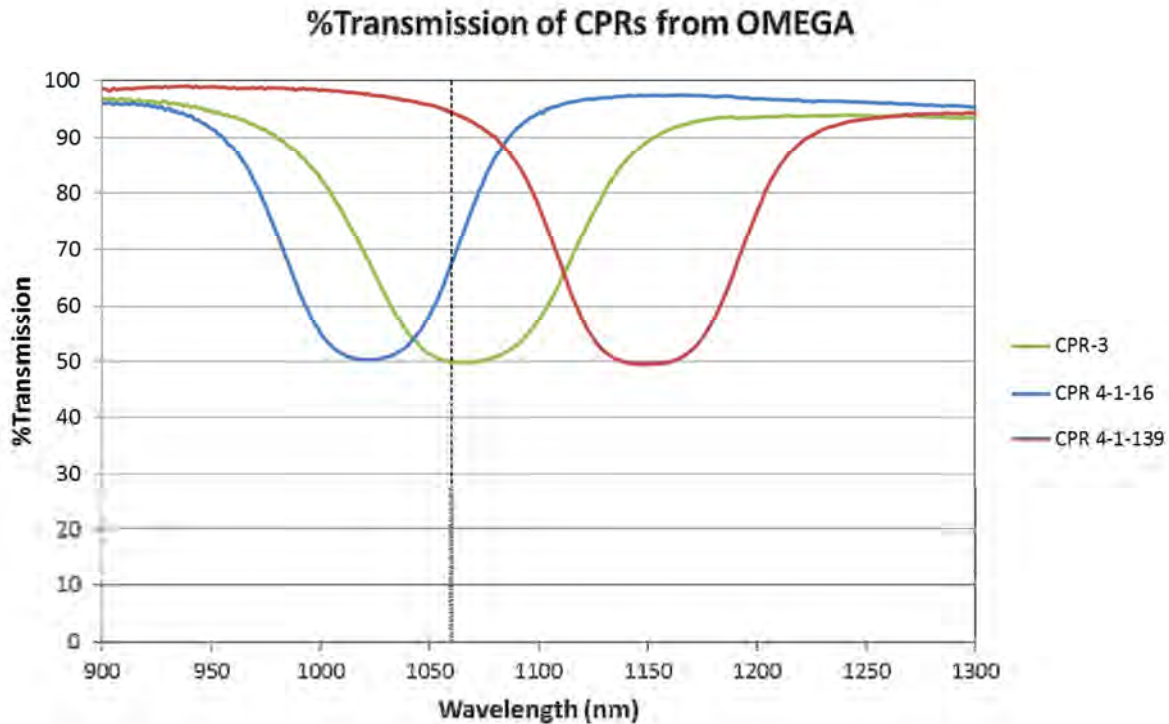


Figure 3. The percent transmission (% T) of three CPRs from the OMEGA system. Because the spectrophotometer emits equal amounts of right and left circularly polarized light, 50% transmission indicates that the CPRs are reflecting the correct amount of light. The dotted line indicates the specified λ_c at normal incidence (1060 nm). CPR-3 is performing well, but CPR 4-1-16 and CPR 4-1-139 have shifted to the blue and red, respectively, and are ineffective polarizers at 1060 nm.

2.4. Possible Cause of Degradation

Many factors can influence and change the selective reflection of LCPs, including temperature, variance in the chemical composition of the LC batches, chemical reactions, and mechanical deformation. The first two factors can be eliminated: the LC mixture used in the CPRs was chosen for its minimal temperature sensitivity and LC batches were found to be consistent with each other. The possibility of either chemical or mechanical change must still be investigated. Assuming that the temperature dependence of the refractive index of the LC fluid is negligible,

Eq. 1 suggests that the spectral shift is due to a change in pitch length. Thus, factors that change the pitch length must be examined.

A hypothesis proposing a mechanical origin for changes in the selective reflection was constructed based on an article by Bailey *et al.*,⁴ in which Bailey described an electrically induced distortion of substrates which led to a change in the pitch length. In the case of OMEGA CPRs, a mechanically induced pitch distortion causing the LCP degradation is a plausible mechanism which could produce either a red or a blue shift. This hypothesis also supports the lack of correlation with device age, device location in the laser bay or storage, and LC batches.

Assuming that there is nowhere for the LC fluid to flow and redistribute itself, a change in gap thickness would require that the spacing between the molecular layers changes as well, thereby altering the effective pitch length. In theory, for a material with $n = 1.57$ and a $\lambda_c = 1060$ nm, a gap thickness change of ~ 0.5 microns, or a pitch length change of about 2.8%, corresponds to a 30 nm shift to the red or blue (see Appendix B).

3. Experimental

The main goal of this project was to investigate the possibility of mechanical degradation of the CPRs by studying the relation between gap thickness and λ_c . Devices were characterized and the central wavelengths of the CPRs were monitored during all experimentation using the Perkin-Elmer Lambda-900 Spectrophotometer, which measures the percent transmission (%T) of samples across a spectrum of wavelengths.

Two sets of CPRs were investigated. The first was a set of “old” CPRs that were stored in a drawer in the Materials Lab for approximately 15 years. The age, LC fluid composition, substrate type, type and thickness of the spacers, epoxy composition, and coating of the CPRs are

unknown (see Appendix C). The second was a set of “new” CPRs removed from the OMEGA system because they were no longer effective at 1053 nm and needed to be replaced.

3.1. Characterization and study of “old” and “new” devices

The “old” CPRs were scanned in the Lambda-900 from 900 to 1300 nm to obtain the %T and λ_c of each CPR. Each CPR was scanned at the center of its clear aperture, and each was found to be red-shifted. The “new” CPRs, whose λ_c had already been determined *in situ* in the Laser Bay, were scanned from 800 to 1500 nm at $\frac{1}{2}$ cm intervals across their diameters to assess the uniformity of device performance. In some CPRs the λ_c was fairly uniform across the device, while in others the λ_c varied by as much as 14 nm across the device. This variation could suggest that the gap is not uniform across the diameter (Fig. 4), but results are not conclusive. Note that four of these “new” CPRs are blue-shifted and the other five are red-shifted. So far, no correlation has been found between the direction of spectral shift and the variations across the diameter. This data was used as a reference in later experiments (see Appendix C).

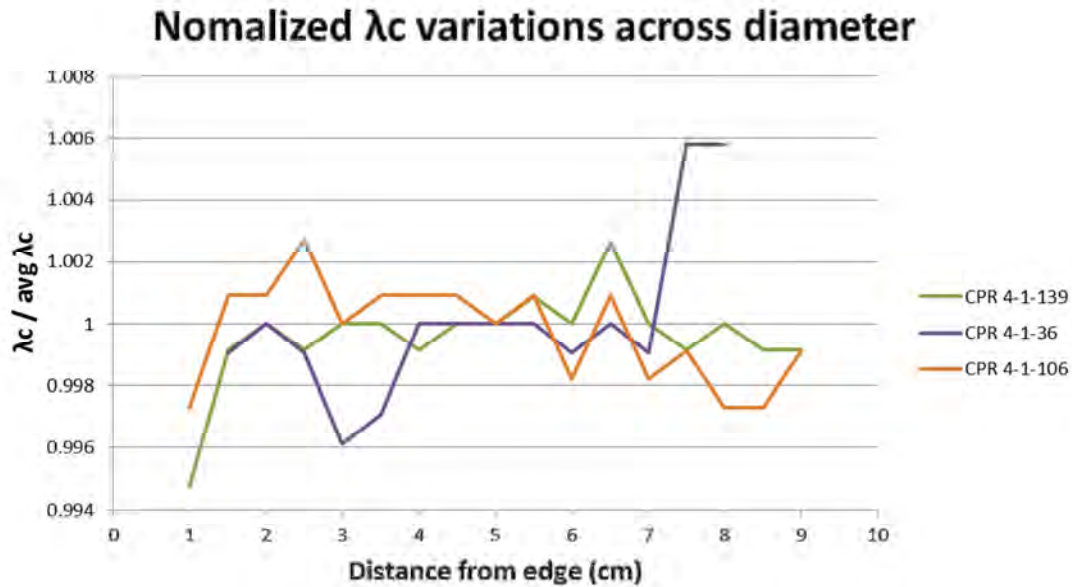


Figure 4. The central wavelengths, λ_c , of three of the scanned CPRs. There are variations in λ_c across the diameters of these CPRs.

3.2 Inducing a change in selective reflection

Several experiments were devised in order to study the effect on λ_c of increasing or decreasing gap thickness. The temperatures of the CPRs and the Lambda-900 testing chamber were not controlled over the duration of these tests. Experiments had been conducted to verify that small temperature fluctuations do not affect the λ_c .

3.2.1 Wedged Cell: Comparing gap thickness and λ_c

A wedged cell (Cell-104) was made by setting a small piece of 12.3 micron Mylar spacer on one end of a microscope slide, placing a line of OMEGA CPR LC fluid parallel to the length of the slide, and dropping another slide on top. Epoxy (5-minute by Devcon) was applied and allowed to cure. The cell was then scanned in the Lambda-900 at 5-mm intervals from the Mylar spacer

along the length of the cell. A correlation was observed between the gap thickness of the cell and the λ_c (Fig. 5); as the gap thickness increased, so did the λ_c .

It is important to note that while this cell assembly was performed at room temperature, the OMEGA CPRs are assembled at an elevated temperature with LC fluid in the isotropic phase. Filling the CPRs in the isotropic phase allows the LC to be aligned more easily; however, filling in the isotropic phase is not required to align the LC fluid.

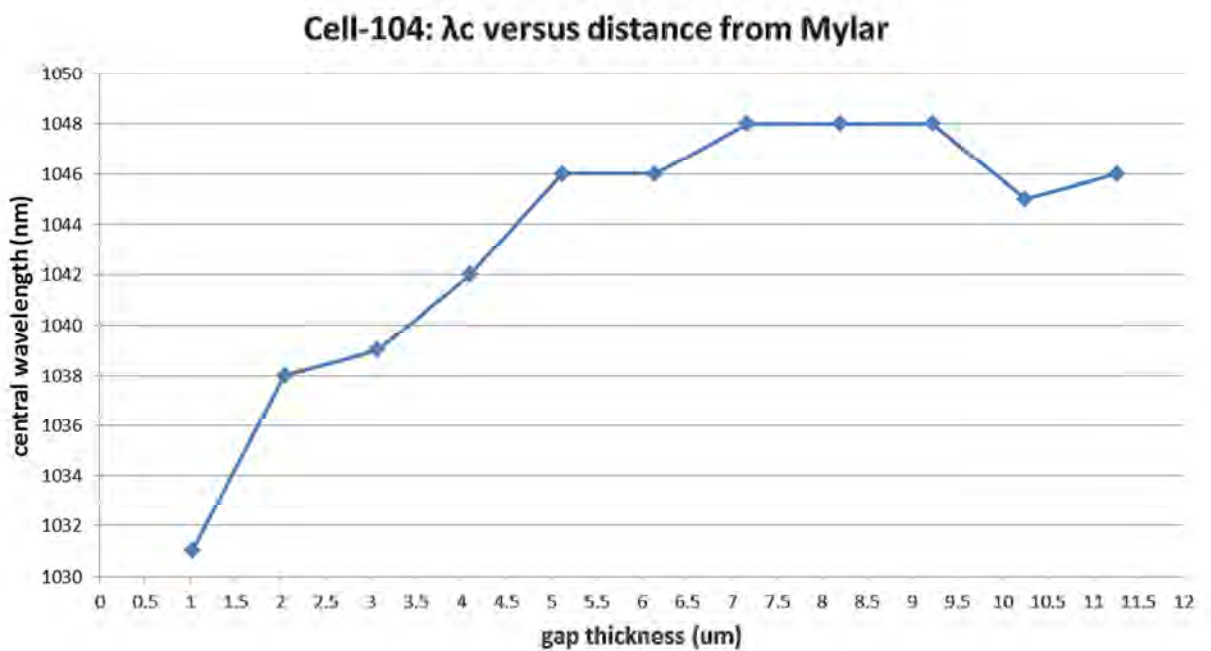


Figure 5. Central wavelength, λ_c , of a wedged cell (Cell-104) as a function of gap thickness. As the distance from the spacer increased, the gap thickness decreased, and the λ_c decreased.

3.2.2 Compressing the device gap

Using a small C-clamp, pressure was applied to CPR-730 and CPR-132 in several separate tests to study the relationship between changing gap thickness and λ_c .

During each test, rubber was placed on the ends of the clamp to protect the substrates. The edge of the clamp was lined up with the fiducial mark on each CPR, placed 1 inch in from the edge of the CPR, and tightened just enough to grasp the device. The device under test (with the clamp) was placed in the Lambda-900 (Fig. 6(b)). The clamp was tightened at one-quarter turn intervals, and the %T was measured at each interval using the Lambda-900. The total clamp forces were quantified using a Shimpo Digital Force Gauge (Fig. 6(a)). During the second and third tests on CPR-132, the CPR was placed in a holder to prevent it from rolling sideways or tilting relative to the incident light, thereby increasing the accuracy of the transmission scans. The CPR-730 tests were performed within one week of each other, as were the CPR-132 tests. For each CPR, the clamp was tightened and loosened three times, and the CPRs were scanned in approximately the same location each time.

Number of quarter turns	Approx. newtons applied
1	9
2	28
3	55
4	87
5	115
6	183
7	213 (estimated)
8	240 (estimated)

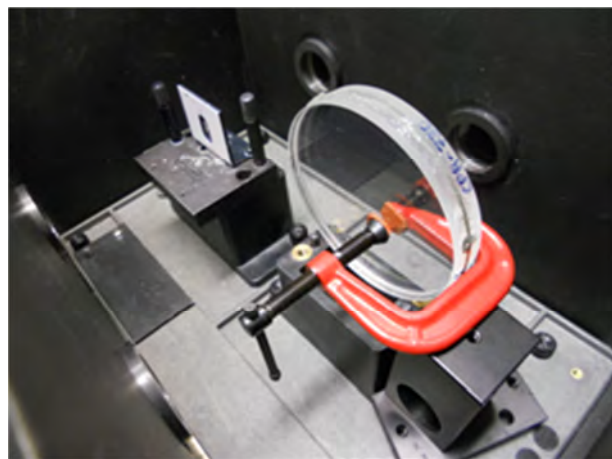


Figure 6. (a) Approximate newtons applied to the CPRs. (b) CPR-730 and clamp in the Lambda-900 testing chamber.

The tests on CPR-730 (Fig. 7) suggest that there is a correlation between λ_c and applied pressure – as the pressure increased, the λ_c decreased. The incident light was approximately normal to the device, and the λ_c began to shift towards the blue when the applied pressure reached a threshold of about 60 newtons. The λ_c of CPR-132 did not show the same dependence on applied pressure (Fig. 8).

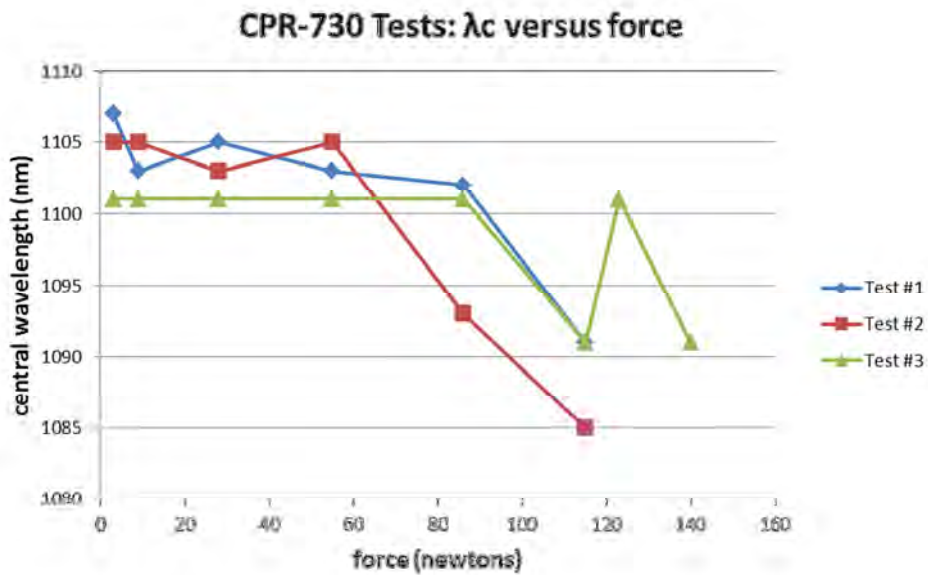


Figure 7. The correlation between λ_c and force applied to CPR-730 for all three pressure tests. It seems that as pressure was increased, the gap thickness and λ_c decreased. It is believed that the outlier at ~125 N was caused by inaccuracy of the transmission scan.

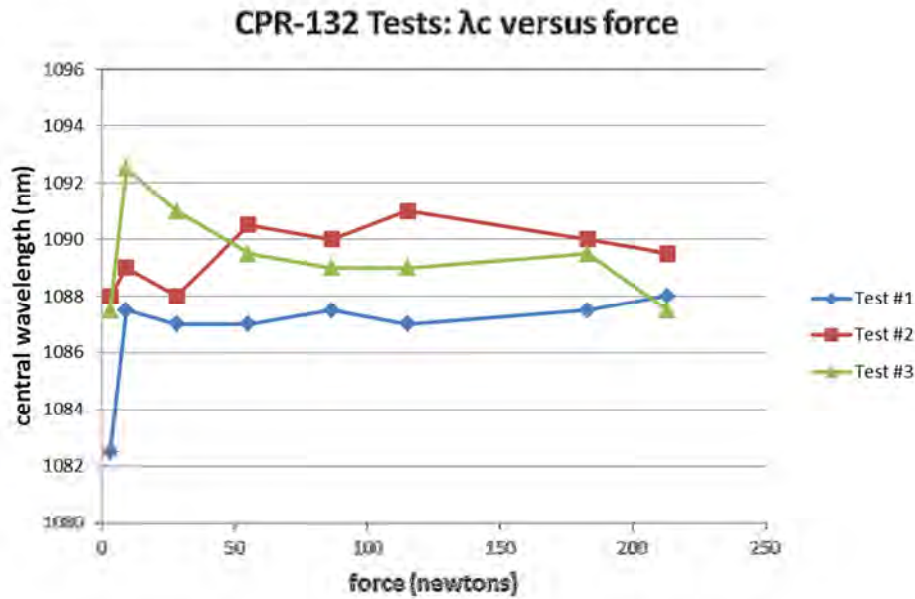


Figure 8. The central wavelengths and force applied to CPR-132 for all three pressure tests. In contrast to Figure 7, no clear correlation is seen between applied pressure and λ_c .

The central wavelengths of CPR-730 and CPR-132 were found according to the equation

$$\lambda_c = \frac{h_1 + h_2}{2} \quad (\text{Eq. 2})$$

where h_1 is the estimated half maximum on the left side of the %T curve and h_2 is the estimated half maximum on the right side of the %T curve.

The results of the tests on CPR-730 show a definite correlation between applied pressure and λ_c .

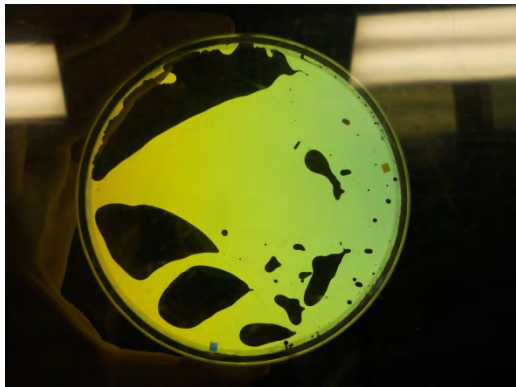
However, the results of the tests on CPR-132 do not necessarily show a correlation. Additional testing needs to be carried out to more fully understand these results.

3.2.3. Expanding the Device Gap to Increase λ_c

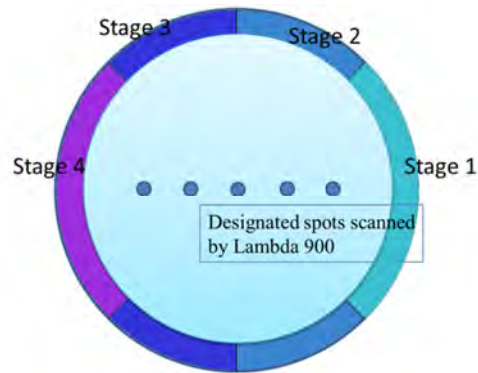
This experiment was instrumental in the development of a procedure for disassembling CPRs.

(See Appendix D for full procedure.)

Before any epoxy was removed, CPR-443 was scanned in the Lambda-900 across its diameter in five spots designated by a mask (Fig. 9(b)). The epoxy was then removed in stages (Fig. 9(b)) using a razor blade and pick. After each stage was removed, CPR-443 was scanned in the same five spots. Air bubbles entered the CPR when the first stage of epoxy was removed, and the bubbles continued to migrate throughout the CPR over the course of the experiment (Fig. 9(a)). Once the CPR had equilibrated for several days, it was again scanned in the Lambda-900 to obtain the equilibrium λ_c .



(a)



(b)

Figure 9. (a) CPR-443 viewed between crossed polarizers after 50% epoxy removal. Note that the dark areas are air bubbles and the LCs appear yellow/green. (b) Depiction of spots scanned by Lambda-900 and epoxy-removal stages of CPR-443.

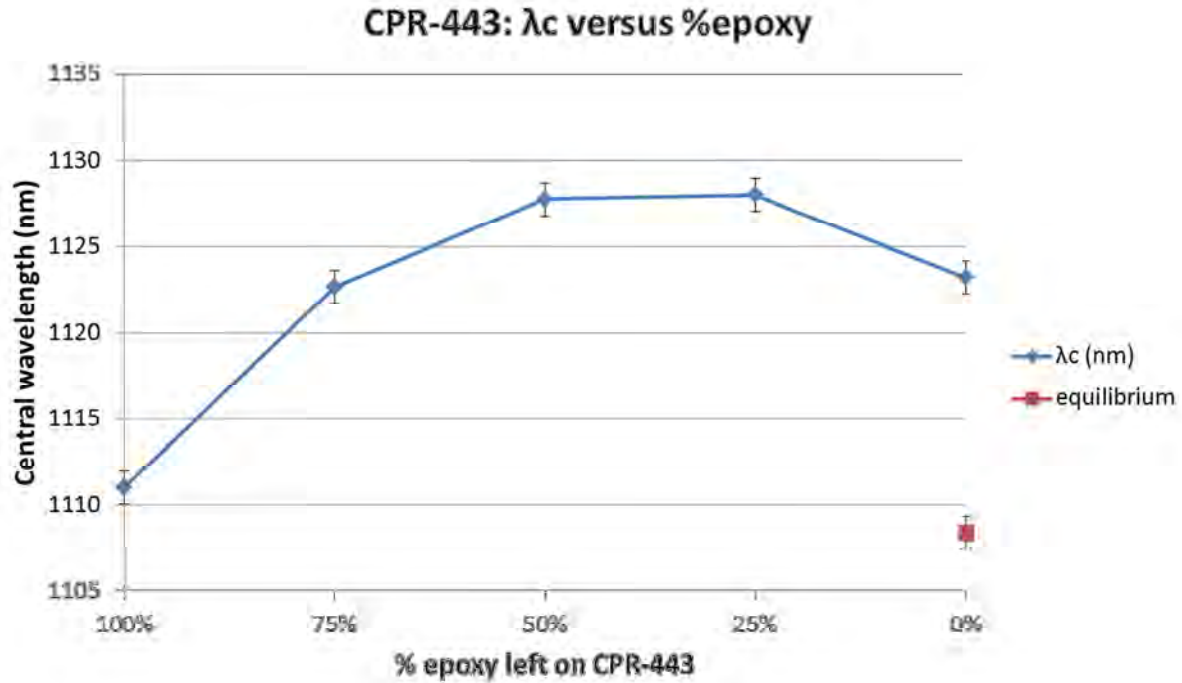


Figure 10. The λ_c increased as epoxy was removed and air bubbles entered the gap between the substrates.

The experiments described in Section 3.2.2 dealt with decreasing the gap thickness, whereas this experiment increased the gap thickness. The results are shown in Fig. 10. As more epoxy was removed and additional air bubbles entered the gap between the substrates, the λ_c increased from its value measured at the onset of disassembly until all the epoxy was removed. These results suggest that the bubbles pushed the substrates apart and increased the gap thickness, which led to an increase in λ_c . Final scans showed that once the air bubbles and LC fluid distribution equilibrated, the λ_c returned to the value recorded at the start of the experiment, which in turn suggests that the pitch length returned to its value from the beginning of the experiment.

Before the experiment began, the λ_c of CPR-443 was measured to be 1111 nm. If it is assumed that the proposed hypothesis is correct, and that the original λ_c of CPR-443 was 1060 nm, it is

not clear why the λ_c only returned to 1108 nm when the epoxy was removed. It is possible that the hydrostatic pressure of the LC fluid prevented the gap thickness from changing further, or that a chemical change in the LC fluid has occurred.

4. Conclusions

Various experiments were carried out to investigate the hypothesis that a mechanically induced pitch distortion is causing the LCP performance degradation. While some experiments produced inconclusive results, others gave direct evidence that a mechanical effect, the changing of gap thickness, could be directly related to the spectral shifts. Experiments such as the wedged cell and the CPR-730 clamp tests, which compressed the device, suggest that gap compression correlates to a blue shift. The disassembly of CPR-443 points to gap expansion as a possible cause of a red shift. The results of these experiments support the hypothesis that a changing gap thickness could be a cause of degradation. However, further investigation (Section 5) is required to fully understand the reason for LCP performance degradation.

5. Future Work

More research needs to be carried out to prove or disprove the hypothesis of a mechanically induced pitch distortion. Future work will include:

- Studying a correlation (if any) between λ_c and barometric pressure

It is possible that barometric pressure could play a role in changing the gap thickness of the CPRs on a day to day basis. The central wavelengths of several existing CPRs will be monitored, and the central wavelengths will be compared to daily fluctuations in barometric pressure. Building CPRs in a controlled environment and with known gap thicknesses will

also allow investigation of this possible correlation, by facilitating study on changes in gap thickness.

- Building new cells using old LC fluid

A CPR would be disassembled and the LC fluid retrieved. That LC fluid would then be used to build a new CPR. The optical properties and λ_c of both the old and new CPRs could be analyzed and compared to determine if the LC fluid is degraded, or if its surroundings could be causing the λ_c shift. The LC fluid from CPR-443 could potentially be used for this type of experiment.

- Investigating the possibility of chemical degradation of the LC fluid

Chemical degradation could be caused by numerous factors, such as degradation by flashlamp light, by laser light, or by reactions with the epoxy seal.

Crystallization outside the clear aperture of several degraded devices was also observed.

Properly functioning devices will be examined for the presence of crystals, and the cause of this crystallization will be researched.

- Utilizing the Exicor 450XT (Mueller Matrix) Polarimeter

Due to the optical activity of the LC fluid, the polarimeter can be used to measure the UV optical rotation of the CPRs, and a technique utilizing this property will be developed for analyzing the thickness of the gap and LC fluid.

6. References

- [1]: Chandrasekhar, S. 1993. *Liquid Crystals*. Cambridge Monographs on Physics. Bristol, England. Page 268. Note that the full equation is used in Appendix A.
- [2]: Jacobs, Stephen D.; Smith, Douglas; Rigatti, Amy; Marshall, Ken; Puchebner, Birgit; and Lund, Lance. 1993. *Manufacturing Procedure, Liquid Crystal Optics, F-FJ-P-01 Revision A, OMEGA Upgrade*. pgs 56-59. Laboratory for Laser Energetics (January 18th, 1993)
- [3]: Kosc, Tanya Z. and Kelly, Jack. 6 March 2012. Laboratory for Laser Energetics Presentation: *In-Situ Liquid Crystal Polarizer Transmission Measurements: Test Fixture and Preliminary Data*.
- [4]: Bailey, C. A.; Tondiglia V. T.; Natarajan, L. V.; Bricker, R.; Cui, Y.; Yang, D.K.; and Bunning T.J. *Surface limitations to the electro-mechanical tuning range of negative dielectric anisotropy cholesteric liquid crystals*. *Journal of Applied Physics* **111**, 063111 (2012)

Acknowledgements

I would like to express my gratitude to my advisor Dr. Tanya Kosc, and my co-advisor Dr. Stephen Jacobs, for their willing guidance, instruction, and support. I thank Dr. R. S. Craxton for organizing the LLE High School Research Program and providing this unique experience. I would also like to thank all who have helped support this project, especially Brittany Taylor, Mark Romanofsky, and Ken Marshall and the Materials Lab.

Appendix A

Ferguson's equation¹ gives the wavelength of maximum reflection (central wavelength, λ_c):

$$\lambda_c = nP \cos\left[\frac{1}{2} \sin^{-1}(n^{-1} \sin \varphi_i) + \frac{1}{2} \sin^{-1}(n^{-1} \sin \varphi_s)\right],$$

where P is the pitch length, φ_i is the angle of incidence, φ_s is the angle of scattering, and n is the mean refractive index of the LC.

Assuming that the incident light is normal to the pitch, we can let $\varphi_i = \varphi_s = 0$. Thus, $\sin(\varphi_i) = \sin(\varphi_s) = 0$, and we have $\lambda_c = nP$.

Appendix B

Equation 1 tells us that $\lambda_c = n \cdot p$. Thus, $p = \frac{\lambda_c}{n}$.

Assuming an average refractive index ~ 1.57 , the theoretical pitch length for a λ_c of 1060 nm is

$$p = \frac{1060 \text{ nm}}{1.57} \approx 675 \text{ nm}.$$

The theoretical pitch length for a λ_c of 1090 nm (a 30 nm shift to the red) is

$$p = \frac{1090 \text{ nm}}{1.57} \approx 694 \text{ nm}.$$

This corresponds to a $694/675 = 1.028$ or 2.8% increase in gap thickness.

A 2.8% increase in an original gap thickness of 20 microns is 20.564 microns, or a 564 nm change in gap thickness.

The theoretical pitch length for a λ_c of 1020 nm (a 40 nm shift to the blue) is

$$p = \frac{1020 \text{ nm}}{1.57} \approx 649 \text{ nm}.$$

This corresponds to a $649/675 = 0.9615$ or $100\% - 96.15\% = 3.85\%$ decrease.

A 3.85% decrease in an original gap thickness of 20 microns is 19.23 microns, or a 770 nm change in gap thickness.

Appendix C

One set of “old” CPRs was left in the Materials Lab for approximately 15 years. The age, LC fluid composition, substrate type, type and thickness of the spacers, epoxy composition, and coating of the CPRs are unknown. Their diameters are 100 mm. All of these CPRs are red shifted, and many have large areas of bubbles as well as LC fluid.

CPR Designation	Appearance	Approx. λ_c (nm)
CPR-132	No air bubbles	1095
CPR-443	No air bubbles. Currently partially disassembled.	1116
CPR-505	No air bubbles. Disassembled.	1056
CPR-693	No air bubbles.	1066
CPR-715	Approx. 50% air bubbles, 50% LC fluid.	1164
CPR-724	No air bubbles.	1172
CPR-730	No air bubbles	1108
CPR-732	Approx. 35% air bubbles, 65% LC fluid.	1140
CPR-733	Approx. 25% air bubbles, 75% LC fluid.	1120

The second set comprised “new” CPRs removed from the OMEGA system

CPR designation	Lowest λ_c (nm)	Highest λ_c (nm)	Appearance
CPR-3	1065	1065	100-mm, no crystallization
CPR 4-1-16	1018	1025	135-mm, crystallization outside clear aperture
CPR 4-1-36	1027	1037	135-mm, crystallization outside clear aperture
CPR 4-1-106	1105	1111	135-mm, minimal crystallization outside clear aperture
CPR 4-1-138	1036	1039	135-mm, minimal crystallization outside clear aperture
CPR 4-1-139	1142	1151	135-mm, no crystallization
CPR 4-1-141	1099	1108	135-mm, minimal crystallization outside clear aperture
CPR 4-1-146	1025	1039	135-mm, crystallization outside clear aperture

Appendix D

The epoxy seal of CPR-505 was removed using a razor blade and pick. The hydrostatic pressure of the LC fluid prevented the substrates from being sheared apart, so the CPR was placed on a Thermolyne (Sybron) Nuova II hot plate. It was covered with a petrie dish in order to heat the CPR more uniformly.

The initial temperature of the hot plate was 22°C. The hot plate dial was set to 3 (approximately 50° C), and after about 15 minutes, air bubbles began forming about the circumference of the CPR and slowly moving towards the center. After another 10 minutes, the dial was turned to 4 (75°C – 84°C), and the temperature of the top substrate was measured to be 46°C.

Throughout the experiment, the air bubbles continued to redistribute and migrate toward the center of the CPR. By observing the interference fringes in the air bubbles, it was deduced that the CPR was bowing out at the center. After 45 minutes of heating, the substrates were sheared and successfully slid away from each other.

A Teflon spatula was used to scrape the LC fluid from each substrate into a small vial. The remaining LC was rinsed into a petri dish using hexane, and the hexane/LC fluid mixture was poured into another small vial. This vial was placed on a hot plate at $\sim 24^{\circ}\text{C}$, and the hexane was evaporated off over the course of approximately 24 hours.

Opacity effects in inertial confinement fusion implosion

Jesse Pan

Webster Thomas High School, 800 Five Mile Line Road, Webster, NY, 14580

LLE Advisor: Suxing Hu

March 2013

1. Abstract

During direct-drive inertial confinement fusion (ICF) implosion experiments, laser beams are used to compress a deuterium-tritium (DT) capsule. However, radiation from the coronal plasma surrounding the capsule can be absorbed by the capsule's shell, which thereby becomes preheated. LLE's simulation programs, such as the one-dimensional hydrodynamics code LILAC, use the Astrophysics Opacity Table (AOT) to determine the x-ray absorption by the DT fuel shell. Recent studies have shown that Quantum Molecular Dynamics (QMD) simulations are more accurate for calculating the opacities and can result in a DT absorption coefficient many times higher than the AOT prediction, varying directly with the photon energy. To examine this absorption-enhancement effect on ICF implosions, multipliers to the AOT opacities were used in LILAC simulations. The simulation results show that a factor-of-2 increase in the opacity can lead to dramatic effects in target performance: the peak density drops 20%, the areal density ρR decreases by 10%, and the neutron yield decreases by 40%.

2. Introduction

At the University of Rochester's Laboratory for Laser Energetics (LLE) and the National Ignition Facility (NIF), research is done on laser fusion. There are two main types of laser fusion: direct drive and indirect drive. The Laboratory for Laser Energetics deals mainly with direct drive. Direct drive means that a target is irradiated directly by the laser beams, as opposed to indirect drive, where the target's surrounding is hit by the laser beams, heating the area as well as the capsule.

The target is a spherical cryogenic capsule approximately 10 μm thick with a diameter of $\sim 860 \mu\text{m}$, coated on the inside with approximately 65 μm of deuterium-tritium (DT) ice, and filled with three atmospheres of DT. The laser is the 60 beam OMEGA laser system, one of the most powerful in the world. During inertial confinement fusion, the laser pulses partially ablate the surface of the capsule, causing it to rocket off, and compress the capsule. The deuterium and tritium are compressed together. On account of the large electrostatic repulsion between the two nuclei, a large amount of energy needs to be put into the fusion process. At a sufficiently high temperature, the deuterium and tritium combine to form helium, a neutron, and large amounts of energy.

The amount of energy produced by the inertial confinement fusion process can be measured by its neutron yield. LLE uses simulation programs, such as the one-dimensional hydrodynamics code LILAC, to predict such values. A major factor affecting inertial confinement fusion is opacity. Opacity is defined as a measure of impenetrability of electromagnetic or other kinds of radiation. The simulation program LILAC was modified to account for newer research

revealing a more accurate measure of opacity. The method of calculating opacity currently employed by the LLE simulation programs uses the Los Alamos Astrophysics Opacity Table (AOT) [1]. The Quantum Molecular Dynamics (QMD) model [2] is a newer method of calculating opacity.

3. Differences Between QMD and AOT

The QMD approach is believed to be more accurate than the AOT approach because it takes into account many aspects neglected by the AOT approach for calculating the opacities. The QMD approach includes innately transient effects such as the association/dissociation of chemical bonds, and ionization/recombination. As a result, the pressure obtained by using the QMD model demonstrates not only the constituency of the fluid at the given temperature, but also density effects [3]. The AOT model also uses an equation of state model that is based on the Saha equation. However, the Rydberg sequences are cut off by the plasma corrections. The QMD model uses a corrected version of the Saha equation which is solved iteratively to obtain a set of ion abundances, bound state occupancies, and free electrons. The AOT model doesn't fully account for molecular formation. As demonstrated in Figure 1, the QMD model's calculations result in much higher absorption values than those yielded by the AOT model. Despite the left half of the graph showing the QMD model having a lower absorption than the AOT model, that portion is insignificant because the photon energy is never that low during inertial confinement fusion implosions. This means that the DT shell is absorbing more electromagnetic radiation than previously assumed in the simulation programs and the final output will be different.

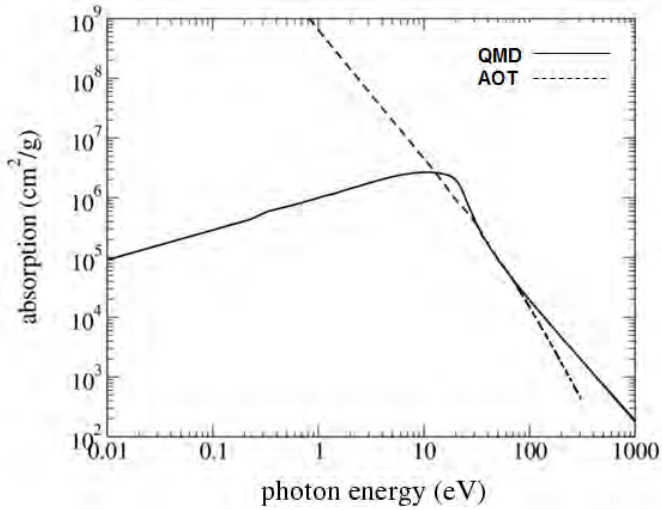


Figure 1: Graphical display of the absorption rates of the QMD model and the AOT model against various levels of photon energy at T=48000K and $\rho =0.65 \text{ g/cm}^3$

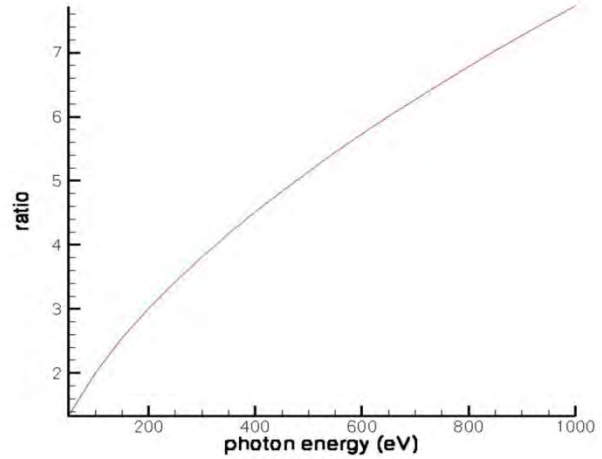


Figure 2: Graphical display of the ratio of the QMD to the AOT absorption rates. Conditions are the same as in figure 1.

3.1 Quantitative difference between QMD and AOT

As a direct result of these and other factors, the QMD model has shown that the actual DT absorption can be many times higher than the DT absorption value obtained by using the AOT model for photon energies above 200 eV. The photon energies important to OMEGA laser implosions range from 100 eV to 5000 eV. As demonstrated in figure 2, the ratio of the QMD prediction to the AOT prediction increases significantly with the photon energy in the $h\nu < 1\text{-keV}$ range.

4. Modification to the LILAC simulation program, and results of the simulation

The LILAC program was modified to test what happens if the overall opacity value is multiplied by a factor of 2. The value of 2 was chosen to test the sensitivity of the simulation to changes in the opacity variable. The simulation led to significant changes in the results for the

neutron yield when compared to an original run without the modifier in place. As seen in figures 3 and 4, the original run's DD and DT neutron yields are almost twice as high as those of the run with the modifier implemented. The decrease in the neutron yield shows that not as much of the deuterium reacted with the tritium, which results in less energy being produced. The high sensitivity suggests that making the switch from the AOT model to the QMD model will significantly alter the results.

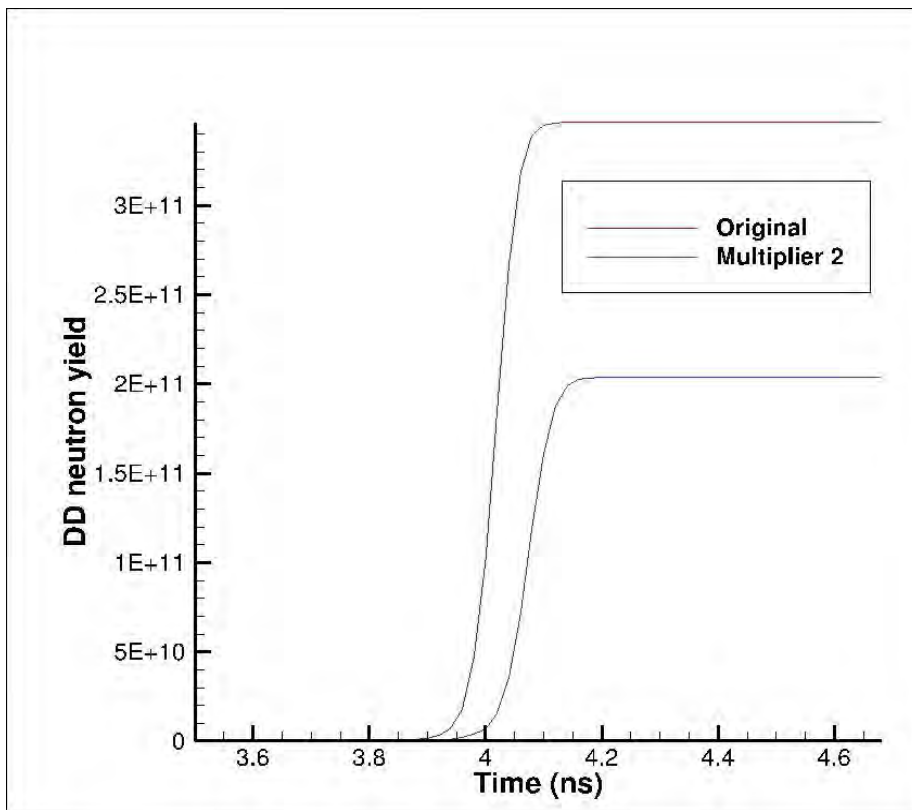


Figure 3: Cumulative DD neutron yield against time for the original run and the modified run

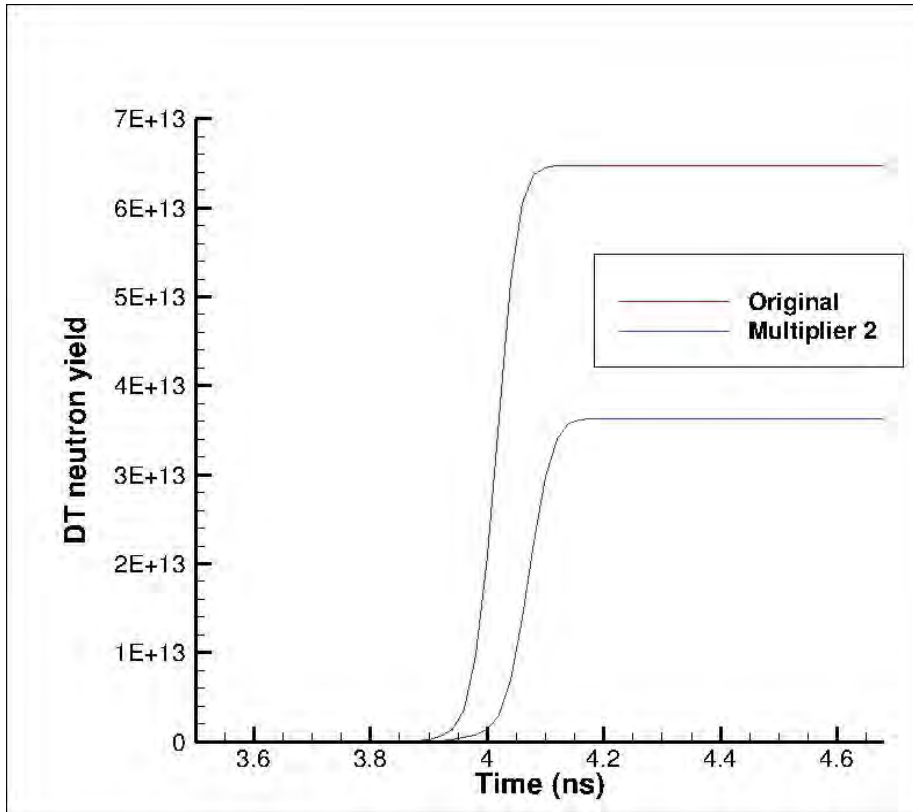


Figure 4: Cumulative DT neutron yield against time for the modified run and the original run

As seen from figure 5, a drop in density between the original run and the run with the multiplier of 2 was observed. This is due to an increase in absorption of radiation in the shell of the deuterium tritium capsule. The radiation converts to heat, making the capsule more difficult to compress, effectively dropping the density. Areal density, defined as the integral of the mass density with respect to radius from the center of the target to infinity, is an important measurement in inertial confinement fusion because energy from fusion reactions is redeposited in the fuel, initiating thermonuclear ignition if the areal density is high enough. As demonstrated by figure 6, the areal density also drops significantly. This occurs for the same reason that the mass density dropped. The peak areal density dropped 10% from 0.32 g/cm^2 to 0.29 g/cm^2 . The peak mass density dropped 20% from 254 g/cm^3 to 204 g/cm^3 . The modified simulation also produces a 40% drop in both DD neutron yield and DT neutron yield. The DD

neutron yield dropped from 3.5×10^{11} to 2.0×10^{11} . The DT neutron yield dropped from 6.5×10^{13} to 3.6×10^{13} . From the equation for the dominant fusion reaction, ${}^2_1\text{H} + {}^3_1\text{H} \rightarrow {}^4_2\text{He} + {}^1_0\text{n}$, a neutron is produced whenever a deuterium molecule and a tritium molecule react, along with a large quantity of energy. The decline in the neutron yield therefore shows that fewer reactions are taking place and that the energy output from the inertial confinement fusion implosion is smaller.

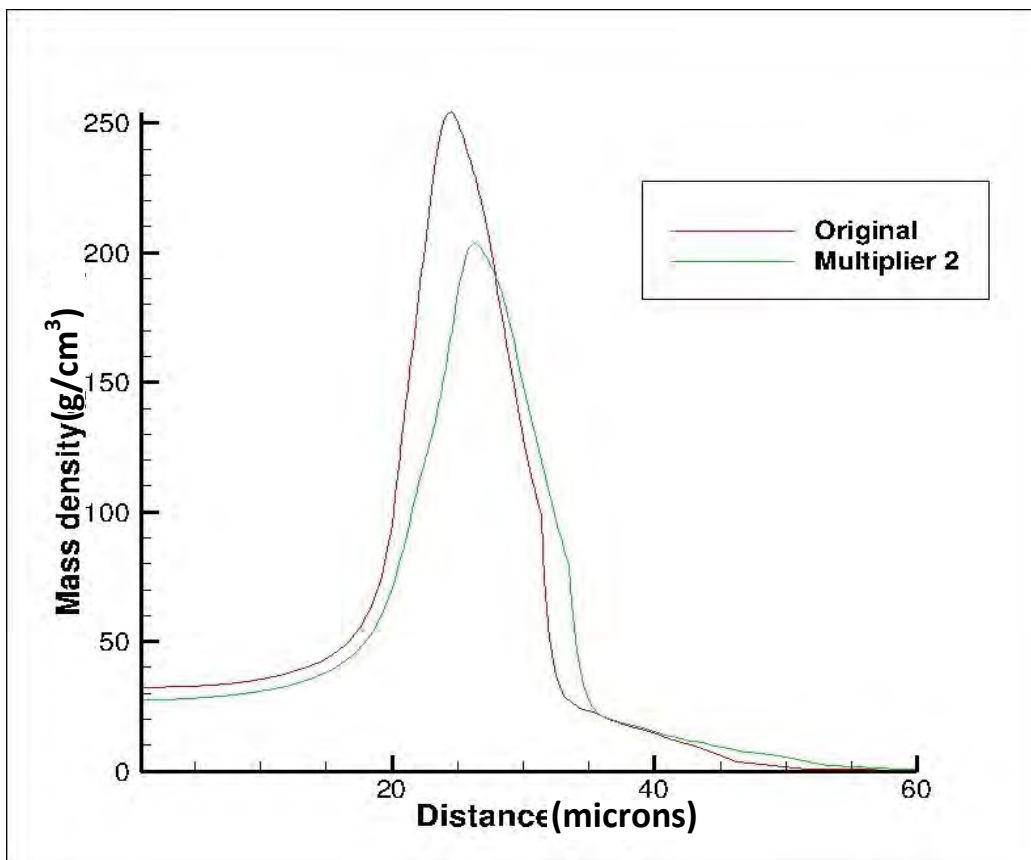


Figure 5: Mass density against the radius in the original run and the modified run.

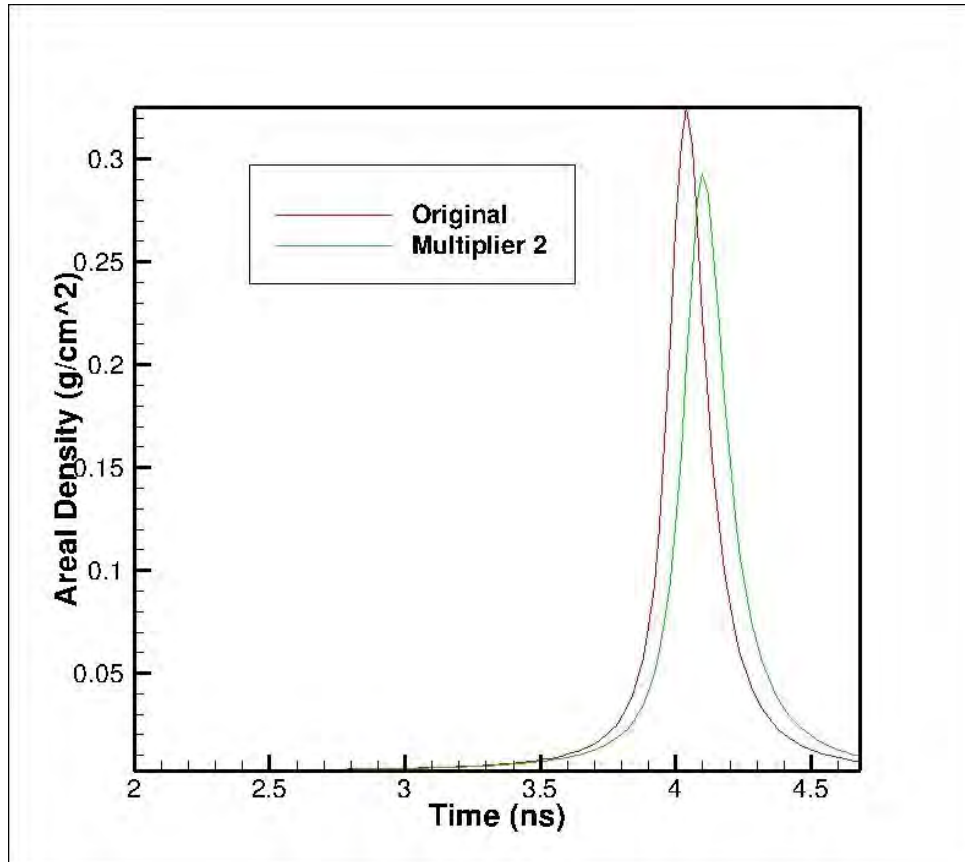


Figure 6: Graphical display of areal density against time for the original run and the modified run

5. Conclusion

The newer QMD model for calculating opacity should be implemented in LLE's simulation programs. It takes many factors into account that the original AOT model did not consider and should provide more accurate results. The ratio between the QMD opacity and the AOT opacity increases significantly as the photon energy increases. The sensitivity of the simulation to opacity was proven to be high, which means that getting more accurate opacity calculations will greatly improve simulation accuracy. Changes to the target design should be explored to compensate for the opacity effects.

6. Future work

This project paves the way for much future work. It is clear that more emphasis should be placed on researching opacity values. The significance of having accurate opacity values has been demonstrated, so more accurate simulations require more accurate opacity values. Also, the program was only modified with a multiplier of 2. The realistic QMD predicted values should be implemented. This is expected to lead to significant changes in the predicted neutron yield. Finally, the modifications should be implemented in all of LLE's hydrodynamic simulation programs, and not only LILAC.

7. Acknowledgements

I could not have completed my project without the help of my peers. I'd like to thank my supervisor, Suxing Hu, most of all for his abundance of advice throughout the project. I'd also like to thank R. Stephen Craxton for having this program and giving high school students a wonderful opportunity to apply their knowledge by doing real research. I'd also like to thank my fellow high school interns for their occasional advice throughout the program and help with minor setbacks.

References

1. W. F. Huebner, A. L. Merts, N. H. Magee, Jr., and M. F. Argo, Astrophysical Opacity Library, Los Alamos National Laboratory, Los Alamos, NM, Report LA-6760-M (1977)
2. S. Mazevet, L. A. Collins, N.H. Magee, J.D. Kress, J.J. Keady, "Quantum Molecular Dynamics calculations of radiative opacities," *Astronomy & Astrophysics*, **405**, L5, 2003
3. S.X. Hu, B. Militzer, V.N. Goncharov, S. Skupsky, "First principles equation-of-state table of deuterium for inertial confinement fusion applications," *Physical Review B* **84**, 224109, 2011

*Deformable Grating Design Optimization for Large-Aperture Pulse Compressor
Systems*

Mitchell Perry

Brighton High School
Rochester, New York

Adviser: Dr. Jie Qiao

Laboratory for Laser Energetics

University of Rochester
Rochester, New York

November 2012

1. Abstract

The Matlab global optimization toolbox was used to optimize actuator positions for designing a deformable grating. It is desired to amend the pulse compression system in the OMEGA EP laser to use 1.5 m monolithic diffraction gratings to temporally compress previously stretched and amplified light. Due to gravity, internal stresses, and temperature drops acting on the glass substrate during the coating process, deformations in the grating inevitably form, resulting in surface wavefront errors. The ANSYS® modeling program, whose finite element capabilities enable it to more accurately model irregular surfaces, is used to analyze grating substrate deformations. An adaptive optical system using pressurized actuators has been devised to limit the size of these irregularities with an effective seven-actuator configuration already established. A genetic algorithm provided by the Matlab global optimization toolbox is used to optimize the locations of individual actuators. A location-optimized seven-actuator design has been achieved using a two dimensional, centrally constrained model, with the final wavefront having a root-mean-square (RMS) error of 0.0013 μm , improved from an initial wavefront RMS of 0.28 μm . Future actuator designs will develop alongside the grating model.

2. Introduction

The OMEGA EP (extended performance) laser system was designed to be an addition to the original OMEGA laser system. Through chirped pulse amplification [1], the OMEGA EP system is capable of achieving picosecond pulse widths and petawatt powers. The laser sends out an initial short pulse that is too weak for fusion but too strong to pass through glass amplifiers. As shown in Fig. 1, the beam is sent through a stretching system that stretches the pulse temporally before it is run through an amplification system. Once amplified, the beam is sent through a compressor consisting of four sets of tiled grating assemblies, each having three interferometrically aligned grating tiles measuring 0.47 m x 0.43 m x 0.1 m [2, 3].

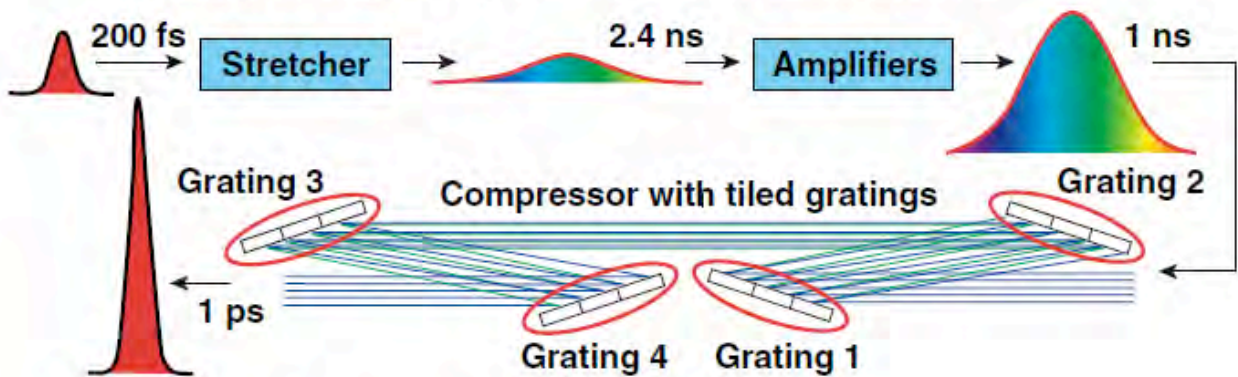


Fig. 1: The OMEGA EP short pulse system. A short pulse of light is stretched and amplified before being sent through a compression system.

The current short pulse system uses tiled-grating compression due to the size limitation of the available gratings, which requires shadowing the input beam across grating-tile gaps, resulting in an energy loss of almost 18%. As a solution, meter-sized monolithic diffraction gratings are desired to eliminate the energy lost

and the challenging tile-to-tile sub-microradian alignment associated with manufacturing the three-tile gratings.

While the monolithic large-aperture gratings would eliminate energy loss and make installation and maintenance easier, these tiles are more prone to deformations due to gravity and temperature gradients along the grating. Such deformations cause laser beam irregularities and spatially varying temporal distortion, resulting in a beam that is less concentrated both spatially and temporally and, therefore, less powerful. A system of actuators along the back of the grating may be an effective solution to the problem of grating deformations. A seven-actuator design has been proposed [5] that corrects a grating with an initial RMS of $0.28 \mu\text{m}$, as seen in Fig. 2, resulting in a corrected wavefront with an RMS of $0.0028 \mu\text{m}$.

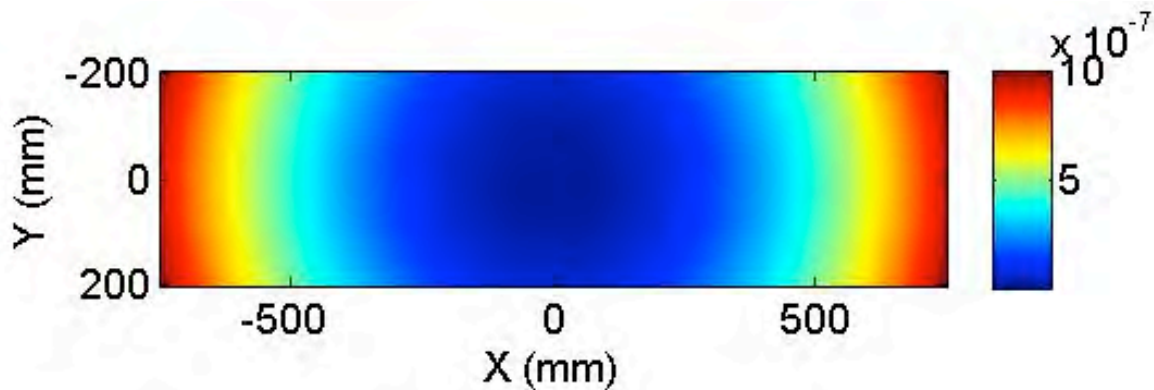


Fig. 2: The initial wavefront to be corrected. The deformed wavefront had a peak-to-valley of $1 \mu\text{m}$ and an RMS of $0.28 \mu\text{m}$. The contour levels are given in m.

The goal of this work was to use the MATLAB global optimization toolbox to optimize the location of actuators along the grating to best minimize wavefront

deformations. A genetic algorithm was used to position seven actuators along the grating, resulting in an RMS lower than that of the previous seven-actuator set up.

3. Grating deformations modeled with ANSYS

ANSYS (Analysis System)[4] is a modeling program that was used to model the deformable compression gratings proposed for the OMEGA EP compression system. ANSYS uses finite-element analysis to give a more accurate realization of the grating and its deformations. It breaks down a complex geometry into many small elements through a meshing tool. While the surface as a whole cannot be modeled polynomially, these smaller elements can, with the sum of the elements giving an accurate shape of the grating.

To determine grating deformations, ANSYS analyzes the stress acting on the grating from some external force. Such stress in a given dimension is illustrated by the equation for the stress σ_x along the x direction:

$$\sigma_x = \frac{E}{(1+\nu)(1-2\nu)} \cdot ((1-\nu)e_x + \nu e_y + \nu e_z) - \frac{E\alpha\Delta T}{1-2\nu}$$

where E is the Young's modulus, which is the stiffness of a material (for BK7, the grating's substrate material, the Young's modulus is 82 GPa); ν is the Poisson's ratio, or how much a material moves in one direction when pushed in the orthogonal direction (equal to 0.21 for BK7); α is the coefficient of thermal expansion (equal to 7.1×10^{-6} for BK7); ΔT is the temperature change on the gradient; and e is the strain acting on the grating in the x, y, or z direction. This method of analysis was used to

calculate the grating deformations due to temperature gradients, gravity and stress from actuator displacements.

To analyze grating deformations, a model of a multilayer dielectric (MLD) grating, which consists of a BK7 substrate and 20 dielectric layers of alternating high and low refractive index layers, here HfO_2 and SiO_2 , respectively, was created in ANSYS (Fig. 3).

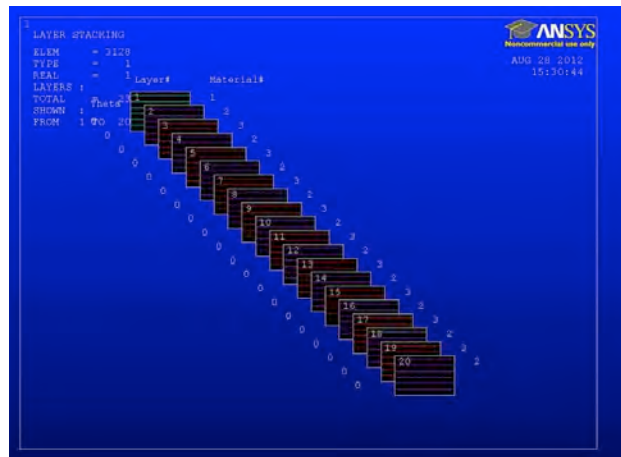


Fig. 3: An ANSYS model of a MLD grating, used to analyze the deformations of the grating from external stresses.

The model was held at the central node in the center of the substrate, and the deformations caused by temperature gradients and gravity were inspected. Temperature changes caused the grating to deform due to the nature of the materials the grating is composed of. The BK7 substrate (thermal expansion coefficient = 7.1×10^{-6}) has a higher thermal expansion coefficient than that of HfO_2 (3.8×10^{-6}) and SiO_2 (0.7×10^{-6}). Therefore, as the temperature drops from 200 degrees Celsius (the temperature at which the MLD layers are coated) to 20 degrees

Celsius, the substrate layer contracts more than the coatings, pulling the grating into a parabolic shape (Fig. 4 (a)). In a similar manner, because the mass of the substrate makes up a majority of the grating's total mass, it bends under gravity more than the substrate layers, once again pulling the grating into a parabolic shape. After testing a number of substrate thicknesses, it was apparent that surface deformation decreases as the substrate thickness increased, as seen in Fig. 4 (b).

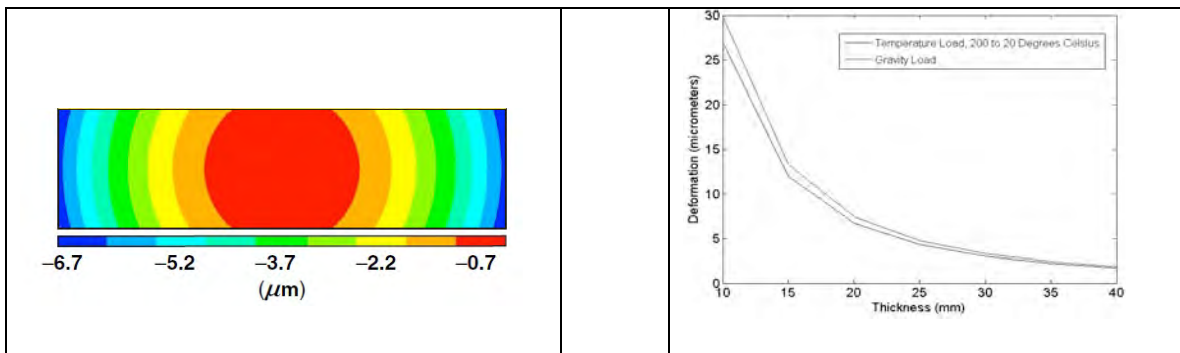


Fig. 4 (a) Thermally-induced surface deformation of a 1.5 m x 0.41 m grating exhibiting a convex-shaped parabola; (b) Deformation due to gravity and thermal loads, both decreasing as the substrate thickness increases.

4. Use of ANSYS and Matlab routines to optimize actuator positions

The initial seven-actuator design that was proposed to correct a 1 micron parabolic wavefront error on a 1.5x0.41x.020 m BK7 substrate was used as the starting point for optimization. Boundary conditions were set for the actuators, allowing each to move 200 mm to the left or right along the grating and 50 mm up and down. The starting positions for each actuator are shown in Fig. 5:

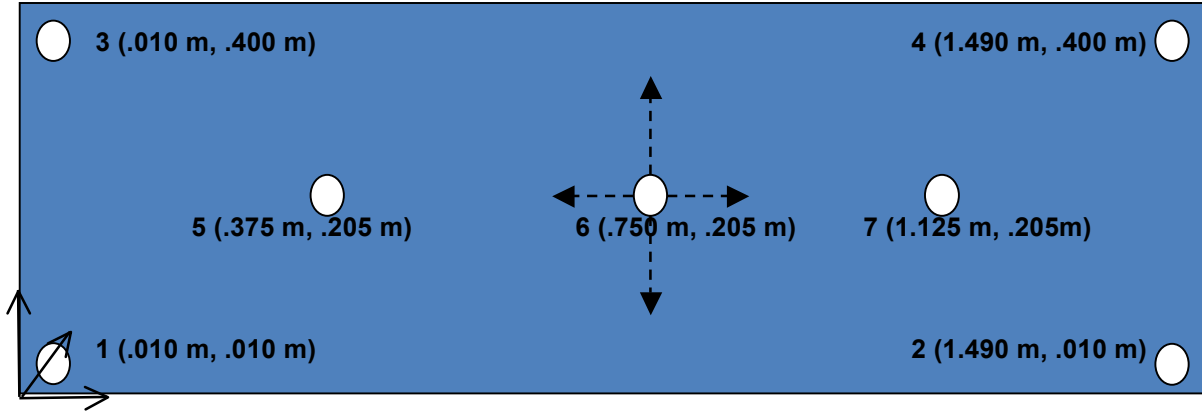


Fig. 5: Diagram of the initial actuator design. A seven-actuator configuration was the starting point for optimization. Each actuator's movement was constrained.

For every actuator configuration, Matlab runs the locations through ANSYS, which then determines the influence function for that design. The influence function is the response of each node – the points on the substrate – to the movement of a particular actuator. It varies depending on the geometrical layout of all the actuators and constraints of the substrate on which the actuators are attached. The required actuator displacements for a desired wavefront can be calculated by:

$$\begin{bmatrix} D_1 \\ \vdots \\ D_M \end{bmatrix} = \begin{bmatrix} P_1 A_1 & \cdots & P_1 A_M \\ \vdots & \ddots & \vdots \\ P_N A_1 & \cdots & P_N A_M \end{bmatrix}^{-1} \begin{bmatrix} Z_1 \\ \vdots \\ Z_N \end{bmatrix}$$

where D_1 through D_M are the displacements of each of the M actuators; $P_1 A_1$ through $P_N A_M$ are the influence of each actuator M on each node N on the surface, and Z_1 through Z_N are the surface deformations at each node specified by the inverse of the wavefront to be corrected. The determined actuator displacements D_1 to D_M can be used to subsequently create a surface that cancels out the uncorrected wavefront and minimizes the grating deformations.

The Matlab genetic algorithm, part of the Matlab global optimization toolbox that contains routines for finding the global minimum of the output of a user-defined merit function, was used to optimize the actuator locations. The objective of the optimization was to minimize the merit function, which was defined as the RMS of the difference between the surface figure generated by the actuators and the wavefront to be corrected. The input variables were the initial actuator locations and their boundary conditions. From these inputs, the Matlab global optimization toolbox would create an initial “population” of randomly generated actuator configurations, as seen in Fig. 6 . The Matlab genetic algorithm would then run each of these configurations in ANSYS through the merit function and would determine which configurations generated surface figures that best cancelled out the initial deformation. The most “fit” configurations would then reproduce – either by combining with another fit configuration or by altering itself – creating a new generation of configurations. This process continues until some stopping criterion is met – this could be a time limit, a certain number of generations, or a minimum difference in average values from one generation to the next. Matlab eventually narrows in on one configuration that best minimizes the merit function.

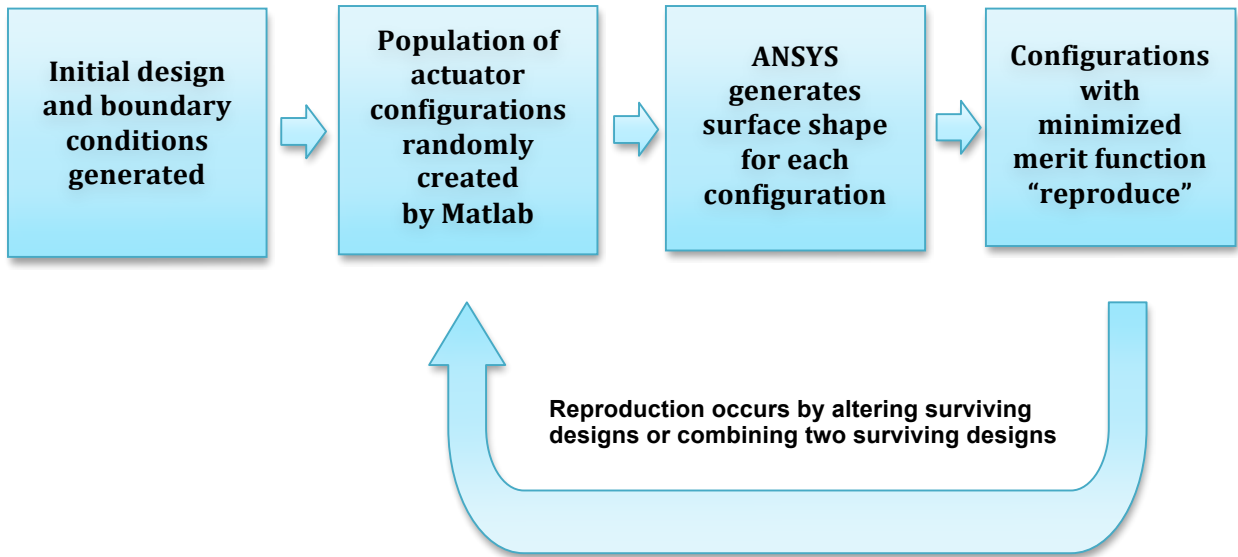


Fig. 6: Algorithm used to optimize actuator positions. The algorithm was looped through until one of a number of criteria was met.

5. Results

The Matlab global optimization toolbox optimized the initial seven-actuator design to minimize the RMS of a deformed-grating wavefront. The configuration was used to correct the wavefront error of a parabolically deformed grating held at its center node with an RMS of $0.28 \mu\text{m}$ and a peak-to-valley of $1 \mu\text{m}$. The final RMS and peak-to-valley after optimization were $0.0013 \mu\text{m}$ and $0.15 \mu\text{m}$, respectively. The final wavefront is shown in Fig. 7.

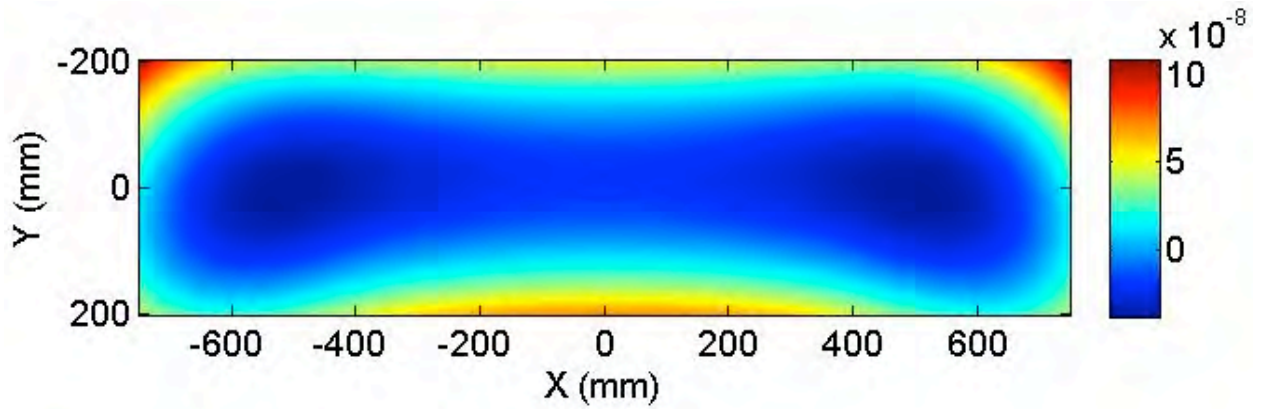


Fig. 7: The final corrected wavefront after optimization of the seven-actuator design. The configuration achieved a wavefront RMS of $0.0013 \mu\text{m}$. The contour levels are given in meters.

The optimized actuator set up better minimized the deformable grating RMS than the initial seven-actuator design, which achieved a final RMS of $0.0028 \mu\text{m}$ and a final peak-to-valley of $0.094 \mu\text{m}$ and whose wavefront can be seen in Fig. 8:

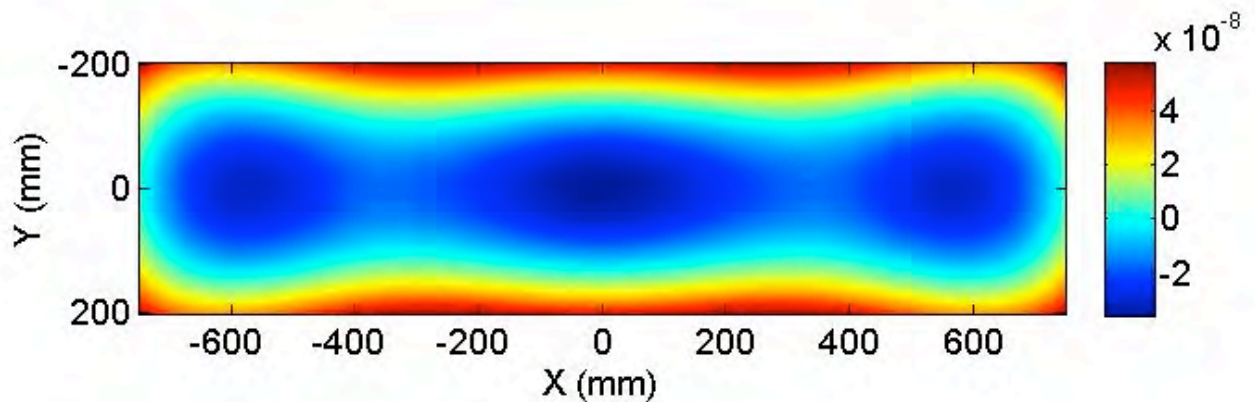


Fig. 8: The wavefront created by the initial seven-actuator design. The configuration achieved a wavefront RMS of $0.0028 \mu\text{m}$.

While the initial design achieved a lower peak-to-valley than the optimized design, the most drastic deformations on the optimized corrected surface occur in the upper corners. These are above the beam, which takes up the central $\pm 185 \text{ mm}$ of the grating vertically.

6. Conclusion

ANSYS was used to model deformations of a 1.5 m x 0.41 m x 0.02 m compression grating caused by gravity and temperature change. An initial seven - actuator design was optimized using Matlab's global optimization toolbox with a user-defined merit function to minimize the RMS of the grating deformation. While the optimized design achieved a final wavefront with an RMS of 0.0013 μm , down from 0.0028 μm from the initial design, the optimized final wavefront had a peak-to-valley of 0.15 μm , higher than the initial design's 0.094 μm .

As seen in Fig. 7, the optimized set up was not a symmetrical pattern of actuators, contrary to what one would expect. Most likely the boundary conditions were not optimum or the optimization time was not long enough to allow the model to reach a symmetrical design. Future research could focus on expanding the finite-element analysis to include internal nodes of the substrate for internal stress analysis, improving the specifications for boundary conditions, and a longer runtime for optimizing the actuator locations.

Acknowledgements

I'd like to thank Dr. Jie Qiao for being my research advisor along with Xiang Liu and Jonathan Papas for helping me along with my research project.

References

1. D. Strickland, G. Mourou: "Compression of amplified chirped optical pulses", *Opt. Commun.* 56, 219 (1985)
2. J. Qiao *et al* "Demonstration of large-aperture tiled-grating compressors for high-energy, petawattclass, chirped-pulse amplification systems," *Opt. Lett.* 33, 1684(2008)
3. J. Qiao *et al* "Demonstration of large-aperture tiled-grating compressors for high-energy, petawattclass, chirped-pulse amplification systems," *Opt. Express* 15, 9565 (2007)
4. <http://www.ansys.com>
5. Dr. Jie Qiao

*Optical Modeling and Analysis of a High Throughput and High Temporal Resolution
Spectrometer*

Raz Rivlis

Brighton High School

Rochester, New York

Adviser: Robert Boni

Laboratory for Laser Energetics

University of Rochester

Rochester, New York

Summer, 2012

1. Abstract

A newly designed UV spectrometer will replace the current 351 nm, full aperture backscatter (FABS) spectrometer that is used in the OMEGA laser system. The FABS spectrometer has a time resolution of 270 ps. The new spectrometer will improve the temporal resolution to 10 ps, while maintaining signal throughput by superimposing 27 separate spectra onto the detector. This is accomplished by placing a 27-element roof mirror array between two identical diffraction gratings operating at opposite orders. The retro-reflecting property of the roof mirror array breaks the 270 ps pulse front tilt into 27 10 ps pulse front tilts. FRED, an optical design program, was used to model the spectrometer. Image rotation, pulse front tilt, and images from other grating orders were analyzed. It was found that image rotation can be corrected by rotating the input slit. The separation between the roof mirror array and the gratings was chosen to prevent images from other grating orders from reaching the detector. The pulse front tilt analysis demonstrates that the spectrometer will achieve the desired 10 ps time resolution.

2. Introduction

The OMEGA laser system is used to study the direct drive approach to inertial confinement fusion. In the OMEGA system, a FABS spectrometer collects 351 nm light that scatters back into the laser path.¹ The spectrometer, coupled to a streak camera, is used to measure the spectral shift of the backscattered light as a function of time, giving information on the evolution of a target irradiated by the OMEGA laser.^{1,2,3} The current spectrometer has a time resolution of 270 ps, but by masking 2/3 of the light, the temporal resolution is reduced to 90 ps. Our goal is to obtain better time resolution, without sacrificing throughput.

When using a single grating, throughput and time resolution are linked. Improving time resolution generally requires masking the grating, which reduces throughput, as shown in Figure 1. When light reflects off a grating, the angle of the reflected light differs from that of the incident light. This causes a delay between two light paths separated in space due to a difference in path length.

To increase the throughput, while maintaining resolving power and time resolution, one possible solution is to operate multiple spectrometers in parallel as shown in Figure 2. The input is an f/4 fiber optic cable. To obtain the desired time resolution, we could mask the input down to f/108. If we could instead split the input into 27 f/108 sections, we would lose no light from the input, and we would obtain the desired time resolution. The total throughput is the sum of those from each of the individual spectrometers. However, building such a spectrometer would be highly impractical, as it would require alignment of a huge number of small optical elements.

Instead, we explore a method to break up the pulse front tilt, effectively creating multiple spectrometers in parallel.

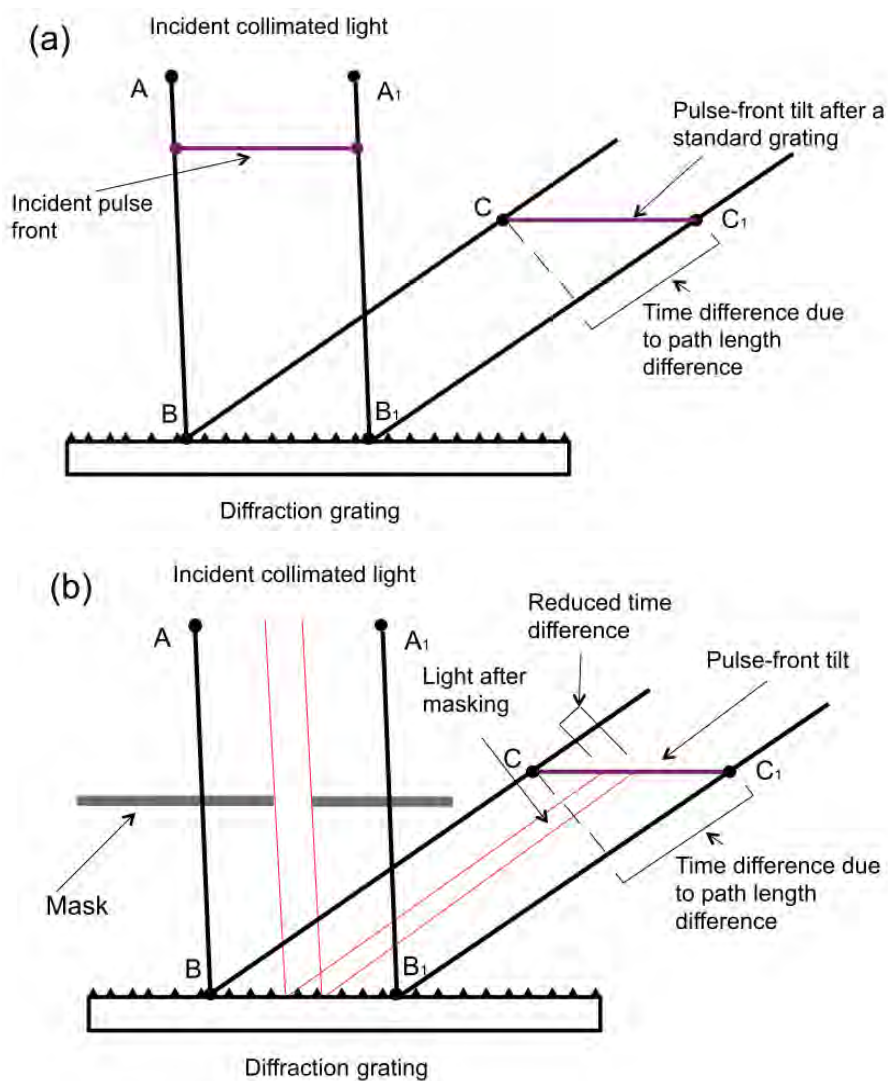


Figure 1:

(a) A standard spectrometer, with a large pulse front tilt and a large throughput. The output light is focused by lenses (not shown) to separate the different wavelengths in the incident beam.

(b) The same spectrometer, masked to reduce pulse front tilt. This also reduces the throughput.

3. Design of Spectrometer

In this section we describe how a roof mirror array can be used to improve time resolution of the spectrometer, without sacrificing throughput. The concept was originated by R. Boni.⁴

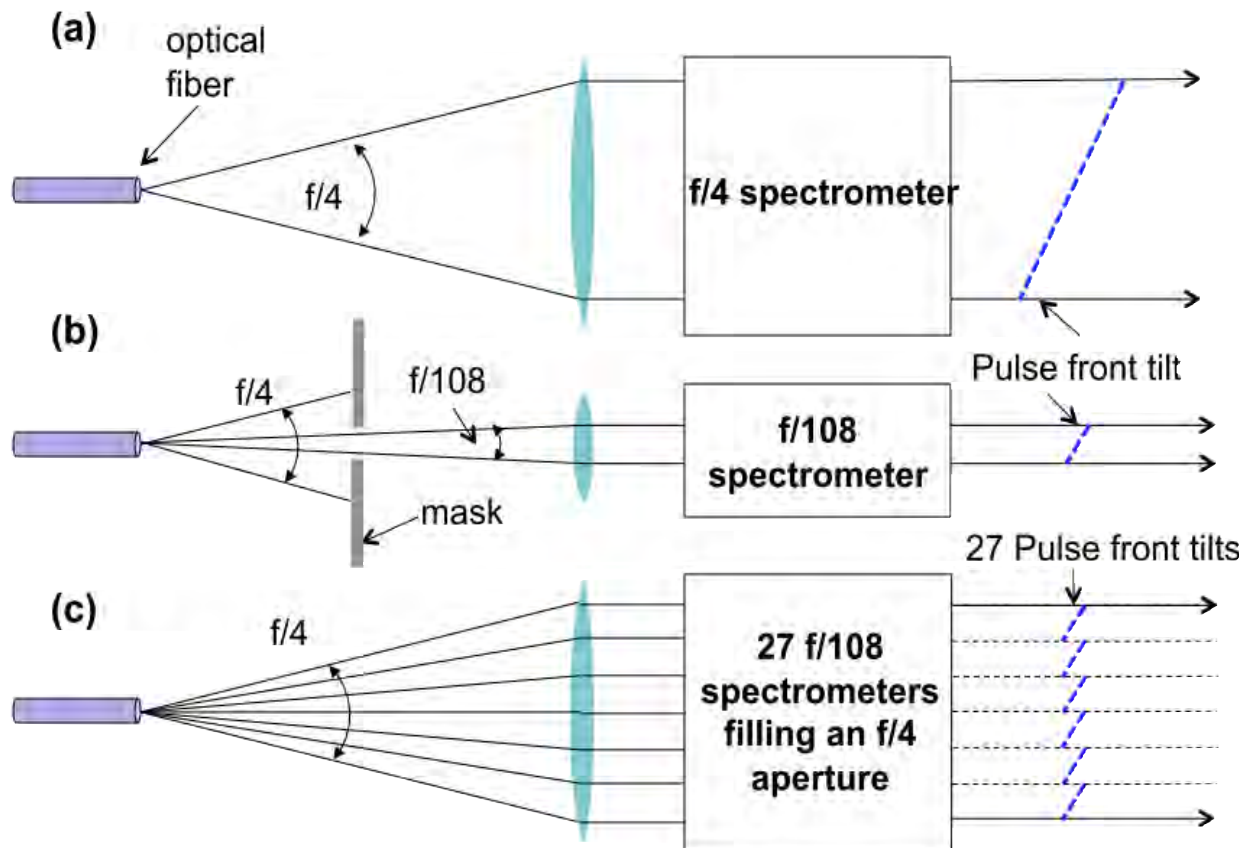


Figure 2: (a) A standard $f/4$ spectrometer with a large throughput and large pulse front tilt. (b) An $f/108$ spectrometer with a small pulse front tilt and small throughput. (c) 27 $f/108$ spectrometers used in parallel to fill an $f/4$ cone, resulting in a high throughput and high time resolution.

3.1 Use of a roof mirror array to improve time resolution

A roof mirror is two mirrors oriented 90 degrees from each other. A roof mirror array is a series of roof mirrors, as shown in Figure 3. While roof mirrors are not uncommonly used, roof mirror arrays have never been built to optical quality. Placing a roof mirror array between two diffraction gratings operating at opposite orders causes the pulse front tilt to segment. As shown in Figure 3, the roof mirror segments the pulse front tilt from the first grating by flipping each segment of the reflected pulse front tilt. However, there is still a

large overall pulse front tilt. The second grating removes this, but keeps the small segments, creating multiple small pulse front tilts. This improves the total time resolution, while preserving the throughput of the incoming light.

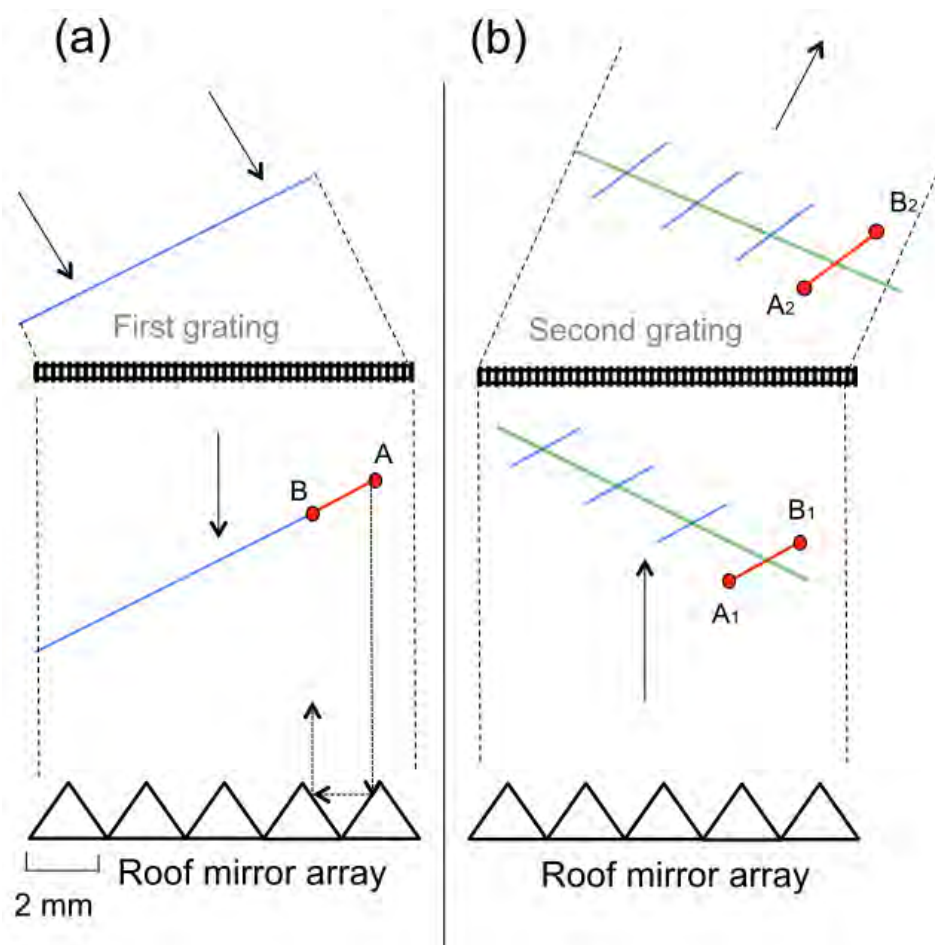


Figure 3: This schematic illustrates the use a roof mirror array between two gratings to reduce the pulse front tilt. Gratings are drawn as transmission gratings to aid visualization. Each point A corresponds to the same ray, as does each point, B. (a) Incoming light passes through the first grating, creating a large pulse front tilt. (b) The pulse front tilt is segmented by the roof mirror array. The green line would be the reflection off an ordinary mirror. The large pulse front tilt is canceled out by the second grating, operating at opposite order from the first one. The tilt for each segment is doubled as it passes through the second grating.

3.2 Choice of Grating Order to Improve Efficiency

We will operate the gratings at plus and minus 7th order. By operating the gratings at 7th order we can use a grating with wide groove spacings. This is seen from the grating equation:

$$n\lambda = d(\sin\alpha + \sin\beta) \quad (1)$$

where n is the order, λ is the wavelength of light, d is the distance between grooves, α is the incident angle, and β is the resultant angle.⁵ For fixed incident and resultant angles, larger d corresponds to larger n . Increasing the groove spacing is desirable because it increases efficiency. Efficiency is reduced when the groove spacing approaches the wavelength of light because p-polarized light experiences edge effects. This is shown in Figure 4. The drawback to operating at high orders is that it causes nearby orders to be closer to the desired order. This increases the risk that nearby orders are imaged on the detector. This problem is examined below.

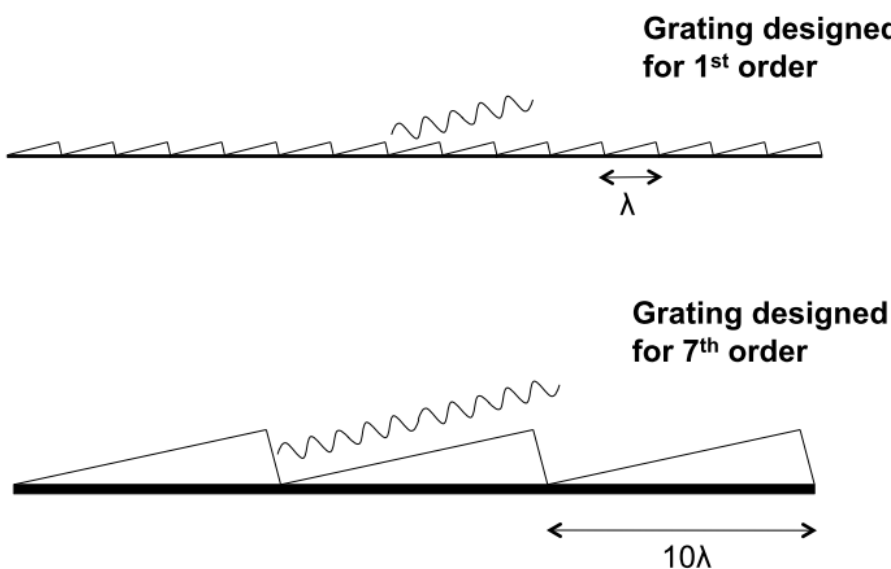


Figure 4: This shows how the groove spacing approaches the wavelength of light (λ) at 1st order, but not 7th. This causes loss of light from p-polarization due to edge effects. S-polarized light is unaffected because its polarization follows the long axis of the grooves.

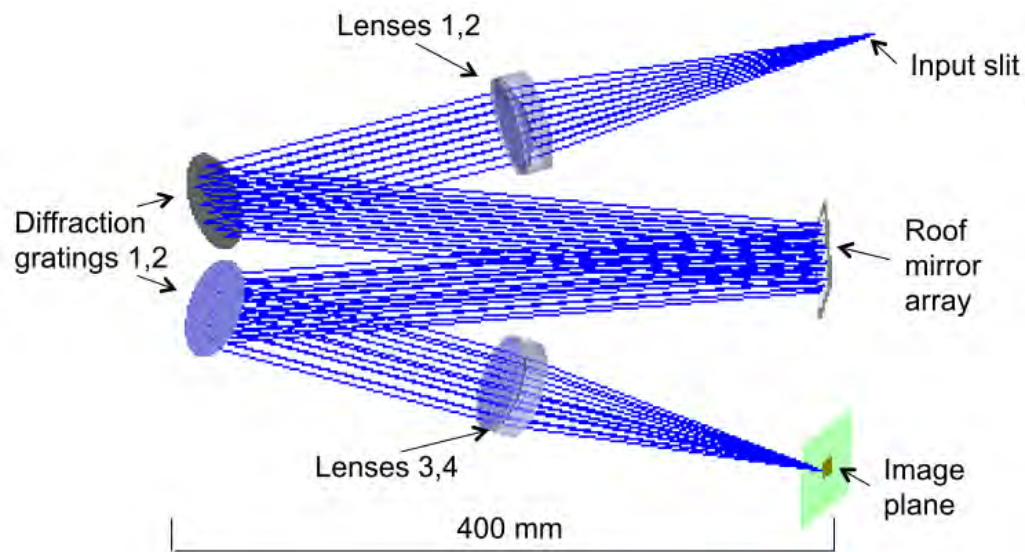
3.3 Initial Design

The initial design was done by R. Boni,⁴ using OSLO, an optical modeling software. OSLO was used to optimize the lens placement to achieve the smallest spot size in the image plane. However, OSLO was unable to check the temporal resolution, image rotation, and order crosstalk.

4. *Optical Modeling*

The spectrometer design was analyzed using FRED Optical Engineering Software, developed by Photon Engineering,⁶ that simulates the propagation of light through an optical system by raytracing. FRED allows the user to control the light source, scattering, and grating orders. We used FRED to model a slit input source, model multiple grating orders, measure image rotation, and determine the pulse-front tilt.

Figure 5 shows the optical layout and the ray path at 7th order. The detector we are using is a ROSS streak camera, and it will be located at the image plane. The streak camera will record a one dimensional slit over time, with high temporal resolution. The ray path shown in Figure 5 does not lie in a single plane. This is because the roof mirror array is a one dimensional retro mirror, and if the ray path was not taken out of plane, the gratings would have to lie in the same physical space. Tables 1 and 2 list properties of the optical elements. Both Table 1 and Figure 5 show the final design resulting from this work. The primary modification to the initial design is the roof mirror to grating distance as discussed in Section 4.4. In Table 1, the distance to the next element is measured along the ray path. Because the spectrometer operates near 351 nm, CaF₂ and fused silica lenses are used for their high UV transmittance.

**Figure 5:**

Raytrace diagram as modeled by FRED.

Note that the ray path does not travel in a single plane.

Table 1: Optical elements of the spectrometer: The radii of curvature for each element are listed along with its material and the distance to the next element along the ray path.

Optic	Front Radius of Curvature (mm)	Back Radius of Curvature (mm)	Thickness (mm)	Aperture (mm)	Material	Distance to next element (mm)
Lens 1	291	59.6	8	35	Fused Silica	.072
Lens 2	59.6	-145	18	35	CaF ₂	200
Grating 1	-	-	-	36	-	400
Roof Mirror	-	-	-	27 by 30	-	400
Grating 2	-	-	-	36	-	200
Lens 3	-145	59.6	18	35	CaF ₂	.072
Lens 4	59.6	291	8	35	Fused Silica	227

Table 2: Tilt of the elements, relative to the previous element along the ray path: At the input slit, the Z direction is along the ray path, X is arbitrarily chosen, and Y is perpendicular to X and Z.

Optic	Tilts
Grating 1	11.37° X tilt, 6° Y tilt
Roof Mirror Array	-6° Y tilt
Grating 2	-32.68° X tilt, 6° Y tilt

4.1 Image rotation

The FRED model showed that the spectrometer rotated the image as shown in Figure 6(a). This rotation occurred because the ray path was out of plane, and some elements are tilted around both X and Y axes (see Figure 5 and Table 2). The streak camera window is approximately 0.2 mm. This rotation seen in Figure 6(a), over the width of the window, which is in the x axis in the figure, causes the spectrum to blur by around 0.05 nm. The streak camera records only one spatial dimension, so all horizontal information is lost. The rotation cannot be removed by rotating the detector, because we would not detect the light at the edges of our desired frequency range. The bands would no longer be rotated or blurred, but the edges of the spectrum would fall outside the window. The rotation can be corrected by rotating the input slit instead. We used the FRED model, as shown in Figure 6(b), to determine that the input slit must be rotated 7.5° in the opposite direction to the rotation to remove it. This value was determined by trying a few different values and minimizing the modeled image rotation.

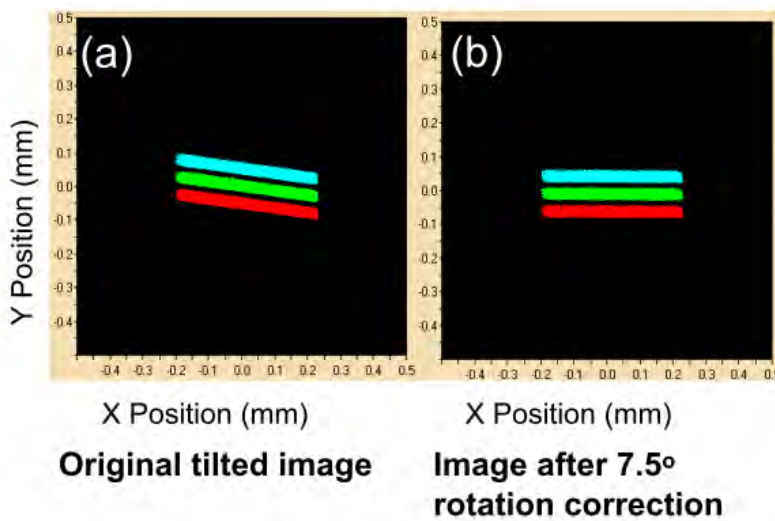


Figure 6: (a) Spot diagram at the image plane. Note that each color rotates individually. (b) Spot diagram at the detector after the input slit has been rotated 7.5°.

Red = 351.05 nm light
 Green = 351 nm light
 Blue = 350.95 nm light

4.2 Spatial resolution and resolving power at 7th order

FRED was used to model the spatial resolution and resolving power. Using a spot diagram at the image plane, where the detector will be located, we determined that the spectrometer has a spatial resolution of 50 microns, and a resolving power of 0.05 nm. This means that the spectrometer will detect wavelengths 0.05 nm apart, and will image them 50 microns apart. Figure 7 is an expanded view of Figure 6(b). The figure suggests that we could detect a smaller wavelength difference; however, we lose some resolution from the streak camera. The streak camera's pixel size is 50 microns, so the spectrometer creates no additional loss of resolution. This model is consistent with the OLSO model. However, the FRED model is more accurate, because it takes into account rays from the entire input slit. OSLO can only model point sources.

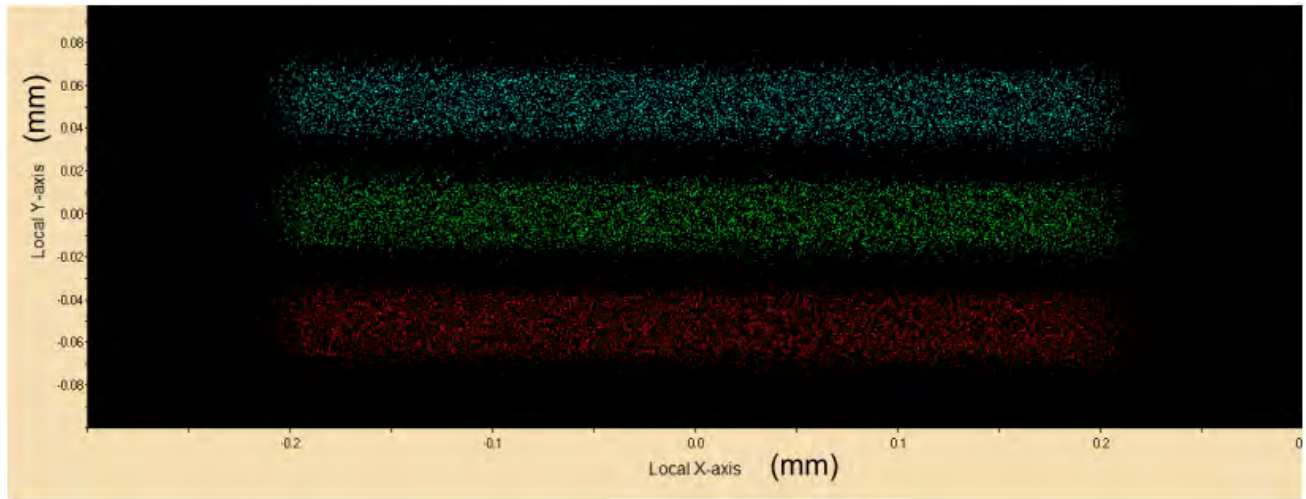


Figure 7: Spot diagram from the spectrometer at the image plane. Red spots are light at 351.05 nm, green at 351 nm, blue at 350.95 nm. Along the Y axis, there are 50 microns of dispersion between each band of light. The spot width is 40 microns.

4.3 Temporal resolution

Most spectrometers do not need to operate at high temporal resolution, so raytracing software is not designed to measure pulse front tilt. However, the FRED model can be used to determine the physical path length of each ray. From this we can calculate the pulse front tilt. We measured the physical path length from the source to a plane right before refocusing (right before lens 3; see Figure 5). We recorded the X and Y position of each ray at the final plane. We normalized all these distances, so that we had the difference in X, Y, and path length. We then converted the path length difference to a time difference. Next, we used Matlab to make a plot of time delay vs. position in the column of light, as shown in Figure 8. This plot clearly shows how multiple pulse front tilts are created by the roof mirror array. Furthermore, the model output verified that we obtained the desired time resolution of 10 ps.

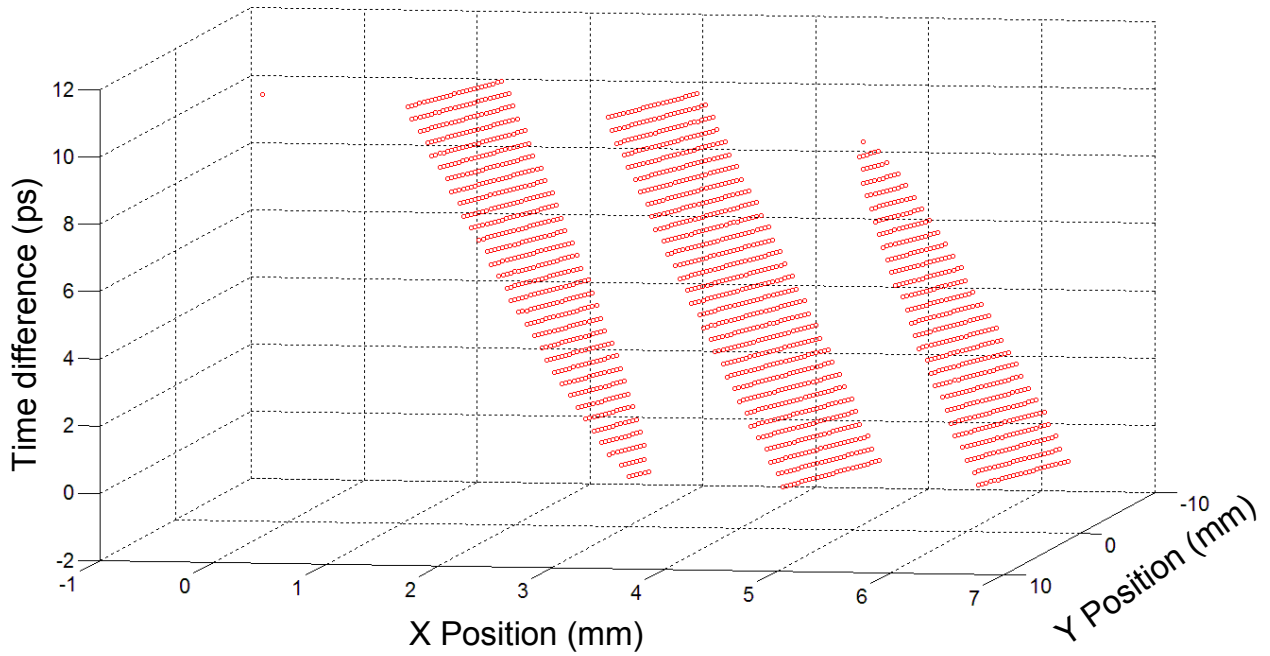


Figure 8: Plot of time difference against position in the column of light. Because this plot only shows 3 of the 27 pulse front tilts, and is not in the focal plane, three groups are seen. Note that each of these pulse front tilts is only 10 ps wide, as seen on the Z axis. The model successfully shows each individual pulse front tilt.

4.4 Order crosstalk

A problem that must be considered is the risk of nearby orders imaging onto the detector, known as crosstalk between orders. Figure 9 shows the initial FRED model, taking into account 6th, 7th, and 8th orders. To completely examine this problem, we calculated the resultant angles and linear displacement for all orders from both gratings between $n = 0$ and 9. We used the following variations on the grating equation (Equation 1),

$$\beta_1 = \text{asin}(n_1\lambda/d - \sin\alpha_1) \quad (2)$$

$$\alpha_2 = \beta_1 + 65.38^\circ \quad (3)$$

$$\beta_2 = \text{asin}(n_2\lambda/d - \sin\alpha_2) \quad (4)$$

where α_1 is the incident angle on the first grating, α_2 is the incident angle on the second grating, β_1 is the resultant angle from the first grating, β_2 is the resultant angle from the second grating, n_1 is the first grating order, n_2 is the second grating order, d is the groove spacing, and λ is the wavelength. Our wavelength is always 0.351 micrometers, α_1 is always 11.37° and d is always 1/300 mm. The conversion from β_1 to α_2 comes from the physical layout of the spectrometer; 65.36° is the angle between the 2 gratings. This is calculated from the angles in Table 2 and is equal to 32.68×2 . Using these three equations, we calculated the resultant angle for the different order combinations. We then subtracted 11.37° from each resultant angle, giving us the angle to the center of the detector plane. We took the tangent of the resultant angle and multiplied by the focal length of the second lens system to determine the location of the image on the detector.

We considered two criteria for significant order problems: the resultant distance was close to the desired image, and the ray path intersected the roof mirror array. There were only four significant order combinations that are potentially a problem and these are listed in Table 3. We used our FRED model to predict the locations and intensities of these problematic orders in the image plane, and these are shown in Figure 10. Our computations of the image locations (in Table 3) agree with those computed using the FRED ray tracing model.

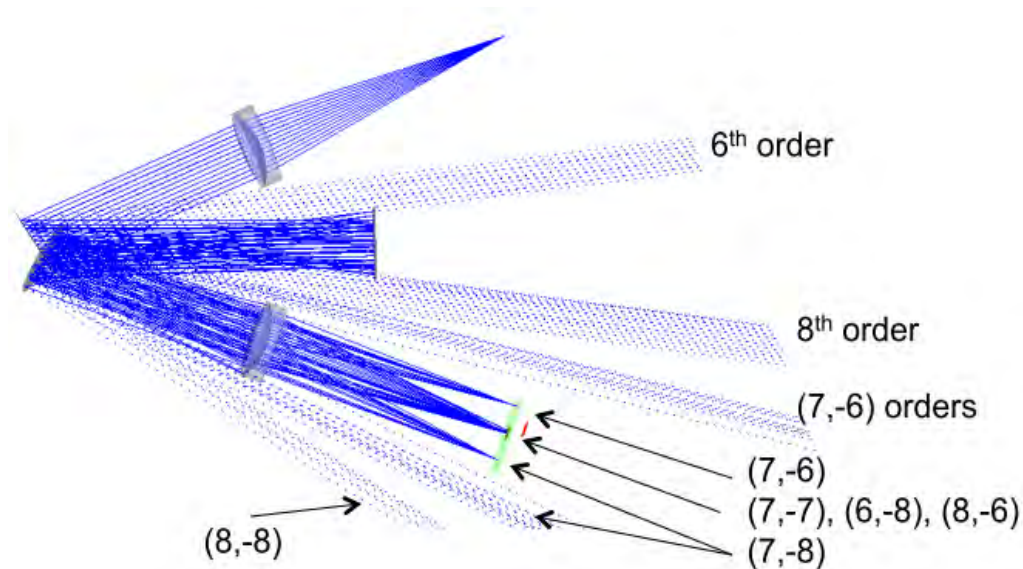


Figure 9: Raytracing showing the various order combinations that could cause order crosstalk. The center spot on the image plane is three spots caused by three different order combinations. The detector lies in the green plane, but is smaller. The (7, -6) and (7, -8) orders do not intersect the detector.

Table 3: Location of images from contaminating orders: Distance of image, in the image plane, from the 7th order image for nearby grating orders, in mm. These distances were calculated using Equations 2, 3, and 4.

Order of First grating	Order of Second Grating		
	-6	-7	-8
6			2.15
7	-24.23	0	24.76
8	1.83		

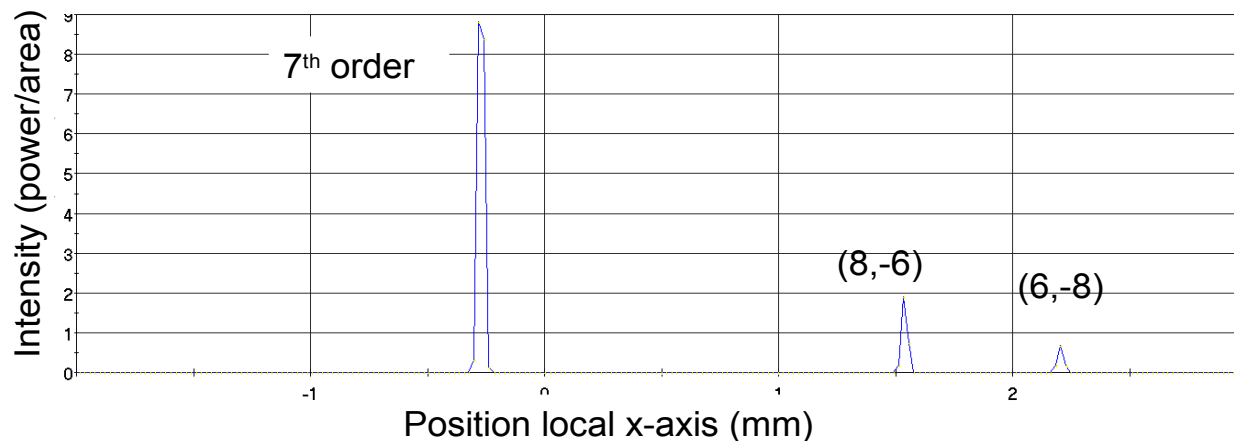


Figure 10: This graph plots light intensity (y axis) vs. position of focal plane (x axis) in mm, computed in FRED. The image near $x = 0$ is the 7th order image. The other two images correspond to the (6, -8) and (8, -6) order images as shown in Table 3.

To eliminate the (6, -8), and (8, -6) orders, we modified the design so fewer rays from these orders intersect the roof mirror array. We did this by moving the roof mirror array from 300 mm, where it originally was, to 400 mm. If we moved the roof mirror array back further, even fewer rays would intersect it, but the spectrometer would become bigger and more awkward to build and use in the OMEGA target bay. Figure 11 shows the 6th and 8th order paths missing the roof mirror. We ran a FRED model that takes into account the efficiencies of the gratings to estimate the intensity of the brightest undesired order image. We find that with the new design, the brightest undesired order is a factor of 100 below the primary image, as seen in Figure 12. An image that dim would not be detected, and so is irrelevant.

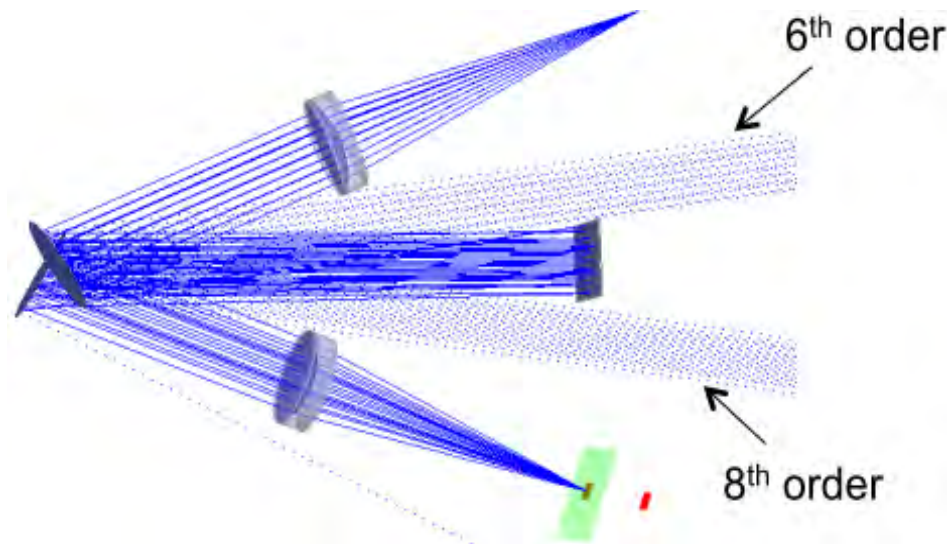


Figure 11: Raytracing showing 6th and 8th orders missing the roof mirror, after increasing the roof mirror-grating distance.

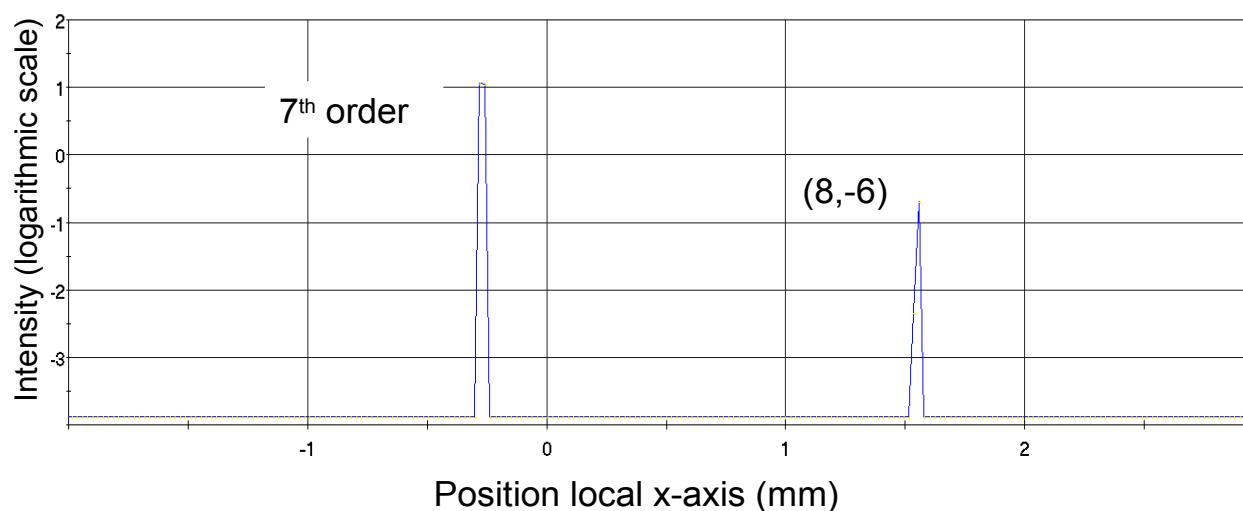


Figure 12: Intensity vs. X-axis position, The image near $x = 0$ is the 7th order image. The other image corresponds to the (8, -6) order image. Note that this image is 2 decades dimmer than the desired image.

The other two order combinations that could be problematic are the (7, -6) and (7, -8) orders (shown in Table 3). These cannot be removed by moving the roof mirror array, as their rays follow the same path as the desired image until the second grating. However, they do not actually image on the detector (see Figure 9). They image near the detector instead. This means that they will only become a problem if light of other frequencies enters the spectrometer. We

determined using FRED that light more than 30 nm from the central wavelength will image onto the detector. To avoid this, we will add a 30 nm bandpass filter, centered on 351 nm. This filter will remove these undesired orders.

5. Summary and Future Work

We have designed a spectrometer that drastically improves temporal resolution, while preserving throughput. This spectrometer will replace the 351 nm backscatter spectrometer in the OMEGA system, and will improve the temporal resolution by a factor of 9, to 10 ps, and the throughput by a factor of 3. The design was modeled using FRED, and shows that a roof mirror array between two gratings is an effective way to reduce pulse front tilt. We discovered that the input slit must be rotated 7.5° to align the image with the streak camera window. The location of the roof mirror array was moved to remove an undesired order. It will be located 400 mm from the gratings. A 30 nm bandpass filter to remove other undesired orders.

The current spectrometer is used to study plasma instabilities that prevent high efficiency compression of the target and absorption of laser light in direct drive inertial confinement fusion experiments.^{2,7,8} Efficient fusion will not be achieved if these instabilities prevent compression of the fuel. When ion-acoustic waves (sound waves in a plasma) are excited by laser light, they evolve on a time scale of 10 ps. Current diagnostics cannot achieve this resolution.⁸ Temporally resolving the scattered light will allow us to measure the temporal evolution of the ion-acoustic waves, allowing us to design experiments with higher efficiency compression. Very few measurements have been made of this ion-acoustic wave scattering process at this resolution.

Acknowledgments

I would like to thank Mr. Ted Kinsman, my physics teacher, for encouraging me to apply to this program and writing my recommendation for this program. I would like to thank Wolf Seka, Dustin Froula, and Steven Ivancic for helpful discussions. I would especially like to thank my adviser, Mr. Robert Boni, for all the help and time he gave me, as well as Dr. Stephen Craxton for running the program. I would also like to thank the Lab for Laser Energetics for supporting this high school program.

References

1. W. Seka, C. Stoeckl, V. N. Goncharov, R. E. Bahr, T. C. Sangster, R. S. Craxton, J. A. Delettrez, A. V. Maximov, J. Myatt, A. Simon, and R. W. Short, *Absorption Measurements in Spherical Implosions on OMEGA*. Bull. Am. Phys. Soc., 49 179 (2004).
2. W. Seka, D. H. Edgell, J. P Knauer, J. F Myatt, A. V. Maximov, R. W. Short, T. C. Sangster, C. Stoeckl, R. E. Bahr, R. S. Craxton, J. A. Delettrez, V. N. Goncharov, I. V. Igumenschchev, and D. Shvarts, *Time-Resolved absorption in cryogenic and room-temperature direct drive implosions*. Physics of Plasmas, 15, 056312 (2008).
3. W. Seka, V. N. Goncharov, J. A. Delettrez, D. H. Edgell, I. V. Igumenschchev, R. W. Short, A. V. Maximov, J. Myatt, and R. S. Craxton, *Time-Dependent Absorption Measurements in Direct-Drive Spherical Implosions*. Phys. Rev A, 36, 3926 (1987).
4. Robert Boni, private communications.
5. Palmer, Christopher. *Diffraction Grating Handbook Fifth Edition*. 2002 Pg 17.
6. Photon Engineering website, <<http://www.photonengr.com/>> September 18, 2012.
7. W. Seka, D. H. Edgell, J. F Myatt, A. V. Maximov, R. W. Short, V. N. Goncharov, and H. A. Baldis, *Two-Plasmon-decay instability in direct-drive inertial confinement fusion experiments*. Physics of Plasmas, 16, 052701 (2009).
8. D. H. Froula, L. Divol, A.A. Offenburger, N. Meezan, T. Ao, G. Gregori, C. Niemann, D. Price, C.A. Smith, and S. H. Glenzer, *Direct Observation of the Saturation of Stimulated Brillouin Scattering by Ion-Trapping Induced Frequency Shifts*. Phys. Rev. Letters, 93, 035001

Prediction of Getter Bed Regeneration Intervals through Absolute Humidity and Flow Rate

Lucas Aaron Shadler
West Irondequoit High School
Rochester, NY

2012 LLE Summer Internship
Advisor: Wade Bittle

Abstract

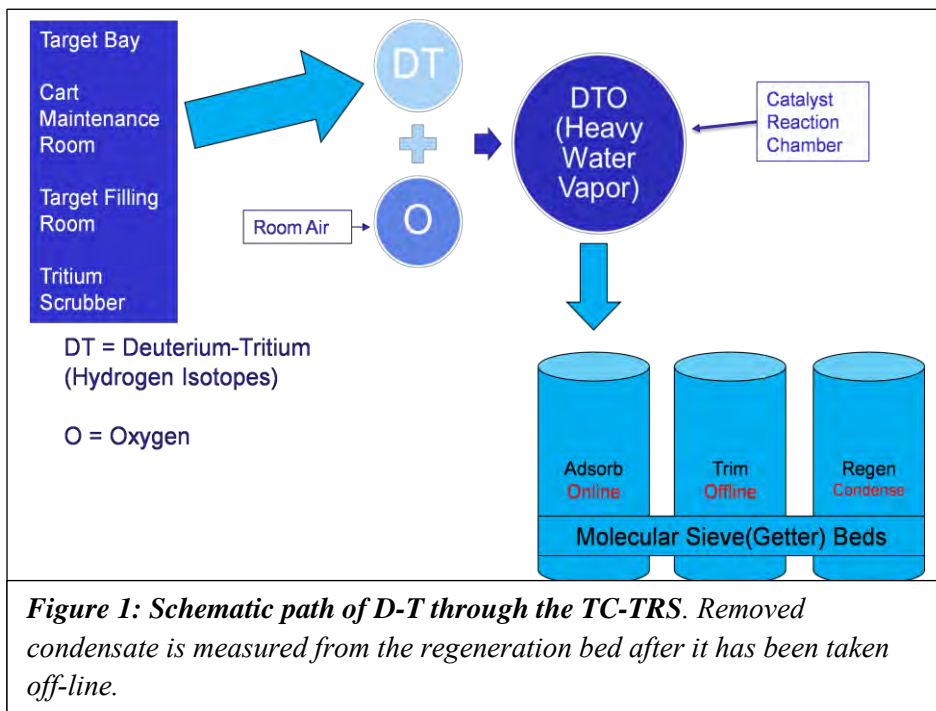
The Target Chamber Tritium Removal System (TC-TRS) intercepts deuterium-tritium (DT) from LLE operations to contain DT for proper removal and storage. It combines DT gas with oxygen within a catalyst reaction chamber to form tritiated water vapor. This vapor is passed through a molecular sieve (“getter”) bed, where the tritiated water is collected and contained until the bed can be taken offline and the water extracted. Extraction is presently done on a set date each month, yielding varying quantities of condensate depending on the volume of gas passed through the TC-TRS from the OMEGA systems during the water collection period. This method ignores real-time bed fill level knowledge, which could potentially lead to an overflow. A MATLAB code was written to compute the amount tritiated water accumulated in the beds. The code analyzed historic data from the TC-TRS with respect to flow volume and the total tritiated water condensate removed during each time interval. The code utilizes an estimate of the average absolute humidity of the incoming vapor, a quantity that expresses the amount of water per flow volume and is not at present directly measured. The code can be used predict the amount of water collected by a given flow volume. Greater accuracy can be achieved if an absolute humidity sensor is added to the incoming air flow.

1. Introduction

The TC-TRS, or Target Chamber Tritium Removal System^[1], effectively removes radioactive isotopes of hydrogen from the OMEGA target chamber and target handling systems during experimental operations. It is necessary to collect these isotopes for proper removal and storage at the LLE facility. Currently each molecular sieve (“getter”) bed is taken offline to be regenerated once each month, with bed fill level roughly estimated by active use time. This

method poses the risk of varying quantities of condensate removed and in a particularly busy month the bed risks overflow. Thus, using MATLAB^[2], computational code was developed that can determine the current capacity to within 30% based on real-time readings of the flow rate into the TC-TRS from the target handling systems and target chamber. Improved accuracy can be achieved through optimization of the placement of the flow rate sensor within the TC-TRS and the addition of a real-time humidity sensor in the incoming air flow path.

2. The TC-TRS



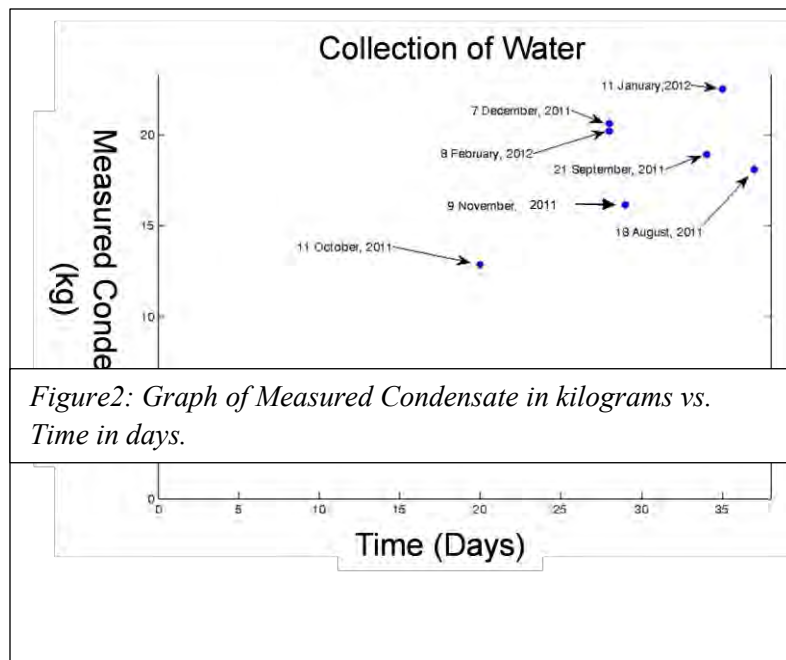
Deuterium and Tritium are isotopes of hydrogen that are created as waste from OMEGA operations. These isotopes are radioactive, and the lab is required to limit the emissions of

DT into the atmosphere. The lab remains well below this limit through the TC-TRS, the key gas processing system in this project. As shown in [Figure 1](#), the D-T is collected from operational areas including the Target Chamber, The Cart Maintenance Room, the Target Filling Room, and the Tritium Scrubber. It is passed through a catalyst reaction chamber, which combines the D-T with Oxygen to create DTO, more commonly known as heavy water. This heavy water passes

through a molecular sieve (“getter”) bed, which contains pores sized optimally to capture the heavy water. There are three getter beds stationed in the TC-TRS; one is set to adsorb the water, one to regenerate after the water is collected, and the third to collect any residual water vapor from the bed that’s regenerating, referred to as the “trim” bed. These getter beds operate in a cycle that is currently checked manually at approximately one-month intervals. Although this process proves functional, there have been cases of overflowing, which results in down time for the getter bed and more man hours to reset the bed cycle. Regenerating the beds prematurely also presents an inefficient use of available man-hours.

The first course of action was to look for a function that could describe the relationship between getter bed time spent collecting condensate and how much condensate was removed during the regeneration. With a plethora of historic data to pull from^[3], points can be plotted of condensate removed vs. time, as shown in Figure 2. The plotted data was almost completely

random, and a closed form expression for condensate removed as a function of time is not attainable. This makes sense, as OMEGA operations change on a daily basis to meet the demands of the target handling schedule and OMEGA target experiments. Thus the problem was approached from a real-time perspective using system sensor data.



3. Calculation of Condensate Mass

The most accurate measurement for the condensate accumulation rate would be achieved using dew point, pressure, temperature and flow rate sensors positioned in the incoming air flow of the TC-TRS. The flow rate in standard cubic feet per minute (SCFM) can be converted to meters cubed per minute, by equation 1, which assumes standard temperature and pressure

$$Flow\ Rate\ \left(\frac{m^3}{min}\right) = \frac{Flow\ Rate(SCFM)}{35.288}. \quad (1)$$

The flow rate in m³/min will be in the correct units to fit with the other equations. Dew point can be converted to water vapor pressure by equation 2^[4].

$$P_w = A * 10^{\frac{m}{T_d} + 1} \quad (2)$$

where A, m and Tn are all constants based upon the temperature range, T_d is the dew point in degrees kelvin (K), and P_w is the water vapor pressure in Pa. The existing TC-TRS vapor pressure sensor data was not used because it also accounted for a carbon backflow. Using the vapor pressure from equation 2, the absolute humidity AH (g/m³) can be calculated by equation 3

$$AH = \frac{C * P_w}{T} \quad (3)$$

where C = 2.16679 gK/J (a constant), and T is the temperature in degrees kelvin (K).

Utilizing equation 4, the accumulated mass of the heavy water collected during a period of time can be determined.

$$Condensate_{Total}(g) = \sum_{n=1}^k AH_n \left(\frac{g}{m^3} \right) * Flow Rate_n \left(\frac{m^3}{min} \right) * \Delta t_n (min), \quad (4)$$

where k is the number of sample intervals and Δt_n is the length of a sample interval. This calculation was performed using a MATLAB program. It is assumed in the calculation that AH and Flow Rate remain constant throughout each sample interval. Accuracy may be improved using higher-order integration schemes in which an interpolation function is utilized for those values as determined by the trends of neighboring sample points. To verify the methods utilized the calculated condensate weight was compared with the getter bed condensate measured and recorded in TC-TRS archived operations data.

To demonstrate the meaning of dew point temperature, an experiment was designed where 50 milliliters of room temperature (about 27 degrees Celsius) water was placed into an aluminum soda can. A temperature probe on the inside of it measured the water temperature and an environmental data logger measured the ambient dew point. Ice cold water was gradually added to the water in the can, and the changes in temperature were recorded while observing the outside of the can surface for condensation. Condensation occurred at a temperature reading of 13.26 degrees Celsius, while the reading on the experimental logger for the dew point was 13.3 degrees.

4. Operation of MATLAB Program

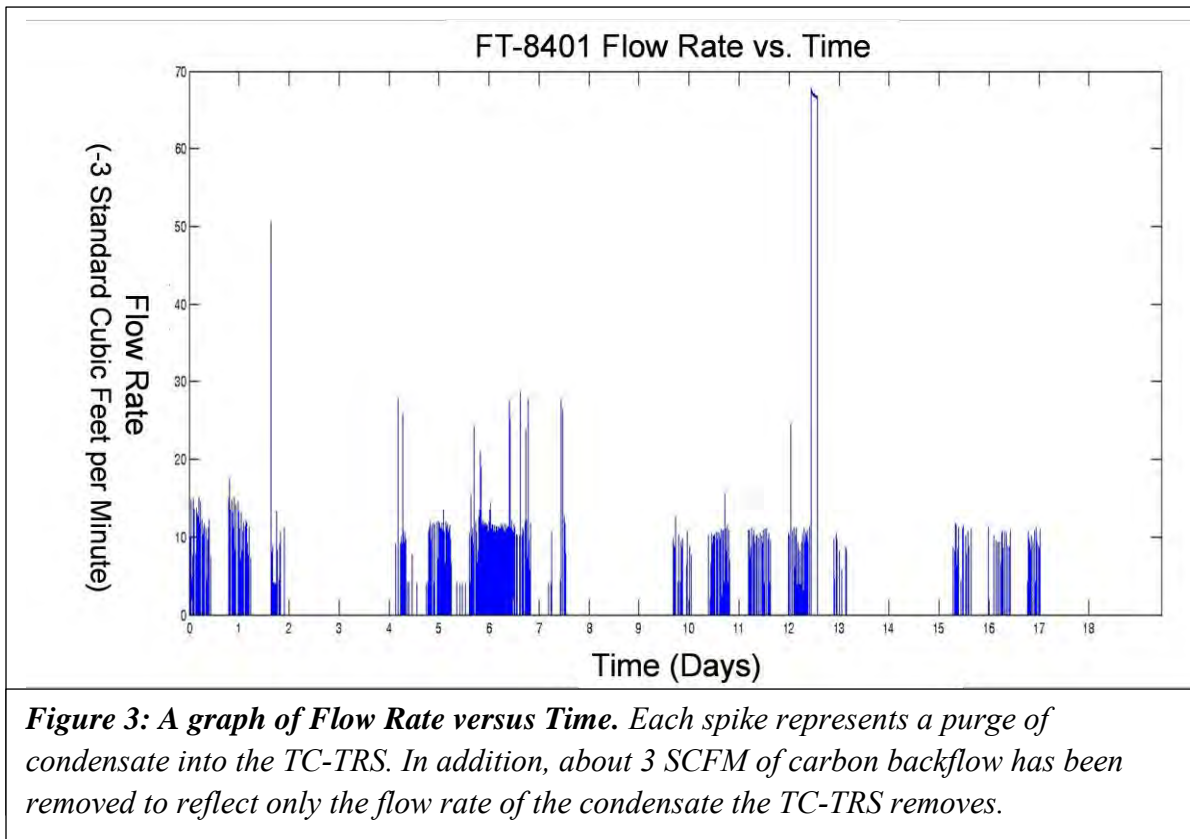


Figure 3 represents the flow rate over a full adsorption interval for one getter bed. The randomness of these points indicates that the processes within OMEGA that contribute to flow into the TC-TRS were not predictable. Since the flow rate, dew point, pressure, and temperature sensors refresh multiple times every minute, each day yields thousands of data points. TC-TRS files that were archived were reconfigured as CSV, or Comma Separated Variable files. Each file contained the identification of the specific sensor, and the raw data measured.

Initially, the dew point sensor data was used to calculate the condensate based on equations 2-4 since this was assumed to be the most accurate method. Since the measured condensate removed from each archived data set was known, the accuracy of the method could

be directly assessed. Unfortunately, it became clear that a large error was produced using the dew point sensor data. The calculations were not close to the archived removed condensate data. It is believed that this error is the result of the dew point sensor being positioned away from the flow-rate sensor, so that the measured dew point is not that of the actual incoming flow. In the future, a dew point sensor placed in the incoming flow would provide an accurate reading.

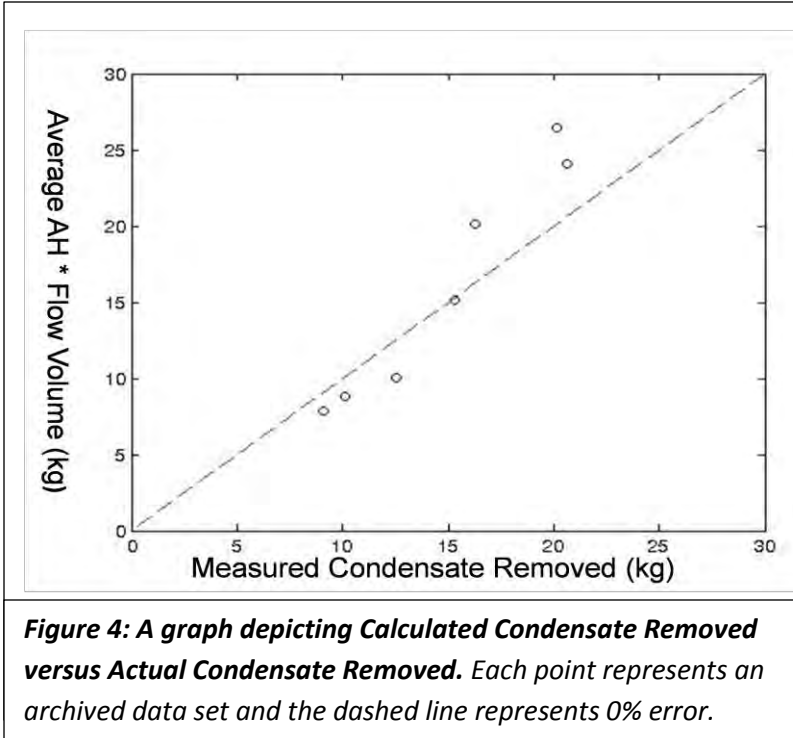
5. Improved Method

Since a dew point sensor was not available that could relay accurate information on the incoming airflow, an alternate method was pursued toward calculating the incoming absolute humidity. The current approach is based on calculating an average absolute humidity for the incoming air flow utilizing archived data. As stated earlier in equation 4, the total condensate equals the product of each individual flow rate and each individual absolute humidity times the sample interval. An average absolute humidity can then be calculated for each archived data set using equation 5.

$$\text{Average AH} \left(\frac{g}{m^3} \right) = \frac{\text{Condensate Total}(g)}{\sum_{n=1}^k (\text{Flow Rate}_n) * \Delta t_n \text{ (min)'}} \quad (5)$$

Each archived getter bed regeneration average absolute humidity was calculated. By finding the mean of this set, an overall average absolute humidity of 12.5 g/m³ was determined.

Using this average absolute humidity, the archived data sets were used once more. Using the flow rate data from these sets in [Figure 4](#), the calculated mass of condensate removed was plotted against the measured condensate removed. Overall, the data points lie close to the dashed line, which represents 0% error. The values



on some time intervals were overestimated or underestimated up to 30% deviation from the actual condensate removed, [Figure 4](#) indicates that using the average absolute humidity can provide a good estimate of the total condensate in the getter bed at any given time to within less than 30% deviation.

6. Conclusion

With the current code, the condensate removed can be calculated to within 30%. This will help workers avoid regenerating the getter beds too early, and can provide a warning when the bed is filling quicker than expected. In the future, a dew point sensor placed in the flow of incoming TC-TRS air has the potential to provide greater accuracy and become a great improvement to the efficiency of the TC-TRS operations at LLE.

7. References

1. OMEGA Target Chamber Tritium Removal System (TC-TRS), UR/LLE drawing number E-TR-I-02, Rev. m, 19 October,2011.
2. MATLAB^R, version 7.5.0.342(R2007b), The Mathworks,Inc., 3 Apple Hill Dr., Natick, MA 01760 USA
3. Consultation with Powell, L., Bittle, W., Janezic, R., Brumbaugh, M., University of Rochester, Laboratory for Laser Energetics.
4. Vaisala, “Humditiy Conversion Formulas”, Vaisala Oyj, Helsinki Finland, 2012

8. Acknowledgements

I would like to thank all staff at the LLE and the University of Rochester for giving me this opportunity to work over the summer. It was truly a once in a lifetime chance to experience the laser lab from my perspective. I would like to thank Mr. Bittle and Dr. Craxton for mentoring me through this entire internship and leading me in the right direction. Finally, I would like to thank my newfound friends, my fellow interns, who made this entire journey very enjoyable and memorable for me.

The Dependence of Plasma Ionization Equilibrium on Electron and Radiation Temperatures

Julia L. Tucker

Brighton High School
Rochester, NY

Advisor: Dr. Reuben Epstein

February 26, 2013

Laboratory for Laser Energetics
University of Rochester
Rochester, NY

Abstract

The atomic-physics radiation-transport simulation program PrismSpect [Prism Computational Sciences, Inc., Madison; WI., J. J. MacFarlane, I. E. Golovkin, P. Wang, P. R. Woodruff, and N. A. Pereyra, *High Energy Density Phys.* **3**, 181 (2007)] has been used to calculate the ionization state of germanium and silicon additives under conditions expected in plastic ablator shells imploded by indirect drive [J. D. Lindl, *et al.*, *Phys. Plasmas* **11**, 339 (2004)] on the National Ignition Facility (NIF) [G. H. Miller, *et al.*, *Opt. Eng.* **43**, 2841 (2004)]. The ionization equilibrium of the shell dopants may be altered by external radiation emitted by the hohlraum wall during the implosion and by the compressed deuterium-tritium (DT) core during ignition [S. P. Regan, R. Epstein, *et al.* *Phys. Plasmas* **19**, 056307 (2012)]. PrismSpect allows the user to vary the plasma conditions, the plasma composition, and the external radiation temperature and to view the spectra, mean charge, and fractional ionization species populations produced. A radiation-modified version of the Saha equation has been numerically programmed in Matlab [MATLAB version 7.10.0, Natick, Massachusetts: The MathWorks Inc., 2010] to provide an additional view of the effects of radiation on the ionization state of the shell additives. The PrismSpect and radiation-modified Saha results show that a radiation temperature around 300 eV, which is characteristic of the radiation emitted by a hohlraum, does not noticeably affect the ionization for electron temperatures above about 500 eV, and radiation emitted by a DT core does not substantially affect the ionization equilibria.

Introduction

Fusion occurs when intense heat and pressure are applied to an appropriately designed spherical target, causing the target to implode. When a target implodes, the outer portion of the target gives off energy and compresses the rest of the target inward. The compressed components of the target turn into plasma, fuse, and emit energy. This heat and pressure is applied through the use of many laser beams, all hitting the target at once from different angles.¹

There are two ways to implode a target: through direct-drive fusion and indirect-drive fusion. In direct-drive fusion, the lasers come in from all directions and directly hit the target to cause it to implode.² In indirect-drive fusion, the target is placed in a hollow gold cylinder called a hohlraum. The lasers enter through the open ends of the hohlraum and hit the inner walls of the cylinder. X rays are then radiated from the walls and heat the target. The targets are composed of a fuel mixture of deuterium and tritium (DT) gases, which are isotopes of hydrogen. The outermost layer of the gases is frozen, making the target “cryogenic”, and is covered in a plastic shell.

Target shells used in both direct-drive and indirect-drive fusion experiments can be doped with a concentration by atom of up to about 1% silicon (Si) or germanium (Ge).³ A Si shell dopant heats the shell by absorbing radiation from the ablation region, or the region that first gives off energy after being heated by the lasers. This radiation expands the shell and decreases its density, making the target more stable during implosion. Both Si and Ge dopants help protect the DT ice layer from being preheated by x rays emitted by the hohlraum in indirect-drive experiments on the National Ignition Facility (NIF).⁴ Hohlräume emit x-ray radiation with a radiation temperature of up to 300 eV, which could affect the ionization of the dopants when they mix with the hot, compressed DT core. The imploded core also emits radiation,

approximated here by a modified Planck spectrum with characteristic spectral and radiation temperatures. Radiation from either a hohlraum or a DT core can alter the ionization equilibrium of the shell dopant, which would then affect various properties of the plasma, such as its thermal conductivity, equation of state, and optical properties.

1. PrismSpect

PrismSpect⁵ is an atomic-physics radiation-transport program used to simulate the atomic level populations and radiative emission of plasmas over a range of controllable parameters, including temperature, density, and the radiation environment. After all the necessary information, such as target composition and size, has been entered, the program produces the resulting spectra, ionization, and line intensities. These results show the effect of radiation on the ionization. The overall mean charge, the electron density, the mean charge of each element in the plasma, and the ionization species fractions of each element are obtained. PrismSpect calculations are based on a detailed accounting of atomic states, allowing the user to choose which atomic states and configuration detail levels should be included. The calculations take into account a multitude of electron-electron and electron-photon interactions, such as collisional ionization, collisional (or 3 body) recombination, excitation, decay, photoionization, radiative recombination, stimulated emission, spontaneous emission, photoexcitation, and dielectronic recombination.^{6,7} The program includes the option to expose the target to an external radiation source.

PrismSpect also allows the user to choose among a few basic plasma configurations. Targets can be zero-width, planar, or spherical, and external radiation, if included, can be one-sided or two-sided. Electron temperature and mass density can be specified. The ability to control the

composition and configuration of the plasma and the atomic model through the user interface (Fig. 1) provides for a wide variety of simulations. The atomic kinetic model can be local thermodynamic equilibrium (LTE), or non-LTE. In LTE, all temperatures, such as radiation temperature and electron temperature, are equal, and conversely, non-LTE encompasses everything else. When a target is in non-LTE, where it is not exposed to any external radiation, and where all the self-emitted radiation escapes freely, the target is in collisional-radiative equilibrium (CRE).

2. Plasma Properties

When a target is in non-LTE and exposed to external radiation, the ionization equilibrium of the shell dopant generally differs from when it is in LTE. Mean charge is the best single-parameter representation of the ionization state. It takes into account all of the various fractional ionization species. When the radiation temperature equals the electron temperature of the plasma, thermal equilibrium is restored. LTE conditions prevail, and the mean charge and fractional ionization species populations of the non-LTE target exposed to radiation become equal to those of an LTE target, as seen in PrismSpect results plotted in Fig. 2.

Optical depth, τ_ν , is a measure of the opacity of an object to light of frequency ν propagating along a given path. The intensity of light is diminished as it passes through an object along this path by the factor of $e^{-\tau_\nu}$. For a uniform sphere of radius R , the optical depth can be expressed as the product of the mass density, ρ , target radius, R , and the mass-absorption coefficient, μ_ν , $\tau_\nu = \rho R \mu_\nu$. As an object increases in mass density or radius, it becomes more optically thick and reabsorbs more self-emitted radiation, and this causes LTE conditions to be restored. As the

matter becomes more in equilibrium with its own radiation, its emission spectrum more closely resembles a Planck spectrum, as given by Planck's Law,

$$B_\nu(T) = \frac{2h\nu^3}{c^2} \frac{1}{e^{h\nu/kT} - 1}, \quad (1)$$

where $B_\nu(T)$ is the emitted specific intensity, h is Planck's constant, ν is the photon frequency, c is the speed of light, k is Boltzmann's constant, and T is the plasma temperature.⁶ The graphs in Fig. 3 show emission spectra in units of specific intensity, ergs per cm² per steradian per second per electron volt, for spherical targets at a temperature $T=100$ eV and at two areal densities, $\rho R = 0.001$ g/cm² and 0.1 g/cm². The blue line in each is the emission spectrum of the plasma, and the red line shows the Planck spectrum at $T=100$ eV. At the higher density, the target is optically thick over nearly the entire spectrum. This produces an LTE radiative equilibrium where the specific intensity of the target emission (blue curve) is equal to the Planck spectrum (red curve) given by Eq. (1).

3. Hohlraum Radiation

3.1 Modified Saha Equation

The Saha equation⁸ gives the ratio of the densities of two successive ionization state populations, n_1 and n_2 , in a plasma in LTE and is dependent on electron temperature, T_e , the electron density, n_e , and the ionization energy, χ . It is

$$\left(\frac{n_2}{n_1}\right)_{LTE} = \frac{1}{4\pi^{3/2} (n_e a_0^3)} \frac{g_2}{g_1} \left(\frac{kT_e}{\chi_H}\right)^{3/2} e^{-\chi/kT_e}, \quad (2)$$

where a_0 is the Bohr radius, g_1 and g_2 are the statistical weights of the two successive ionization states, and χ_H is the hydrogen ground-state ionization energy. The Saha equation was modified in the following way to include the non-LTE effects of photoionization and stimulated radiative recombination by external radiation.⁹

In steady state, the non-LTE ionization equilibrium of two ionization species occurs when the total ionization and recombination rates are in balance. This can be expressed as

$$n_1 [C_{12}(T_e, n_e) + R_{12}(T_e, T_R)] = n_2 [C_{21}(T_e, n_e) + R_{21}(T_e, T_R, n_e) + A_{21}(T_e, n_e)], \quad (3)$$

where $C_{12}(T_e, n_e)$ and $C_{21}(T_e, n_e)$ are the electron-collisional ionization and recombination rates, respectively, $R_{12}(T_e, T_R)$ and $R_{21}(T_e, T_R, n_e)$ are the photoionization and stimulated recombination rates, and $A_{21}(T_e, n_e)$ is the radiative recombination rate. Photoionization and stimulated recombination are driven by the ambient radiation field, which is assumed to be the Planck spectrum at a radiation temperature T_R given by Eq. (1). The collisional ionization and recombination processes are detailed-balance inverses of each other, so, in the absence of all radiative processes, and in steady state, they will produce the same LTE population ratio given by the Saha equation Eq. (2),

$$\left(\frac{n_2}{n_1}\right)_{LTE} = \left(\frac{C_{12}(T_e, n_e)}{C_{21}(T_e, n_e)}\right). \quad (4)$$

Using this expression, the non-LTE (NLTE) radiative equilibrium expression, Eq. (3), can be written as a correction to the LTE Saha result as,

$$\frac{(n_2/n_1)_{NLTE}}{(n_2/n_1)_{LTE}} = \frac{1 + R_{12}(T_e, T_R)/C_{12}(T_e, n_e)}{1 + [R_{21}(T_e, T_R, n_e) + A_{21}(T_e, n_e)]/C_{21}(T_e, n_e)}. \quad (5)$$

This two-species model neglects excited states and ionization species, other than the two considered, and autoionization and dielectronic recombination¹⁰ are neglected. Consequently, it

is not an approximation that can be relied on for quantitative calculations. It is useful for identifying ranges of conditions where radiation can be an important ionization effect, and it can be corroborated at specific temperatures and densities with PrismSpect⁵, which does not make these approximations.

The semi-classical collisional ionization rate is given by

$$C_{12}(T_e, n_e) = n_e 8a_0^2 \sqrt{\frac{2\pi\chi_H^4}{m_e (kT_e)^3}} \left[\frac{kT_e}{\chi} e^{-\chi/kT_e} - E_i\left(\frac{kT_e}{\chi}\right) \right], \quad (6)$$

where $E_i\left(\frac{kT_e}{\chi}\right)$ is the exponential integral $E_i(x) = \int_x^\infty e^{-t} \frac{dt}{t}$, and m_e is the electron mass. The collisional recombination rate $C_{21}(T_e, n_e)$ is obtained from Eqs. (2), (4), and (6). The radiative transition rates can be written as photon-frequency integrals over the ambient isotropic radiation specific intensity $I(\nu)$ and the corresponding frequency-dependent Einstein coefficients:^{7,8,10} $A_{21}(\nu)$ for spontaneous emission, $B_{21}(\nu)$ for stimulated emission, and $B_{12}(\nu)$ for photoionization,

$$A_{12}(T_e, n_e) = \int_0^\infty A_{12}(\nu) d\nu, \quad (7)$$

$$R_{12}(T_e, n_e) = \int_0^\infty B_{12}(\nu) I(\nu) d\nu, \quad (8)$$

and

$$R_{21}(T_e, n_e) = \int_0^\infty B_{21}(\nu) I(\nu) d\nu. \quad (9)$$

Under LTE conditions, where $T_R = T_e$, so that $I(\nu) = B_\nu(T_e)$ and the species populations assume their LTE values, the Einstein coefficients must be consistent with the radiative detailed balance between photoionization and its reverse processes, spontaneous and stimulated radiative recombination. This condition is expressed as¹⁰

$$n_1^{LTE} B_{12}(\nu) B_\nu(T_e) = n_2^{LTE} [A_{21}(\nu) + B_{21}(\nu) B_\nu(T_e)] . \quad (10)$$

With this expression and Eq. (1), all three Einstein coefficients can be obtained from one. We choose to write the photoionization Einstein coefficient as

$$\frac{h\nu}{4\pi} B_{12}(\nu) = \frac{64\pi}{3\sqrt{3}} \alpha a_0^2 \frac{P}{z^2} \left(\frac{\chi}{h\nu} \right)^3 \quad (11)$$

in terms of the Kramers photoionization cross section,

$$\sigma_K(\nu) = \begin{cases} \frac{64\pi}{3\sqrt{3}} \alpha a_0^2 \frac{P}{z^2} \left(\frac{\chi}{h\nu} \right)^3 ; h\nu \geq \chi \\ 0 ; h\nu < \chi \end{cases} , \quad (12)$$

where $\alpha \cong 1/137$ is the fine-structure constant.⁸ The stimulated recombination emission coefficient

$$\frac{\chi}{4\pi} B_{21}(\nu) = \frac{64\pi}{3\sqrt{3}} \alpha a_0^2 \frac{P}{z^2} \left(\frac{\chi}{h\nu} \right)^4 \left(\frac{n_1}{n_2} \right)_{LTE} e^{-h\nu/kT_e} \quad (13)$$

and the spontaneous radiative recombination emission coefficient

$$\frac{c^2}{8\pi} A_{21}(\nu) = \frac{64\pi}{3\sqrt{3}} \alpha a_0^2 \frac{P}{z^2} \frac{\chi^3}{h^3 \nu} \left(\frac{n_1}{n_2} \right)_{LTE} e^{-h\nu/kT_e} \quad (14)$$

are identified using Eqs. (1), (10), and (11). Note that the expressions in Eqs. (13) and (14) are zero for $h\nu < \chi$, following Eq. (12). Consequently, the integration limits in Eqs. (7)-(9) become $\nu = \chi/h$ and $\nu \geq 0$.

Using Eqs. (1), (6)-(9), (11), (13), and (14), Eq. (5) can be evaluated, simplified, and expressed in the form

$$\frac{(n_2 / n_1)_{NLTE}}{(n_2 / n_1)_{LTE}} = \frac{1 + F(T_e, n_e) \int_{\frac{\chi}{h}}^{\infty} \frac{dv}{v} \frac{1}{(e^{\frac{hv}{kT_R}} - 1)}}{1 + F(T_e, n_e) \int_{\frac{\chi}{h}}^{\infty} \frac{dv}{v} \frac{e^{\frac{hv(\frac{1}{kT_R} - \frac{1}{kT_e})}}}{(e^{\frac{hv}{kT_R}} - 1)}}, \quad (15)$$

where

$$F(T_e, n_e) = \frac{\frac{64\pi}{3} \sqrt{\frac{\pi}{3}} \left(\frac{kT_e}{\chi}\right)^{3/2} \left(\frac{\chi}{ch}\right)^3 \frac{z}{n_e p^2}}{\frac{kT_e}{\chi} e^{-\chi/kT_e} - E_i \left(\frac{kT_e}{\chi}\right)}. \quad (16)$$

In the modified equation, the mean charge, z , and the principal quantum number, p , are variables that affect the ratio, in addition to the radiation temperature, T_R . The modified Saha equation continues to show a strong dependence on electron temperature and electron density and includes a radiative ionization and stimulated recombination correction factor applied to a collisional ionization and recombination ratio. The correction includes the function $F(T_e, n_e)$ and integrals over the Planck spectrum and absorption cross-section. The CRE value of n_2/n_1 is obtained for $T_R = 0$. When $T_R = T_e$, LTE conditions are restored, as confirmed by the PrismSpect results, and the radiation-modified Saha ratio given by Eq. (15) is equal to one. The T_R value that doubles the $T_R = 0$ value of the ratio given by Eq. (15) is taken somewhat arbitrarily as corresponding to the level of radiation required to significantly affect the ionization equilibrium. Doubling this ratio of successive species populations raises the average charge of that element, z_{avg} , by less than half a unit of charge. This is easily seen for T_e, n_e conditions where $n_1 = n_2$ at $T_R = 0$, for example, where $z_{avg} = (z_1 + z_2)/2$. Raising T_R from zero enough to double n_2/n_1

raises n_2 and lowers n_1 , bringing n_2 closer to, but not beyond its peak value, where $z_{avg} \leq z_2$.

Since $z_2 = z_1 + 1$, the change from $z_{avg} = (z_1 + z_2) / 2$ to $z_{avg} \leq z_2$ amounts to a change

$$\Delta z_{avg} \leq 1/2.$$

3.2 Analytical Results

A program was created in MATLAB¹¹ to evaluate the Saha equation correction given by Eq. (15). Fig. 4 shows results from this program. The graphs represent temperature space as a $T_e - T_R$ plane. To indicate the areas of significant radiation effects for Si and Ge, each graph has a red curve that shows where the Saha correction ratio doubles the Saha population ratio given by Eq. (2). The blue shaded area below the curve represents a radiation effect that is too small to be significant. The pink shaded area above the red curve represents where the radiation temperature will alter the ionization equilibrium significantly. The change from insignificant to significant radiation is simply a matter of our use of the doubled population ratio as a criterion to define where the effects of the radiation have become significant. Actually, the radiation effects change gradually as T_R increases continuously in moving from below to above this curve. Using this criterion, then, Fig. 4 shows that a hohlraum radiation temperature of around 300 eV does not significantly change the ionization equilibrium for electron temperatures above about 500 eV.

3.3 PrismSpect Results

PrismSpect was used to calculate mean charges of Si and Ge dopants for a range of radiation temperatures at various electron temperatures (Fig. 5). One can see that the mean charge of each dopant is quite static for a relatively high electron temperature of 2000 eV, but when the electron

temperature is lowered to 500 eV, the mean charge changes more noticeably at higher T_R . For both electron temperatures, the range of radiation temperatures characteristic of hohlraum interiors, up to 300 eV, does not produce a significant photoionization effect on the mean charge ($\Delta z \leq 1/2$), which is consistent with the conclusion drawn from the modified Saha results in Fig. 4. For the lower electron temperature, the radiation temperature must be at least ~ 400 eV to increase the mean charge by one charge unit, which can be considered significant, and the radiation temperature must be above the range of values shown in these graphs to have a significant effect at higher electron temperatures.

4. OMEGA Implosion Radiation

As a target implodes, its core radiates, and the radiation absorbed by the shell dopant may affect the ionization of the shell dopant. A simulation⁹ of the direct-drive OMEGA shot #62205 using the one-dimensional hydrodynamics code LILAC¹² was used to calculate the emission of the core of a representative cryogenic implosion. This emission takes place 4.2 ns after the onset of the laser pulse on the target, which has imploded at this time to a DT sphere with a radius of 25 microns, an areal density of 75 mg/cm^2 , and an electron temperature of 2000 eV. The emission spectrum is plotted as the “Simulated Intensity” in Fig. 6, and can be used as external radiation input in PrismSpect in order to view the effects of core radiation on the dopant. This external radiation can be represented in PrismSpect most generally by a two-temperature specific intensity of the form

$$I_\nu = \left(\frac{T_R}{T_S} \right)^4 B_\nu(T_S) \quad . \quad (17)$$

This uses the radiation temperature T_R and a separate spectral temperature T_S to give a specific intensity with the spectral form of a Planck spectrum of temperature T_S and a spectral integral equal to that of a Planck spectrum of temperature T_R . A spectral temperature of 330 eV and a radiation temperature of 600 eV created a (purple) curve that fit the DT emission best. The Planck spectrum and its two-temperature generalization provide a well-understood and convenient parameterized representation of spectral intensity in studying the effects of externally applied radiation. The correct T_R and T_S were found by minimizing the spectral integral of the square of the difference between the simulated spectrum and the spectrum created using Eq. (17). This created the curve that most closely followed the simulated spectrum for photon energies around its peak intensity.

At low photon energy, the emission spectrum of the DT core in Fig. 6 follows a Planck spectrum of temperature equal to the core temperature $T = 2000$ eV, represented by the blue curve, as is expected, since the core is optically thick at the lowest photon energies. At higher photon energy, the emission spectrum, represented by the green curve, could be modeled by the equation

$$I_\nu = Ae^{-h\nu/kT} \quad , \quad (18)$$

with an upgraded version of PrismSpect. In Eq. (18), the intensity depends on a constant, A, the photon energy, ν , and the temperature, T. The green curve shows that this spectrum for $A = 4 \times 10^{19}$ and the same core temperature $T = 2000$ eV fits the DT emission better for high photon energies than the modified Planck spectrum presented by Eq. (17).

The radiation temperature of 600 eV, with a corresponding spectral temperature of 330 eV, was tested in PrismSpect to see how core radiation at these temperatures affect the mean charge.

Figure 7 shows the dependence of Si mean charge on electron temperature for three mass densities. It is clear in Figure 7 that the core radiation has a stronger effect on the mean charge for the lowest mass density. As the mass density increases, the mean charge of an irradiated plasma becomes almost identical to that of a plasma that is not exposed to radiation for the entire range of electron temperatures shown. This can be explained by the fact that, as density increases, ionization by electron collisions becomes more frequent than photoionization caused by radiation, thus reducing the effect of external radiation on the ionization. The core radiation, therefore, is unlikely to significantly alter the ionization of the plasma.

5. Conclusion

The program PrismSpect was used to simulate the effects of external radiation emitted by a hohlraum and a target core on the ionization equilibria of Si and Ge dopants. A program in MATLAB was also used to view the effects of radiation via a modified Saha equation that takes radiation temperature into account. Though both hohlraum radiation and core radiation have the potential to alter the ionization equilibrium of shell dopants, neither were found to change the equilibrium a significant amount under conditions of interest.

References:

1. Lois H. Gresh, Robert L. McCrory, and John M. Soures, *Inertial Confinement Fusion: An Introduction*, Laboratory for Laser Energetics: Rochester, NY, 2009.
2. J. D. Lindl, *et al.*, Phys. Plasmas **11**, 339 (2004).
3. S. P. Regan, R. Epstein, *et al.* Phys. Plasmas **19**, 056307 (2012).
4. G. H. Miller, *et al.*, Opt. Eng. **43**, 2841 (2004).
5. Prism Computational Sciences, Inc., Madison, WI.; J. J. MacFarlane, I. E. Golovkin, P. Wang, P. R. Woodruff, and N. A. Pereyra, High Energy Density Phys. **3**, 181 (2007).
6. L. Motz and A. Duveen, *Essentials of Physics* (Wadsworth, New York, 1967).
7. Y. B. Zel'dovich, Y. P. Raizer, W. D. Hayes, and R. F. Probstein, *Physics of Shock Waves and High-Temperature Hydrodynamic Phenomena* (Academic Press, New York, 1966) Vol. I.
8. G. C. Pomraning, *The Equations of Radiation Hydrodynamics* (Pergamon Press, New York, 1973).
9. R. Epstein, LLE, private communications (2012).
10. D. Salzman and A. Krumbein, J. Appl. Phys. **49**, 3229 (1978).
11. MATLAB version 7.10.0, Natick, Massachusetts: The MathWorks Inc., 2010.
12. J. A. Delettrez, R. Epstein, M. C. Richardson, P. A. Jaanimagi, and B. L. Henke, Phys. Rev. A **36**, 3926 (1987).

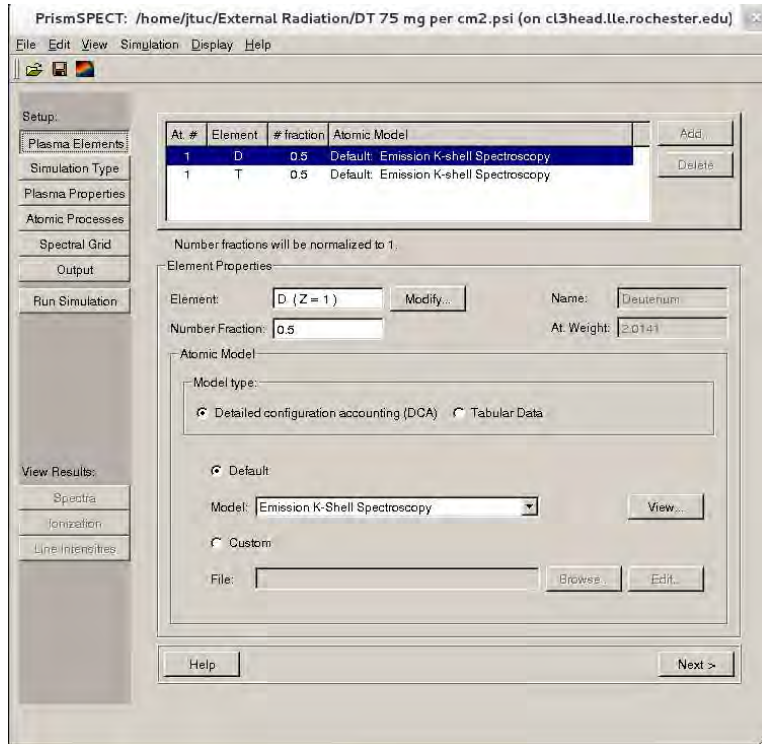


Figure 1: A screen-shot of the PrismSpect⁵ user interface shows the elemental composition of the plasma and lists further categories for specifying further conditions in the tabs on the left hand side.

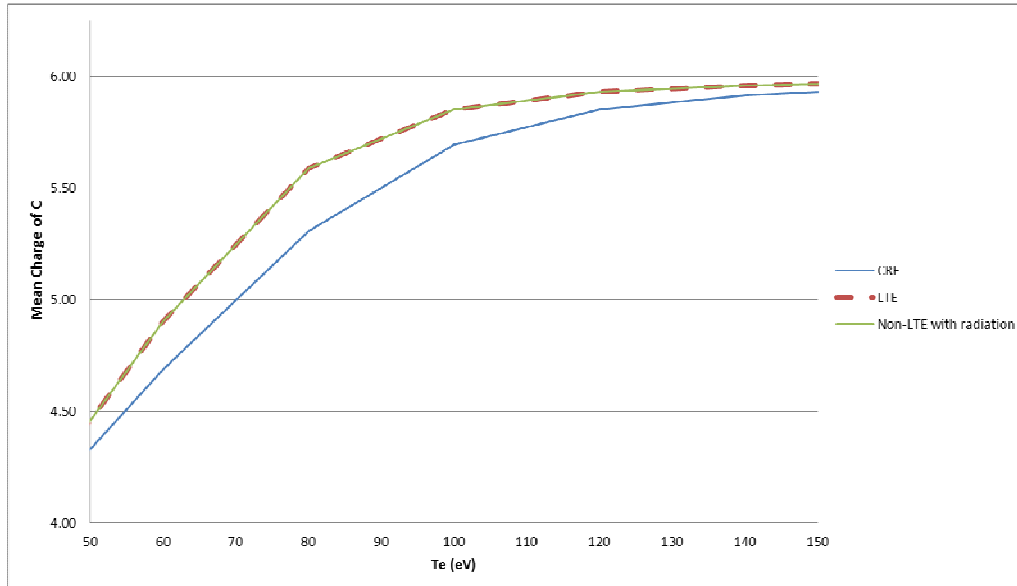
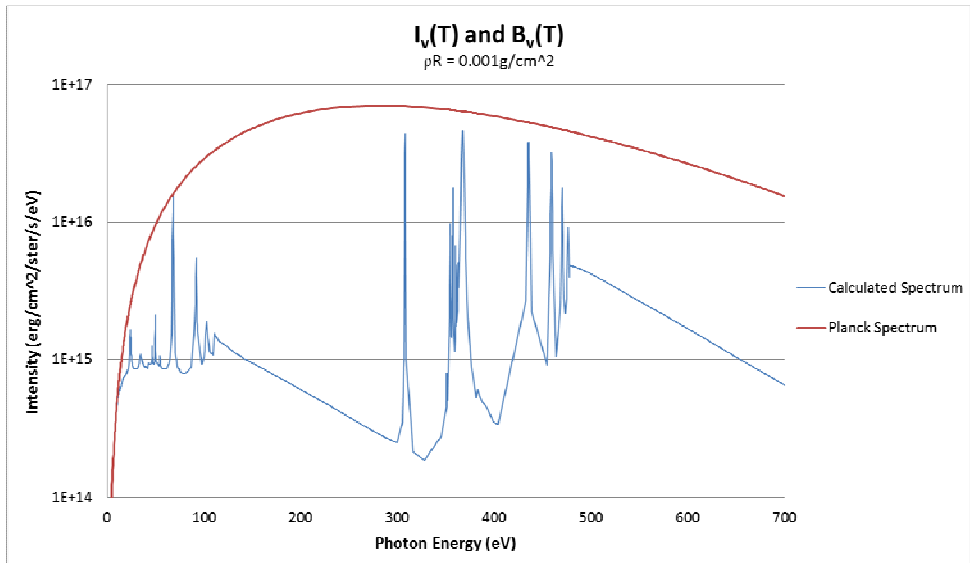
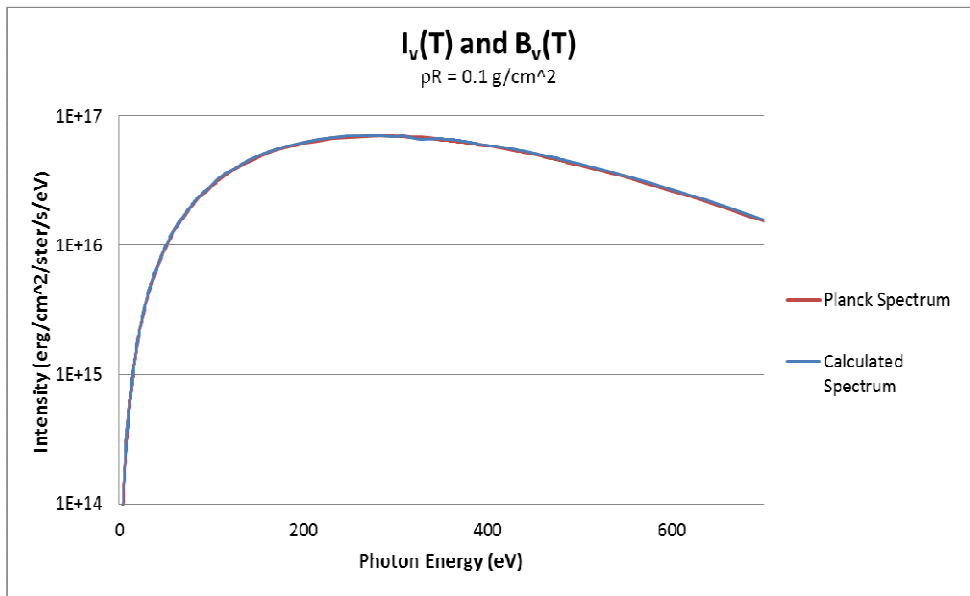


Figure 2: The effect of external radiation on the mean charge of carbon under target conditions in non-LTE with an electron density of $2.93 \times 10^{21} \text{ cm}^{-3}$. When radiation is applied that is the same temperature as the plasma temperature, the non-LTE curve exactly follows the LTE curve.



(a)



(b)

Figure 3: These two graphs show the emission spectra for a homogenous carbon sphere at a temperature of 100 eV. Graph (a) is for a target with an areal density of 0.001 g/cm^2 , while graph (b) has an areal density of 0.1 g/cm^2 . In graph (b), the two curves coincide completely so that only one may be visible.

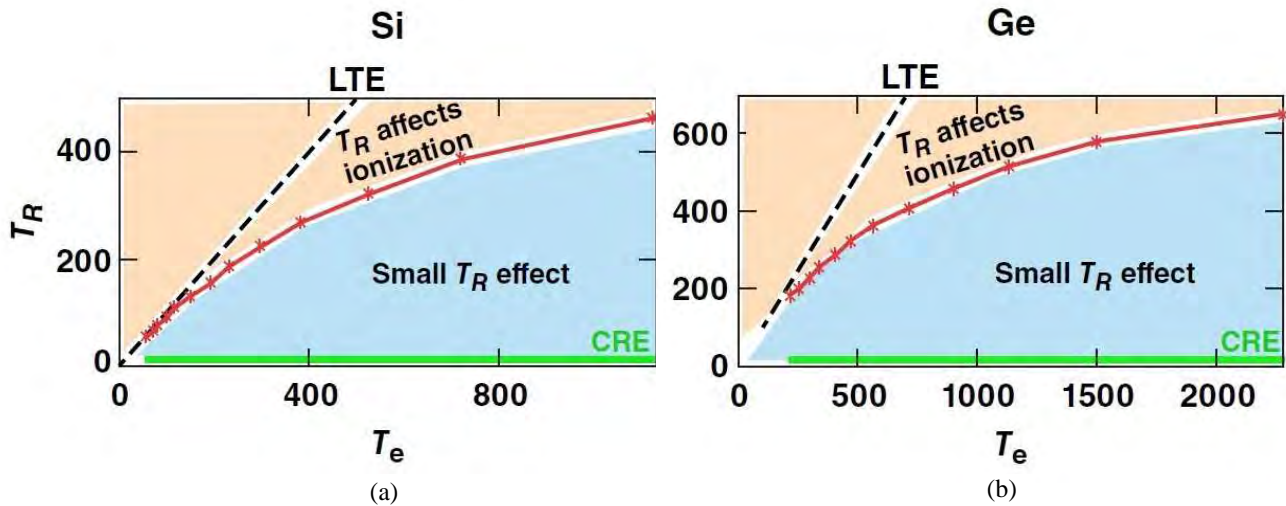


Figure 4: Regions where radiation either does or does not have a significant effect on the ionization state of a plasma for varying T_R and T_e . Plot (a) is for a Si plasma with an electron density of $1.3 \times 10^{23} \text{ cm}^{-3}$, and plot (b) is for a Ge plasma with an electron density of $1.2 \times 10^{23} \text{ cm}^{-3}$. The black line represents LTE conditions ($T_R = T_e$), the green line represents CRE conditions ($T_R = 0$), and the red curve represents where the Saha correction factor given by Eq. (15) doubles the ionization species population ratio given by the Saha equation, Eq. (2).

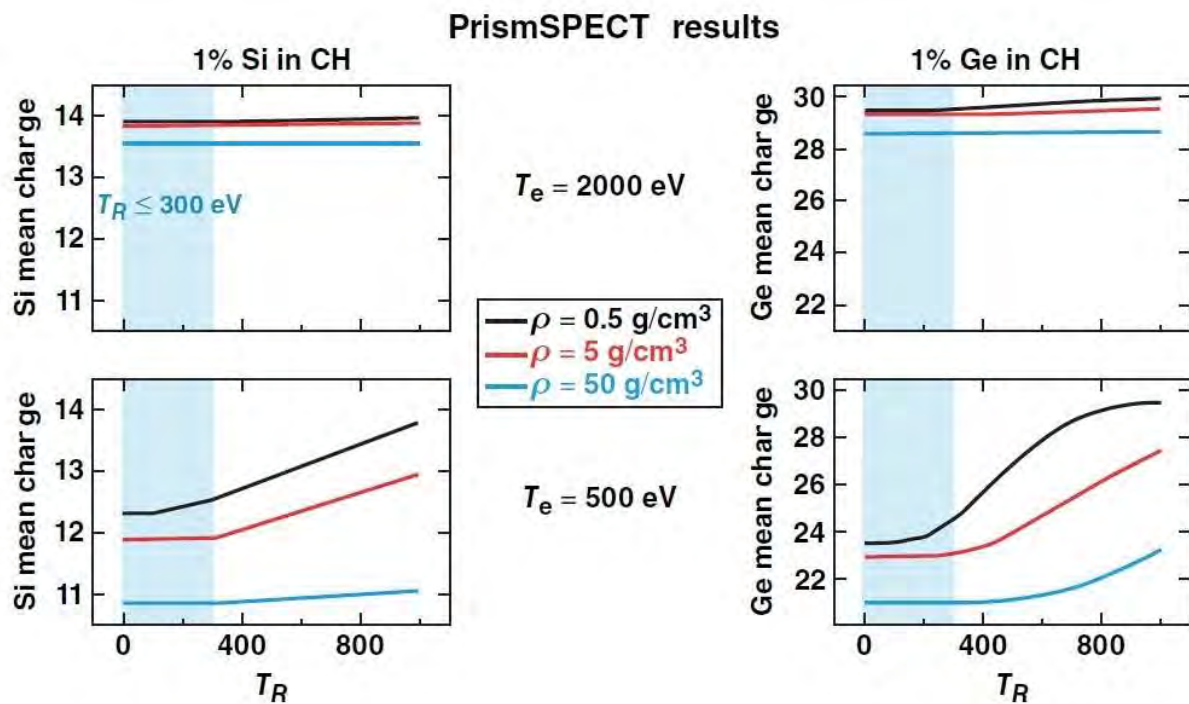


Figure 5: Dependence of the mean charge on radiation temperature for CH plasmas with a 1% Si or Ge dopant. The top set have an electron temperature of 2000 eV, and the lower set have an electron temperature of 500 eV. The different colored lines represent different mass densities.

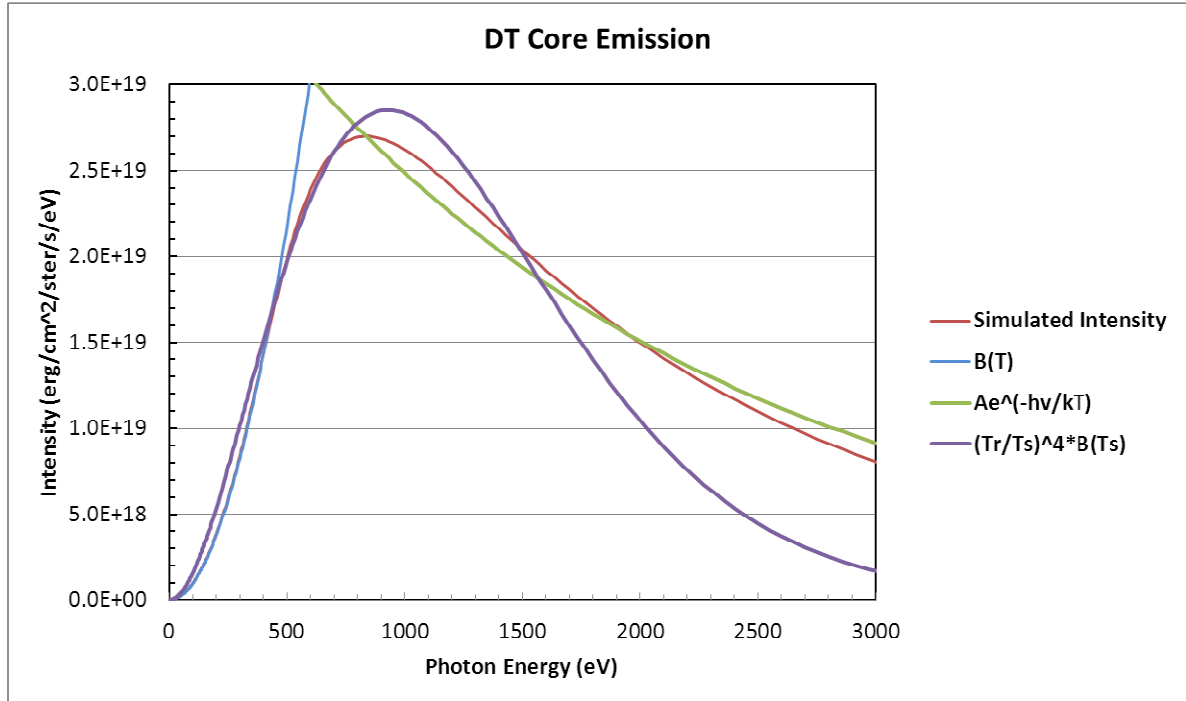


Figure 6: The red curve in this graph shows the emission of a DT core with mass areal density of 75 mg/cm^2 and core temperature $T = 2000 \text{ eV}$ at 4.2 ns into the implosion. The purple curve shows this spectrum as modeled by Eq. (17) with $T_S = 330 \text{ eV}$ and $T_R = 600 \text{ eV}$ and used as input to Spect3D. The blue curve shows a Planck spectrum at the core temperature, and the green curve shows the emission spectrum as modeled by Eq. (18) with $A = 4.0 \times 10^{19}$ and the same core temperature.

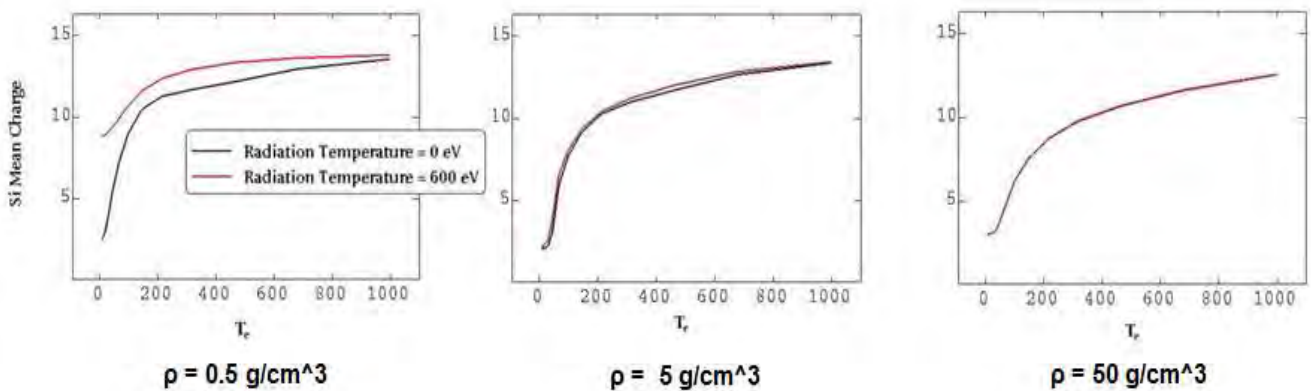


Figure 7: Mean charge of Si plasma dopant as a function of electron temperature T_e for three values of mass density ρ , with and without core radiation, as modeled by Eq. (17) with $T_S = 330 \text{ eV}$ and $T_R = 600 \text{ eV}$. The mean Si charge is strongly affected only at the lowest density.

*Electronic Analysis of Pulse Propagation
through an X-Ray Framing Camera*

Jack Valinsky

Brighton High School

Rochester, New York

Advisers: Dr. William Donaldson & Dr. Dustin Froula

Laboratory for Laser Energetics

University of Rochester

Rochester, New York

November 2012

1. Abstract

Voltage pulses sent through x-ray framing cameras (XRFC's) used on the Omega laser system act as shutters, creating rapid time-delayed snapshots of a target during implosion with sub-nanosecond resolution. The program TOAST (Transmission line Optimization And Studying Tool) was written to model the propagation of a voltage pulse through the micro-channel plate (MCP) of an x-ray framing camera, which was treated as a transmission line. The current produced by the x-rays hitting the MCP was found to affect the voltage pulse; the sensitivity of the framing camera is therefore dependent on the intensity of the x-rays illuminating the MCP. Voltage reflections occur due to the incident x-rays changing the impedance of the MCP, distorting the time resolution of the camera. Simulation of the velocity of the voltage pulse allows for a more accurate determination of the time between snapshots. TOAST allows for a potential method of correcting XRFC images for distortions that is more accurate than flat-fielding.

2. Introduction

Nuclear fusion is a potential source of clean, sustainable energy that is under research and development in the United States and other countries. Energy is produced in nuclear fusion reactions by a process where lighter atomic nuclei fuse together to form a heavier nucleus. One such facility that is investigating the processes underlying nuclear fusion is the Laboratory of Laser Energetics (LLE) at the University of Rochester. Inertial confinement fusion is studied at LLE with the 60-beam OMEGA laser system by heating and imploding cryogenic targets. The small spherical plastic targets are filled with DT gas, a mixture of deuterium and tritium (isotopes of hydrogen), and chilled to cryogenic temperatures to form a layer of DT ice inside the target shell [1].

While heated uniformly with lasers, the outer plastic shell ablates outward as the contents of the target are imploded. The implosion of the deuterium and tritium results in conditions of high pressure and temperature. As a result of the high temperatures, positively charged nuclei of deuterium and tritium are able to overcome their repulsion forces and fuse together to form a helium nucleus and a high energy neutron. These neutrons comprise most of the energy released by the fusion reaction. High pressure conditions guarantee that a large number of fusion reactions occurs before the target explodes. Breakeven is achieved when the energy released by the fusion reactions is greater than the energy input of the lasers. Once high enough energy gain is achieved, laser fusion can be used as a viable source of energy [1].

X-rays are produced during the implosion of the target, which lasts approximately one nanosecond. Imaging devices like streak cameras and x-ray framing cameras (XRFC's) utilize this x-ray radiation to monitor the deformation of the target as it implodes. Streak cameras have a

time resolution that can be as short as one picosecond, which is much smaller than that of XRFC's; however, they can only provide imaging in one dimension. This results in a great loss of information. The resolution of XRFC's is limited by their frame rate to about 40 picoseconds, but XRFC's produce two-dimensional images of the target during its implosion [2]. Uniform compression is essential for maximum energy output [1].

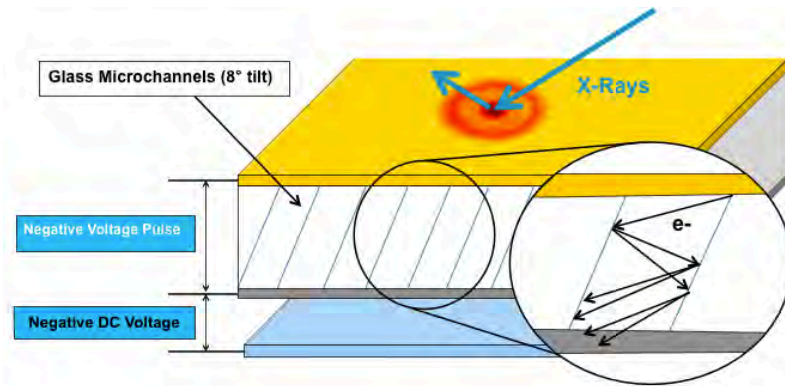


Fig. 1. Physical Diagram of an XRFC. An XRFC consists of an MCP placed between two metal electrodes and a phosphor screen underneath. A negative voltage pulse is applied to two metal electrodes (gold and silver) and is propagated through the MCP. Positive voltage is applied to the surface of the phosphor screen.

XRFC's consist of a doped-glass micro-channel plate (MCP) sandwiched between two metal electrodes (top gold, bottom silver) and a phosphor screen (Fig. 1). Incoming x-rays from the imploding target strike the top electrode and kick off electrons that hit a phosphor screen, producing light. Collecting this light to form an image can be achieved with a film pack or a CCD camera. A negative voltage pulse sent through the MCP acts as a shutter. When the pulse passes through a section of the MCP, an electric field is generated that accelerates electrons down the channels of the MCP.

Without the voltage pulse, few electrons reach the phosphor and only a dim image is produced. The channels of the MCP are at an 8° tilt. As an electron travels down through the MCP, it will strike the walls of a channel. With the added energy picked up by the electron from accelerating through the electric field, more electrons can be kicked off the wall of the channel when it hits. This causes an avalanche of electrons as each new electron picks up energy from the electric field, knocking off more electrons. The cycle repeats down the length of the channel.

Positive DC voltage is applied to the phosphor screen to pull electrons off of the bottom electrode to develop an image [2].

An XRFC may be designed to take one or multiple images. Multiple images may be obtained by projecting several x-ray images across the MCP. However, only where the voltage pulse is currently passing through (and thus causing a gain in electrons) is the image strong enough to be captured by film or a CCD camera [2].

XRFC images must undergo post-processing due to distortions introduced by the MCP. The current method of correcting framing images, known as flat-fielding, takes a data image and divides it by an image produced by a uniform x-ray exposure at the same intensity. This method makes the assumption that the relationship between x-ray intensity and the recorded signal of the XRFC is linear. However, at a certain threshold intensity of x-rays one may get a 10% reduction in signal compared with the linear assumption; at higher x-ray intensities this would be more pronounced.

In this work, mathematical formulas and a computer program (TOAST) were developed to simulate the propagation of a voltage pulse through an XRFC. The simulation calculates the changes in voltage and current over an adjustable number of nodes across the MCP of an XRFC as a voltage propagates in the presence of a distribution of x-rays. Results from the simulation indicate that the relationship between x-ray intensity and the signal received by the camera is in fact nonlinear, thus showing that the underlying assumption in flat-fielding XRFC images is incorrect. The computer program allows for a potentially more accurate determination of the speed of the pulse through the MCP as well as correction of distortions in the images introduced by the camera itself.

3. Mathematical Model

3.1 The XRFC

For the purpose of simplicity, the model constructed in this project was one-dimensional, but it is sufficient to provide useful insight on the complex interactions that occur between the camera, incident x-rays, and propagated pulse. A transmission line was used to model an XRFC [3].

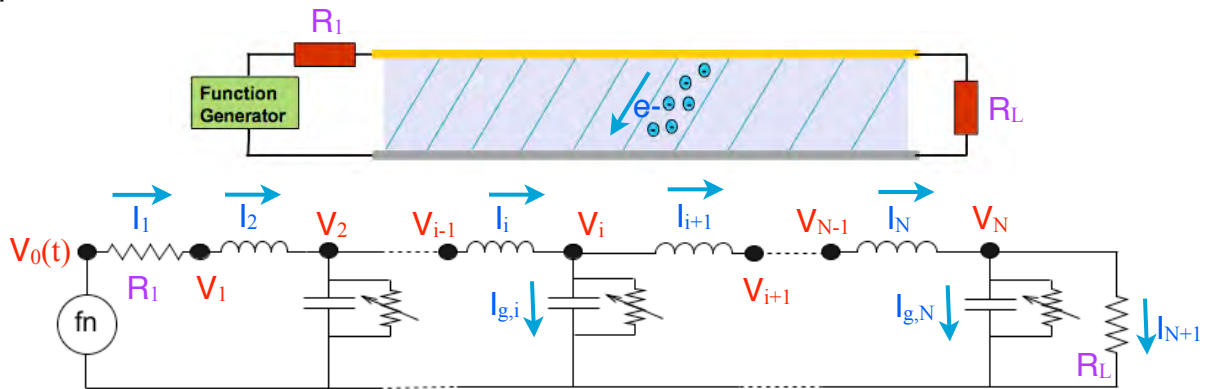


Fig. 2. Physical and Circuit Diagrams of an MCP.

There are two terminal resistances at the beginning and end of the MCP. As x-rays strike the MCP, a current is produced that is modeled by a variable resistance. Note that the circuit may have any number of nodes.

Parallel sheets of metal will produce a capacitance in the presence of electric current. The sheets of metal will have an inductance in the presence of an alternating current source (AC), such as a pulse. As shown in Fig. 2, the capacitances and inductances of the metal electrodes are modeled as capacitor and inductor pairs connected in a series/parallel combination [3]. Incident x-rays strip electrons from the surface of the top metal electrode and the electrons are then accelerated down the channels of the MCP by the electric field produced from the negative voltage pulse. This produces currents in the MCP as modeled by variable resistances. A transmission line is a circuit that allows for the propagation of a pulse. The MCP of the XRFC functions as a modified transmission line with the added reduction in current induced by an x-ray

source. Terminal resistances shown in the diagram are crucial, as shown later, for preventing large voltage reflections at the ends of the MCP.

For this model, equations relating voltage and current of the discrete components for an AC circuit are necessary to simulate the propagation of the voltage pulse [3]. The equations for a resistor, capacitor, and inductor are given as follows:

$$V=IR \quad (1)$$

$$V=\frac{Q}{C}=\frac{\int Idt}{C} \quad (2)$$

$$V=L\frac{dI}{dt} \quad (3)$$

where V is voltage, I is current, R is resistance, Q is charge, C is capacitance, L is inductance, and t is time [3]. Solving equation 1 in terms of I yields:

$$I=\frac{V}{R} \quad (4)$$

For equation 2, one must first take the derivative of both sides,

$$\frac{dV}{dt}=\frac{I}{C} \quad (5)$$

linearizing the derivative, then solving for I gives the form:

$$I=\frac{V-V'}{\Delta t}C \quad (6)$$

Dividing L from both sides of equation 3 and then integrating with respect to t gives the form of:

$$\int_{t'}^t \frac{V}{L} dt = \int_{t'}^t dI = I - I' \quad (7)$$

Using a trapezoid approximation for the integral and rearranging terms gives the equation:

$$I = \frac{I}{L} \left(\frac{V+V'}{2} \right) \Delta t + I' \quad (8)$$

Note that the substitutions $dI=\Delta I=(I-I')$ and $dt=\Delta t$ were made. All prime values in equations represent the previous time step. These equations are used to solve for current at each of the

nodes of the circuit modeling the XRFC. In the circuit diagram in Fig. 2, the nodes are given by the black dots. There are three type of nodes; the first node in between the terminal resistor R_1 and first inductor, all of the middle nodes (with units consisting of inductors, capacitors, and variable resistors), and the last node that is like a middle node with a terminal resistor R_L .

Applying Kirchoff's continuity law at each of the nodes (Fig. 2), three sets of equations are produced:

$$I_1 = I_2 \quad (9)$$

$$I_i = I_{g,i} + I_{i+1} \quad (10)$$

$$I_N = I_{g,N} + I_{N+1} \quad (11)$$

where I_1 is the current through the first terminal resistor, I_2 is the current through the first inductor, I_i is the current into node i from the previous inductor, $I_{g,i}$ is the current from node i through the current capacitor and resistor pair, I_{i+1} is the current from node i into the next inductor, I_N is the current into node N from the last inductor, $I_{g,N}$ is the current from node N into the last capacitor and resistor pair, and I_{N+1} is the current from node N into the last terminal resistor [3].

Substituting equations 4, 6, and 8 into equations 9, 10, and 11 yields:

$$\frac{V_0(t) - V_1}{R_1} = \frac{\Delta t}{2L} (V_1 - V_2 + V_1' - V_2') + I_2' \quad (12)$$

$$\frac{\Delta t}{2L} (V_{i-1} - V_i + V_{i-1}' - V_i') + I_i' = \frac{C}{\Delta t} (V_i - V_i') + I_{i+1}' + \frac{\Delta t}{2L} (V_i - V_{i+1} + V_i' - V_{i+1}') \quad (13)$$

$$\frac{\Delta t}{2L} (V_{N-1} - V_N + V_{N-1}' - V_N') + I_N' = \frac{C}{\Delta t} (V_N - V_N') + \frac{V_N}{R_L} \quad (14)$$

where $V_0(t)$ is the voltage from the pulse generator, R_1 is the first terminal resistor, R_L is the last terminal resistor, V_1 is the voltage from the first terminal resistor, V_2 is the voltage from the first inductor, V_i is the voltage at the current node, V_{i-1} is the voltage at the previous node, V_{i+1} is the

voltage at the next node, V_{N-1} is the voltage at the second to last node, and V_N is the voltage at the last node, which is also the voltage across the last terminal resistor [3]. At this stage the variable resistances of Fig. 2 used to model currents due to x-rays have not been included.

Finally, solving for voltage and rearranging equations 12, 13, and 14 so that all the current values are on one side and previous time steps are on the other gives:

$$\left(\frac{1}{R_1} + \frac{\Delta t}{2L}\right)V_1 - \frac{\Delta t}{2L}V_2 = -I_2' + \frac{V_0(t)}{R_1} - \frac{\Delta t}{2L}(V_1' - V_2') \quad (15)$$

$$\left(\frac{\Delta t}{L} + \frac{C}{\Delta t}\right)V_i - \frac{\Delta t}{2L}V_{i-1} - \frac{\Delta t}{2L}V_{i+1} = I_i' - I_{i+1}' + \frac{C}{\Delta t}V_i' + \frac{\Delta t}{2L}(V_{i-1}' - 2V_i' + V_{i+1}') \quad (16)$$

$$-\frac{\Delta t}{2L}V_{N-1} + \left(\frac{1}{R_L} + \frac{\Delta t}{2L} + \frac{C}{\Delta t}\right)V_N = I_N' + \frac{\Delta t}{2L}(V_{N-1}' - V_N') + \frac{C}{\Delta t}V_N' \quad (17)$$

In order to calculate the voltage for each node, Eqs. 15-17 show that the voltages and currents from the previous time step need to be known. At $t=0$, V' and I' are zero at each node. For the first step in the simulation, the only non-zero term on the right hand side of Eqs. 15-17 is $V_0(t)/R_1$. Solution of these equations provides the voltages at the end of this step. The currents at the end of this step are then obtained from Eq. 8. A bootstrap process occurs where these voltages and currents become the V' and I' values for the next time step.

Equations 15, 16, and 17 are a linear system of equations that can be written as a matrix equation:

$$[A][k]=[D] \quad (18)$$

where A is a matrix containing all the coefficients on the left hand side of equations 15, 16, and 17; k is a column vector containing all the unknown voltages; and D is a column vector of the

constants on the right hand side of equations 15, 16, and 17 (previous time step) for each node.

The matrix equation is in the form:

$$\begin{bmatrix} b_1 & c_1 & & & 0 \\ a_2 & b_2 & c_2 & & \\ & a_3 & b_3 & \ddots & \\ & & \ddots & \ddots & c_{N-1} \\ 0 & & & a_N & b_N \end{bmatrix} \begin{bmatrix} V_1 \\ V_2 \\ V_3 \\ \vdots \\ V_N \end{bmatrix} = \begin{bmatrix} D_1 \\ D_2 \\ D_3 \\ \vdots \\ D_N \end{bmatrix} \quad (19)$$

In the program TOAST, the fast and efficient tridiagonal matrix method was used to solve this equation. Tridiagonal matrices contain entries of 0 except for the main (b), super (c), and sub-diagonals (a). The matrix equation can be written in the form,

$$a_i V_{i-1} + b_i V_i + c_i V_{i+1} = D_i \quad (20)$$

Except for the first and last entries of the a, b, and c diagonals, an entry a_i contains the coefficient of V_{i-1} , an entry b_i contains the coefficient of V_i , and an entry c_i contains the coefficient of V_{i+1} . The entry b_1 contains the coefficient of V_1 , c_1 contains the coefficient of V_2 , a_{N-1} contains the coefficient of V_{N-1} , and b_N contains the coefficient of V_N . This is due to the fact that the equations for the first and last nodes (Eqs. 15 and 17) have only two variables.

As mentioned previously, Δt is the time step of numerical derivation for calculating the voltage values in the simulation of the XRFC for the program TOAST. Later on it will be shown to be the time step for numerical integration to calculate the raw XRFC image(s) of the simulation. It must be significantly smaller than the time delay constant (τ) of the transmission line ($\Delta t \ll \tau$). The time delay constant is the time at which the circuit will appear as it would at $t = \infty$. For example, at $t = \infty$ capacitors will appear to be breaks in the circuit and the voltage V_i will be seen across the last terminal resistor. The time delay constant is given by the equation:

$$\tau_{TX \text{ Line}} = \sqrt{LC} \quad (21)$$

where L and C are inductances and capacitances per unit length Δx (distance between nodes) [4].

The characteristic impedance of the transmission line (Z_0) governs the velocity at which the voltage pulse can propagate through. Higher impedance results in a slower velocity, whereas lower impedance results in a faster velocity. For a stripline MCP, the experimentally derived equation is:

$$Z_0 = \frac{\eta_0}{\sqrt{\epsilon_r}} \left(\frac{a}{b} + \frac{1.0}{\pi} \ln(4) + \frac{\epsilon_r + 1.0}{\pi} \ln \left(\frac{\pi e \left(\frac{a}{b} + 0.94 \right)}{2.0} \right) + \frac{\epsilon_r - 1.0}{2\pi\epsilon_r} \ln \left(\frac{e\pi^2}{16.0} \right) \right)^{-1} \quad (22)$$

where η_0 is the impedance of free space (about $120\pi \Omega$), ϵ_r is the relative permittivity constant of the MCP dielectric (3.8 for glass), a is half the width (w) of the stripline, and b is half the height or thickness (h) of the stripline [5]. The relationship between the terminal resistances and the characteristic impedance of a transmission line is very important because when they are matched a pulse consisting of a perfect sine wave will have all of its energy absorbed completely by a terminal resistor. More energy being absorbed at the end of the line means a less powerful voltage reflection when the pulse hits the back of the line and rebounds. Voltage reflections can cause great distortions in XRFC images. A perfect sine wave is impossible to create and more complex shapes are required for an XRFC; however, closely matching terminal resistances to the characteristic impedance minimizes voltage reflections [4].

Capacitance (C_0) and inductance (L_0) of the transmission line (not per unit length) are related to the characteristic impedance by the equation:

$$Z_0 = \sqrt{\frac{L_0}{C_0}} \quad (23)$$

Capacitance of the transmission line is given by the equation:

$$C_0 = \frac{\epsilon_r \sigma}{h} \quad (24)$$

where σ is the surface area of the MCP (width w multiplied by length λ of the MCP):

$$\sigma = \lambda w \quad (25)$$

and ϵ is the absolute permittivity of the MCP dielectric calculated by the equation:

$$\epsilon = \epsilon_r \epsilon_0 \quad (26)$$

where ϵ_0 is the permittivity of free space. Substituting in equation 24 for C_0 and solving equation

23 for L_0 yields the equation for finding the inductance of the line:

$$L_0 = Z_0^2 \left(\frac{\epsilon \sigma}{h} \right) \quad (27)$$

Thus, the inductance per unit length or the inductance per node (L) is simply:

$$L = \frac{L_0}{\lambda} \quad (28)$$

The induced currents from the incoming x-rays striking the MCP change the impedance of the line, thus continuously altering the velocity of the voltage pulse. Without the effects of the incoming x-rays, the velocity (v) of a voltage pulse propagating unhindered through a

transmission line can be expressed as a relationship between the relative permittivity of the MCP

dielectric (ϵ_r) and the speed of light (c): $v = \frac{c}{\sqrt{\epsilon_r}}$ (29)

Finally, the voltage pulse itself was modeled by a simple square wave, although more complex pulse shapes can be and often are used. A super-gaussian equation was used to approximate a perfect square wave:

$$V_0(t) = V_0 \exp \left(- \left(\frac{t - t_0}{\tau_w} \right)^a \right) \quad (30)$$

where V_0 is the maximum voltage of the pulse, t_0 is the halfway time of the pulse, τ_w is the pulse width, and a determines how “flat” and “square-like” the pulse is (a high a value is desired).

High voltage pulses are required for a gain to occur on the MCP of the XRFC. A pulse width of 50 ps and a time delay on the pulse of 50 ps from the start of the simulation were used.

3.2 X-ray Gain and Induced Current

As mentioned previously, the propagating voltage pulse produces a gain in the MCP. This is due to a negative electric field produced by the pulse that accelerates electrons through the channels of the MCP. These electrons gain enough energy to knock off more electrons from the walls of the channels, which are at an 8° tilt so that electrons will strike the walls more frequently. Throughout the channels of the MCP, the cycle of electrons gaining energy and kicking off more electrons creates an avalanche of electrons which is the source of the gain. The gain (G) of the MCP, defined as the number of electrons produced per x-ray photon, is given by the voltage to a power (x) multiplied by a constant of proportionality (k) [2]:

$$G = k(V^x) \quad (31)$$

From the Photonis material data sheets on their XRFC's, a power of 8.399 and a k value of $1.27064 \cdot 10^{-22}$ were determined [6]. The power is roughly the average number of times an electron would strike the walls of a channel in its path through the MCP [2]. The number of electrons (N_e) in a section of the MCP increases due to the x-ray flux and decreases as a result of electrons created by the avalanche leaving through the bottom surface of the MCP. It is governed by the following equation:

$$\frac{dN_e}{dt} = G\phi_{x\text{-ray}} - \frac{I_{x\text{-rays}}}{q_e} \quad (32)$$

where $\phi_{x\text{-ray}}$ is the number of x-ray photons incident per unit time, $I_{x\text{-rays}}$ is the current leaving through the bottom of the MCP, and q_e is the charge of an electron. The x-ray flux is

related to the intensity (ψ) in Watts/cm² of incoming x-rays and the work function of the gold electrode (W_{Au}):

$$\phi_{x-ray} = \frac{\psi p w \Delta x}{W_{Au}} \quad (33)$$

where $w\Delta x$ is the surface area of the node. Porosity (p) is included in the equation due to the fact that the top metal electrode is not solid gold, but it is perforated to allow electrons generated at the top of the electrode by incident x-rays to travel down into the channels of the MCP.

The current leaking through the node on the MCP is given by the equation:

$$I_{x-rays} = n_e q_e v (w \Delta x) \quad (34)$$

where n_e is the number of electrons per unit volume at the bottom of the MCP and v is their final velocity after acceleration through the MCP (calculated below). In this model n_e is approximated by N_e/δ , where δ (equal to $hw\Delta x$) is the volume of the node. This gives

$$I_{x-rays} = \frac{N_e q_e v}{h} \quad (35)$$

so that equation 32 becomes:

$$\frac{dN_e}{dt} = G\phi_{x-ray} - \frac{N_e v}{h} \quad (36)$$

This is integrated over a time step Δt to give

$$N_e = N_e' + \Delta t \left(G\phi_{x-ray} - \frac{N_e' v}{h} \right) \quad (37)$$

Equation 37 states that the current number of electrons at any time t is the number of electrons that were in the node at the previous time step plus the number of electrons generated by striking x-rays minus the number of electrons that have since left the node. Initially, N_e' is equal to zero. In solving Eq. 37 care is taken to ensure that Δt is sufficiently small that N_e does not become negative.

The current $I_{x\text{-rays}}$ is added to the current at a node from the propagating pulse. One consequence of this is that it steals energy from the voltage pulse. The voltage pulse under a section of the MCP that is illuminated by x-rays will be attenuated. To produce an image or signal (S) from the simulated XRFC, the $I_{x\text{-rays}}$ currents at each node are simply integrated for the time interval [a,b] of the simulation:

$$S = \int_a^b I_{x\text{-rays}} dt \quad (38)$$

To calculate the velocity v of the electrons leaving the MCP, note that the strength of the electric field (E) from the voltage pulse is related to the voltage at a node i (V_i) and the separation between electrodes (in this case the thickness h of the MCP) by the equation:

$$E = \frac{V_i}{h} \quad (39)$$

The force on an electron (F_e) from the E-field is related to q_e and the strength of the field:

$$F_e = q_e E \quad (40)$$

Applying Newton's second law of motion, one obtains the form:

$$F_e = q_e E = m_e a_e \quad (41)$$

where a_e is the acceleration of the electron due to the E-field and m_e is the mass of the electron.

The mass of one electron is approximately $9.10938 \cdot 10^{-31}$ kg and the charge of one electron is $1.602177 \cdot 10^{-19}$ C. Solving for a_e yields the equation:

$$a_e = \frac{F_e}{m_e} \quad (42)$$

The distance traveled by a projectile is related to its initial velocity (v_0), acceleration (a_e), and time (t). The vertical distance traveled by an electron in a channel is thus given by:

$$d_y = v_0 t + \frac{1}{2} a_e t^2 \quad (43)$$

After an electron has traveled down a portion of a channel, it is assumed that it will

lose all kinetic energy due to collisions with the wall so that the previous velocity v_0 is always zero. The average distance traveled by the electron is the quotient of the thickness h of the MCP divided by the average number of hits against the wall. From equation 31 the average number of hits is x , which is approximately 8.399. Substituting in for d_y :

$$\frac{h}{x} = \frac{h}{8.399} = \frac{1}{2} a_e t^2 \quad (44)$$

Now the equation can be solved for t :

$$t = \sqrt{\frac{2h}{8.399a_e}} \quad (45)$$

The final velocity can be calculated from the initial velocity, acceleration, and time:

$$v = v_0 + a_e t \quad (46)$$

Substituting in equation 45 for t yields:

$$v = \sqrt{\frac{2ha_e}{8.399}} \quad (47)$$

Equation 47 gives the velocity of an electron as it accelerates through the E-field created by the voltage pulse propagating through the MCP. This velocity is crucial for calculating the current through a node $I_{x\text{-rays}}$ induced by x-rays as mentioned above. The current feeds back into the transmission line equations (Eqs. 15-17) and the detected signal on the CCD camera depends on the total charge provided by this current.

Results

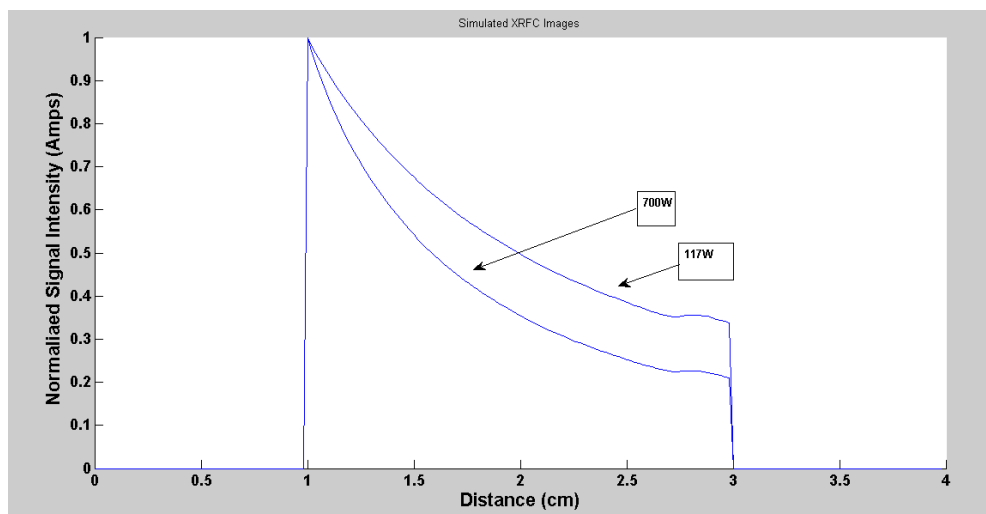


Fig. 3. Time-integrated signal as a function of distance along an MCP calculated by TOAST, run at two different x-ray intensity levels, 700 and 117 W/cm². Notice the attenuation of the voltage pulse as it traveled through a portion of the MCP (1 cm to 3 cm) illuminated by x-rays. Higher intensity resulted in more attenuation.

Utilizing equation 38, graphs were calculated of the signal that a phosphor screen would see from a simulated XRFC in TOAST with the portion of the MCP from 1 cm to 3 cm uniformly illuminated by x-rays. Figure 3 shows two such graphs for different x-ray intensities, illustrating that attenuation of the voltage pulse occurred as it traveled through the portion of the MCP illuminated by x-rays. Experimental data taken from shot #64187 conducted on the OMEGA laser system [7] and shown in Fig. 4 agrees qualitatively with the simulation results. Two different exposures of an XRFC were done, both with a uniform source of x-rays. The first exposure was done with a normal flat-fielding exposure of x-rays. The second XRFC had a mask that only allowed a small sliver of x-rays to reach the MCP. This showed a much less attenuated signal as the pulse swept across the XRFC compared with the one with full exposure.

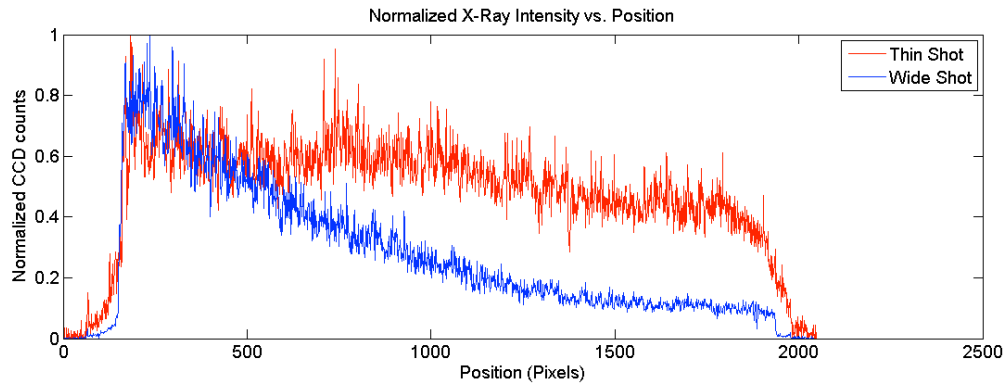


Fig. 4. Normalized X-ray Intensity vs. Position for two XRFCs on OMEGA Shot 64187
The first exposure (blue) was from a normal uniform x-ray source used in flat-fielding images. The second image (red) had a mask that only allowed a small sliver of x-ray light through (width about 1 mm reduced from 6 mm). Average x-ray intensity on the OMEGA system is approximately 700 W/cm^2 .

Voltage reflections were also shown to occur in the simulation as seen in Fig. 5. TOAST has the ability to draw an animation of the propagating pulse as it moves through the XRFC.

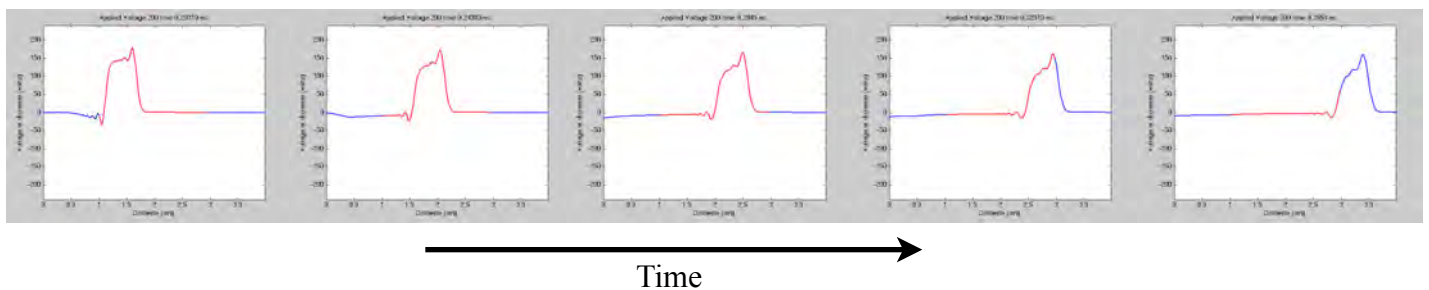


Fig. 5. TOAST Animation
These are snapshots of an animation generated by TOAST of the propagation of a voltage pulse through an XRFC. The red region is illuminated by x-rays of intensity 700 W/cm^2 . Note the attenuation of the voltage pulse under the illuminated section of the MCP.

Voltage reflections occurred at the terminal ends of the transmission line as well as at boundaries of illuminated and non-illuminated portions of the XRFC. Higher intensity x-rays and voltage pulses produced greater reflections. The closer the terminal resistances matched the impedance of the line, the smaller the reflections were. However, reflections will always occur at boundaries between two different x-ray intensities. Figure 5 also shows significant distortion of the initial voltage pulse.

4. Conclusion

A one-dimensional mathematical model was produced to characterize an XRFC. The propagation of a pulse through the MCP of an XRFC was simulated using a computer program. Results indicate that the relationship between the intensity of x-rays hitting the XRFC and the signal recorded is not linear as assumed while using flat-fielding correction methods for raw XRFC images.

XRFC images are used to monitor the deformations of the shell during implosion, so one major consequence of the current method of correcting images is that the shell thickness would be inaccurately portrayed. Being able to accurately measure the shell thickness is vital in analyzing how successful certain beam configurations are for inertial confinement fusion on laser systems such as OMEGA. A potential solution for this problem would be to utilize a simulation of the XRFC such as TOAST and use as input the raw XRFC image. The outputted image would then be fed back into the program iteratively until the changes between images are minimal. Through each generation, the image will be closer to the original x-ray source.

Further research will aid in the development of the code. The goal is to incorporate other effects such as crosstalk between different sections of the XRFC itself as well as improving and adjusting models for the MCP and incoming x-rays. Running multiple instances of TOAST in parallel would potentially allow for the generation of two-dimensional images, which would provide a much more effective visualization of the interaction of the pulse with the XRFC system.

Acknowledgements

I would like to thank Dr. William Donaldson and Dr. Dustin Froula for advising and helping me with the project, Mr. Raymond Bahr for the use of a Manson source, and program director Dr. R. S. Craxton for coordinating the program for all the students involved. In addition, thanks to the Laboratory for Laser Energetics for the wonderful research opportunity.

References

- [1] Gresh, Louis H. *Inertial Confinement Fusion An Introduction*. University of Rochester, Rochester. March 2009. Print.
- [2] D. K. Bradley, P. M. Bell, J. D. Kilkenny, R. Hanks, O. Landen, P. A. Jaanimagi, P. W. McKenty, C. P. Verdon, "High-Speed Gated X-ray Imaging for ICF Target Experiments," *Rev. Sci. Instrum.* 63 (10), 4813-4817 (1992).
- [3] "Transmission-Line Modeling of Photoconductive Switches," W. R. Donaldson and L. Mu, in *Optically Activated Switching III*, edited by R. A. Falk (SPIE, Bellingham, WA, 1993), Vol. 1873, pp. 201-207.
- [4] Brophy, James J. *Basic Electronics for Scientists*. New York: McGraw-Hill Inc., 1972. Print.
- [5] Wadell, Brian C. *Transmission Line Design Handbook*. Boston: Artech House Inc., 1991. Print.
- [6] <http://www.photonis.com/en/ism/38-longlife-micro-channel-plates.html>. Web. Nov. 10, 2012.
- [7] J. Kwiatkowski, F. J. Marshall, and W. Armstrong, private communication (2012).

Dynamic Mechanical Analysis of Cryogenic

Target Materials

Charles Wan

Penfield High School

Advisor: Kenneth L. Marshall

University of Rochester

Laboratory for Laser Energetics

Summer High School Research Program 2012

Abstract:

Adhesive strength is of critical importance for cryogenic laser-fusion targets when bonding the plasma-polymerized polystyrene copolymer plastic target shell to the support stalk (a narrow-diameter fiber of silicon carbide or Zylon PBO). Norland 68 and Dymax 921 gel, two rapid-curing, low-to-medium viscosity UV curable adhesives, are currently used for target fabrication depending on which fiber material is employed. Neither of these adhesives is rated for operation at cryogenic temperatures, and the interfacial bonding strength of these adhesives to the target shell has not been thoroughly characterized, other than through in-use testing. To compare the interfacial strengths of these two adhesives, a sample preparation method involving a polystyrene loop glued to a polystyrene strip was developed and tested with a Perkin Elmer DMA8000 dynamic mechanical analyzer. This instrument is capable of determining mechanical properties over a wide range of temperatures and dynamic loads. Although results showed some scatter in adhesive-strength data points for both Norland 68 and Dymax 921 gel at cryogenic temperatures, test runs revealed that a decrease in temperature resulted in an increase in interfacial bond strength between the adhesives and the polystyrene. Further research in sample preparation could lead to more consistent results.

Introduction:

The Laboratory for Laser Energetics at the University of Rochester conducts nuclear fusion through the direct-drive approach to inertial confinement fusion using the 60-beam OMEGA laser. In a direct-drive shot, lasers irradiate a cryogenic spherical target containing deuterium and tritium (isotopes of hydrogen). If the target reaches a

density of 200-300 g/cm³ and a temperature of approximately 100 million degrees Celsius, a state of ignition can be achieved, in which the fusion reactions of the hydrogen are self-sustaining.¹ Nuclear fusion is a source of clean, renewable energy, and could be a solution to sustainability issues.

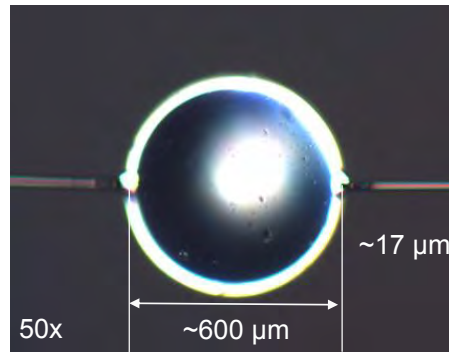
Cryogenic targets are glued to support stalks at room temperature with either Norland 68 or Dymax 921 gel, depending on which fiber material is employed. In the Type 1 geometry, a single stalk of 17 μm silicon carbide fiber is attached to the target with Norland 68, while in Types 4,5, and 6, a tripod with a 14 μm PBO fiber is attached to the target with Dymax 921 gel.² Targets are glued to the stalks at room temperature, bonding the adhesive to the plasma-polymerized polystyrene copolymer plastic shell of the target. The entire setup is cooled at a slow rate until ~20 K is reached. The cooling process can last tens of hours, even days.³ Targets are cooled to cryogenic temperatures to deposit a uniform DT ice layer inside the target. The main purpose of freezing targets is for efficiency; a frozen solid has a much higher density than a warm gas, which makes the initial compression require less energy.¹ Prior to the shot, while targets are sitting stationary, being cooled, or being transferred, several failure modes can occur. In extremely rare cases, the bulk adhesive will fracture. Sometimes, fibers will detach from the target and the adhesive. However, the most prevalent failure mode by far is that the target will separate from the adhesive while the adhesive remains intact. This indicates that the interface of the adhesive bonded to the polystyrene experienced failure. Since little prior research has been conducted in this area of interfacial strength, objectives included characterizing this strength and making comparisons between the adhesive strengths of Norland 68 and Dymax 921 bonded to polystyrene.

The Perkin Elmer DMA 8000 dynamic mechanical analyzer is an instrument capable of determining mechanical properties over a wide range of temperatures and dynamic loads. The DMA 8000 was used to measure the interfacial strengths of Norland 68 and Dymax 921 gel to polystyrene. The DMA measured the amount of force required to break samples that were created specifically to fit the DMA's loading geometry. The DMA has been used to measure properties such as Young's Modulus, tensile strength, compressive strength, damping, and strain to failure in high performance organic fibers and polymers such as Zylon PBO, Kevlar, and M5 PIPD.^{4,5,6,7}

Experimental:

Since the DMA 8000 requires a specific loading geometry, a sample preparation method had to be developed. The initial attempt to create samples involved taking two 17 μm silicon carbide fibers and gluing them with Norland 68 to opposite ends of a 600 μm solid polystyrene microsphere (Figure 1(a)). Once the fibers were attached, the adhesive was cured and the ends of the fibers were glued across a hole-punched paper so that samples could be loaded and tested with the DMA (Figure 1(b)). This sample preparation method was designed to closely mimic actual target fabrication.

a.)



b.)

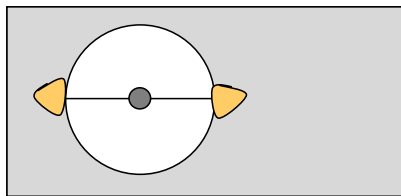


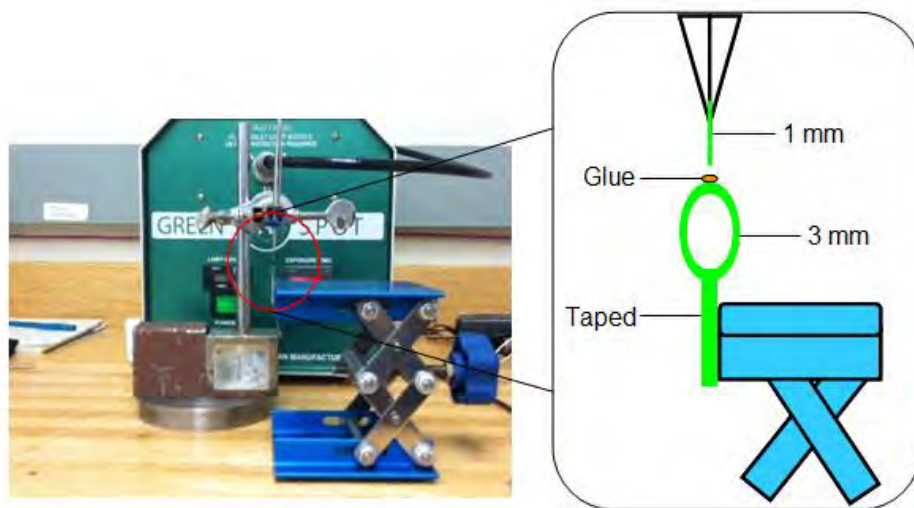
Figure 1: Original sample preparation method. a.) The attachment of the silicon carbide fibers with Norland 68 adhesive to the polystyrene ball is viewed under a Leica microscope. b.) The attached fibers to the polystyrene were glued onto a hole-punched sheet of paper, which was then used to test the strength of the polystyrene to the adhesive in the DMA 8000.

However, some major setbacks prevented this method from being successful. On average, sample preparation time was more than two hours. The glue spot connecting the polystyrene to the silicon carbide experienced natural variation that was uncontrollable. Additionally, samples being loaded into the DMA often had fibers detach from the sphere. Samples were too delicate and fragile, and small amounts of stress or force caused failure.

As a result, a new sample preparation method was developed that was both time efficient and compatible with the DMA. This method, shown in Figure 2, involved gluing a polystyrene strip to a polystyrene loop with 0.5 μL of adhesive. A polystyrene loop was formed by taping the ends of a 3 mm thick, 53 mm long polystyrene strip together. Once

the loop was formed, it was attached to the side of a lab jack. A single polystyrene strip 1 mm wide was held by a chemistry clamp with tweezers. 0.5 μL of adhesive was put on the loop, and the lab jack elevated the polystyrene loop with the adhesive into the polystyrene strip. Once this was done, the adhesive was cured for twenty seconds with a Green Spot UV light source with a wavelength of 300-480 nm. The entire procedure took less than ten minutes, allowing for an efficiency previously unachievable with the old sample preparation method.

a.)



b.)



Figure 2: Pictures of sample preparation setup, materials, and completed sample. a.) The chemistry clamp holds the polystyrene strip, while the polystyrene loop is attached to the blue lab jack. The entire setup is placed in front of the Green Spot light source for immediate curing. b.) This is a completed sample.

Finished samples were loaded into the DMA 8000 (Figure 3). Both room temperature and cryogenic tests were conducted for Norland 68 and Dymax 921 gel samples. For cryogenic tests, samples were cooled at a rate of 5 K/min until 98 K was reached in an effort to mimic the extremely slow cooling rate of actual targets. (Samples were not tested at 20 K because the DMA 8000 is unable to conduct tests at temperatures lower than 98 K.) The lower cooling rate ensured that the adhesive would break in a manner that tested the interfacial strength between the polystyrene and the adhesive, as opposed to the bulk adhesive strength itself. Once samples had been cooled, an increasing load rate of 0.5 N/min was applied on the samples until breakage occurred. The mean force to breakage was measured with the DMA 8000's software on Microsoft Excel.

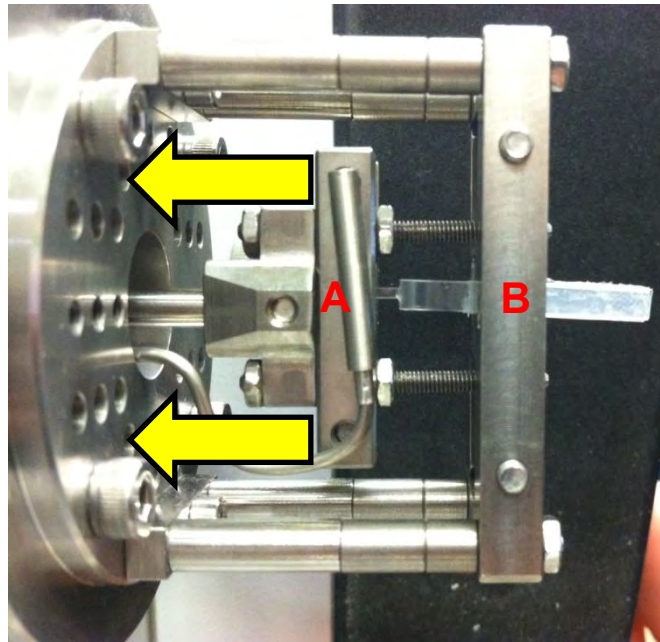


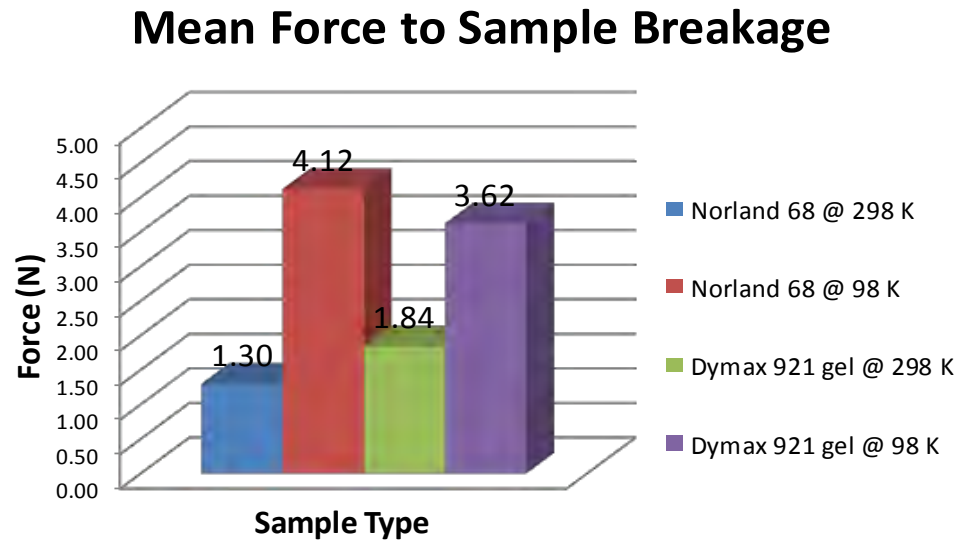
Figure 3: Sample loaded into DMA for testing. Clamp “A” applies the increasing load to the strip, while Clamp “B” holds the loop end of the sample. The force required to break the sample is then measured.

Results and Conclusion:

The results are summarized in Figure 4. The interfacial strength between the polystyrene and the adhesives increased as temperature decreased. For both adhesives, the mean force required to break samples at cryogenic temperatures was higher than the mean force required to break them at room temperature. Although Norland 68 samples required slightly more force at cryogenic temperatures to break than Dymax 921 gel samples, an insufficient number of data points prevented a statistically significant comparison between the two adhesives. Standard deviations also exist within results that make a direct comparison between the interfacial strength of the Norland 68 and Dymax 921 gel with polystyrene not possible due to a relatively wide variation in data.

Of additional importance was that the Norland 68 and Dymax 921 gel samples broke in a “golf-tee” formation (Figure 5), in which the bulk adhesive was not fractured, but the adhesive cleanly broke from the polystyrene on the loop. This is of critical importance because it indicates that the mean force to breakage was measuring the interfacial strength between the polystyrene and the adhesive, as opposed to the bulk adhesive strength.

a.)



b.)

Temp. (K)	Adhesive	Trials	Total Force (N)
298	NOA 68	10	1.30±0.52
	Dymax	8	1.84±1.16
98	NOA 68	9	4.12±0.86
	Dymax	7	3.62±1.15

Figure 4: Summary of results. a.) A graph of mean force to breakage for Norland 68 and Dymax 921 gel at both room and cryogenic temperatures. b.) A table that summarizes results with number of trials and standard deviation for each condition.

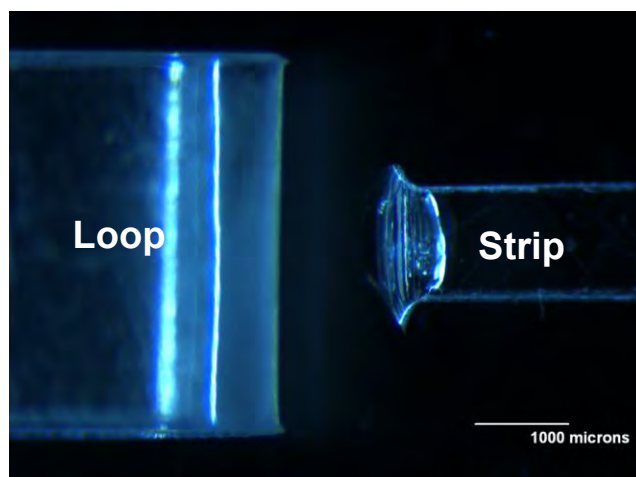


Figure 5: Microscope view of sample after load was applied. The “golf-tee” formation is evident, as the adhesive on the strip made a clean break from the loop.

Future Work:

Since a relatively large standard deviation exists, additional research is needed to maximize consistency in data. Some aspects of the sample preparation method can be altered to achieve more precision. For example, standardizing the glue spot dimensions could stabilize results. Although a volume of 0.5 μL is already the standard, the three-dimensional shape of the glue spot tends to experience variation, which could impact the consistency of results. Additionally, an alternate curing system which would take the entire sample preparation setup and place it onto a turntable with the UV light shining on the sample from a fixed source could lead to more precise data points (Figure 6).

Once consistent data is achieved, future work could focus more on characterizing mechanical properties such as the average strength, Young’s Modulus, damping, and viscoelastic nature of the adhesive to polystyrene interface.

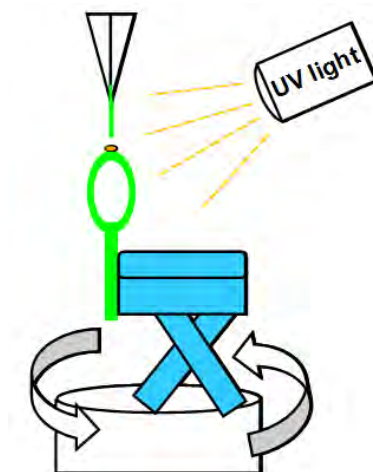


Figure 6: Possible rotating curing system. The entire sample preparation setup would be placed on a rotating stand, as illustrated. A rotating curing system would ensure that the adhesive would be cured in a standardized, consistent method.

Acknowledgements:

I would like to thank the Laboratory for Laser Energetics and Dr. R. Stephen Craxton for giving me the opportunity to conduct research and for reviewing my project report. I would also like to thank my advisor, Mr. Kenneth L. Marshall, for giving me instruction and guidance throughout this experience. Likewise, I am grateful for the additional support from Dr. Stephen Jacobs. Finally, I would like to acknowledge Mathias Ferber, Mackenzie Hall, and Debbie Saulnier for their assistance with the completion of my project.

References:

- 1.) L.H. Gresh, R. L. McCrory, J.M. Soures, “*An Introduction to Inertial Confinement Fusion*,” Laboratory for Laser Energetics, Rochester, March 2009.
- 2.) Brian Rice, Ken Marshall, Stephen Jacobs, “*Project for Target Vibration Reduction at Time of Shot*,” Presentation, March 1st, 2012.
- 3.) Dave Turner, private communication.
- 4.) Mackenzie Hall, “DMA Measurements and comparisons of M5 PIPD and Zylon PBO fibers,” Memorandum, May 25th, 2012.
- 5.) “Assessment of compressive properties of high performance organic fibers,” A. Andres Leal, Joseph M. Deitzal, John W. Gillespie Jr., *Computing Science and Technology* 67 (2007) 2786-2794.
- 6.) “Interfacial behavior of high performance organic fibers,” A. Andres Leal, Joseph M. Deitzal, Steven H. McKnight, John W. Gillespie Jr., *Polymer* 50 (2009) 1228-1235.
- 7.) “Compressive Strength Analysis for High Performance Fibers with Different Modulus in Tension and Compression,” A. Andres Leal, Joseph M. Deitzal, and John W. Gillespie Jr., *Journal of Composite Materials* (2009) 43: 661.